

nature

SCIENCE AND SOCIOLOGY
Made for each other

FIGHTING ADDICTION
Pharmacology meets
behavioural therapy

BLACK-HOLE BINARIES
First of many?

ACTIN-BASED MOTILITY

Signalling network dynamics in
vaccinia-infected cells

REPORTS
Cellular motility

What price health?

When it comes to health care, the balance between cost and effectiveness is a difficult one to strike. The injection of \$1.1 billion into the US system therefore needs to produce sustainable results.

A middle-aged man appears in a US emergency room complaining of chest pains. Tests show that an arterial blockage is starving his heart of oxygen. He could have treatment A, or treatment B. Which one should he and his doctors choose?

The best treatment, presumably, is the one that is more likely to improve his health. But all too often, medical science doesn't know which one that is. This lack of information persuaded US lawmakers to give \$1.1 billion to 'comparative effectiveness' research in the economic stimulus bill last month. Now, health-care policy-makers and researchers must ensure that they make the most of this money.

There is nothing really new about comparative effectiveness research. Defined broadly, it includes anything from literature reviews to head-to-head trials of treatments, drugs, diagnostic procedures or prevention methods. What is new is that the United States is beginning to acknowledge that it needs to do much more of this type of work if it is to mould an affordable, sustainable and effective health-care system.

The new money will be split between the National Institutes of Health (\$400 million), the Agency for Healthcare Research and Quality (\$300 million) and the Department of Health and Human Services (\$400 million). The Institute of Medicine, part of the National Academies, will provide recommendations on how the money should be spent. The agencies must take care to allocate the funding in the most effective way — by focusing on conditions that have the most impact on a population, say, or in which the research will have a real effect on medical practice — not just on those that have the most effective lobbyists. When a clinical trial can cost tens of millions of dollars, \$1.1 billion doesn't sound like much.

A question of cost

Where the really tough questions arise, however, is in how this information will be used. Sometimes the decision is easy: treatment A is much better than B, so A should become standard practice. But what if treatment A is only a little bit better than B, yet costs ten times as much — is it worth it? Decisions about clinical effectiveness are difficult to divorce from those about cost effectiveness.

Some of these decisions are already being faced by countries with established systems for judging clinical and cost effectiveness. The United Kingdom's National Institute for Health and Clinical Excellence (NICE), which advises the country's National Health Service on what it should pay for, is often held up as an exemplar of sophisticated analyses.

In the United States, however, any such discussion has long been political anathema. Many individuals there find it unthinkable to be refused a treatment simply because it is deemed too expensive. Powerful lobbies from pharmaceutical companies and medical associations concur; they do not want to risk having profitable drugs or services excluded from coverage. But the practical effect is that

the health-insurance companies are left to make those decisions by limiting how much they will pay out for any given treatment — with little good evidence about what actually works. This is one reason why the US health-care system costs more than \$2 trillion a year — it is by most measures one of the most extravagant and wasteful in the Western world. At some point, US policy-makers and US citizens alike will have to follow the lead of their counterparts in the United Kingdom and elsewhere, and start making systematic, evidence-based decisions about what to pay for and what to exclude.

These decisions involve cold, hard calculations about the quality and value of life — and how to balance what is good for the individual against what is good for society. When a new cancer drug costs hundreds of thousands of dollars and extends a life by a few months, it uses up money that could pay for many thousands of check-ups or hip replacements that could eventually extend more lives for longer. These are the highly complicated estimates that researchers try to build into their models. NICE's decisions can be enormously unpopular: the agency faced a barrage of criticism in 2008, for example, when it recommended that four kidney-cancer drugs should not be used.

"The US health-care system is by most measures one of the most extravagant and wasteful in the Western world."

Shared resources

One way in which researchers could help is by improving their analytical tools and sharing their information and analyses. A shared database of existing clinical evidence with standardized end points and patient information, for instance, would relieve researchers from having to start literature reviews from scratch each time. Likewise, sophisticated models of disease built on genetic and other information could help researchers model the effects of a particular treatment.

Scientists should also factor in population subgroups when planning their effectiveness research. Treatment A might be better for the population as a whole, but there may be groups, determined by their genetic make-up or disease type, for which B is best. Ideally, these two strands of research would go hand in hand. The \$1.1 billion should not be siphoned off to solve academic puzzles about human genetic variation — but variation should be incorporated where it can help answer questions about who should receive which treatment.

A or B? Evidence is the right place to look for the answer. But for all the health care that can be bought for \$1.1 billion, much more could be bought if comparative effectiveness became a sustainable operation rather than part of a one-off spending spree. Policy-makers and researchers should therefore be careful to show what this money can buy.

Down, but not out

NASA should work immediately to replace the lost Orbiting Carbon Observatory.

Climate scientists suffered a tremendous loss last week when a failed launch attempt sent the Orbiting Carbon Observatory (OCO) plummeting into the ocean near Antarctica. In conjunction with the Greenhouse Gases Observing Satellite (GOSAT) recently launched by Japan, the OCO could have redefined the way that researchers think about the global carbon cycle, and laid the foundations for a long-term global carbon-monitoring programme. It is an unfortunate testament to the OCO that the reasons to fly such a mission are just as valid today as they were when the idea was put forward a decade ago. NASA should accordingly move with all haste towards an OCO II.

Although small changes to improve the device without significantly extending the schedule are welcome, the goal should be speed. NASA has some spare equipment, including detectors, and the agency should therefore be able to get a replacement into space within a few years. This might even allow the OCO to operate in concert with GOSAT for a time, as originally planned, which would allow scientists to better calibrate and understand the quirks of both machines.

The US\$273-million OCO was designed to test a conceptually simple technique for using reflected sunlight to probe carbon dioxide concentrations in the air column below the satellite. This would have allowed scientists to assess the movement of CO₂ throughout the atmosphere, which is just as important to scientists as it is to

policy-makers who are debating international carbon controls. GOSAT provides less detail but greater context by simultaneously measuring CO₂, methane and water vapour.

If money were the deciding factor, perhaps it would make sense to simply wring everything possible out of GOSAT. The new data could then be integrated into the development of a next-generation carbon-monitoring satellite, which would do everything the OCO could do and more. But now is not the time to be frugal.

Indeed, thanks to the recently passed stimulus bill, it is raining dollars in Washington. NASA has already received \$1 billion from the bill, \$400 million of which is slated for Earth science and climate research. Even after paying for an OCO II — which could be delivered more quickly and for less money than its predecessor — NASA would still have plenty of cash left for other projects. In addition, spending money on a replacement would create as many new jobs as anything else at NASA.

In the meantime, NASA could improve its ground measurements and expand the use of aircraft, which offer cheaper and faster opportunities to get high-quality data from all over the world. Given the scientific and geopolitical issues at stake, NASA would be wise to develop a long-term strategic plan for assessing global carbon flows. In particular, it should join with the space agencies of the world to develop a coordinated plan for an international network of satellites to monitor greenhouse gases. As an added bonus, such an approach would build in redundancies that would make a similar “mishap”, to use NASA’s lingo, a bit less consequential. ■

“NASA would be wise to develop a long-term strategic plan for assessing global carbon flows.”

Advice needed

The Obama administration should ensure that science informs the US strategy on nuclear waste.

The fall from grace of Yucca Mountain as the site for a giant government nuclear-waste repository has been a long time coming. Ever since it was named as the sole site for the final disposal of high-level waste in 1987, political opposition has been growing, as has the population of nearby Las Vegas.

That opposition found strength in the weakness of the scientific case for the repository. Lawmakers originally chose Yucca Mountain on the basis of Nevada’s low population and political vulnerability, leaving scientists to find a justification after the fact. But much of what the researchers found undercut the decision. The seemingly quiet desert around the mountain went through a spate of volcanic activity as recently as 75,000 years ago, and although the region seems dry, rain seeps surprisingly quickly through fissures in the rock.

These facts have eroded the once-solid political case for Yucca, and, together with questions of data integrity and technical independence, created a climate favourable to its cancellation. This year, with Barack Obama as president and Harry Reid (Democrat, Nevada) as Senate majority leader, the project could well be dealt a final blow.

Obama says that his administration will devise a new strategy for

nuclear-waste disposal. Policy-makers will presumably be looking at various options including geological disposal, reprocessing of spent fuel and long-term storage at reactor sites. Each option has its advantages and drawbacks, but whatever decision is made, the administration must ensure that the scientific rationale is established beforehand, not the other way around.

In particular, the White House should include scientists in its policy discussions from the start. It should allow its ideas to be peer reviewed, both in the open scientific literature and by independent bodies such as the National Academy of Sciences. Finally, it should work with Congress to ensure that whatever legislation is needed to enact its strategy is similarly underpinned by strong science.

None of this means that the government’s nuclear-waste strategy should be determined by science alone. The final decision will have to balance the conflicting commercial, military and public interests in waste disposal — and the political process, not science, is the only way to do that. In striking that balance, US policy-makers could look to Sweden and Finland, which are shepherding their own, scientifically sound proposals for long-term storage facilities through lengthy political and safety reviews.

That process will take those nations years to complete, and it could take even longer in the decentralized US political system. But as the 20-year, \$9.5-billion Yucca Mountain experiment proved, choosing political expedience over scientific integrity will ultimately lead to a solution that satisfies no one. ■

RESEARCH HIGHLIGHTS

ASTRONOMY

Galactic striptease

Astrophys. J. **692**, 298–308 (2009)

Most astronomers agree that spiral galaxies, which were dominant billions of years ago, morphed into the lens-shaped galaxies that are so prevalent today. One idea describing how this happened assumes the existence of regions of hot gas in the intergalactic space of massive galaxy clusters. The hot gas strips away gas in spiral galaxies as they whip through the intergalactic space, turning them into lenticulars.

But David Wilman of the Max Planck Institute for Extraterrestrial Physics in Garching, Germany, and his colleagues have observed lenticular galaxies forming as easily in sparse groups of galaxies, in which the stripping effect of hot gas is negligible. This suggests that, as some astronomers had suspected, galactic mergers are instead an important mechanism.

PLANT SCIENCE

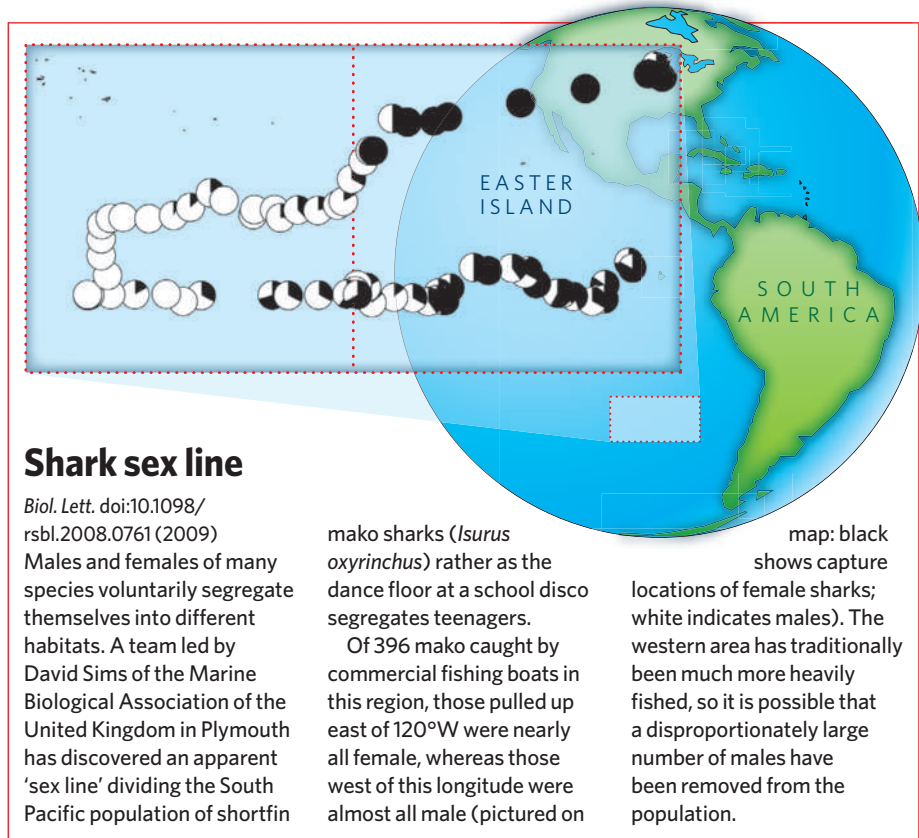
Pigment puzzle

J. Am. Chem. Soc. doi:10.1021/ja809065g (2009)

Researchers at Florida International University in Miami have discovered the 'animal' pigment bilirubin in the seeds of the white bird of paradise tree, *Strelitzia nicolai*. This is the first example of bilirubin occurring naturally in plants.

Cary Pirone and her colleagues cannot yet account for the presence of the bright orange substance, which is a product of the breakdown of the haem chemical group that, in animals, is found in haemoglobin. In plants, haem's normal metabolic product is the light-sensing pigment of the important protein phytochrome.

Although the plant the team studied has white flowers (pictured), the seed part, called the aril, has the hue of oxygenated blood.



Shark sex line

Biol. Lett. doi:10.1098/rsbl.2008.0761 (2009)

Males and females of many species voluntarily segregate themselves into different habitats. A team led by David Sims of the Marine Biological Association of the United Kingdom in Plymouth has discovered an apparent 'sex line' dividing the South Pacific population of shortfin

mako sharks (*Isurus oxyrinchus*) rather than the dance floor at a school disco segregates teenagers.

Of 396 mako caught by commercial fishing boats in this region, those pulled up east of 120°W were nearly all female, whereas those west of this longitude were almost all male (pictured on

map: black shows capture locations of female sharks; white indicates males). The western area has traditionally been much more heavily fished, so it is possible that a disproportionately large number of males have been removed from the population.

ZOOLOGY

Nightingale serenade

Proc. R. Soc. B doi:10.1098/rspb.2008.1726 (2009)

Male nightingales that sing during the night are serenading females, whereas those that sing at dawn are letting other males know that the territory is occupied, report Tobias Roth of the University of Basel in Switzerland and his co-workers.

The researchers caught ten female nightingales (*Luscinia megarhynchos*) and moved them 70 km to a site in the Rhine Valley in France where the team has studied nightingales since 1994. Radio transmitters glued on the backs of the incomers revealed that unpaired females fly around at night visiting several males, at a time when bachelor males are singing more frequently than paired males. All males sing vociferously during the dawn chorus, however.

GENETICS

Hopping hope

Science doi:10.1126/science.1163040 (2009);

Nature Biotechnol. doi:10.1038/nbt.1526 (2009)

Recent studies of human tumours have suggested that solid cancers carry a host of different genetic mutations. Working out

which of these set off the disease is tricky, but a team led by David Largaespada of the University of Minnesota in Minneapolis has found a way.

The group engineered mice that contain a jumping gene, or transposon, that can be switched on or off in specific tissues. When it is turned on, it hops around the genome, disabling other genes by inserting copies of itself into them.

Largaespada and his colleagues have used this approach to identify 77 genes potentially involved in human colorectal cancer and 19 that are strongly implicated in liver cancer, some of which were not previously known to be mutated in human tumours.

NEUROSCIENCES

Child abuse 'scars' DNA

Nature Neurosci. **12**, 342–348 (2009)

Childhood abuse may leave its mark on DNA in ways that have an effect on stress responses decades later.

Previous research has shown that rat pups reared by inattentive mothers accumulate more methyl groups on a region of DNA that regulates the expression of a receptor for glucocorticoid hormones. As a result, fewer receptors are made, potentially enhancing the animal's response to stress.

Now Michael Meaney of McGill University in Montreal, Canada, and his colleagues have tested brain samples from people who committed suicide, and found that those with a history of childhood abuse had a similar methylation pattern to the neglected rat pups. They also had fewer than average glucocorticoid receptors. These measures did not differ between people with no history of abuse who killed themselves and unabused people who died by other means.

MECHANICS

Good vibrations

Phys. Rev. Lett. **102**, 080601 (2009)

Harvesting energy from ambient vibrations, such as those created by walking or the shaking of moving vehicles, is one way to obtain low-cost and renewable power for small electronic devices. Most examples so far convert vibrations into electrical energy using 'linear' oscillators, which miss out much of the typically broad frequency spectrum of vibrations.

Nonlinear oscillators — for example, bistable ones with two stable oscillating states — can do a better job, according to Francesco Cottone at the University of Limerick in Ireland and his colleagues. Their proof of principle is an inverted pendulum comprising a piezoelectric beam, which produces electricity when it bends. This generates four to six times more power from ambient vibrations when it oscillates in a bistable rather than a linear manner.

PALAEOCLIMATOLOGY

Global cooling

Science **323**, 1187–1190 (2009)

Large parts of Antarctica became suddenly and substantially icy about 34 million years ago. Oxygen-isotope records suggest that a simultaneous accumulation in ice cover happened in the Northern Hemisphere, which is now challenged by Zhonghui Liu of Yale University and his colleagues.

They calculate sea-surface temperatures for the period using a pair of chemical proxies (tetraether and unsaturated alkenone) found in sediment cores retrieved from 11 locations around the world. According to their calculations, high-latitude cooling averaged 5 °C.

After plugging their numbers into an ocean-circulation model, the team calculated that ocean cooling could explain the discrepancy in oxygen-isotope records: a Northern Hemisphere glaciation would not have been required.

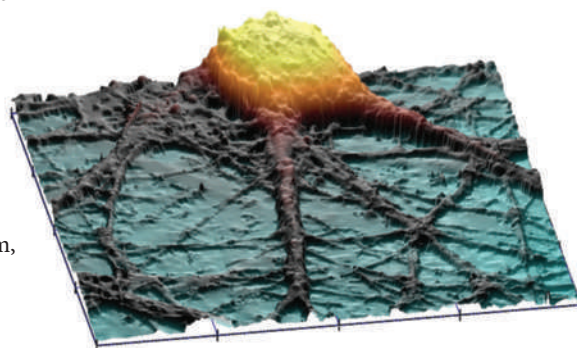
MICROSCOPY

Pogo-stick pictures

Nature Methods doi:10.1038/nmeth.1306 (2009)

There is as yet no way to produce images that capture the three-dimensional convolutions of a living cell's surface without running the risk of deforming the cell. But a team led by Yuri Korchev of Imperial College London, UK, thinks it has cracked the problem by modifying a technique used on relatively flat surfaces called scanning ion conductance microscopy.

The team's method builds up pictures by measuring changes in the ion flow through a fluid-filled nanopipette when its tip comes close to a cell. The team's innovation involves having the pipette 'hop' — that is, approach the sample from above any of its surface features — rather than scanning across the surface. Their image of a mouse cochlear hair cell is shown below.



METAMATERIALS

Taming terahertz

Nature Photon. doi:10.1038/nphoton.2009.003 (2009)

Unlike X-rays, terahertz or 'submillimetre' radiation can penetrate organic samples without damaging them, and so holds promise for medical diagnostics. But there is a stumbling block on the path to such technologies: terahertz waves have proved difficult to manipulate.

Hou-Tong Chen at the Los Alamos National Laboratory in New Mexico and his colleagues have now developed a device that controls the phase of terahertz waves. This makes it possible for researchers to store and transmit information with terahertz radiation by varying the voltage across a 'metamaterial' — one made from tiny components that are similar in size to the wavelength of the terahertz waves.

The metamaterial modulator works as well as analogous devices for manipulating optical waves, but at much higher speeds.

P. NOVAK ET AL.

JOURNAL CLUB

Paolo Tammaro
University of Manchester, UK

A physiologist notes the similarities between animal and plant electricity.

Almost all organisms run on electricity. As an undergraduate, I was intrigued by the fact that the long, single cells of the freshwater plant *Nitella* are nearly identical to those of single nerve fibres. These plant cells generate slow action potentials that are similar to those of human or animal nerves. But the electrical components that span plant and animal membranes — the ion channels and transporter proteins — are usually quite different, as are some of the ions they transport.

Earlier this year, however, two researchers in Italy found that a single mutation can turn an important transport protein from a component that is compatible with animal electrical systems into one that is appropriate for plants. They studied the protein CLC-5, which is abundant in the intracellular vesicles of kidney cells. There, it exchanges chloride ions for protons, and in so doing regulates the vesicles' acid content (G. Zifarelli and M. Pusch *EMBO J.* **28**, 175–182; 2009).

The researchers knew that CLC-5 resembled the plant transporter at CLCa, but they had no idea how closely. In plant vacuoles, which are formed by the fusion of several vesicles, at CLCa exchanges not chloride but nitrate ions for protons. The difference is vital: nitrate is necessary for plants to grow and is stored in the vacuoles of root and shoot cells, whereas chloride has a very different role. It is needed for photosynthesis and for the opening and closing of stomata, which matters mostly in the leaves.

Merely substituting one serine amino acid in CLC-5 with a proline changed the protein from a chloride transporter into a nitrate transporter. I find this fascinating because it provides an even more striking example of the similarities that animals and plants can share, even though their biologies are generally very different.

Discuss this paper at <http://blogs.nature.com/nature/journalclub>

Something wiki this way comes

Last autumn, Merck & Co. announced the closing of subsidiary Rosetta Inpharmatics in Seattle, Washington (see *Nature* **456**, 26–28; 2008). Last week, Rosetta's founder **Stephen Friend** and scientific director **Eric Schadt** announced a bid to sustain the company's innovative network approach. With logistical support from Merck and US\$5 million in catalyst money from private sources, the duo hope to lay the foundations for a non-profit, open-access research platform called Sage. Its aim: building comprehensive databases that scientists can use to develop more predictive models of disease.

What is the impetus for doing this now?

Stephen Friend: In the past 3–6 months, we have seen examples showing that you can build models of disease that are predictive enough that you want to hang new data on them. Our feeling has been that biology has mostly been archivists building up stacks of data, but not really being able to leverage the data that others have used. The Human Genome Project, for example, has provided linear data that set out the variations, rather than giving us an understanding. We have seen examples generated by Eric and his group, in mice and in humans, that showed it is possible to build frameworks that other people could add data to — and at that point, the scale and scope became very large. And we felt that it was right to go ahead and start that now.

How will Sage be structured?

Eric Schadt: We want this to be open access, and we don't want it to be perceived as owned or dominated by anybody. So I think it is very important that it should be at multiple sites, housed in universities through the incubator phase. We're looking in the Seattle area — it will be the first spot we transition into — where we're still in negotiations with the University of Washington and the Fred Hutchinson Cancer Research Center. And then also our lead potential candidate sites — these haven't been nailed down yet but we are in active discussions — are with Yale University as well as in the Bay Area, at the University of California, San Francisco.

How do you envision the evolution of this open-platform system?

ES: We view the incubation period as being 3–5 years. After that time, this stuff all gets turned loose, in a similar way to Facebook. Facebook started at Harvard University, learned all the necessary rules, developed those tools, and then expanded to other universities, and then to the entire public. That is the kind of thing that, at the end of 3–5 years, we'd be opening up: a truly open-access public platform.



MERCK & CO.

Stephen Friend (left) and Eric Schadt want to launch a predictive open-access medical database.

SF: I think one of the things that has got us excited is that Sage (<http://sagebase.org>) provides us with a mechanism by which important efforts that are already going on in understanding patients — in the National Institutes of Health, in government, in Europe, among companies, among private foundations — all get to come together and aggregate.

What areas of medical research might benefit most from your efforts?

SF: During the incubator phase, we felt as though we have to limit it to two or three disease areas. Because so much of the data generated already is in the area of metabolic diseases, diabetes and obesity, we feel as though that has to be one of the core areas. Another core area that we think is ripe for this type of analysis is oncology. And we're looking to see what other area we might do.

What effect might this have on how scientists approach these disease models?

SF: There is an opportunity to revolutionize how biologists who are in individual labs interface with those who build large data sets. There is a real separation between haves and have-nots that has meant that the people who have intense knowledge of disease biology at a protein–protein, biochemical level, are not

able to interface with those who are building the more genomics-oriented data sets. Our hope is that this can bring together those two groups to work on models in which individual experiments can actually inform the large sets.

ES: This is one of the first efforts to provide these individual researchers with a way to access that scale of information in ways they understand and that affect their research.

Where do you see this effort heading within the next 10 years?

ES: My vision, 5–10 years from now, is of an open-access platform through which research scientists, clinicians and maybe even patients can access petabyte [10^{15} bytes] and maybe even exabyte [10^{18} bytes] scales of data. Where models of disease are actively being used to inform decision-making. And not just where people take, but where they contribute back. So as scientists query their data sets against this platform, they are actively contributing that data to the platform to make it even better. You can think of it as a Wikipedia type of thing where you have this active-contributor network-based approach that just makes the information more and more informative. ■

Interview by Bryn Nelson.

SPECIAL REPORT

Public universities left reeling by recession

Slumping state revenues are putting US public universities under pressure. **Rex Dalton** reports on how one institution is coping.

TUCSON, ARIZONA

At the University of Arizona in Tucson, the weekly finance cabinet meeting now resembles a council of war. Under the watchful eye of Hopi warriors in a painting, president Robert Shelton and other top administrators try to plot a course through financial and political landmines.

In January, the state of Arizona cut \$55 million from the \$418 million it had planned to give the university this fiscal year. That came atop a \$20-million cut, out of \$438 million, last July. Even more bad news is expected for the fiscal year beginning 1 July.

It is a dire scene being echoed at campuses across the United States as public universities struggle through the annual legislative budget processes in the worsening economic downturn. Private universities are facing their own challenges, including plummeting endowments¹ and shrinking philanthropic gifts. The problem for public universities, though, is especially acute in the sunbelt states such as Arizona, where the burst of the housing bubble has hit tax revenues hard and slashed the budgets of universities that, until recently,



had ambitious expansion plans.

Driven by the philosophy that technological discoveries make a state competitive, universities and legislatures nationwide — particularly in states experiencing rapid population growth — have been pouring public dollars into research

programmes.

California created major research complexes associated with University of California campuses, but since then has struggled to fund their operating budgets. Florida set up satellite complexes of some of California's powerhouses, such as the Scripps Research Institute in La Jolla, which last week dedicated its facility in the Florida town of Jupiter.

Arizona pumped more than \$500 million into research facilities, and the Arizona College of Medicine and Arizona State University (ASU) collaborated to build a satellite campus in downtown Phoenix². That medical complex was supposed to serve as the heart of a larger biotechnology cluster³ — but after a cut in the building budget of nearly \$100 million in January, the partner universities are now looking instead to secure \$375 million in bond



The University of Arizona has used state monies to fund ambitious expansion plans.

funds this spring in order to keep the project on track.

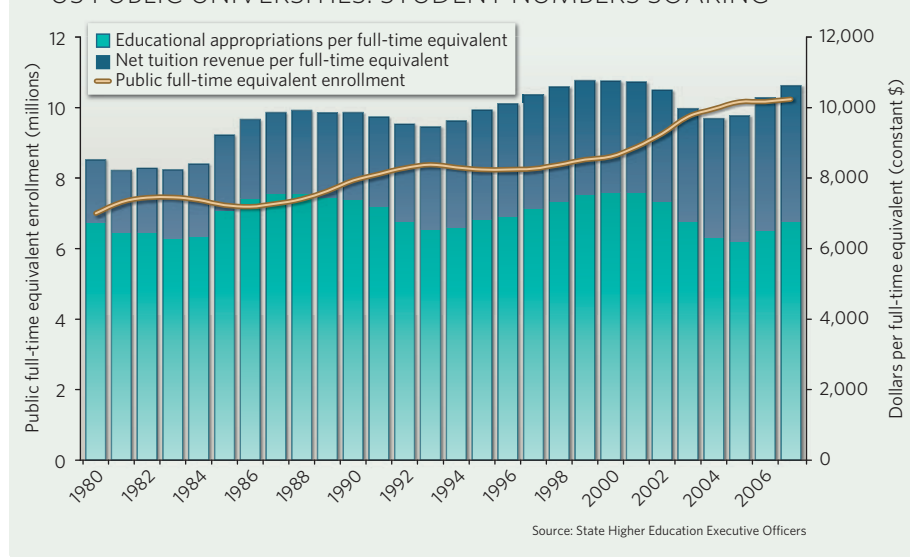
In Florida, the University of Central Florida (UCF) in Orlando and Florida Atlantic University in Boca Raton are similarly building new medical schools as state funding evaporates⁴. UCF's first \$92-million research facility is set to open in April, but the university started the second \$62-million medical education building on a \$40-million credit line, because expected state funds were not forthcoming. How does the university expect to pay the credit line back? "Lots of bake sales and car washes," says provost Terry Hickey, in the gallows humour of the day. Both universities are now lobbying the state for money; UCF's first 40-student class is due to start in August. "We will fund it one way or another," Hickey says.

Anti-education stance

Arizona's problem is particularly challenging because it faces not only the recession pressures but also a state legislature stocked with Republican ideologues who talk of eliminating the nearly \$1 billion provided annually to the University of Arizona, ASU and Northern Arizona University in Flagstaff. "It is a militia legislature," says Meredith Hay, provost at the University of Arizona. "They are playing politics with the university budgets."

Hay, a cardiovascular physiologist, arrived in May from the University of Iowa, where she had served as vice-president for research. In Iowa

US PUBLIC UNIVERSITIES: STUDENT NUMBERS SOARING





City, she had dealt with challenging legislators, but nothing like she has experienced in Arizona. “They want to go backward,” she says.

Leading the way in the legislature’s push to slash university budgets is state Senator Russell Pearce. A former longtime sheriff’s deputy in Phoenix known for putting county prisoners in tents to swelter in the summer heat, he argues that state funds are best spent on law enforcement. Shelton says that Pearce has argued for ‘a zero budget’ for state universities, saying university education should be privatized. (Pearce received a college degree from the University of Phoenix, the largest for-profit university in the nation.)

Like many states, Arizona’s legislature meets for set times, then sends its budget to the governor for approval. Former Arizona governor Janet Napolitano, a Democrat who presided over many of the recent university expansions, has left to join Barack Obama’s administration as secretary of homeland security. Napolitano was replaced by Arizona’s secretary of state Jan Brewer, a career Republican politician. Brewer is expected to support cuts proposed by the Republican legislators, who control both state houses. Neither Brewer nor Pearce responded to *Nature*’s requests for comment, but the next step in the process will come this spring, as the outlook for the state’s annual tax revenue becomes clearer.

Hay and Shelton will be on the front line of that battle, marshalling numbers to strengthen

their arguments. The University of Arizona receives around \$500 million annually in external grants for all research. It is consistently a top recipient of physical-science research funds from the National Science Foundation; in 2007, it was first among all universities in this category, beating out such private heavyweights as the California Institute of Technology in Pasadena. With federal research budgets climbing (see page 18), there could be more on the way. Last month, at a legislative committee hearing at a local high school, Shelton and Hay argued forcefully that state investments are similarly needed: “Every state dollar appropriated to Arizona generates \$6 to \$7 in economic activity,” Shelton told the assembled crowd.

Fund raising

Even so, Hay spends much of her days trying to figure out new revenue sources. At US universities, a provost is a chief operating officer, handling daily administration while the president grapples with the broader issues. Last month, as a *Nature* reporter shadowed Hay for a day, she and Shelton went to the war room to debrief from a meeting the evening before with key legislators and the university’s board of regents. Under discussion were nitty-gritty details of how to increase tuition without violating the state constitution, which requires low levies. One tough question is how to raise class enrollment fees — the current fee of \$270 may increase several-fold — in a way that would be accepted by both legislators and students.

At the same time, some of the very researchers the universities have sought to attract are



“It is a militia legislature. They are playing politics with the university budgets.”

— Meredith Hay

leaving, turned off by the state legislature’s anti-education stance. University of Arizona chemist Mary Wirth is a perfect example. After five years, a colleague notes, “she didn’t see a future here”. The day *Nature* visited, Wirth was buying a house in Lafayette, Indiana, having been recruited by Purdue University. “I probably wouldn’t have talked to Purdue if things were different here,” she says. “I haven’t had a salary increase in five years.” Her husband Dennis Evans, also a chemist at the university, will depart with her.

Wirth had been exactly the sort of person the sunbelt universities were trying to attract.



DEVELOPMENT FUNDING
African grant comes with no strings attached.
www.nature.com/news

PUNCHSTOCK

An interdisciplinary researcher, she worked at the university’s BIO5 Institute and founded a spin-off company through Arizona’s Center for Innovation. The company, bioVidria, capitalizes on her team’s research showing that slides or wells coated with silica can produce faster and more distinctive reads during low-expression microarray analyses⁵. Ironically, the director of BIO5, plant biologist Vicki Chandler, also departed last month, to head science at the Gordon and Betty Moore Foundation in California.

Asked about such losses, Hay puts on a good poker face. But she continues to struggle with which finances to cut. More than 90% of department budgets at the university involve staff, so few cuts can be made without affecting personnel. For researchers, that means potential cuts in teaching-assistant allocations, which translates to more professorial teaching and less lab time. For students, that means that degrees in less popular specialities — such as some types of engineering — are being phased out. And for youngsters considering a science career, it means closings or minimal visiting hours at museums. These include the Flandrau Science Center that heralds Arizona’s internationally renowned successes in optics and astronomy, including the Phoenix mission to Mars.

Over the past few months, Hay has emerged not with a reputation as a hatchet wielder, but as an academic executive who has learned quickly how to work with faculty leaders. Nutrition scientist Wanda Howell, who is in her second elected term as head of the 1,400-member faculty, says that Hay has gone from talking about what cuts had to be made to working with the faculty to boost university strengths to overcome the financial crisis. “Hay is a phenomenon,” says Howell. “She is incredibly bright; there isn’t much she misses.”

Back in her office, Hay stares at a desk covered with financial documents. “Now the real work I have to do,” she says. Top of the list is figuring out how to keep the university tuition — currently at about \$5,550 per year for resident undergraduates — affordable.

But as the finance cabinet meets in the war room, times are so tough there is talk of keeping university account balances liquid enough to pay monthly bills, in case the legislature slashes yet more. If Arizona is a bellweather of what other public universities can expect, there is little reason to expect the war to end anytime soon. ■

1. Hand, E. *Nature* **457**, 11–12 (2009).
2. Macilwain, C. *Nature* **446**, 968–970 (2007).
3. Dalton, R. *Nature* **446**, 971–972 (2007).
4. Dalton, R. *Nature* **442**, 729 (2006).
5. Zheng, S. *et al. Anal. Chem.* **79**, 3867–3872 (2007).

UNIV. ARIZONA

US climate-research shake-up recommended

The US government's climate-research programme should adopt an interdisciplinary approach that engages policy-makers to address adaptation and mitigation strategies. That's the conclusion of a National Research Council committee report, released on 26 February.

The committee found that the Climate Change Science Program (CCSP) has been hindered by a lack of research into the social sciences, which has never garnered more than 3% of the programme budget. The CCSP should address issues at the local and regional levels, including the effects of drought, extreme weather and shifting ecosystems.

The report recommends that the programme establish a "climate observing system" that includes the physical, biological and social aspects of global warming. The committee also recommended that, instead of issuing separate reports on different topics, the CCSP should return to a single national assessment involving stakeholders across all disciplines and agencies.

Italy plans nuclear plants in cooperation with France

Respective Italian and French energy utilities Enel and EDF last week agreed a joint venture aimed at building four new nuclear reactors in Italy.

The plants would be the first to be built in the country since a national referendum in 1987, held in the wake of the Chernobyl reactor accident, shut down Italy's nuclear power industry.

Obama has second go at choosing US health chief

Governor Kathleen Sebelius of Kansas (Democrat) was nominated to head the US Department of Health and Human Services by President Barack Obama on 2 March. If confirmed by the US Senate, Sebelius (pictured) will play a key role as the president seeks to overturn restrictions on federal funding for human embryonic stem-cell research (see *Nature* 457, 1068–1069; 2009).

Sebelius's nomination may speed the naming of other leaders in the vast department of 65,000 employees, including the chiefs of the National Institutes of Health, the Food and Drug Administration and the Centers for Disease Control and Prevention.

The nomination comes a month after a previous nominee, Thomas Daschle, formerly the top Democrat in the Senate, withdrew under fire for failing to pay \$128,000 in back taxes.



D. KOHL/AP

The deal accompanied an agreement on nuclear cooperation between the French and Italian governments signed on 23 February. Enel says it aims for the first plant to be operative by 2020, which London-based nuclear consultant John Large describes as a "very tight" deadline. High capital costs, local protests at sites as they are selected, and an insufficient regulatory framework to satisfy private investors could yet stymie the plans, says Large.

Industry minister Claudio Scajola said parliament would pass legislation in April paving the way for an Italian nuclear revival.

Korean egg-donor lawsuit thrown out of court

On 18 February, Seoul District Court in South Korea rejected a lawsuit about the egg-donation procedures used in the cloning research of disgraced former Seoul National University researcher Woo Suk Hwang.

Two women brought the lawsuit against

the Korean government, MizMedi Hospital and Hanyang University Hospital in April 2006. The women had donated eggs for Hwang's research at those hospitals (see *Nature* 440, 1102; 2006).

The women claimed that they had suffered physical and psychological damage because they were not informed about the risks of the procedure, and that the Korean government bore some responsibility because of its uncritical support of Hwang's research. The lawsuit, which requested 32 million Korean won (US\$20,000) in damages, was supported by more than 30 women's advocacy groups.

The government's legal case against Hwang on counts of fraud, embezzlement and violation of the country's bioethics law continues.

Ranbaxy censured by FDA over falsified data

Ranbaxy Laboratories — India's biggest drug maker and one of the largest generics firms in the world — has been slapped with tough penalties by the US Food and Drug Administration (FDA) after it was caught repeatedly falsifying data from one of its four Indian manufacturing plants.

The FDA action revokes some 25 existing approvals of drugs made at Ranbaxy's factory at Paonta Sahib in Himachal Pradesh, and stops an unnamed number of pending applications for drugs from the same plant.

Details released by the agency on 25 February reveal that, since at least 2006, Ranbaxy employees refrigerated samples that were supposed to be stored at room temperature to test their stability over time. In another instance, the plant misreported stability test results that were conducted over days instead of months.

The company issued a written statement saying that it "will continue to cooperate" with the US agency.

For a longer version of this story see <http://tinyurl.com/ba5tnk>

Europe delays decision on GM crop approvals

The European Commission's regulatory committee for genetically modified (GM) crops has failed to agree on whether to approve two maize (corn) crops for cultivation — 1507, jointly developed by Pioneer Hi-Bred International and Dow AgroSciences, and Syngenta's Bt-11.

The committee, which met on 25 February and might have ended Europe's decade-long hiatus on approvals, now passes the responsibility for making a decision to Europe's environment ministers, who must make a decision within 90 days of the committee meeting (see *Nature* 457, 946–947; 2009). Currently, MON801 maize is the only GM crop approved for cultivation at the European level, although it is banned in France, Greece, Austria and Hungary. On 2 March, European Union environment ministers voted against the commission's request to overturn the bans in Austria and Hungary.



W. KRECHTOWSKI/ZEFA/CORBIS

The climate to get things done

Despite huge obstacles, political forces in Washington may finally get greenhouse-gas legislation moving, says **David Goldston**.

Last week, in his first address to Congress, President Barack Obama laid out an ambitious agenda that includes tackling the fiscal 2010 budget, financial reform, health insurance, education, Social Security and Medicare, and greenhouse-gas restrictions. Of these daunting issues, climate change may be the most complex and problematic — both politically and intellectually.

Some of the challenges are obvious: no other issue entails trying to eliminate a fundamental building block of the industrial economy like carbon-based fuels, or purposely raising the price of a basic commodity such as energy. Passing a bill to accomplish that would require Herculean efforts, even without a worldwide economic meltdown.

But the hurdles for enacting a climate law are even higher because there has been little public discussion about a bill, and the issue ranks low on the public's list of concerns. During the presidential campaign, both candidates mentioned climate change only in passing — just enough for those already concerned to note the nod in their direction — and the media didn't press the matter because the candidates agreed on the need for action. Obama has called for climate legislation in several speeches since his election, but his remarks have been lost in the noise of the economy screeching to a halt.

Congress itself is equally unprepared. Major legislation generally requires several years of engaged discussion and passage of more minor efforts to become law. That's how the political and substantive puzzles got worked out with, for example, civil rights and clean air and water legislation. But Congress has not yet truly got its hands dirty on climate legislation. The Senate has had only limited debate on bills that had no chance of passing; the House of Representatives has never even moved a climate bill through committee.

Scientific uncertainties are likely to complicate the picture. Up to now, science has generally figured in the climate debate in a simple and simplistic fashion: conservatives deny the ever-growing scientific consensus that man-made climate change is real, and



PARTY OF ONE

proponents of action respond by making it sound as if all scientific questions about climate are resolved. But in a fully fledged climate debate, much tougher questions will have to be asked — questions about what level of emission cuts over what time period will be needed to stave off what kinds of damage. Scientific answers to those questions are much less clear, and science alone will not be able to guide legislators, as decisions on how to handle uncertainty and risk are fundamentally matters of political values.

Other countries' track records are not promising. The Australian parliament could block Prime Minister Kevin Rudd's cap-and-trade programme, which is under attack from all quarters as details become known. And a proposed carbon tax helped sink the opposition in last year's Canadian elections.

So, against this bleak backdrop, have those predicting action on climate change in this US Congress too willingly suspended their disbelief? Probably not. There are, for the first time, strong factors militating in favour of legislation. The most important is the commitment of key political leaders, starting with the president. No previous president has risked political capital on the issue, but Obama included specific targets for greenhouse-gas reduction in the budget outline he released last week.

Also important is a change of committee chairs in the House. The committee that oversees climate legislation is now led by Henry Waxman (Democrat, California), a proficient legislator and the first avid proponent of climate action to hold that seat. Waxman has promised to get a climate bill out of committee by the end of May, leading one environmental

lobbyist to remark, only half jokingly, "The Waxman staff doesn't have time to get something to eat."

Obama and his allies will have to struggle, though, to cobble together the 218 votes in the House and 60 in the Senate needed to pass a bill. Divisions are regional as much as partisan, with members from coal-mining and coal-burning areas especially hard to win over. A common parlour game in Washington is figuring out how to get the requisite number of votes, and no one is there yet. Lobbyists from all sides are leaning heavily on members who seem undecided — which includes more than a quarter of the members of the House.

One change in the political climate that may make it easier to garner votes is the greater openness to government regulation in the wake of the financial crisis. Support for climate-change legislation depends as much on attitudes towards government as it does on opinions about global warming. But those attitudes remain in flux; Obama was careful in his speech to Congress to forswear 'big government' and to laud private enterprise even as he called for new federal programmes. The lingering unease about government may create a tactical dilemma for climate-bill sponsors. Waxman's inclination has been to produce as strong a bill as possible — and to encourage pressure from his left — on the theory that the bill will be weakened through the legislative process. But too strong an initial bill in this environment could scare away needed votes.

The devil will be in the detail; climate-change bills in the abstract won't win enough converts. Picking up votes might involve cutting countless deals to address members' local interests — or the process could end up yielding an entirely different bill. Ideas that have been viewed as politically untenable — such as a carbon tax — are already gaining some support as climate legislation becomes a genuine possibility, and the headaches inherent in negotiating a cap-and-trade system could push more members into the tax camp. A few years ago, the idea of having the government auction at least some carbon credits (rather than give them out for free) seemed like the pipe dream of a few economists, but now it's a feature of almost every climate bill. And rebating all of the auction (or tax) revenues is an idea that is gaining steam.

The path to a climate bill is likely to be an obstacle course on which obstructions appear or change position without notice. But remarkably, it looks at last like a course that may be played through to the finish line. ■

David Goldston is a visiting lecturer at Harvard University's Center for the Environment. Reach him at partyofonecolumn@gmail.com.



Being Bob Langer

Running one of the biggest academic labs in America gives Robert Langer almost 100 people to help and advise; his BlackBerry gives him the rest of the world. **Helen Pearson** joins the throng.

At 16.26 in the afternoon on an icy Tuesday in January, Robert Langer is in his office at the Massachusetts Institute of Technology (MIT) with a Harvard University freshman called Lulu Rebecca Tsao. Langer met Tsao last year in Finland when he and her stepfather were collecting awards from the Millennium Prize Foundation. Now she is in Cambridge, she has come to ask his advice on which projects to do, and Langer offers to show her around the lab. A quick tour would be great, she says.

It will have to be quick. In my hand there is a three-page printout of the day's schedule provided by Bethany Day, the assistant who keeps Langer's diary. He has four minutes until what would be the fourteenth meeting since breakfast — if he had had breakfast. And his research lab is not a thing to tour in four minutes: try four hours. It is the biggest in the chemical-engineering department, and probably the biggest in MIT. It may well be one of the biggest academic labs in the world under a single principal investigator. Its 1,300 square metres take up most of this floor of MIT's building E25 and some of a floor above. But Langer doesn't mention any of that. He leads us from room to room pointing out postdocs and pausing at embryonic stem-cell cultures.

At the doors, he peers over the top of his glasses at a list of key codes that Day has helpfully printed out while he carefully punches numbers into the locks.

Langer has a lab of more than 80 people, has authored in excess of 1,000 papers and holds more than 300 patents with almost as many pending. Those patents have been licensed or sublicensed by more than 200 companies, about two dozen of which Langer took a key role in founding. His 73-page CV (in small font, single spaced) starts with a 1970 chemical engineering degree at Cornell University in Ithaca, New York, and ends with patents pending in biodegradable shape-memory polymers. I have come to spend the day with him to get a sense of how it is possible for such a monster of productivity to do what he does — and why he does it.

In answer to the latter question, he says that he has only ever wanted to help people, make them happy and do good in the world. "If people feel good about themselves, they will solve problems." When I first heard this, the previous evening, I thought it sounded trite. By the time he, Tsao and I are touring the lab, I've come to think it pretty unvarnished truth.

"If people feel good about themselves, they will solve problems."

— Robert Langer



Langer is up and pulling on his shorts. When his father died from heart disease aged 61, Langer, then 28, gave up eating meat and started exercising, something he now does for two hours or more each day. Now 60, he uses the time in his home gym to work and read, sometimes scrawling notes on the gym-machine console. This morning, he reads *The Boston Globe*, starts skimming through the nearly 200 grant proposals he is reviewing for the Bill & Melinda Gates Foundation's Grand Challenges in Global Health and listens to country music — his favourite. He skips breakfast but for a few sips of Diet Coke.

These first hours, I must admit, are hearsay. I had suggested that our day together run from waking to sleeping but Langer — in consultation with his wife — understandably declined.



Langer picks me up at the hotel near his office in his beige Mercedes-Benz E350. It's only a few blocks to his office, but the trip is long enough

H. PEARSON

to pass two or three of the biotechnology companies he has started. Langer traded up from a clapped-out Ford Pinto to a Mercedes Baby Benz when he received his first consulting fee in the 1980s. He gets a new one every five years.



I am not the only media person around today. A film crew is setting up in Langer's office; he puts on a jacket (his black jeans and brown shoes are out of shot) and starts answering questions about his achievements. It's an educational video for the website of the Charles Stark Draper Prize, a US\$500,000 award sometimes called a Nobel prize for engineering. Langer won it in 2002. The woman organizing the shoot told me that some of the other winners were impossible to pin down, but Langer was happy to oblige.

Langer recently read *Outliers*, a book in which Malcolm Gladwell makes the case that exceptional people get where they are partly because of the exceptional circumstances in which they find themselves, rather than through exceptional ability or sheer hard work. Langer concurs. There is a personal aspect, he says, "a combination of stubbornness, risk taking, perhaps being reasonably smart and wanting to do good". But there is also just the chance of what turns up. As a young chemical engineer keen not to work in an oil company he tried to find a position in teaching or at a medical school instead. He had no success until Harvard University's Judah Folkman gave him a job isolating molecules that inhibit blood-vessel growth. It was the right place: Langer says he was like a kid in a candy store, overcome by the sheer number of interesting medical problems that might yield to his engineering know-how and imagination. He isolated the angiogenesis inhibitor Folkman wanted (R. Langer *et al. Science* 193, 70–72; 1976) and went on to make a porous polymer that controlled the rate at which such large molecules were released (R. Langer and J. Folkman *Nature* 263, 797–800; 1976). The ideas took some time to catch on: both biologists and polymer chemists found them absurd. Now he is widely credited with founding the fields of controlled-release drug delivery and tissue engineering.



Phil Hilts, who heads MIT's Knight Science Journalism Fellowships programme, wants some advice on good people in nanotechnology to invite to a 'boot camp' for journalists. He is possibly the 15th person to ask Langer for some advice so far today. Everyone wants

access to his network and his experience, and he obliges. In *The Audacity of Hope*, Barack Obama recounts asking Langer's advice on stem-cell research in 2006. Langer replied that more stem-cell lines would be useful, but "the real problem we're seeing is significant cutbacks in federal grants".



On the way to and from the bathroom, Langer deals with seven or eight e-mails, including editorial advice on a paper being considered for *Proceedings of the National Academy of Sciences*. A passion for his BlackBerry is another link to Obama. At every moment he is not talking to someone directly, he slumps into a characteristic stoop over the device. His computer, by contrast, has not even been switched on so far today. All its processing power would make little difference to the speed at which Langer — a one-finger typist — sends messages. Not that much difference could be made. There is rarely more than a few minutes between sending Langer an e-mail and receiving a BlackBerry reply.



We walk across the snowy MIT campus to the room where he will be lecturing. On the way he points out the brown scaffold skeleton of the new David H. Koch Institute for Integrative Cancer Research; his lab will move there in 2010. He will increase his lab space to almost 1,900 square metres, although he says he plans to give his existing lab members more space rather than recruit more staff.



Langer wolfs down some (vegetarian) lasagna and a chocolate cookie, then starts his lecture. (Another of his five full-time administrators, Ilda Thompson, spends much of her time putting together his talks from six or seven templates.) This one is for undergraduates, part of a programme to teach them about 'real life' skills such as starting companies. "We have the Tiger Woods, the Michael Jordan of engineering," says programme director Susann Luperfoy as she introduces him.



Everyone who is even remotely thinking about starting a biotechnology company should listen to this lecture; it would probably save millions in wasted venture capital. Langer has boiled

down the requirements for starting a biotech company to a set of clear bullet points. (Do you have a platform technology, a seminal paper and a blocking patent? If not you may be in trouble). Then he recounts six of his own success stories. "Dazzling," says my neighbour at the table as Langer rounds up his talk.

As we walk back to his office, a small Mars rover appears to be making its way through the snow. "These kinds of things happen at MIT," he says.



Langer is embracing Smadar Cohen, once his postdoc and now a professor at Ben Gurion University in Tel Aviv, Israel. He says that nothing makes him prouder than his 180–200 former students and postdocs now heading academic labs of their own. Cohen is involved in a new biotech 'incubator' for promising academic research projects called Pharmedica, based in Haifa, Israel.

She and Yoram Rubin, the chief executive, have flown here largely for 30 minutes of Langer's time; their questions are how to raise money and which field to specialize in.

Langer tells them that their incubator needs to be closer to having a product if they want to persuade venture capitalists to invest the sums that they are thinking about (\$10 million). "I always think to put money in they need to be scared enough that if they don't, they're going to lose something big," says Langer. In terms of specializing, he says, "you have to look at what the cutting areas are and who has the intellectual property (IP) rights". Neuroscience is a huge area, they agree. But, he adds, "I don't like to set boundary conditions before you need to".



A no-show. Natalia Rodriguez, an undergraduate student who has been working in Langer's lab for the past two and a half years, has never had a one-on-one meeting with Langer. Today she had scheduled 15 minutes. Where is she?



Langer has essentially built his own interdisciplinary research institute in E25 — chemical engineers, cell biologists, chemists, physicists, material scientists, geneticists, medical doctors, mechanical engineers and mathematicians. "I don't think you could do a lot of the things we are doing without a lot of people," he says. To run the group, he has three right-hand people, senior researchers at MIT who have elected to

stay in his lab. One is Dan Anderson, who has come to the office to talk about further expansion. "We need to hire more people and figure out how to get them," he says. The reason they need to expand is that the Juvenile Diabetes Research Foundation, which has awarded the lab a large grant to develop biocompatible polymers for encasing pancreatic islet cells, has recommended they get an immunologist on board. They talk about hiring a joint-postdoc with another lab, but then Langer says, "it's probably easier to have our own". He picks his book of National Academy Fellows off the shelf and turns to immunology. "I knew quite a few of these people. Frank Austen. Fred Alt. Irv Weissman, he's really interested in tissue engineering."



Charles Jennings wants to consult Langer about an IP issue. As head of the neurotechnology programme at MIT's McGovern Institute for Brain Research, it has fallen to Jennings to hammer out an IP agreement for discoveries made by researchers at the institute — somewhat like a prenuptial agreement for future income. In general, MIT policy is that income from IP is split three ways between the inventors, their department and MIT. Jennings has drafted an agreement to sort out how this would work at the McGovern Institute, which often involves collaboration across several departments. Langer is concerned that MIT's Department of Brain and Cognitive Sciences (BCS) might not like it. They agree it would be bad, as Langer says, if three years from now "the head of BCS says how did you guys pull this off? We got nothing and you get 100%."



A smell of perfume fills the air. Rob Robillard and three well-made-up young women (Jamie, Amber and Michelle) file into the office. As well as starting a bevy of companies that make biomedical devices, drugs or delivery systems, Langer also helped found Andora, which is now called Living Proof. The company, also based in Cambridge, uses chemical engineering to design hair and beauty products. Robillard is the chief executive.

Its first product, No Frizz, seals the gaps in the hair shaft so that water cannot enter, thus attempting to live up to its name. The three young women will be training beauty consultants across the United States when it is officially



Robert Langer's papers make covers — as does he.

launched there in February (and on the QVC shopping channel). "It's spreading through the MIT campus," says Robillard. Through starting this company, Langer now has his (frizzy) hair cut for free by a top hair stylist.



Langer parcels out wisdom and contacts in 15- and 30-minute slots. To the undergraduate student wanting advice on courses: "The most important thing you can learn is fundamentals." If you want a placement in a company, "we can arrange that", he says. He gives Tsao the lab tour. A button has come undone, unnoticed, on his shirt. Langer told me earlier

that he does wonder whether he needs to be better at saying no to things. But "I don't like to hurt people's feelings", he says.



We are slightly late to meet Rodriguez, whose appointment was rescheduled. She missed her original slot because she was trapped in an elevator for 45 minutes. She looks close to tears, but not because of the elevator; she's having difficulty deciding whether to accept a job offer from Merck, or whether to go to graduate school. Langer tells her there is no wrong choice. "What do you feel in your heart you want to do?" he says. "I think I'm gonna work," she says eventually, looking unconvinced.



Langer walks upstairs to a conference room filled with a throng that, in most other labs, would be an all-hands meeting. But this is just the undergraduates who work here; he has organized a pizza and soda session in an attempt to make himself accessible. As they

introduce themselves (he doesn't know all their names), their varied projects outline the sheer scope of the lab's activities: stem-cell regeneration; contact lenses that release drugs; lipid parcels that deliver small RNAs; biomaterials for insulin delivery; DNA vaccines.

What is your favourite discovery, they ask. (His 1976 *Nature* paper.) Where do you like to travel best? (Paris. Maui. Where the food is good.) Are you still intimidated by talks? (No.) Where do you find your inspiration? (TV shows, music, reading, no single mechanism.) How do you balance everything? (Exercise a lot.) If you did it all over again, what would you do differently? (He wouldn't change anything.) Will America still be a power in future research? (Yes.) What was your worst mistake? (Even mistakes teach you to be better.) He answers them all, between three pieces of pizza.



Langer's computer is still sitting unused as we leave the office. He drops me back at the hotel — I'm exhausted. On his way home he stops for an ice cream — coffee chip frozen yoghurt with hot fudge sauce. He spends an hour on the exercise bike. Sometimes he reads *People* magazine or watches the Boston teams play. Tonight he reads CVs, revises a paper for *Angewandte Chemie* and prepares his talk for the World Economic Forum in Davos, Switzerland, later in the month. He listens to his daughter — one of three teenagers — practise the presentation for her Friday chemistry class on smart polymers. "She did it all herself," he says. "She has four citations and an interview with me. I don't do her homework. I explained some of the chemistry." Then he does another hour on the cross-trainer and treadmill. No dinner speech today, and his own bed to look forward to: comparatively relaxed.



While packing for tomorrow's trip to Tampa, Florida, for the Armed Forces Institute of Regenerative Medicine, Langer panics: where are his passport and phone? They're in his coat.



Langer's BlackBerry is charging in the bathroom. He is in bed. I can't tell you what he dreams of. But if I had to guess it would be about happy, helped people.

Helen Pearson is Nature's biology features editor.



RETHINKING REHAB

Alcoholics Anonymous and its spin-off programmes have been helping people with addictions for decades. **Jim Schnabel** talks to the neuroscientists who are looking deeper into the approach.

In the depths of the Depression, in a Manhattan alcoholism clinic, a ruined Wall Street speculator named Bill Wilson had a vision. His room suddenly blazed “with an indescribably white light” and he experienced euphoria and a godlike “presence”, followed by a “great peace”¹. Like St Paul after his experience on the road to Damascus, Wilson soon turned away from his old, inebriated life and became an evangelist — preaching a radical, spiritual cure for alcoholism.

That cure grew into the modern addiction rehabilitation industry, which even today is dominated by Wilson’s Alcoholics Anonymous (AA) paradigm and its ‘twelve-step’ approach to recovery. Perhaps unsurprisingly, given its spiritual origins, this approach has had an uneasy relationship with the evidence-based culture of medical research. Both perceive addiction as a chronic disease; but whereas scientists seek rationally targeted interventions to blunt drug cravings, AA and related programmes tend to feature group therapy, tearful confessions and

the call to “surrender to a higher power”.

In the past few years, however, these two cultures have been finding common ground. Neuroscientists have begun to recognize that some of the most important brain systems impaired in addiction are those in the prefrontal cortex that regulate social cognition, self-monitoring, moral behaviour and other processes that the AA-type approach seems to target. “A lot of the treatment programmes out there are targeting these systems without necessarily knowing that they are doing it,” says Nora Volkow, director of the National Institute on Drug Abuse in Bethesda, Maryland.

Researchers are now searching for ways to boost these prefrontal systems even further — not to remove the need for twelve-step and other behaviourally oriented treatment programmes, but to enable people with addictions to get more out of them. “It completely changes the way that we look at medications,” Volkow says.

Until recently, addiction researchers focused almost entirely on ‘limbic’ circuits in the brain

that mediate fear and desire. These dopamine-fuelled networks are effectively hijacked by addictive drugs and behaviours so that the person ends up wanting, and compulsively seeking, little else but the next fix. Drugs such as methadone and naltrexone can blunt the activity of these circuits, but they are not a cure.

Impulse management

While doing neuroimaging studies at the Brookhaven National Laboratory in Upton, New York, in the 1990s, Volkow was one of the first researchers to suggest that abnormalities in the prefrontal cortices of drug users might weaken the systems that normally counteract drug cravings². Since then, the prefrontal regions and their links to the limbic system have garnered more and more attention, and researchers are now attempting “a very extensive evaluation of how the different areas in the prefrontal cortex participate in the process of drug addiction”, Volkow says.

The prefrontal cortex — the most recently

W. RYAN

evolved set of structures in the brain and the one that most clearly differentiates humans from other species — is the headquarters for the circuits that help shape feelings and behaviour according to long-term goals, moral strictures and social cues. These systems are extensively wired into limbic regions, and are often portrayed as a 'braking' system to resist impulsive behaviour. The slow development of prefrontal structures after birth tracks the maturation of children into adults, and people whose prefrontal areas are damaged by trauma or stroke, for example, seem to have lost some control of the brakes and are apt to be childishly impulsive and uninhibited in their behaviour.

With tools such as psychological tests and brain imaging, researchers have been finding similar braking problems associated with drug use and are starting to tease apart the mechanisms involved. Some have shown that people with drug addictions are poor at monitoring their own behaviour³, making appropriate decisions and inhibiting impulses — and these behavioural findings have been matched to functional magnetic resonance imaging (fMRI) data that show reduced activity in the corresponding prefrontal areas. Animal studies have supported the human ones by showing, for example, that monkeys given cocaine swiftly develop prefrontal impairments⁴. And other researchers have found that stress, which frequently triggers drug use and relapse in people with addiction, seems to do so at least in part by shutting down prefrontal functions⁵. "We're really starting to understand the molecular basis of why this cortex falls apart with drugs of abuse, and during stress, and how those two interact," says Amy Arnsten at Yale University School of Medicine in New Haven, Connecticut.

If the cortex falls apart with drug abuse, then it may be impossible to recover from an addiction without putting it back together. In unpublished studies, Hugh Garavan and his colleagues at Trinity College, Dublin, have found that cocaine users and tobacco smokers who go through treatment and are able to stay abstinent for more than a year "seem to show hyperactivity in these prefrontal control centres" in fMRI images. Garavan says that this extra activity seems to be especially prominent during the first few weeks of abstinence, hinting at "a heavy reliance on these prefrontal

centres to avoid falling off the wagon".

The recognition that prefrontal systems might need boosting in people with addictions has helped fuel a new interest in whether AA and similar behavioural treatments are already having these kinds of effects. "It behooves us to try to understand how [twelve-step approaches] link to what we're addressing in terms of intervention," Volkow told the annual meeting of the Society for Neuroscience in Washington DC last November. So far, these treatment programmes have been difficult to study formally, says Martin Paulus, a psychiatrist who is researching addiction

at the University of California, San Diego. "It's very much a voluntary-based programme, with little standardization, and the whole programme thrives on anonymity."

But much of what is known about the AA approach suggests that it aims to protect or enhance prefrontal circuits. In the protected environment of a rehab centre, drugs and other cues associated with drug taking are gone and stressful situations that suppress prefrontal activity are minimized. Volkow notes that the feeling of ceding control to a higher power is

"The inverse association between religion and addiction is one of the most unsung findings in the entire literature on drug and alcohol abuse."

— Michael McCullough



Bill Wilson (left) set up Alcoholics Anonymous in 1935. Its twelve-step paradigm is widely used to treat addiction.



also likely to "enhance your sense of security, decreasing stress and anxiety". Similarly, says Garavan, the confessions of bad behaviour and other "strategies that push users to become more aware of their drug-related actions presumably aim to boost their capacity for self-monitoring, which is largely a prefrontal function".

The social environment in rehab is another factor that works in part through prefrontal systems. "Our brains have evolved to be very sensitive to social cognition and social reinforcers," says Volkow. By putting people with drug addictions into a group with anti-drug values, "you are providing them with a very powerful reinforcer", she says.

Spiritual control

And then there is religion, which has been shown to have a strong inverse association with drug addiction. Psychologist Michael McCullough, who studies religion and behaviour at the University of Miami in Florida, calls this inverse association "one of the most unsung findings in the entire literature on drug and alcohol abuse". Both adults and children deemed religious by various measures "drink, smoke and do drugs less often", McCullough says. "If they get into trouble with drinking and drugs and smoking, they're more likely to be able to get away from those problems."

McCullough suggests that when a person commits to any cultural system that regulates behaviour, the psychological effort to conform strengthens the brain systems that mediate self-monitoring and self-control. "What makes religion unique, I think, is that the code of conduct isn't just laid down by your parents or your friends or your principal at school, but ostensibly by the individual who is superintending the Universe, so it has an extra moral force." Some religious rituals, he says, have been shown to provoke enhanced activity in prefrontal regions⁶. "It's as if certain forms of prayer and meditation are pinpointing precisely those [prefrontal] areas of the brain that people rely on to control attention, to control negative emotion and resolve mental conflict."

However the twelve-step strategies actually work on the brain, "there is now excellent documentation that those who attend AA-type programmes regularly do very well by anyone's standard", says Thomas McLellan, director of the Treatment Research Institute in Philadelphia, Pennsylvania. The problem, McLellan says, is that the vast majority of people who enter such programmes do not go regularly — they drop out after a few days or weeks — and are more than likely to relapse.

Anna Rose Childress, a psychiatrist at the University of Pennsylvania School of

Medicine in Philadelphia, has encountered a similar resistance to treatment in the crack cocaine users she has studied. In her lab she uses a cognitive behavioural training technique — like “prefrontal pushups”, she says — that tries to make these users more aware of their drug-related actions and the consequences. But her studies indicate that “most of our cocaine patients are not great at it”.

Results such as these raise what Childress and others call the “chicken or egg question” — is drug use the cause of users’ prefrontal problems, or do they have pre-existing defects that make them susceptible to addiction? As Garavan puts it: “A lot of people might be able to enjoy drugs but there’s only a certain percentage who actually go on to become addicted. And maybe part of that is because these people lack that prefrontal-mediated control over behaviour”.

Some research already links prefrontal-related conditions such as impulsivity and attention deficit hyperactivity disorder (ADHD) to a heightened risk of later drug use. But to really start answering the chicken or egg question, says Childress, “you would need some good large-scale developmental studies for one thing; you would like to look at adolescents before they’ve ever touched drugs”. Garavan and several dozen other European researchers are now participating in a project that aims, in part, to do just that. Known as IMAGEN and begun in late 2007, the five-year, €10-million (US\$14-million) project funded by the European Commission will ultimately enrol 2,000 14-year-olds and follow them through their late teens. Principal investigator Gunter Schumann, a psychiatrist at Kings College, London, says that the testing will include fMRI and structural MRI, as well as a full genome scan. He expects to start publishing findings in the next few years.

Quenching the flame

In the meantime, researchers are pursuing other ways to boost prefrontal systems — and medicines for ADHD seem an obvious place to start. Attention-enhancing drugs such as methylphenidate and atomoxetine boost the activity of key receptor systems in the prefrontal cortex, in particular those for noradrenaline and dopamine. Some evidence already suggests that patients with ADHD are less likely to go on to abuse drugs if they are receiving medication for their condition⁷. And earlier this year, a team led by Daina Economidou at the University of Cambridge, UK, reported that atomoxetine helped rats with an ADHD-like impulsivity to resist a relapse to cocaine-seeking⁸.

The National Institute on Drug Abuse has



AA-type group behavioural therapy may tap into brain regions neuroscientists think are crucial in overcoming addiction.

also been supporting studies of cognitive and behavioural strategies, and Volkow says that she is particularly enthusiastic about an approach that involves “real-time fMRI feedback”. Developed by researcher and entrepreneur Christopher deCharms earlier this decade, the technique involves placing drug users in an fMRI machine and showing them a symbolic representation — a flame — of the fMRI-measured brain activity that corresponds to their cravings. The users are then asked to apply their own cognitive exercises, such as imagining their child is with them, to quench their cravings and douse the flame. After half a dozen sessions with this feedback the user will, in principle, develop cognitive circuitry that is more efficient at suppressing craving and that can then be used in ordinary life. A version of the technique, used for pain relief, has already shown some efficacy in a small clinical trial⁹, and deCharms and his Silicon Valley start-up, Omneuron, are currently running a small trial

in smokers — with plans for a follow up with some of Childress’s cocaine users.

For some people, even the most sophisticated therapies may not be enough to rescue a prefrontal cortex that has been damaged by genetics, development and perhaps decades of drug use. “It’s like somebody who has had a stroke and is paralysed,” says psychologist Antoine Bechara at the University of Southern California, “and you tell them, well, you should walk, you should exercise. But the part of the brain that allows them to do that is not there and they just cannot do it”.

To Bechara, a more efficient approach would be to protect and strengthen these critical brain regions as they are developing. As an example, he cites preliminary data from a study in China. “There are children who grow up whose parents make all the decisions for them, and others who are encouraged to make decisions and are rewarded or punished for their bad decisions,” he says. “The latter children grow up to show better performance on measures of decision making, and there is even a hint of evidence from fMRI that the kids with that latter kind of parenting style have better prefrontal cortex function.”

Even for those beyond the influence of parenting style, researchers hope that a little lift in prefrontal efficiency could go a long way. Such a boost, says Paulus, could be “the critical piece that helps prevent the person from getting onto a very destructive pathway”.

The question now is how best to give that boost. As researchers come to understand the neural mechanisms of addiction better, the twelve-step approach may give way to more secular strategies. But it seems unlikely that all behavioural approaches will soon be replaced by a pill. “I think most researchers would say, and I know I would say, that medicines should be used in the context of a good behavioural programme,” says Childress, “because a person is essentially trying to restructure a lot of behaviour, and the more support that you can provide for that, the better.”

Jim Schnabel is a freelance writer based in Maryland.

1. Wilson, B. *Bill W: An Autobiography* (Hazelton-Pittman Archives Press, 2000).
2. Volkow, N. D. et al. *Am. J. Psychiatry* **148**, 621–626 (1991).
3. Hester, R., Simões-Franklin, C. & Garavan, H. *Neuropsychopharmacology* **32**, 1974–1984 (2007).
4. Olausson, P. et al. *Ann NY Acad. Sci.* **1121**, 610–638 (2007).
5. Hains, A. B. & Arnsten, A. F. *Learn. Mem.* **15**, 551–564 (2008).
6. Azari, N. et al. *Eur. J. Neurosci.* **13**, 1649–1652 (2001).
7. Wilens, T. E. et al. *Arch. Pediatr. Adolesc. Med.* **162**, 916–921 (2008).
8. Economidou, D. et al. *Biol. Psychiatry* doi:10.1016/j.biopsych.2008.12.008 (2009).
9. deCharms, R. C. et al. *Proc. Natl Acad. Sci. USA* **102**, 18626–18631 (2005).

BSIP/LAURENT/LESACHE/SPL

J. VARNEY/SPL

S. DOERING/VISUM/STILL PICTURES

CORRESPONDENCE

Caution urged in trial of stem cells to treat spinal-cord injury

SIR — As you point out in your News story 'Stem cells ready for prime time' (*Nature* **457**, 516; 2009), the recent approval by the US Food and Drug Administration (FDA) of the first clinical trial to use derivatives of human embryonic stem (ES) cells is an important development. But the indication, namely spinal-cord injury, raises concerns and important caveats.

First, the choice of a body area that is not simple to access is surprising in the context of what is meant to be primarily a safety trial. The field needs reliable information with regard to possible immune rejection of the transplanted cells and their potential to de-differentiate *in situ* after implantation.

Second, the benefits are not likely to be easy to assess, given what has been experienced with animal models of spinal-cord lesion. Difficulties in reproducing the lesion and in assessing both the damage and regrowth of axons after experimental manipulations have made results hard to interpret. It is generally agreed that cut axons cannot readily regrow in adult mammals, but it is not clear why. Damage caused by inflammatory cells, scar formation and decreased intrinsic growth drive of adult neurons, as well as the inhibitory effect of myelin in the central nervous system, may all play a part.

The trial approved by the FDA consists of injecting oligodendrocyte precursors into the spinal cord of patients soon after injury, implying that a lack of such precursors may be the key issue. Oligodendrocyte precursors do seem to myelinate axons after lesion in rodents (H. S. Keirstead *et al.* *J. Neurosci.* **25**, 4694–4705; 2005). However, the results still need to be interpreted in the context of what goes wrong after spinal-cord injury, including the possibility that axonal elongation

may actually be impaired by oligodendrocyte-derived products.

Nonetheless, the generation of virtually pure populations of oligodendrocyte precursors is impressive, one of very few cases of cellular homogeneity of a differentiated cell type generated from ES cells (G. I. Nistor *et al.* *Glia* **49**, 385–396; 2005). This achievement opens the way to studying the impact of mutations after reprogramming somatic cells from patients, and drug screening in a relevant cellular context.

Given the controversy over the use of human ES cells in some countries, it is to be hoped that the triumphant announcement of the approval of this clinical trial will not prove to be a prime-time setback. Regenerative medicine using human ES cells is an exciting prospect, but the field still needs time to mature. The primary concern of scientists involved in stem-cell research is not to satisfy the short-term expectations of analysts and investors, but to improve public health with the help of innovative, safe treatments.

Yves Barde Biozentrum, University of Basel, Klingelbergstrasse 50–70, 4056 Basel, Switzerland
e-mail: yves.barde@unibas.ch

Cuts to research funding could hurt health care too

SIR — The rapidly deepening financial crisis, reported on *Nature's* Recession Watch site (<http://tinyurl.com/d4gy28>), raises important questions about the future of medical research at a time when health care itself is under pressure.

As the crisis grows in pace and extent, it is difficult to predict its full effects, even on state-backed organizations such as the US National Institutes of Health (NIH) and the UK Medical Research Council (MRC) and National Health Service (NHS). Organizations such as the MRC and NIH, which receive direct

funding from governments, also work closely with research councils, industry and other stakeholders to produce high-quality research. Active research aids decision-making about health standards, health policy and discovery of new drugs and treatments. There is evidence that doing research during medical training enhances a student's vision and performance later in academic research.

If funding to research organizations is reduced, the results may not be seen for three to five years — but they will be devastating. Global measures need to be taken to secure both domestic health-care requirements and research funding.

First, it is imperative to continue to improve standards of health care and patient safety. Second, additional funds must be allocated to continue health care research while safeguarding basic health needs. Finally, alternatives for financing health care and research should be explored. An amalgamation between health-care and research agendas could shield organizations from disastrous expenditure in this financially grim period.

Kamran Ahmed, Hutan Ashrafian
Department of Biosurgery and Surgical Technology, Imperial College London, St Mary's Hospital Campus, London W2 1NY, UK
e-mail: k.ahmed@imperial.ac.uk

Separate name for fungus's sexual stage may cause confusion

SIR — I applaud the discovery by C. M. O'Gorman and colleagues of a sexual stage in the medically important fungus *Aspergillus fumigatus* (*Nature* **457**, 471–474; 2009). However, I question the introduction of a new scientific name for it, *Neosartorya fumigata*.

Mycologists know from morphological and now molecular phylogenetic evidence that the asexual *A. fumigatus* belongs

with species that also produce a *Neosartorya* sexual stage. In the molecular era, the need for a single species to have separate scientific names for its various asexual stages has become obsolete. Species with no sexual stage can be placed with those that have. Even in the 1960s, *Aspergillus* monographer Kenneth Raper used one name for one fungus in *Aspergillus*.

Mycology is unique in permitting different binomials to be applied to the various sporing stages of the same living species. The need to evolve from this archaic position to that of a single name for one species in all its sporing states was advocated by Don Reynolds and John Taylor in 1991. In 2005, the XVII International Botanical Congress established a committee to consider options for changing the pertinent rules: that committee is due to report in 2011.

O'Gorman and colleagues did not contravene the current international rules in introducing *N. fumigata*, but have precipitated a potential source of confusion. That name is now available to apply to all stages of this fungus, including the asexual. The scientific community faces the prospect of reference to this species, even when dealing with just the asexual stage, using only the *Neosartorya* name.

The pragmatic approach is to use only the name *A. fumigatus*, regardless of whether the sexual or the asexual stage of the fungus is being referred to. This would be in line with the practice in *A. nidulans*, where the available name *Emerella nidulans*, based on the sexual stage of that species, is largely ignored.

David L. Hawksworth Facultad de Farmacia, Universidad Complutense de Madrid, Plaza Ramón y Cajal, Madrid 28040, Spain; and Department of Botany, Natural History Museum, Cromwell Road, London SW7 5BD, UK
e-mail: d.hawksworth@nhm.ac.uk

Contributions may be submitted to correspondence@nature.com and will be edited.

ESSAY

We cannot live by scepticism alone

Scientists have been too dogmatic about scientific truth and sociologists have fostered too much scepticism — social scientists must now elect to put science back at the core of society, says **Harry Collins**.

The term 'science studies' was invented in the 1970s by 'outsiders', such as those from the social sciences and humanities, to describe what they had to say about science. Science studies have been through what my colleagues and I at the Cardiff School of Social Sciences, UK, see as two waves. In wave one, social scientists took science to be the ultimate form of knowledge and tried to work out what kind of society nurtures it best. Wave two was characterized by scepticism about science.

The recent dominance of this second wave has unfortunately led some from science studies and the broader humanities movement known as post-modernism to conclude that science is just a form of faith or politics. They have become overly cynical about science.

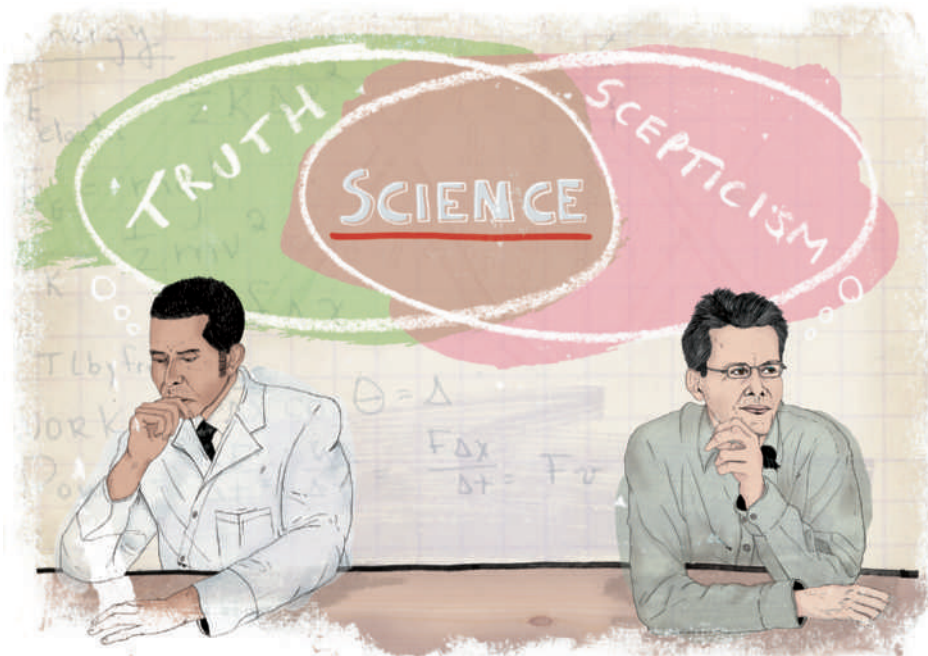
The prospect of a society that entirely rejects the values of science and expertise is too awful to contemplate. What is needed is a third wave of science studies to counter the scepticism that threatens to swamp us all.

We must choose, or 'elect', to put the values that underpin scientific thinking back in the centre of our world; we must replace post-modernism with 'elective modernism'. To support this, social scientists must work out what is right about science, not just what is wrong — we cannot live by scepticism alone. Natural scientists, too, have a part to play: they must reflect on and recognize the limits of their practice and their understanding. Together, we must choose to live in a society that recognizes the value of experience and expertise.

This third wave will be resisted. Post-modernists have become comfortable in their cocoon of cynicism. And some natural scientists have become too fond of describing their work as godlike. Others are ready to offer simple-minded criticisms of deeply held beliefs. But the third wave is needed to put science back in its proper place.

Logic of science

The first wave of science studies largely coincided with post-war confidence in science, drawing on the success of physicists during the Second World War. During this period, philosophers attempted to define the underlying logic of the sciences, culminating



J. TAYLOR

"The prospect of a society that entirely rejects the values of science is too awful to contemplate."

in Karl Popper's notion that the criterion of scientific validity was the ability to state the conditions under which a claim could be proven false. Social scientists such as Robert Merton additionally documented the norms of the scientific community: science must be unbiased, disinterested, a free public good and subject to organized critical review. These norms seemed to be at the heart of the science that defeated fascism. Unsurprisingly, they fitted neatly with democratic ideals so, conveniently, democracy could be described as the best political system because it produced the best science.

The second wave was a child of the broader cultural revolution of the 1960s, as everything from sex to ideology loosened up. In science-studies circles, the authority of science went the way of the shirt and tie. It was shown that many kinds of scientific activities did not fit the philosophers' models and ignored the norms, and yet were still successful.

One of my contributions to this second wave was to demonstrate that scientists could not always check a result by simply repeating it, because what counted as a satisfactory

repetition was not clear if a controversy ran deep. Take, for example, physicist Joseph Weber's claim to have detected gravitational waves in the 1960s. It was very difficult to disprove this experimentally, because Weber and his allies would not accept that those who could not repeat the results had tried hard enough. A single negative experiment or observation could not prove the theory false, so Popper's idea was itself flawed.

Historians showed that both the 1887 Michelson–Morley experiment on light travel and Arthur Stanley Eddington's 1919 eclipse observations, both said to provide key empirical support for Einstein's theories, were actually open to a variety of interpretations, even though the textbooks continued to offer myth-like accounts of the experiments' decisiveness¹.

This type of analysis — in which it is shown that science cannot avoid human influence — came to be called social constructivism and remained a little-known speciality until the early 1990s. Then some scientists began a war with the social constructivists, throwing them into the spotlight. Suddenly, sociologists were being blamed for the growing troubles of science, from the rejection of confidence in genetically modified foods to the diminution

of funding, symbolized by the demise in the United States of the Superconducting Super Collider in 1993.

It was said that sociologists were trying to undermine science. But we were not questioning the results of the great experiments, merely examining how the consensus about their interpretation was established. The conclusions of most of us were moderate: science could not deliver the absolute certainties of religion or morality, and scientists were not priests but rather skilful artisans, reaching towards universal truths but inevitably falling short. Far from being anti-science, we were trying to safeguard science against the danger of claiming more than it could deliver. If science presents itself as revealed truth it will inevitably disappoint, inviting a dangerous reaction; even the most talented craftsmen have their off-days, whereas a god must never fail.

Warriors disarm

By around 2000, the production of books, papers and conferences contributing to the science wars had pretty well stopped, whereas science studies grew in size and influence. Serious sociologists and serious scientists made friends and occasionally published joint works². Society could not simply return to the way things were during wave one, as the science warriors would have preferred; the scepticism born of the second wave could not simply be forgotten.

By definition, the logic of a sceptical argument defeats any amount of evidence; one can deduce that no inference from observation can ever be certain, that one cannot be sure that the future will be like the past, and that nothing is exactly like anything else, making the process of experimental repetition more complicated than it seems. The work of sociologists was simply to show how this played out in the practice of the laboratory.

Nowadays, however, I wonder if the science warriors might have been right to be worried about the (unintended) consequences of what social constructivists were doing. We may have got too much of what we wished for. The founding myth of the individual scientist using evidence to stand against the power of church or state — which has a central role in Western societies — has been replaced with a model in which Machiavellian scientists engage in artful collaboration with the powerful.

The modern social analyst of science has no more to say about the failure of Trofim Lysenko's theories of biological inheritance during Stalinist times than the failure of the Soviet Union — both simply lost a political battle.

One can justify anything with scepticism. Recently a philosopher acting as an expert witness in a court case in the United States claimed that the scientific method, being so ill-defined, could support creationism. Worse, scientific and technological ideas are nowadays being said to be merely a matter of lifestyle, supporting the idea that wise folk may be justified in choosing technical solutions according to their preferences — an idea horribly reminiscent of 'the common sense of the people' favoured in 1930s Germany. Some social scientists defend parents' right to reject vaccines and other unnatural treatments because a lack of danger cannot be absolutely demonstrated. At the beginning of the century, President Thabo Mbeki's policies denied anti-retroviral drugs to HIV-positive pregnant mothers in South Africa. Some saw this as a justified blow against Western imperialism, given that the safety and efficacy of the treatment cannot be proven beyond doubt.

A third wave of science studies would mean breaking away from now-routine and secure criticism, and instead taking the risks involved with the synthesis and generalization that build human culture. Mbeki claimed that anti-retroviral drugs had not been proven to reduce mother-to-child transmission of HIV, and pointed out that some scientists claim the drugs are poisonous. He was right. The hard problem for social studies of science is to show why, although he was right in logic, he was wrong for all practical purposes. Just showing there is some doubt about an issue, or another side to the story — at which we social scientists are nowadays unbeatable — does not inform you what to do in a case such as this.

Expertise defined

One way to try to crack the hard problem is to analyse and classify the nature of expertise to provide the tools for an initial weighting of opinion. The result of such an exercise is the creation of some new classes of expert (such as people whose expertise is based on experience rather than training and certificates), and the exclusion of some old classes (such as scientists speaking outside their narrow areas of specialization). My colleagues and I have summarized this approach in a kind of 'periodic table' of expertises³. Using this approach, it can be shown that Mbeki's ideas about the danger of anti-retrovirals were developed by reading the views of a small group of maverick scientists on the

Internet and advising his ministers to do the same. But the view gained from the Internet is not always the view developed within the scientific community. Although in principle the logic of the mavericks' position cannot be defeated, a policy-maker should accept the position of those who share in the tacit knowledge of the expert community.

It is not only social scientists who would have to change their approach under elective modernism. If we are to choose the values that underpin scientific thinking to underpin society, scientists must think of themselves as moral leaders. But they must teach fallibility, not absolute truth. Whenever a scientist, acting in the name of science, cheats, cynically manipulates, claims to speak with the voice of capitalism, the voice of a god, or even the voice of a doctrinaire atheist, it diminishes not only science but the whole of our society.

In a society informed by elective modernism, free criticism of ideas would be a good thing; the right way to pursue knowledge about the natural world would be through observation, theorization and experiment, not revelation, tradition, the study of books of obscure origin or the building of alliances of the powerful. Science's findings are to be preferred over religion's revealed truths, and are braver than the logic of scepticism, but they are not certain. They are a better grounding for society precisely, and only, because they are provisional. It is open debate among those with experience that is the ultimate value of the good society.

Science, then, can provide us with a set of values — not findings — for how to run our lives, and that includes our social and political lives. But it can do this only if we accept that assessing scientific findings is a far more difficult task than was once believed, and that those findings do not lead straight to political conclusions. Scientists can guide us only by admitting their weaknesses, and, concomitantly, when we outsiders judge scientists, we must do it not to the standard of truth, but to the much softer standard of expertise. ■

Harry Collins is director of the Centre for the Study of Knowledge Expertise Science at Cardiff University, UK. He is currently working on a book about tacit and explicit knowledge.
e-mail: collinshm@cf.ac.uk

1. Collins, H. & Pinch, T. *The Golem: What You Should Know About Science* (Cambridge Univ. Press, 1998).
2. Labinger, J. & Collins, H. *The One Culture: A Conversation About Science* (Chicago Univ. Press, 2001).
3. Collins, H. & Evans, R. *Rethinking Expertise* (Chicago Univ. Press, 2007).

Listen to Harry Collins at www.nature.com/podcast.

"Some natural scientists have become too fond of describing their work as godlike."

"Post-modernists have become comfortable in their cocoon of cynicism."

BOOKS & ARTS

Biologist in the Beltway

Nobel prizewinner Harold Varmus's autobiography reveals his skill and passion for research and politics, and shows why he is one of Barack Obama's top science advisers in Washington DC, explains **Iain Mattaj**.

The Art and Politics of Science

by Harold Varmus

W. W. Norton: 2009.

256 pp. \$24.95, £16.99

Anyone knowing, as I did, that Harold Varmus began graduate studies in English literature before switching to science would be forgiven for expecting a book that explores the relations between art, science and politics. Indeed, the original idea behind the series of three public lectures on which the book is loosely based was to re-examine the science and humanities 'two cultures' concept of physicist and novelist C. P. Snow. Instead, Varmus has produced a diverse series of essays focused on aspects of his own life. Varmus describes his choice of science as a career, his research and his experience as director of the US National Institutes of Health (NIH), the world's largest biomedical research funding organization. His views on various fields of science politics, in which he is or has been engaged, complete the book.

Varmus's path from college to cancer research makes interesting reading, especially to a European reviewer for whom such a change in direction would require restarting university from scratch. While majoring in English at Amherst College, Massachusetts, he fulfilled his pre-medical requirements. He then began graduate studies in English literature at Harvard University, but found time to attend a few Harvard Medical School classes with college friends. His doubts about finding an interesting career in literature and a fascination for advances in understanding biology and its medical relevance — fuelled among other things by a visit to Moscow, where he heard about Marshall Nirenberg's account of helping to crack the genetic code — led Varmus to successfully reapply to medical school. Despite his father being a physician, his parents were less than overjoyed at Varmus's return to the 'conventional' path. Families can be hard to please.

Chance soon intervened in the shape of the Vietnam war. On graduation, Varmus deferred the draft by doing two years of training at the NIH. This first introduction to basic laboratory research with Ira Pastan — who is still a prolific biomedical researcher — used bacterial viruses to select and identify individual genes that regulated the expression of other genes.



Harold Varmus's team spirit has helped him succeed both in the lab and elsewhere.

Compared with the intellectual distance Varmus had already covered, it was a relatively small step from there to his work with virologist J. Michael Bishop and others, and to the discovery that the cancer-causing *src* gene of the Rous sarcoma virus was a variant form of a conserved host gene rather than a viral peculiarity. Others quickly discovered numerous cellular genes that can cause cancer when mutated, and Varmus was awarded the Nobel prize. Varmus's description of the satisfactions he found in experimental research, particularly in the early days, is a lucid exposition of why science can be such a rewarding career.

Less satisfying is the section on his directorship of the NIH. Varmus declared of his role: "The inevitable point of departure must be money." By this standard, his tenure between 1993 and 1999 was a huge success. It saw an unprecedented government pledge to double the NIH budget between 1998 and 2003. But the book does not give a satisfactory explanation for this political success, or of Varmus's undoubtedly important role in it. Those of

us who watched from overseas with admiration and envy would have liked to learn more about how it was achieved. His ability to connect basic research to medical application is frequently evident elsewhere in the book. Was this a result of learning on the job, or does it partly explain why he was such a successful advocate for the NIH?

It would also have been interesting to hear Varmus's opinion on whether the bust in NIH funding that followed the increase could have been cushioned. The unfettered growth of biomedical institutions across the United States during the boom years soon outstripped the NIH budget's growth, leading to damagingly low success rates for NIH funding programmes when the budget plateaued. Should, and could, the NIH have a role in coordinating more sustainable growth?

In another section, Varmus describes his own research in some detail. It is fun to remember just how indirect and crude many of the molecular technologies available to us in the 1970s and 1980s were, compared with today. He then describes three areas in which science and politics are intertwined — stem-cell research, global-health research and practice, and open-access publishing. In all three, Varmus provides balanced summaries of the current scientific potential and political debate while leaving no doubt as to his own position. Particularly in the case of open access, his advocacy combines passion with logic into a very persuasive argument.

The Art and Politics of Science is a fascinating but deliberately incomplete and stylistically patchwork autobiography. Varmus reveals a sharp, analytical intelligence as well as great enthusiasm for his work and profession. His preference for working as part of a team and his ability to do so is repeatedly demonstrated throughout the book. This suggests he has the modesty required to allow others to take their share of the credit. The sections on becoming a scientist and on his NIH directorship are accessible, but those describing his own research and current areas of science-policy debate are more appropriate for science professionals, policymakers and administrators. Varmus's personality shines through. ■

Iain Mattaj is director general of the European Molecular Biology Laboratory, Heidelberg, Meyerhofstrasse 1, 69117 Heidelberg, Germany. e-mail: dg-office@embl.de

K. SRAKOCIC/AP

Artistic responses to Darwinism

Darwin: Art and the Search for Origins

Shirn Kunsthalle, Frankfurt, Germany
Until 3 May 2009.



Darwin200

When he boarded HMS *Beagle*, Charles Darwin made room in his luggage for a copy of Alexander von Humboldt's *Personal Narrative*, the account of the German explorer's 1799–1804 journeys in Latin America. Humboldt's view of the natural world was a major influence on the young Darwin, until his own experiences led him to a different interpretation. Where Humboldt the romantic saw unity and harmony, Darwin the scientist saw strife and struggle.

With the spread of illustrated print magazines, artists of the time could hardly overlook the debate among scientists, theologians and philosophers over Darwin's destabilizing theories of evolution and ruthless natural selection. The exhibition *Darwin: Art and the Search for Origins*, running until 3 May at the Shirn Kunsthalle in Frankfurt, Germany, looks at how artists responded in the century following the publication of Darwin's *On the Origin of Species*.

Some of the works are straightforward attempts to promote one side of the argument, but most incorporate concepts that evolutionary theory made inevitable, such as 'deep time'. Not all of the displayed works embrace Darwinism; for example, those of Frederic Edwin Church (1826–1900) tried to reconcile

geological and religious accounts of Earth's history in support of anti-evolutionist positions. But the attitude of his contemporary, Martin Johnson Heade (1819–1904), shifted in favour of Darwinism as he became more familiar with it — as his sublime late series on hummingbirds and orchids shows.

Some of the most interesting artistic responses to Darwinism happened in German-speaking countries in the intellectual wake of Humboldt. The exhibition includes many works by Ernst Haeckel (1834–1919), the German scientist and artist who promoted Darwin's theories in continental Europe with his exquisite illustrations of sea creatures, particularly



the radiolarians. But it is also replete with works less well known as Darwinian.

Arnold Böcklin's *Meeresidylle* (1887) references the evolutionary continuity of humanity with creatures of the sea. It was painted a few years after the Swiss artist forged a friendship with Anton Dohrn, a former student of Haeckel who established a zoological institute in Naples, Italy. The institute's mission was to collect empirical data substantiating Darwin's ideas. Böcklin's work was steeped in mythology, and few critics understood it. Karl Scheffler was an exception: in 1921 he proclaimed Böcklin to be "the painter and poet of Darwinism".

The exhibition also contains works by the convinced Darwinist, Gabriel von Max (1840–1915). As a friend of Haeckel, von Max was a passionate naturalist, but eventually departed from Haeckel's view that humans were the pinnacle of Darwinistic achievement. He came to prefer the pet monkeys he used as models, painting them carrying out human activities (as in *Monkey Before A Skeleton*; pictured, left) such as teaching or learning. In another famous image, his monkeys are portrayed as art critics (see *Nature* 438, 289; 2005).

A successful artist in his day, von Max made enough money to accumulate a vast collection of more than 60,000 zoological, anthropological and ethnological objects. Sold to the German city of Mannheim in 1917, renowned prehistorian Carl Schuchhardt described it as "the richest and most interesting private collection in the field of science since the death of Goethe". Part of this collection is included in this thought-provoking exhibition.

Alison Abbott is *Nature's* senior European correspondent.

The body as a commodity

Biofutures: Owning Body Parts and Information

by Robert Mitchell, Helen J. Burgess
and Phillip Thurtle

Penn Press: 2008. \$39.95, £26 (DVD-ROM)

It is appropriate that a commentary on the possible futures and dangers associated with owning parts of the body — a discussion anchored in biology as information — should be presented as a hypertext DVD rather than as a conventional book. *Biofutures* deploys multimedia information sources, including video, text, interviews, film clips, web links and animations, all accessed through a central menu. The interactive format allows for nonlinear exploration of the three main themes of law,

biology and culture, and users may create their own links with digital bookmarks that can be managed with password protection.

Each theme is subdivided into two chapters based on case studies that have been marked by controversy. In the law section, the case of John Moore in the United States is highlighted by the resulting dispute over the patenting of cell lines derived from his tissue. The DVD also investigates the creation of the patient lobby group PXE International to promote research on the genetic disease PXE, pseudoxanthoma elasticum, and the tensions this created between the community and individual patient rights.

Biology is discussed through the case of the Nexia spider goat, the transgenic goat that contains spider genes that produce a silk-based material in the goat's milk. The lightweight but

strong 'biosteel' will make biodegradable cables with multiple industrial applications. In another case study, the use of cryonics to freeze bodies offers a chance to explore the control of biological clocks in the lab and how this relates to wider economic and financial temporalities.

The section on culture discusses the role of biology-based art as a form of science, a form of critique and a disrupter of natural boundaries. An extended commentary on the fictitious narrative of the films *Jurassic Park* and *Resident Evil* tells us about different possible futures.

Each case study takes about 30 minutes to read and listen to, with an accessible range of clips, interviews and images on each page. Pitched at undergraduate students, it is designed to be used as a teaching aid, bolstered by additional detailed reading. Most sections provide background material, often filmed in labs, such as the creation of immortal cell lines that are key to understanding the John Moore case.

The authors use their broad backgrounds in science policy, history and English literature to locate the question of body ownership within the wider fields of social science and bioethics. Their primary argument is that developments in biocommerce are best understood within the emergence of the 'information society'. Body parts and tissues, such as gene sequences and cell lines, become information products that are mobilized and gain value in the wider tissue economy.

Most importantly, the authors make the point that the tensions this creates — in terms of who should have the right to own tissue — is not specific to nor created by the advent of biotechnology. Instead, debates over ownership rights are endemic to an industrial society where knowledge and information are allowed to take on a commodifiable form, as in a patent. This is nicely captured in the case of John Moore, in which it is observed that "Moore

couldn't own the cell line [because] research would stop — but if no one owned the cell line, research would also stop". The authors explain how each case study reveals a particular aspect of the information society.

Any bioethicist would struggle to find principles that might act as an arbiter of the moral dilemmas posed by the different cases in *Biofutures*. Indeed, the authors steer clear of this, concluding that we need to attain a deeper understanding. There is not one bio-future but many, articulated in both dystopian and utopian images. Futures are traded as expectations that shape markets for biotech products — so the future itself becomes commodified, not just its body parts. ■

Andrew Webster is professor of the sociology of science at the University of York, Heslington, York YO10 5DD, UK, and author of *Health, Technology and Society: A Sociological Critique*. e-mail: ajw25@york.ac.uk

ancestry. How can very different animals such as bats and humans be related? Coyne clarifies the basics of geographic speciation and its importance to evolution: it produces lineages that are initially similar, which then diverge through successive speciation events. Given billions of years of lineage splitting and extinction, the result is bats, humans and everything else on Earth.

Also useful is Coyne's distinction between ancestors and transitional fossils — a common source of confusion. Transitions are exhibited by fossils such as *Archaeopteryx*, which has both dinosaur and bird traits, and the deer-like *Indohyus*, which has traits of both even-toed hoofed mammals and whales, but such fossils may occur at the wrong time or have the wrong suite of features to be ancestral to modern forms. Given the nature of the fossil record, Coyne explains, we would not expect to find or identify ancestral fossils, but we can find cousin species that share transitional features with the elusive direct ancestors. Transitional features therefore delineate how the tree of life branches. Unfortunately, Coyne never quite defines ancestral and derived traits, which would help to clarify the discussion.

A book for the public must simplify, but there lurks the possibility of subsequent distortion. Many people misunderstand evolution as a great chain in which simple forms evolve into more complex ones, rather than the branching and extinction of lineages. Amphibians did not evolve into reptiles, and reptiles did not evolve into mammals and birds. Rather, a population of early tetrapods — four-legged vertebrates — gave rise to a diverse group of organisms that included ancestors of modern frogs and salamanders, and to a separate branch characterized by having an amniotic egg. A primitive amniote gave rise to reptiles and birds on one branch, and mammals on another. Given that the branch leading to mammals preceded that leading to reptiles, it is misleading for Coyne to use the outmoded term 'mammal-like reptiles' instead of 'non-mammalian synapsids'.

It remains a dismal truth that in the United States, almost half of the population does not accept the common ancestry of humans and chimpanzees; anti-evolution sentiments are also manifest in the rest of the developed world, albeit less virulently. Coyne's book will be a good choice to give to the neighbour or teacher who wants to know more about evolutionary biology. Lamentably, his book is still needed. ■

Eugenie Scott is executive director of the National Center for Science Education, Oakland, California 94609, USA, and author of *Evolution vs. Creationism*. e-mail: scott@ncseweb.org

Primed for evolution

Why Evolution is True

by Jerry A. Coyne

Oxford Univ. Press/Viking Press: 2009.
336 pp/304 pp. £14.99/\$27.95



Darwin200

Jerry Coyne, an accomplished population geneticist at the University of Chicago in Illinois, has devoted much time recently to attacking creationism. His articles in popular publications neatly dissect the scientific claims of the creationists, clearly showing their logical and empirical failings. In *Why Evolution is True*, he shifts his concerns to demonstrate to an open-minded reader the strength of evolutionary biology. The book is one long argument for why the theory so often associated with Charles Darwin should — as much as any other well-founded scientific explanation — be recognized as true.

Writing in a conversational yet authoritative tone, Coyne makes evolutionary biology accessible. As befits his speciality, he stresses the genetic foundations of natural selection and adaptation, offering examples from the field and laboratory for how natural selection shapes morphology and biochemistry to adapt species to their environments. Attention is devoted in this balanced book not only to genes and molecules, but also to the fossil record, sexual selection and biogeography. The patterns of distribution of plants and animals over geographic areas provided a key clue to

Darwin, and Coyne gives this finding its due.

Speciation is the missing link in the general public's understanding of evolution, so it is good to see it discussed early in the book and developed fully in a later chapter. Simple natural selection — microbes becoming resistant to antibiotics, weeds developing resistance to pesticides — is not objectionable to evolution sceptics. What they object to is the tree of life — evolution's core concept of common



Archaeopteryx's
fossilized feathers hint
at how birds evolved.

J. EDWARDS/GETTY IMAGES

Q&A: Poetry in the genes

Canadian poet **Christian Bök** plans to encode his verse into DNA that will sit within the genome of a live bacterium. He tells *Nature* why he wants to create an organism that will translate its own poetic response.

What gave you the idea?

Two essays I read inspired my Xenotext experiment to encode a poem inside the cell of another life form. The first reported a project at the Pacific Northwest National Laboratory in Richland, Washington, by Pak Chung Wong, who theorized that it might be possible to encode information as DNA and embed it in a microorganism. He enciphered lyrics to the Disney tune "It's a Small World (After All)", and was able to retrieve the information after several rounds of cell division. The second essay was by Paul Davies, an astrophysicist and exobiologist at Arizona State University in Phoenix. He speculated that the most efficient way for an alien civilization to make contact across stellar distances would be to send out robot emissaries to colonize the Galaxy, then wait until a sentient civilization could discover them. He suggested that such machines already exist — living cells — so perhaps evidence of extraterrestrial communication is already embedded in the DNA of life. I thought, why wait around? Why not make them right now? So I set about seeing if it was technologically feasible to encode a poem as DNA.

Which bacterium will you use?

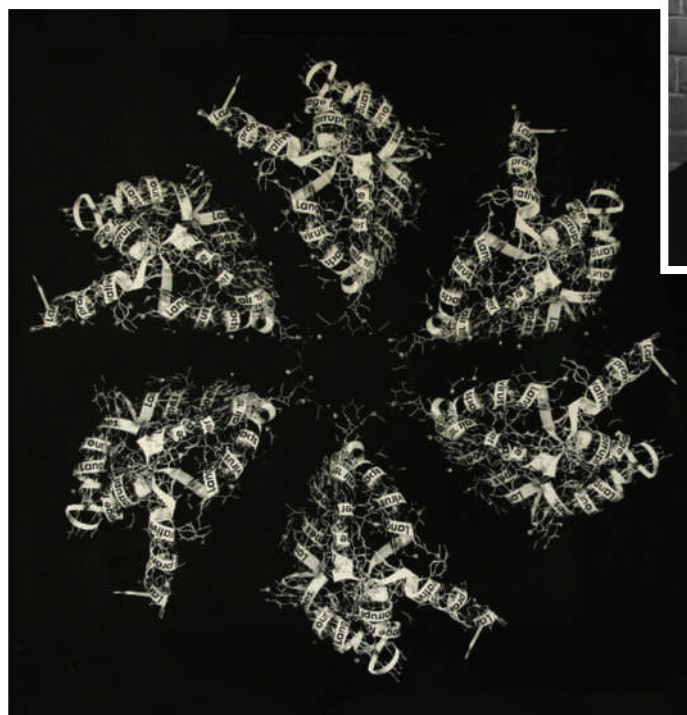
The organism has to be robust. I selected *Deinococcus radiodurans*, an extremophile that can survive heat and cold, dehydration and high doses of γ -radiation. And because the organism can repair its DNA very quickly after genetic mutation, it is highly resistant to evolutionary drift.

How will the poem be encoded?

The poem can be most easily encoded by assigning a short, unique sequence of nucleotides to each letter of the alphabet, as Wong has done. But I want my poem to cause the organism to make a protein in response — a protein that also encodes a poem. I am striving to engineer a life form that becomes a durable archive for storing a poem, and a machine for writing a poem — a poem that can survive forever.

Will future generations decode it?

My project is analogous to building a pyramid and then leaving undecipherable hieroglyphs all over it: later civilizations



E. KOLIN, C. MORRIS

Christian Bök hopes that his DNA-encoded poetry will be deciphered by future generations.

may not understand the language, but its presence will testify to the enduring legacy of our own civilization. An alien readership hundreds of thousands of years from now might recognize that such tampering with an organism constitutes evidence of an advanced intelligence trying to communicate.

What will the poem be about?

I don't know yet — I have to let the vocabulary, derived from my chosen cipher, determine what's possible for me to say based on all the constraints of making a functional sequence. I hope the poem won't be a decision so much as a discovery. Language is very robust. Even under duress, it finds a way to say something uncanny, if not sublime. Poets are always trying to write works that 'come alive' — but I'm trying to write a poem that literally is a living thing.

What is the status of the project?

Stuart Kauffman, a genetics professor at the University of Calgary, Canada, is lending me the expertise of his lab. The scientific portion will cost around Can\$20,000 (US\$16,000) and I hope to complete the

work over the next two years. It will form the premise for a poetic monograph. I will also produce a conceptual art show that will include a sculpture of the gene made from toy molecules, and a diptych of images generated through DNA fingerprinting of the microbe.

Might DNA writing have practical uses?

You could 'watermark' genetically engineered organisms to track their movements through ecosystems, or trace the evolutionary progress of disease, or encode a 'user's manual' within the organism itself. I also imagine the technology could be used cryptographically as a convenient, secretive method of transmitting information. I believe that, in the future, we might want to store data in DNA simply because we want to protect our cultural legacy from planetary disasters — and I hope to be among the first poets to make a work of art out of such a burgeoning technology.

Interview by **Krista Zala**, a journalist based in Victoria, Canada.

e-mail: kzala@nasw.org

STRUCTURAL BIOLOGY

Inside the living cell

David S. Burz and Alexander Shekhtman

Proteins work properly only if they have the correct three-dimensional atomic structure. It is now possible to look at the structures and dynamics of these biological macromolecules as they function inside cells.

The development of structural biology was historically based on the principle of divide and conquer — individual proteins were purified to homogeneity and their atomic structures were solved *in vitro* by using either X-ray crystallography or nuclear magnetic resonance (NMR) spectroscopy. This approach was tremendously successful, and led to the creation of a protein-structure data-bank that currently contains more than 50,000 structures.

But relating *in vitro* protein structures to biological processes that occur inside the cell is not a trivial task. A traditional approach to solving this problem entails mutating a protein's structure at certain sites based on its *in vitro* structure and observing the effects of these changes on the cell. This low-resolution validation of high-resolution structures may still lead to situations where the *in vitro* structure does not fully represent the physiologically active protein structure under the conditions present in a cell. The work presented by Sakakibara *et al.*¹ and Inomata *et al.*² (pages 102 and 106 of this issue) reveals new ways to solve the structures of proteins as they exist inside living cells, ushering in a fresh era of structural biology.

To determine how protein structures are influenced by their intracellular environment, in-cell NMR spectroscopy was developed³. NMR spectroscopy allows one to directly observe NMR-active isotopes of atomic nuclei within any NMR-inactive environment, and can thus be used to analyse isotopically labelled biomolecules inside unlabelled cells. To date, two approaches have been used to deliver labelled proteins into unlabelled bacterial and animal cells. In the first case, target proteins are produced inside the bacteria by growing them on isotopically labelled media; in the second, labelled proteins are microinjected into large cells such as *Xenopus* oocytes (frog eggs)⁴. In these instances, in-cell NMR spectra suggested that protein structures inside cells are very similar

to those solved *in vitro*. The devil, though, is in the detail.

Changes in protein structure that are caused by specific interactions with well-defined binding partners can be identified by solving *in vitro* structures of the protein complexes. A more difficult problem is to address how the numerous, nonspecific, low-affinity interactions, which are

structure is the limited lifetime of the cells inside the NMR sample tube. Standard NMR experiments usually require 1–2 days of data collection, which is an unacceptably long time for live cells. Sakakibara *et al.*¹ shortened this time to 2–3 hours by applying a well-known but seldom-used modification of NMR experiments, and thereby determined the three-dimensional structure of a putative heavy-metal-binding protein, TTHA1718, expressed inside bacterial cells (Fig. 1a). Their procedure, as described in detail in the paper, may well become a new standard for in-cell NMR.

Comparing the *in vitro* and in-cell structures of TTHA1718 revealed that, despite marked similarities, there are structural differences, mostly concentrated in the heavy-metal-binding site and in loop regions that undergo dynamic changes as the protein functions. In contrast to the changes in the binding site, which can be explained by metal ions present in the bacterial cytosol, the structural changes seen in the dynamic loop are probably due to molecular crowding and the viscosity of the cytosol that are characteristic of the cell interior. It will be interesting to discover whether this phenomenon is seen when further in-cell NMR structures become available.

Extending in-cell NMR to study proteins inside human cells presents a further challenge. In general, protein production inside these cells does not reach high enough levels for atomic-resolution in-cell NMR spectra to be collected. The microinjection technique is laborious, and up to now has been limited to large

cells such as *Xenopus* oocytes. Inomata *et al.*² describe an innovative method that avoids using microinjection and makes in-cell NMR in human cells possible. By fusing the labelled target protein with a cell-penetrating peptide (CPP-tag) (Fig. 1b), the target protein can be delivered into the cells, where the peptide tag is then snipped off, allowing the free, labelled target protein to disperse uniformly. Importantly,

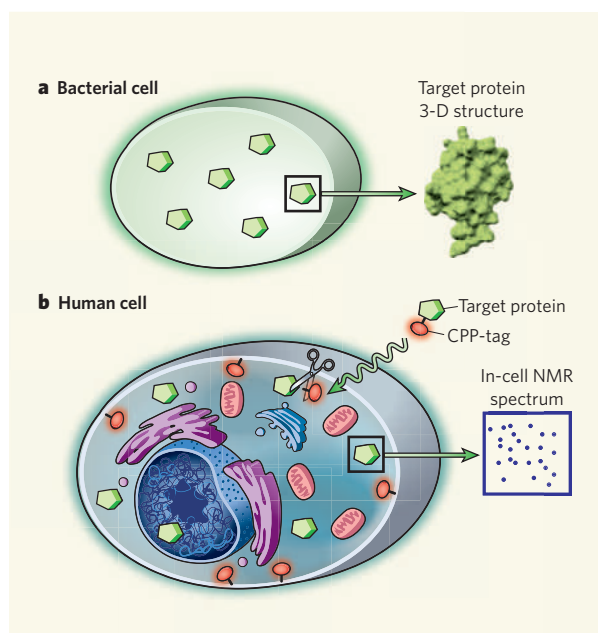


Figure 1 | Analysis of proteins using in-cell NMR spectroscopy. **a**, Sakakibara *et al.*¹ show that atomic structures of proteins expressed inside bacterial cells can be solved by in-cell NMR spectroscopy. **b**, Inomata *et al.*² fused a target protein with a cell-penetrating peptide (CPP-tag) to transfer stable-isotope-labelled proteins into various human cells and collect in-cell NMR spectra at atomic resolution. This approach has not yet been used to determine protein structures but has been applied by the authors to study protein dynamics.

omnipresent in cells, affect a protein's structure. Living cells are extremely crowded environments owing to the high (20–30% by volume) concentration of macromolecules they contain, and this results in small but potentially important changes in protein structure. The papers published in this issue^{1,2} make significant steps towards understanding these changes.

A major hurdle to determining in-cell NMR

the authors found that the tag binds to large intracellular structure(s), making it invisible to NMR and thus simplifying the in-cell NMR spectrum of the target protein.

This method opens the door to determining protein structures inside human cells in the near future, but has already been used by Inomata *et al.* to study in-cell protein dynamics. For example, macromolecular crowding inside the cell should stabilize protein structures. Inomata *et al.* show that, for at least one protein, ubiquitin, introduced into a human cell at physiological concentrations, the opposite is true. Ubiquitin becomes more dynamic in its reactivity and less structured, presumably due to nonspecific, low-affinity interactions with its binding partners. This unexpected result highlights the importance of studying proteins inside living cells.

In-cell NMR is limited by the concentration and structural stability of the protein that can be attained inside cells. In addition, some proteins could be difficult to deliver into the cytosol by fusing them with cell-penetrating peptides. Very large proteins, or proteins that bind to large cellular structures, become invisible and cannot be effectively studied by in-cell NMR. The lifetime of the cells is also a limiting factor, because cell breakdown results in protein leaking away into solution, the condition of *in vitro* NMR. Despite these pitfalls, we are left with an enormous number of proteins that can be studied.

Exploring protein structures and dynamics at the atomic level inside living cells will provide results that cannot be obtained using standard *in vitro* techniques. The comparative simplicity of the in-cell method allows for a myriad of applications. The regulation of metabolic or signal-transduction pathways, mediated by biomolecular interactions, can now be studied in detail. Drug screening using in-cell NMR can function as an *in vivo* assay at atomic resolution, providing information about drug delivery inside the cell, where the drug binds, and whether there is a notable difference between how it binds *in vivo* and *in vitro*. More exotic applications include the study of intrinsically unstructured and amyloid-forming proteins in neurons — such proteins having been implicated in neurodegeneration — or of labelled protein probes in diseased tissue. The ability to observe the structures of proteins in their native environment releases the constraints that have previously limited study of protein structure and dynamics to the test tube. Now that structural biology has moved into the cell, it is likely to stay there. ■

David S. Burz and Alexander Shekhtman are in the Department of Chemistry, State University of New York at Albany, 1400 Washington Avenue, Albany, New York 12222, USA.
e-mail: ashekhta@albany.edu

CONDENSED-MATTER PHYSICS

Carbon conductor corrupted

Michael S. Fuhrer and Shaffique Adam

Atomically thin sheets of graphite are metal-like conductors — until they react with hydrogen, when they become insulators. This curious effect could be an excellent model for studying metal-insulator transitions.

In most solids, electrons behave much like particles of matter: they have a mass, and they speed up and slow down in response to forces. But in graphene — the single-atom-thick sheet of carbon that constitutes the basic building block of graphite — electrons move as if they have no mass^{1,2}, and so behave more like photons. In other words, although electrons in graphene can change their momentum and energy, they cannot speed up or slow down. One would therefore intuitively think that electron flow (electrical current) in graphene could never be completely blocked. But reporting in *Science*, Elias *et al.*³ show that, when graphene reacts with a small amount of hydrogen, its electrons become stuck and the carbon sheet becomes an insulator.

The band structure of a material describes which energy states can be occupied by the material's constituent electrons. Just like other fermions, electrons in a solid fill up the lowest-energy bands first, before filling up bands at higher energies, like water filling a bath. If electrons at the top surface — the Fermi level — of the resulting electron sea can slosh about into the unoccupied part of the band structure, then the solid is said to be a metal, in which electrical currents are created by electrons moving from one momentum state to another (Fig. 1a). But if the electrons are not free to move because of a gap in the band structure, then the solid is a 'band insulator' (Fig. 1b).

There is, however, another way to make an insulator. Electrons are quantum-mechanical objects that behave as waves. Constructive interference of electron waves near any imperfections — disorder — in a solid creates standing waves (Fig. 1c) that are localized in real space, effectively 'freezing' the electron sea⁴. A long-standing conjecture in physics states that electrons in any two-dimensional system will become localized by any disorder, no matter how small. Because all two-dimensional electronic systems contain some disorder, all such systems should therefore be insulators⁵. In practice, however, very low temperatures and/or large samples are needed to reveal this insulating behaviour, and even then the effect is not always seen.

So how does graphene fit into all this? The band structure of graphene can be thought of as a cone balancing on its tip, atop the point of another cone (Fig. 1d). Because there is no bandgap, graphene is a metallic conductor. But graphene differs from other metals when its Fermi level lies at the Dirac point — the point

where the cones touch. There, the top surface of the electron sea becomes vanishingly small. One consequence is that, in contrast to disorder-free metals (which would have infinite conductivity), perfect sheets of graphene are expected to have a conductivity of $4e^2/\pi h$, where e is the electronic charge, and h is Planck's constant. Furthermore, graphene is thought to be the only exception to the localization conjecture: if it contains only 'smooth' disorder in which there are no sharp changes between neighbouring carbon atoms, then graphene remains metallic, and even quantum interference cannot localize its electrons⁶.

In reality, graphene is found to have a sample-dependent, finite minimum conductivity that is always greater than $4e^2/\pi h$ (ref. 1), thus creating a mystery — how could the disorder present in real graphene increase the conductivity above the theoretical value for perfect graphene? Disorder normally increases the scattering of electrons, which decreases conductivity.

The answer lies in the nature of the disorder. Most graphene samples are dirtied by charged impurities that lie near the graphene sheet, either on the surface or in the nearby substrate⁷. These charges have two effects: they create a smooth disorder that scatters electrons (which reduces conductivity), but they also either attract or repel electrons, creating local electron-rich or electron-poor 'puddles' whose Fermi levels lie above or below the Dirac point. The electrons in these puddles increase the conductivity of the sample, counteracting the decrease due to scattering⁸.

By adding hydrogen to graphene, Elias *et al.*³ were able to study a fundamentally different sort of disorder. By reacting all the carbon atoms in a graphene sheet with hydrogen, so that each carbon becomes bonded to a single hydrogen atom, the authors made a new kind of two-dimensional crystal. This material, known as graphane, is expected to be a conventional band insulator⁹.

But at lower doses, hydrogen probably bonds randomly to only a few carbon atoms. Unlike charged impurities, which cause a smooth disorder, hydrogen creates sharply varying disorder, because a carbon atom bonded to hydrogen is very different from its neighbours. The authors³ observed that their partially hydrogenated graphene had greatly reduced minimum conductivity, which varied with temperature and tended towards zero at low temperatures — the signature of an insulator. This is in contrast to graphene containing

1. Sakakibara, D. *Nature* **458**, 102–105 (2009).

2. Inomata, K. *et al.* *Nature* **458**, 106–109 (2009).

3. Serber, Z. *et al.* *J. Am. Chem. Soc.* **123**, 2446–2447 (2001).

4. Selenko, P. *et al.* *Proc. Natl Acad. Sci. USA* **103**, 11904–11909 (2006).

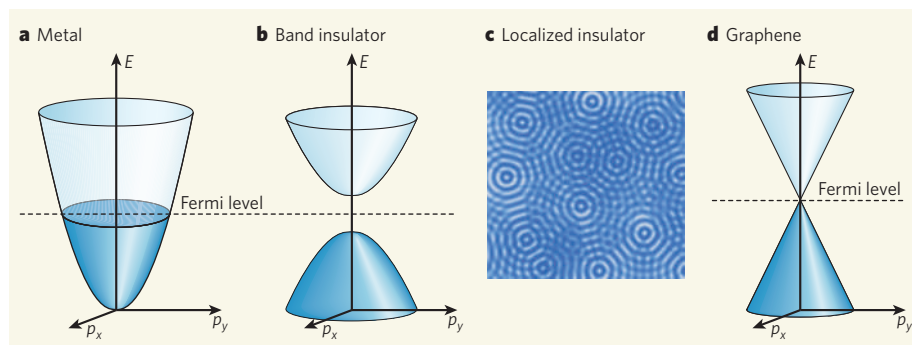


Figure 1 | Metal-insulator transitions. **a**, The electronic energy states of metals form a series of bands. Electrons fill the bands up to a maximum energy defined by the Fermi level. E is energy, p is momentum. **b**, The Fermi level of a band insulator lies in a gap in its band structure. Electrons completely fill the lower valence band, but do not cross into the upper conduction band, and so are not free to form a current. **c**, Imperfections in solids scatter electrons, creating standing waves that also prevent the motion of electrons, so resulting in a localized insulator. **d**, The electronic energy-states of graphene form two cone-shaped bands that meet at their tips. In charge-neutral graphene, the Fermi level lies at the tip of the cones. There is no bandgap, so the material is classed as a metal. Elias *et al.*³ show that when graphene reacts completely with hydrogen, it forms a new material (graphane) that is expected⁹ to be a band insulator. Reaction of graphene with smaller amounts of hydrogen (also demonstrated by Elias *et al.*) might produce sharp imperfections that bring about a localized insulating state.

charge disorder, where the conductivity is temperature-independent at low temperatures¹.

Why are the effects of charged impurities different from those caused by bonding to hydrogen? The unique properties of graphene prevent the slowly varying potential of a charged impurity from completely backscattering (reversing the direction of) electrons. An exciting possibility is that sharp disorder caused by hydrogen

can easily backscatter electrons. The resulting interference of forward- and backward-moving electrons would create localized states at zero temperature, just like those found in other two-dimensional systems¹⁰. Another possibility is that hydrogen locally modifies the band structure of graphene, so creating a band insulator.

More work will be needed to understand

both the electronic structure of hydrogenated graphene and the effects of sharp and smooth disorder on the scattering of its electrons. Nevertheless, these results³ suggest that graphene could be almost the ideal material in which to study transitions of metals to insulators. Unlike other two-dimensional systems, in which electrons are buried at the interface between two materials, graphene's surface is exposed. This allows not only direct imaging of defects by scanning tunnelling microscopy, but also the use of techniques that probe electronic structure, thus creating new windows through which metal-insulator transformations can be viewed.

Michael S. Fuhrer is at the Center for Nanophysics and Advanced Materials, Department of Physics, and Shaffique Adam is at the Condensed Matter Theory Center, Department of Physics, University of Maryland, College Park, Maryland 20742, USA. e-mails: mfuhrer@umd.edu; adam1@umd.edu

1. Novoselov, K. S. *et al.* *Nature* **438**, 197–200 (2005).
2. Zhang, Y., Tan, Y.-W., Stormer, H. L. & Kim, P. *Nature* **438**, 201–204 (2005).
3. Elias, D. C. *et al.* *Science* **323**, 610–613 (2009).
4. Anderson, P. W. *Phys. Rev.* **109**, 1492–1505 (1957).
5. Abrahams, E. *et al.* *Phys. Rev. Lett.* **42**, 673–676 (1979).
6. Bardarson, J. H. *et al.* *Phys. Rev. Lett.* **99**, 106801 (2007).
7. Chen, J.-H. *et al.* *Nature Phys.* **4**, 377–381 (2008).
8. Adam, S., Hwang, E. H., Galitski, V. M. & Das Sarma, S. *Proc. Natl Acad. Sci. USA* **104**, 18392–18397 (2007).
9. Sofo, J. O., Chaudhari, A. S. & Barber, G. D. *Phys. Rev. B* **75**, 153401 (2007).
10. Aleiner, I. L. & Efetov, K. B. *Phys. Rev. Lett.* **97**, 236801 (2006).

DRUG DISCOVERY

Not as fab as we thought

Soumaya Zlitni and Eric D. Brown

Ever since penicillin was isolated from mould, it has been assumed that naturally occurring antibiotics are good starting points for drug-discovery programmes. The latest study shows that this isn't always true.

Drug-resistant bacterial infections continue to occupy the headlines, amid increasingly desperate calls for new antibiotics to treat infectious diseases. Some of the most alarming reports concern 'Gram-positive' pathogens¹, which are a pervasive nuisance in both the clinic and the world at large. The recent discovery² of the potent antibiotic platensimycin was therefore greeted with great enthusiasm. Platensimycin was isolated from soil-dwelling *Streptomyces platensis* microbes, and represents a new class of antibiotic that acts against Gram-positive pathogens. But on page 83 of this issue, Brinster *et al.*³ provide a sobering lesson in what drug discoverers call target validation. The authors show that, although compounds that have the same mechanism of action as platensimycin are effective antibacterials in soil, they are inactive in models that simulate

environments relevant to infection.

The problem with existing antibiotics is that they attack a narrow spectrum of bacterial physiology: most interfere with the synthesis of bacterial DNA, proteins or cell walls. There is therefore great interest in exploring new biological targets for antibacterial therapies. One potential target is fatty-acid biosynthesis, and the past few years have witnessed intense efforts to identify inhibitors of this process.

Fatty acids are organic molecules that contain long, unbranched hydrocarbon chains of up to 18 carbon atoms. Their biosynthetic machinery is encoded by several genes involving the *fab* loci of the bacterial genome. Fab proteins come together to construct fatty acids, two carbon atoms at a time, in a cyclic process. The promise of this biosynthetic pathway as an antibacterial target stems from the fact that it is essential

for the formation of cellular membranes in a wide range of bacterial pathogens. The process is distinct from fatty-acid biosynthesis in humans, suggesting that antibiotics that block this mechanism could be made that are selectively toxic for bacteria.

Several compounds have already been identified that inhibit specific steps in the bacterial biosynthesis of fatty acids. These include synthetic compounds (such as the antituberculosis compound isoniazid and the general-purpose antibiotic triclosan) and naturally occurring compounds (such as cerulenin and thiolaclomycin, both broad-spectrum antibiotics)⁴. The synthetic compounds, however, have had only niche applications — isoniazid in combination therapies and triclosan in soaps and plastics — whereas the natural products have never proved useful in the clinic. Nevertheless, the discovery of platensimycin as a new addition to the roster of fatty-acid biosynthesis inhibitors generated renewed excitement about this antibiotic class.

Yet studies dating as far back as the late 1970s have shown that Gram-positive bacteria can acquire fatty acids from their surroundings and incorporate them into their cell membranes⁵. Given that human serum is a rich source of such acids, these findings seriously undermine the idea that inhibitors of bacterial

fatty-acid biosynthesis could fight infections: the effects of such drugs would be overcome if the pathogens simply take up fatty acids from serum. Brinster *et al.*³ conducted experiments to directly address this contradiction, and present compelling evidence that calls into question the value of antibiotic therapies that target fatty-acid biosynthesis.

The authors began their investigation by treating several clinical isolates of Gram-positive pathogens — including strains resistant to commonly used antibiotics — with triclosan and cerulenin, in growth media that either contained or lacked fatty acids. They found that both inhibitors are quite effective at inhibiting the growth of drug-resistant strains in standard laboratory media (which lack fatty acids), but that this effect was abolished when certain fatty acids were added individually, or when human serum was added. They also observed that the strict requirement for fatty-acid biosynthesis to sustain bacterial growth is superseded when fatty acids are readily available in the growth environment, as demonstrated by the low level of expression of *fab* genes in bacteria that were cultured under these conditions. Moreover, they found that mutant strains of bacteria that were defective in up to five of the *fab* genes flourish in fatty-acid-rich serum.

In vitro experiments are all well and good, but the gold-standard studies for drug discovery are those performed *in vivo*. Most significantly, in animal experiments testing the implications of fatty-acid biosynthesis in host infection, the authors were especially careful to run their tests under conditions that closely reflect real-world infection, a criterion sometimes overlooked in such studies. Together, their results strongly support the conclusion that fatty-acid biosynthesis is a poor target for drugs against Gram-positive pathogens.

This work³ offers a profound lesson in target validation. A cornerstone of modern antibacterial drug discovery is that cellular processes are investigated *in vitro* (Fig. 1), because this is quicker, cheaper and simpler than investigating these processes in animals. Such *in vitro* models are usually fine, because the bacterial processes that are important for life in a Petri dish are also almost always essential for the survival of bacteria that have infected a host — although many more bacterial functions that can't be modelled in a dish will also be crucial for infections. But the current study begs the question: what if functions important for growth in the laboratory are superfluous for growth in a host? In raising this point, Brinster

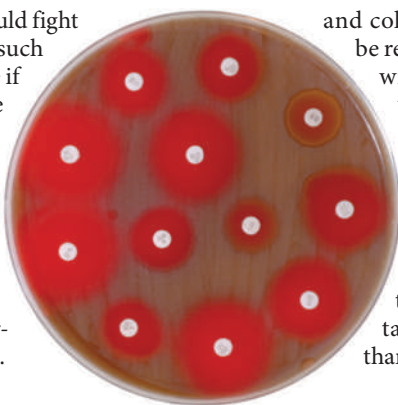


Figure 1 | Sure of the cure? Antibiotics are usually tested for their efficacy *in vitro*. Here, the red regions around antibiotic-impregnated wafers indicate areas of poor bacterial growth. Brinster *et al.*³ show that such assays can be misleading if they don't accurately simulate environments relevant to infection *in vivo*.

and colleagues' work is likely to be regarded as a landmark that will raise the bar for target validation in drug discovery in the future. A likely outcome is that novel biological targets for antibiotics will be scrutinized with many more experiments than before to understand the importance of those targets for infection (rather than just their role in bacterial survival *in vitro*).

This work also challenges common assumptions associated with the discovery of naturally occurring antibiotics from organisms such as streptomycetes. It is tempting to conclude that the very existence of such compounds validates the target of the antibiotic as being suitable for pharmaceutical intervention. This idea stems from the notion that antibiotics are the result of an evolutionary arms race among soil-dwelling bacteria.

But one must be mindful of the environmental conditions that define the limits of this struggle. Antibiotics from streptomycetes have evolved to provide those organisms with an advantage in a soil environment where fatty acids, for example, are in short supply.

Antibiotic drug discovery and development is an onerous process fraught with long development times, high costs and the risk that regulatory agencies will ultimately reject the discoverer's application to sell the fruits of their labours⁶. Brinster and co-workers' work³ will resonate with those working in drug discovery, and will inspire renewed efforts to understand the basis of bacterial pathogenesis.

Soumaya Zlitni and Eric D. Brown are in the Department of Biochemistry and Biomedical Sciences, and the Michael G. DeGroote Institute of Infectious Disease Research, McMaster University, Hamilton, Ontario L8N 3Z5, Canada. e-mail: ebrown@mcmaster.ca

1. Weigel, L. M. *et al. Science* **302**, 1569–1571 (2003).
2. Wang, J. *et al. Nature* **441**, 358–361 (2006).
3. Brinster, S. *et al. Nature* **458**, 83–86 (2009).
4. Heath, R. J., White, S. W. & Rock, C. O. *Prog. Lipid Res.* **40**, 467–497 (2001).
5. Altenbern, R. A. *Antimicrob. Agents Chemother.* **11**, 574–576 (1977).
6. Fernandes, P. *Nature Biotechnol.* **24**, 1497–1503 (2006).

ASTROPHYSICS

Capturing black-hole pairs

Jon M. Miller

The observed growth of galaxies suggests that the black holes thought to lurk at their centres may find each other and merge. A large survey of galaxies has finally netted two black holes in a tight pairing.

The idea of black holes merging may seem like the height of scientific extremity, but such mergers may be commonplace if the prevailing theory of structure formation in the Universe is correct. Scant context is provided by the solar neighbourhood: stars within a galaxy do not merge because they are very small relative to their separations. However, the distances that separate galaxies are not as large in comparison to their size, and observations reaching back to the early Universe strongly suggest that galaxies grow through a hierarchy of mergers¹. In a galactic merger, gravitation and dynamical friction drag black holes to the bottom of the 'gravitational well', where they encounter each other and may eventually merge. Nowhere is this sinking of black holes more apparent than in clusters of galaxies, best exemplified by the nearby Virgo cluster and the monstrous billion-solar-mass black hole at the heart of its central galaxy.

By carefully sifting through 17,500 spectra of quasars — extremely bright galactic nuclei thought to be powered by supermassive black holes — selected from the unprecedentedly

large Sloan Digital Sky Survey² (SDSS), Boroson and Lauer³ (page 53) have identified the first compelling example of a tightly bound black-hole binary system in a quasar known as SDSS J153636.22+044127.0. The pair of black holes is separated by a mere 0.1 parsecs, or about 1,300 times the radius of the event horizon (a boundary in space-time beyond which nothing can escape) of the more massive member. This distance is 13 times shorter than that between the Sun and its nearest neighbour, the Alpha Centauri star system. The finding³ is an important validation of the theory of hierarchical structure growth in the Universe.

Previous work has identified potential examples of black holes on their way to merging, but the case presented by Boroson and Lauer is special because the pairing is tighter and the evidence much stronger. An X-ray image taken with the Chandra X-ray Observatory of the galaxy NGC 6240 reveals two bright nuclei⁴ powered by the accretion of gas onto black holes, but their separation is very large. The precessing radio jet seen in another galactic

nucleus, OJ 287, may be a signature of a binary black-hole system⁵, but this is not the only possible explanation. Recently, evidence of a black-hole pair was claimed in another SDSS quasar, but the binary separation is much larger than that of Boroson and Lauer's system and, again, the case is not closed^{6,7}.

Catching black holes in a final embrace has proved extremely difficult. When the separation is small enough that merging seems inevitable, the limitations of today's observatories make it hard to obtain an image that resolves the binary pairing. Indirect methods, including optical spectroscopy, provide a way forward. Quasars make for an excellent subset of galaxies in which to search for merging black holes. First, quasars are merely supermassive black holes in the process of actively accreting gas; galactic mergers can supply the needed gas. Second, gas accretion may be important in helping black holes spiral closer to one another once they are separated by only about 1 parsec. At this crucial range, loss of orbital energy to gravitational radiation is not yet sufficient to lead to the merging of the black holes. This radiation is a fundamental prediction of the general theory of relativity: massive bodies induce a curvature in spacetime, and orbiting massive bodies induce ripples in spacetime (the gravitational radiation) that propagate at the speed of light.

Satellite imaging of hurricanes often affords a view of the eye wall, where clouds rotate rapidly, and of the outer parts of the hurricane, where rotation is slower. Similarly, in quasars, optical spectra reveal distinct 'broad-line' and 'narrow-line' emission regions in orbiting gas. The broad-line region typically lies about 0.01 parsecs from the black hole, and the narrow-line region at a radius about 1,000 times larger⁸. The differing emission line widths can be ascribed to the fact that Keplerian orbital speeds fall with increasing radius. Boroson and Lauer³ have identified the only case of two eye walls within one hurricane in the selected sample of the Sloan Survey. Their spectroscopic technique is, by its very nature, indirect. But it is fairly robust and draws on common features — the broad- and narrow-line emissions — that spectroscopy clearly demarcates into distinctive physical regimes. At 0.3%, the probability that a superposition of two unrelated quasars has given a false detection is not zero, but the claimed black-hole binarity can be tested through spectroscopic monitoring in the years ahead.

But electromagnetic radiation may not be the optimal way to search for merging black holes. A merging black-hole pair is expected to be a prodigious source of gravitational radiation. Although it has not been detected directly, the orbital evolution of the Hulse–Taylor binary pulsar, which was discovered by Russell Hulse and Joseph Taylor in 1974, can only be explained through gravitational wave losses. The Laser Interferometer Space Array (LISA), a space-based mission that is currently

under development, is designed to detect the radiation carried by such gravitational waves when supermassive black holes merge.

The fact that only one strong binary black-hole candidate has emerged from a selection of 17,500 quasars could suggest that only a modest number of mergers should be expected from LISA observations. But the number of galaxies accessible with LISA is much greater than the number of quasars studied in the Sloan Survey. Moreover, it is possible that binary black holes reside in 'normal' galaxies in which the black holes are not in an actively accreting quasar phase. The results reported by Boroson and Lauer are sure to spur new theoretical and observational work that will affect our understanding

of large-scale structure formation in the Universe, the rate of black-hole mergers and accretion onto supermassive black holes. ■

Jon M. Miller is in the Department of Astronomy, University of Michigan, Ann Arbor, Michigan 48109, USA.

e-mail: jonmm@umich.edu

1. White, S. D. M. in *Cosmology and Large Scale Structure* (eds Schaeffer, R. et al.) 121 (North-Holland, 1996).
2. Schneider, D. P. et al. *Astron. J.* **134**, 102–117 (2007).
3. Boroson, T. A. & Lauer, T. R. *Nature* **458**, 53–55 (2009).
4. Komossa, S. et al. *Astrophys. J.* **582**, L15–L19 (2003).
5. Valtonen, M. J. et al. *Astrophys. J.* **643**, L9–L12 (2006).
6. Komossa, S., Zhou, H. & Lu, H. *Astrophys. J.* **678**, L81–L84 (2008).
7. Heckman, T. M., Krolik, J. H., Moran, S. M., Schnittman, J. & Gezari, S. *Astrophys. J.* (in the press).
8. Peterson, B. M. et al. *Astrophys. J.* **613**, 682–699 (2004).

CANCER

Blood vessels kept quiet

Andrew V. Benest and Hellmut G. Augustin

Tumours must get their oxygen fix, otherwise invasive tumour growth and spread can occur. One way of quelling oxygen-deprived tumours might be through manipulating the oxygen sensor PHD2.

Beyond the limits of diffusion, tumour maintenance depends both on an adequate supply of oxygen and on removal of metabolic waste by the blood. When blood vessels can't supply enough oxygen, tumour cells invade the surrounding normal tissue in search of oxygen and might even metastasize to other tissues. Endothelial cells line blood vessels and so are the gateway to tissue oxygenation. It is therefore essential to define the molecules and pathways in these cells, not only for a better understanding of cancer, but also to develop more effective anticancer therapies. Writing in *Cell*, Mazzone et al.¹ identify the PHD2 protein as a key regulator of oxygen supply to tumours, and suggest that it may be involved in the shaping of blood-vessel networks.

Only a few tumours can prey on the host vasculature, and so most induce new vessels to grow — a process called angiogenesis. In response to tumour-derived angiogenic stimuli, endothelial cells break away from the neighbouring blood vessels and migrate towards the stimuli, subsequently proliferating and becoming organized into a network of new capillaries.

One major angiogenic stimulus that is used by tumours, as well as normal tissues, is vascular endothelial growth factor (VEGF). This is produced in conditions of low oxygen levels (hypoxia) under the control of the HIF family of transcription factors. At normal oxygen levels, HIF-1 α and HIF-2 α are short-lived because PHD proteins (PHD1, 2, 3 and 4) mediate their degradation². During hypoxia, however, PHD proteins are less active, and so HIF-1 α and HIF-2 α can form heterodimers

with HIF-1 β to trigger the expression of genes containing hypoxia-response elements, including the gene encoding VEGF³. Therefore, PHDs act as oxygen sensors to control gene expression during hypoxia by regulating the stability of HIF transcription factors.

Genetic ablation of oxygen sensors has yielded insights into the molecular function of PHDs. For example, *PHD2*-deficient mice die before birth from severe heart and placental defects⁴. Moreover, deletion of this gene in adult mice leads to active angiogenesis of highly perfused blood vessels⁵.

Mazzone et al.¹ generated mice lacking one of the two copies of the *PHD2* gene. They found that these *PHD2*^{+/-} mice develop normally and show no obvious developmental defects. Likewise, when the authors implanted tumours in these mice, they detected no differences in growth rate or microvessel density compared with tumours in normal mice. But the tumours' vascular morphology was strikingly different.

The authors show that the blood vessels of tumours grown in normal mice are disordered and poorly perfused. Blood vessels in tumours grown in *PHD2*^{+/-} mice, however, look more like those of normal tissues, with a regular layer of endothelial cells. Consequently, perfusion and oxygenation of these tumours is improved, and invasion and metastasis by their cells are inhibited (Fig. 1). Intriguingly, deletion of one copy of *PHD2* in endothelial cells alone resulted in similar features for tumour blood vessels to those of *PHD2*^{+/-} mice, which lack a copy of this gene in every cell of their body. This finding indicates that the vascular morphology seen in *PHD2*^{+/-} mice results

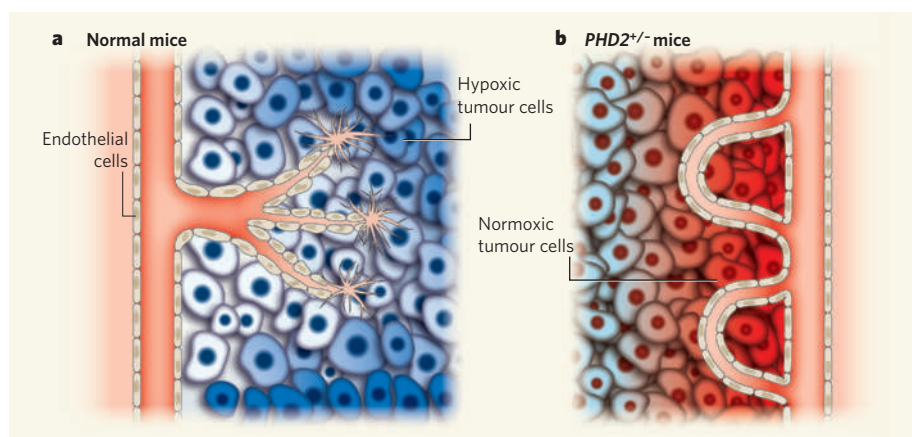


Figure 1 | PHD2 and tumour vasculature. Mazzone *et al.*¹ show that tumours grown either in normal mice or in mice lacking one copy of the *PHD2* gene (*PHD2*^{+/-} mice) show roughly similar growth rates and densities of blood microvessels. **a**, Yet in normal mice, tumours have disordered, poorly perfused blood vessels, which result in a low-oxygen environment and so intense VEGF production. **b**, By contrast, tumour vessels in *PHD2*^{+/-} mice look more like normal blood vessels, with the lining endothelial cells having a regular, flattened shape. These normalized vessels result in better oxygenation of the tumour, which in turn leads to less VEGF production and reduces these cells' response to VEGF by increasing expression of soluble and membrane-bound VEGF receptor-1, as well as VE-cadherin.

from perturbed oxygen sensing specifically in endothelial cells.

In principle, endothelial cells should be the last to experience hypoxia. Tumour cells often take on a cylindrical arrangement around blood vessels, with the most highly oxygenated cells closest to the vessels and hypoxic tumour cells farther away — adjacent to regions with no oxygen and so containing dying cells. Thus, Mazzone and colleagues' observation that endothelial cells contain oxygen sensors indicates that these cells, which are strategically located at the blood–tissue interface, act as gatekeepers for sensing oxygen levels. In agreement with this conclusion, the PHD-protein target HIF-2 α is preferentially expressed in endothelial cells, and its role as an oxygen sensor of the vascular endothelium was reported previously⁶.

Anti-angiogenic cancer therapy often prunes the most immature blood vessels in tumours to leave a thinned, more normal-looking vascular network of main blood vessels. This concept of 'vessel normalization' has received significant attention in recent years, not least because it helps to explain the clinically observed⁷ synergy between anti-angiogenic and chemotherapeutic agents. The 'normalized vasculature' is better perfused and is thought to improve the access of chemotherapeutic drugs to tumours. Mazzone and colleagues' results suggest a mechanism by which this may occur.

Several molecular systems that act in concert have been implicated in vessel normalization, including the balance between VEGF, platelet-derived growth factor-B (ref. 8) and the vessel-destabilizing protein angiopoietin-2 (ref. 9). Mazzone *et al.* now add oxygen sensors to the list of factors regulating normalization of endothelial cells, and they propose that the manipulation of PHD proteins in these cells might have therapeutic potential. Although

a fascinating idea, therapeutic inhibition of PHD2 may be a long shot, as the mechanism underlying oxygen-sensing-dependent vascular normalization that the authors report is poorly understood.

For instance, Mazzone *et al.* implicate soluble and membrane-bound VEGF receptor-1 as well as VE-cadherin protein as PHD2-regulated mediators of endothelial-cell normalization. Although these molecules are major regulators of quiescent endothelial cells, they are not generally associated with angiogenesis-controlling, hypoxia-regulated genes. Moreover, it is surprising that Mazzone *et al.* did not find altered expression of molecules such as VEGF, angiopoietin-2 and its receptor Tie1 in endothelial cells of *PHD2*^{+/-} mice.

When thinking of hypoxia, one usually considers rapid adaptive response programs as being involved. So it could be that the tumour-vessel features seen in *PHD2*^{+/-} mice reflect long-term adaptation of endothelial cells to

the loss of one *PHD2* copy — a 'compensation' feature rather than an indication of a rapid loss of PHD2 regulation, as might be required from a therapeutic point of view.

On the basis of the vessel normalization observed in *PHD2*^{+/-} mice, Mazzone *et al.* describe endothelial cells lining a normalized vessel as 'phalanx cells'. At first sight, to rename a well-known cell — namely, the quiescent, resting endothelium — may seem unnecessary. Yet the introduction of the term phalanx cells comes at just the right time, and regarding them as such could significantly shape future research in vascular biology.

Angiogenesis research has focused strongly on the molecular and functional characterization of two cell types in an angiogenic sprout: the leading 'tip cell' and the subsequently proliferating and remodelling 'stalk cells'¹⁰. Although phalanx cells would conceptually seem to follow stalk cells, at present they are defined only functionally, as no molecular markers for them have been described. Better molecular characterization of phalanx cells might therefore greatly advance the field of vascular biology and pave the way towards cancer therapies that target activated endothelial cells. ■

Andrew V. Benest and Hellmut G. Augustin are in the Joint Research Division Vascular Biology of the Medical Faculty Mannheim, University of Heidelberg (CBTM), and in the German Cancer Research Centre Heidelberg (DKFZ-ZMBH Alliance), INF280, D-69120 Heidelberg, Germany. e-mail: augustin@angiogenese.de

1. Mazzone, M. *et al.* *Cell* doi:10.1016/j.cell.2009.01.020 (2009).
2. Fong, G. H. & Takeda, K. *Cell Death Differ.* **15**, 635–641 (2008).
3. Qing, G. & Simon, M. C. *Curr. Opin. Genet. Dev.* **19**, 1–7 (2009).
4. Takeda, K. *et al.* *Mol. Cell. Biol.* **26**, 8336–8346 (2006).
5. Takeda, K., Cowan, A. & Fong, G.-H. *Circulation* **116**, 774–781 (2007).
6. Licht, A. H., Müller-Holtkamp, F., Flamme, I. & Breier, G. *Blood* **107**, 584–590 (2006).
7. Jain, R. K. *Science* **307**, 58–62 (2005).
8. Greenberg, J. I. *et al.* *Nature* **456**, 809–813 (2008).
9. Nasarre, P. *et al.* *Cancer Res.* **69**, 1324–1333 (2009).
10. Gerhardt, H. *et al.* *J. Cell Biol.* **161**, 1163–1177 (2003).

CHEMICAL PHYSICS

Melted in a flash

A. Cavalleri

The observation that atomic disorder emerges exceptionally fast during laser-induced melting of crystalline bismuth prompts fresh thinking about the nature of this phase transition.

In this issue (page 56), Sciaini *et al.*¹ report on the use of ultrashort bursts of electrons to observe the appearance of microscopic disorder when crystalline bismuth is melted by a laser. They find that melting occurs in less than 200 femtoseconds (one femtosecond is 10⁻¹⁵ s)

— a fraction of the period of an atomic-lattice vibration. This finding revisits a century-old debate about which microscopic properties map the solid and liquid phases onto one another.

The phase transitions we understand

best are those that can be pictured along a continuous, traceable trajectory connecting two known phases that differ mathematically by a single symmetry operation². Liquid-to-gas transitions, in which microscopic order is absent from both phases, can be described in this way provided that the balance between attractive and repulsive forces between the atoms is known and that loss of symmetry is replaced by changes in density.

However, the description of solid-to-liquid transitions is not so trouble-free. The main problem is that when a crystalline solid melts, atoms not only become disordered, but also become free to move about in a network of weak bonds, which are constantly being broken and re-formed. The liquid must then be described not only by the relative positions of the atoms but also by their relative velocities. It is thus difficult to identify a mathematical procedure that maps out the transition between the solid and the liquid, one that describes both the loss of symmetry and the weakening of the bonds.

Some descriptions of melting have focused only on the emergence of structural disorder³, and ignored the mechanical properties of the melt, akin to what would happen if a solid alloy were formed. Other theories describe melting only in terms of the vanishing of rigidity⁴. And indeed, a material in the solid phase, which is resistant to both compression and shear, loses its resistance to the latter when it melts. But this second description ignores the microscopic characteristics of the liquid phase, missing the key physics of disorder, entropy and the existence of latent heat (the amount of internal energy that must be 'traded in' for the increase in disorder).

Microscopic theories of melting are also hard to verify experimentally. The liquid phase does not emerge smoothly with increasing temperature, but rather switches on abruptly. At the melting temperature, randomly fluctuating nuclei of liquid grow and collapse incoherently at many sites in the atomic lattice at once. Melting then avalanches across the solid and the transition is over before one has had time to capture it. Understanding melting at the microscopic level thus requires following the changes associated with the phase transition on atomic lengths and timescales.

For some solids, excitation with optical lasers can weaken the bonds and trigger the transition simultaneously at all lattice sites. Although laser-induced melting does not necessarily follow the same pathway as the thermally driven process, it has the benefit of setting off the transition at a time and place chosen by the experimentalist, and reveals at least one possible microscopic pathway to melting.

In a stable, crystalline lattice of bismuth, moderate optical excitation is known to drive the lattice towards a higher-symmetry, cubic

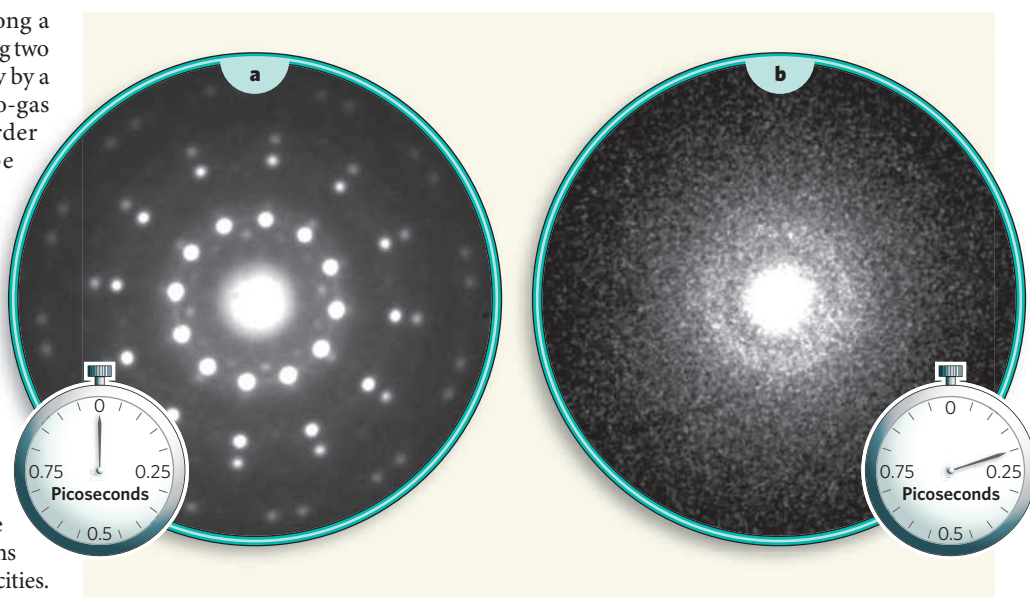


Figure 1 | Speedy melting. Sciaini *et al.*¹ irradiate crystalline bismuth with ultrashort bursts of electrons to monitor the emergence of atomic disorder during laser-induced melting. The images show electron-diffraction patterns observed before (a) and after (b) laser excitation. Atomic disorder emerges in about 200 femtoseconds (0.2 picoseconds). (Modified from a graphic by J. Harms.)

phase^{5,6}. Interestingly, this intermediate cubic phase would not be stable at ambient pressures, and would be expected to melt away as a result of multiple collisions between atoms. This could be a tempting explanation for melting, one that involves the passage through an unstable atomic arrangement before atomic disorder occurs over a timescale of many atomic-lattice-vibration periods. Alternatively, intense optical excitation might simply cause the system to connect to the disordered phase in one go, driven 'downhill' by an internal force that has been unleashed promptly by the laser excitation^{7,8}.

Sciaini and colleagues¹ set out to test these hypotheses. In their experiments, they irradiated films of bismuth with laser pulses, comparing a wide range of laser intensities, and probed the films' atomic structures using ultrafast electron diffraction. This consisted of exposing the films to electron beams of femtosecond duration and taking snapshots of their atomic arrangements (Fig. 1). The authors find that disorder emerges at an increasing rate as the laser's intensity rises, reaching a point at which the sample effectively bypasses any intermediate state. Melting is found to occur within 190 femtoseconds — a fraction of the period of the atomic-lattice vibration.

But how does the laser-excited, ordered solid know how to become disordered without letting its atoms bounce around a couple of times to find the new ground state? Is it possible that the laser-excited solid acquires some aspects of the liquid phase before becoming disordered? Previous studies of phase transitions in semiconductors have already hinted that this could be the case⁹. So might we conclude that melting occurs before the atoms actually move? After all, a crystalline atomic arrangement would be a valid microstate of the

liquid, just as good and as rare as any other. What would have to be liquid-like would be the forces between the atoms and the way the atomic velocities relate.

Or might we conclude that the disordered phase that emerges 200 femtoseconds after excitation is instead still rigid — that is, that the melt emerges only at longer times? The answer might lie in the ultra-fast real-time monitoring of the atomic-lattice-vibration frequencies, which could be achieved using fast optical or X-ray Raman scattering.

Our understanding of the dynamics of phase transitions will ultimately depend on our ability to measure both the positions of the atoms and the rigidities of the bonds. Some recent experiments indicate that such techniques may yield surprises¹⁰. Studies such as that performed by Sciaini and colleagues are not only tackling old questions with new technologies, but also prompting fresh questions about the multifaceted nature of the dynamics of matter. ■

A. Cavalleri is in the Max Planck Group for Structural Dynamics, Centre for Free-Electron Laser Science, University of Hamburg, Hamburg D-22607, Germany.
e-mail: andrea.cavalleri@desy.de

1. Sciaini, G. *et al.* *Nature* **458**, 56–59 (2009).
2. Landau, L. D. & Lifshitz, E. M. *Statistical Physics Pt 2* (Pergamon, 1980).
3. Lennard-Jones, J. E. & Devonshire, A. F. *Proc. R. Soc. Lond. A* **163**, 53 (1937).
4. Born, M. *J. Chem. Phys.* **7**, 591–603 (1939).
5. Sokolowski-Tinten, K. *et al.* *Nature* **422**, 287–289 (2003).
6. Fritz, D. M. *et al.* *Science* **315**, 633–636 (2007).
7. Shank, C. V., Yen, R. & Hirsimann, C. *Phys. Rev. Lett.* **50**, 454–457 (1983).
8. Siders, C. W. *et al.* *Science* **286**, 1340–1342 (1999).
9. Lindenberg, A. M. *et al.* *Science* **308**, 392–395 (2005).
10. Fausti, D., Misocho, O. V. & van Loosdrecht, P. H. M. preprint at <http://arxiv.org/abs/0902.2115> (2009).

IMMUNOLOGY

Cause of death matters

Brigitta Stockinger

The process of programmed cell death can either induce anti-inflammatory immune responses or actively promote inflammation. Whether the dying cell is infected seems to govern which response is triggered.

To deal with invading pathogens efficiently, helper T cells of the adaptive immune system differentiate to form distinct subsets of cells with specific immune functions. Much work has been done on two such subsets, T helper type 1 and type 2 cells (T_H1 and T_H2 cells). But for the past few years, a subset of T cells called T_H17 cells has been in the limelight because of their potential role in autoimmunity, with research being concentrated on elucidating the molecular mechanisms that underlie the cells' differentiation, regulation and function. For example, it has become clear that, *in vitro*, combined action of two immune-mediator molecules, the TGF- β and IL-6 cytokines, is required for the development of human and mouse T_H17 cells (which produce the IL-17 cytokine). But what events trigger the expression of these two cytokines *in vivo*? On page 78 of this issue, Torchinsky *et al.*¹ provide an answer to this question.

Whether TGF- β acts as an anti-inflammatory mediator or stimulates inflammation by inducing the differentiation of T_H17 cells seems to be very much context-dependent. Original observations² indicated that, *in vitro*, regulatory T (T_{reg}) cells, which suppress immune responses, can provide TGF- β for the differentiation of T_H17 cells, but it is now known that virtually all cells in the body can secrete TGF- β . Nonetheless, in response to some pathogens or pathogen components, dendritic cells, which are responsible for presenting antigens to T cells, also secrete IL-6 and TGF- β , leading to T_H17 -cell differentiation³. In keeping with this

finding, local — but not systemic — blockade of TGF- β action prevents T_H17 -cell differentiation and so inhibits the onset of autoimmunity in EAE mice, an experimental model of multiple sclerosis³.

Another study⁴ has shown that ablation of TGF- β production by T cells compromises the differentiation of T_H17 cells and results in immune abnormalities mediated by T_H1 and T_H2 cells. But the question remained: which cell is the most natural source of TGF- β for T_H17 -cell differentiation *in vivo*?

Torchinsky *et al.*¹ propose that the physiological differentiation of T_H17 cells is triggered by the simultaneous synthesis of IL-6 and TGF- β by dendritic cells that have engulfed — through the process of phagocytosis — infected cells undergoing programmed cell death (apoptosis). They show that when infected apoptotic B cells or neutrophils, two other types of immune cell, are maintained in culture with dendritic cells, the dendritic cells express a battery of genes involved in T_H17 -cell differentiation, including genes encoding IL-6, TGF- β and IL-23 (Fig. 1a). These dendritic cells or their secreted products promote the preferential differentiation of T_H17 cells. By contrast, dendritic cells that have engulfed uninfected apoptotic cells induce the differentiation of T_{reg} cells (Fig. 1b).

It has long been known that phagocytosis of apoptotic cells leads to the secretion of various immune-inhibitory cytokines, including IL-10, TGF- β and prostaglandins^{5–7}. It was therefore

assumed that the resolution of inflammation following phagocytosis of apoptotic cells is accompanied by the active suppression of cytokines that stimulate inflammation. Yet Torchinsky *et al.* show that whether the dying cells are infected or uninfected dictates whether an inflammatory situation is ameliorated by the induction of T_{reg} cells or driven to new heights by the induction of T_H17 cells.

The seemingly reciprocal development of inducible T_{reg} cells and T_H17 cells through the effect of TGF- β in the absence or presence of IL-6 was also noted in earlier studies^{8,9} of T_H17 cells, and remains a firmly entrenched idea. But it has yet to be proven that the production of inducible T_{reg} cells by TGF- β has a major role in immune responses *in vivo*. In the peripheral immune system, most T_{reg} cells seem to be derived from the thymus and are maintained by homeostatic mechanisms¹⁰; so whether, under normal physiological conditions, there is even a need for the differentiation of these cells in the peripheral immune system is not known. Furthermore, if an inflammatory context can so easily 'derail' inducible T_{reg} -cell generation towards T_H17 -cell differentiation, it might be rather risky to consider basing therapeutic intervention on the premise that TGF- β secretion induced by phagocytosis of apoptotic cells will lead to T_{reg} -cell induction and so immune suppression.

Torchinsky and colleagues' proposed mechanism¹ may not be the only route to T_H17 -cell differentiation. But their suggestion that bacterial infection, which results in substantial apoptosis, may preferentially drive T_H17 -mediated responses is noteworthy. The authors used the bacterium *Citrobacter rodentium*, which causes excessive apoptosis of intestinal epithelial cells. They find that if apoptosis in response to infection with this pathogen is blocked, there is a fall in the levels of IL-17-expressing T cells in the small intestine and colon.

The differentiation of T_H17 cells has also been associated with particular pathogen-sensing receptors (such as various Toll-like receptors and dectin 1 — a receptor involved in fungal recognition¹¹). The differential role of these receptors in initiating responses mediated by T_H17 cells remains to be determined. Furthermore, one should remember that not all immune-defence responses mediated by the IL-17 cytokine originate from T_H17 cells. It will be interesting to know if and how provision of IL-17 by the innate immune system, and in particular the recruitment of neutrophils (short-lived cells, which are themselves prone to apoptotic death), provide the link between the innate IL-17 response and the induction of an adaptive T_H17 response. ■

Brigitta Stockinger is in the Division of Molecular Immunology, MRC Institute for Medical Research, Mill Hill, London NW7 1AA, UK. e-mail: bstocki@nimr.mrc.ac.uk

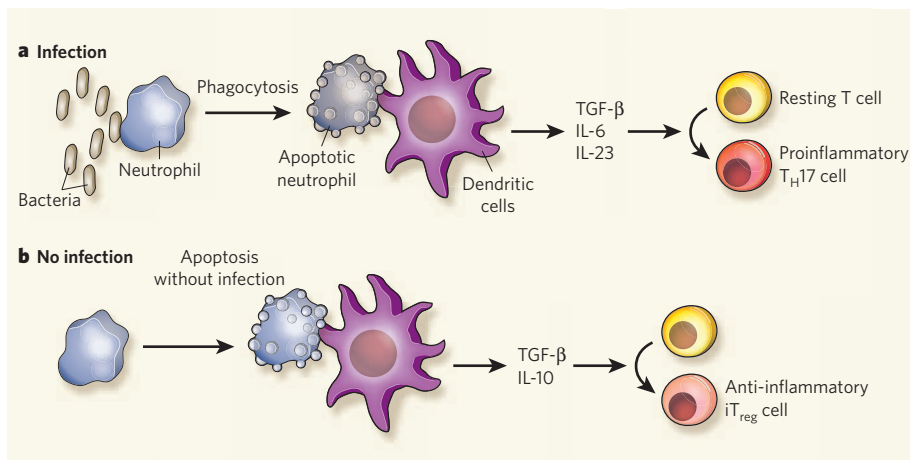


Figure 1 | Infection, apoptosis and immune responses. **a**, Torchinsky *et al.*¹ find that when dendritic cells ingest neutrophils infected with bacteria, they secrete TGF- β , IL-6 and IL-23 cytokines, leading to the differentiation of T_H17 cells, which promote inflammation. **b**, By contrast, ingestion of uninfected apoptotic neutrophils causes the secretion of TGF- β and IL-10 by dendritic cells, promoting *in vitro* differentiation of T cells to induced regulatory T cells (iT_{reg} cells), which suppress immune responses.

1. Torchinsky, M. B., Garaude, J., Martin, A. P. & Blander, J. M. *Nature* **458**, 78–82 (2009).
2. Veldhoen, M. *et al.* *Immunity* **24**, 179–189 (2006).

3. Veldhoen, M., Hocking, R. J., Flavell, R. A. & Stockinger, B. *Nature Immunol.* **7**, 1151–1156 (2006).
4. Li, M. O., Wan, Y. Y. & Flavell, R. A. *Immunity* **26**, 579–591 (2007).
5. Chen, W., Frank, M. E., Jin, W. & Wahl, S. M. *Immunity* **14**, 715–725 (2001).
6. Fadok, V. A. et al. *J. Clin. Invest.* **101**, 890–898 (1998).
7. Voll, R. E. et al. *Nature* **390**, 350–351 (1997).
8. Bettelli, E. et al. *Nature* **441**, 235–238 (2006).
9. Mangan, P. R. et al. *Nature* **441**, 231–234 (2006).
10. Liston, A. & Rudensky, A. Y. *Curr. Opin. Immunol.* **19**, 176–185 (2007).
11. LeibundGut-Landmann, S. et al. *Nature Immunol.* **8**, 630–638 (2007).

PLANETARY SCIENCE

Volatility in Martian magmas

Harry Y. McSween

The geochemistry of the Martian surface has largely been determined by the eruption of magmas to form basaltic rocks. A new line of argument has chlorine as an influential agent in that process.

The volatile constituents of magmas exercise a wholly disproportionate influence on magma behaviour. Although they are present in only tiny quantities, these elements and compounds with low boiling points profoundly affect thermodynamic properties and crystallization patterns, and the characteristics of magmatic flow and eruption. When we speak of magmatic volatiles, we normally mean water and carbon dioxide. But other volatile species might well be important, especially on planets other than Earth. Hence the interest in a proposal, reported in *Chemical Geology* by Filiberto and Treiman¹, that chlorine is one such player.

Mars is thought to be richer in volatile elements than Earth², and has been seen as a good place for further study. The Mars Exploration Rover Spirit has encountered and analysed numerous basaltic rocks during its five-year trek across the Gusev crater. These rocks are produced by volcanic activity, and the abundant vesicles found in some of them (Fig. 1) testify to the presence of significant quantities of volatiles. But until now, water has been assumed to be the main volatile agent, as for instance was the case in the hydrous crystallization experiments performed on a sample of Gusev basalt³.

Filiberto and Treiman¹, however, propose that chlorine may have a central role in the generation and evolution of Martian basalts. They have carried out experiments demonstrating that the effects of chlorine on basalt phase equilibria are similar to those of water. The addition of chlorine shifts the liquidus — the stage at which crystals begin to form — to lower temperatures and enlarges the stability field of pigeonite, a form of pyroxene that is a common constituent of basalts. This is notable because the pressure under which the two minerals olivine and pigeonite first appear together



Figure 1 | Volatile traces on Mars. The vesicular nature of this basaltic rock, photographed on the plains of the Gusev crater, is evidence of the pervasive presence of gas bubbles and so of volatile agents. (Pancam image by the Spirit rover from sol 740.)

is assumed to correspond to the depth at which magma is generated, and that depth is significantly shifted towards the surface if chlorine is the volatile species.

No chlorine-containing minerals have been identified in rocks of the Gusev crater, but that is no surprise because Spirit does not have instruments to do this. Conversely, although high levels of chlorine have been measured chemically by one of Spirit's spectrometers, there is the possibility that those measurements are a reflection of the ubiquitous presence of Martian dust, which contains halides including chlorine.

The broader picture must take account of the fact that much of what we infer about magmatic volatiles on Mars derives from studies of certain Martian meteorites rather than rocks still on Mars. These meteorites — basaltic achondrites, which show the distinctive features of processing by volcanic activity — are remarkably anhydrous, leading some geochemists to speculate that the mantle sources for these

magmas must also have been dry. That view has been challenged⁴ by the need for dissolved water to explain the calcium abundances and soluble-light-element zoning patterns in pyroxene crystals of some Martian basaltic meteorites. In this model, the magmas lost all their water as they were ejected from Mars, aided by the planet's low gravity.

The water contents of Martian meteorites, however, remain a contentious subject. The most persuasive argument for a role for chlorine is based on the absence of water in nominally hydrous daughter minerals (apatite and amphibole, both of which contain chlorine) in melt inclusions trapped in some Martian meteorites⁵.

Filiberto and Treiman's thought-provoking paper¹ will serve a good purpose in prompting renewed debate about volatiles in Martian magmas. But to my mind it is doubtful that magma-borne chlorine would dominate on Mars. The channels and valley networks on Mars were surely eroded by water, and magmas must have delivered that water to the surface. Volcanic rocks in the Gusev crater are estimated to be billions of years old, comparable in age to some of the channels. The existence of hydrogen, which was mapped at high latitudes by Mars Odyssey's Gamma Ray Spectrometer⁶, and which presumably is in the form of subsurface water ice, also points to the outgassing of water from magmas on a global scale.

Finally, however, there is a possible terrestrial connection to Filiberto and Treiman's line of investigation. They point out that lavas in certain tectonic environments on Earth can have a chlorine content of up to 0.7% by weight, and they propose that its effect in terrestrial magmas might be similar to that suggested for Mars.

Experimental evidence^{7,8} supports the idea that water is required to produce two different magmas characteristic of two different tectonic circumstances: so-called andesitic magmas in plate subduction zones, and alkaline magmas in intraplate settings. Filiberto and Treiman speculate that partial melting and fractional crystallization in chlorine-rich terrestrial systems might mimic the effect of water, an idea that merits further testing.

Harry Y. McSween is in the Department of Earth and Planetary Sciences, University of Tennessee, Knoxville, Tennessee 37996-1410, USA.
e-mail: mcsween@utk.edu

1. Filiberto, J. & Treiman, A. H. *Chem. Geol.* doi:10.1016/j.chemgeo.2008.08.025 (2008).
2. Dreibus, G. & Wänke, H. *Icarus* **71**, 225–240 (1987).
3. Monders, A. G., Médard, E. & Grove, T. L. *Meteorit. Planet. Sci.* **42**, 131–148 (2007).
4. McSween, H. Y. et al. *Nature* **409**, 487–490 (2001).
5. Sautter, J., Jambon, A. & Boudouma, O. *Earth Planet. Sci. Lett.* **252**, 45–55 (2006).
6. Feldman, W. C. et al. *Science* **297**, 75–78 (2002).
7. Grove, T. L. et al. *Contrib. Mineral. Petrol.* **142**, 375–396 (2002).
8. Nekvasil, H. et al. *J. Petrol.* **45**, 693–721 (2004).

Molecular basis of transport and regulation in the Na⁺/betaine symporter BetP

Susanne Ressler¹, Anke C. Terwisscha van Scheltinga¹, Clemens Vornrhein², Vera Ott³ & Christine Ziegler¹

Osmoregulated transporters sense intracellular osmotic pressure and respond to hyperosmotic stress by accumulation of osmolytes to restore normal hydration levels. Here we report the determination of the X-ray structure of a member of the family of betaine/choline/carnitine transporters, the Na⁺-coupled symporter BetP from *Corynebacterium glutamicum*, which is a highly effective osmoregulated uptake system for glycine betaine. Glycine betaine is bound in a tryptophan box occluded from both sides of the membrane with aromatic side chains lining the transport pathway. BetP has the same overall fold as three unrelated Na⁺-coupled symporters. Whereas these are crystallized in either the outward-facing or the inward-facing conformation, the BetP structure reveals a unique intermediate conformation in the Na⁺-coupled transport cycle. The trimeric architecture of BetP and the break in three-fold symmetry by the osmosensing C-terminal helices suggest a regulatory mechanism of Na⁺-coupled osmolyte transport to counteract osmotic stress.

Microorganisms must be able to adapt rapidly to extreme variations in salinity, temperature or osmolarity. To avoid dehydration or swelling, the cells adjust their intracellular solute pool¹. Many organisms have developed similar strategies to counteract high osmolarity through the intracellular accumulation of osmolytes^{2–4}, which are often referred to as compatible solutes¹.

Osmolytes are highly polar, organic compounds that can accumulate in the cytosol to molar concentrations⁴. The osmolyte glycine betaine (*N,N,N*-trimethylglycine), often referred to simply as betaine, is widely used in osmoregulation by bacteria^{5,6}, archaea^{7–9}, fungi¹⁰, plants¹¹ and animal cells^{12–14}. Osmolytes promote protein stability through unfavourable interactions with the unfolded state¹⁵, thus counteracting destabilizing agents such as urea, which is physiologically important in mammals^{13,16}. Many microorganisms do not rely on the *de novo* synthesis of osmolytes^{17,18}, but instead use high-affinity transporters to import them from extracellular sources⁶. Osmolyte transporters are thus faced with the problem of binding a substrate that tends to be repelled by the protein surfaces¹⁹.

The osmoregulated betaine transporter BetP of *C. glutamicum*²⁰ is a well-characterized member of the family of betaine/choline/carnitine transporters (BCCTs)²¹, which contains a conserved tryptophan motif in transmembrane helix 8 (TM8). The transport of betaine by BetP is highly specific, and coupled to the symport of two Na⁺ ions²². Betaine uptake is instantly activated by hyperosmotic stress, which causes an increase in cytoplasmic K⁺ concentration sensed by the C-terminal domain of BetP^{23–25}.

We determined the structure of an N-terminally truncated and surface-engineered, but nevertheless active and osmoregulated, BetP mutant. The crystal structure shows BetP to be a trimer with three-fold non-crystallographic symmetry (NCS), whereas it is an asymmetric trimer in the membrane^{24,25}. The transporter core consists of two tightly nested, structurally related inverted repeats of five transmembrane helices each. Its fold resembles that of the Na⁺/alanine transporter LeuT_{Aa} from *Aquifex aeolicus*²⁶, of the neurotransmitter/

sodium symporter²⁷ (NSS) family, the Na⁺/galactose transporter vSGLT from *Vibrio parahaemolyticus*²⁸, of the sodium/solute symporter²⁹ (SSS) family, and the benzyl hydantoin symporter Mhp1 from *Microbacterium liquefaciens*, of the nucleobase/cation symport 1 (ref. 30) family, which do not share any sequence homology with one another or with the BCCT family. Unlike the three other Na⁺-coupled transporters, which represent an outward-facing (LeuT_{Aa}²⁶ and Mhp1³⁰) or an inward-facing conformation (vSGLT²⁸), the X-ray structure of BetP shows an occluded-intermediate, substrate-bound state. Comparison of these structures provides new insights into conformational changes during the transport cycle of Na⁺-coupled symporters. Furthermore, different interactions between neighbouring monomers in the BetP trimer suggest a regulatory mechanism in response to osmotic stress.

Transporter structure

Apart from the extended C-terminal α -helix, the BetP monomer has a nearly cylindrical shape (Fig. 1a). It contains twelve transmembrane α -helices (Fig. 1b) and a curved α -helix (H7, helix 7) at the periplasmic membrane surface. Three helices at the perimeter of the monomer (TM1, TM11 and TM6) run almost perpendicular to the membrane, whereas TM5, TM10 and TM12 are substantially tilted by about $\sim 40^\circ$.

TM3 has a locally unwound segment, approximately halfway across the membrane, that divides it into intracellular (TM3i) and extracellular (TM3e) parts. TM4 and TM5 are connected on the cytoplasmic side by loop 4, which includes an internal 3_{10} helix (IH1). TM9 and TM10 are connected on the periplasmic side by loop 9, which contains a short external α -helix (EH2). TM3, TM4, TM8 and TM9 form an iris-shaped, four-helix bundle with a prominent non-protein density in its centre roughly halfway along TM4 and TM8, adjacent to the unwound region separating TM3i and TM3e. This density was identified by its shape and by structural-substrate coordination homology³¹ as betaine (Fig. 2 and Supplementary Fig. 1a).

¹Max Planck Institute of Biophysics, Department of Structural Biology, 60438 Frankfurt am Main, Germany. ²Global Phasing Ltd, Sheraton House, Castle Park, Cambridge CB3 0AX, UK. ³Institut für Biochemie, Universität zu Köln, 50937 Köln, Germany.

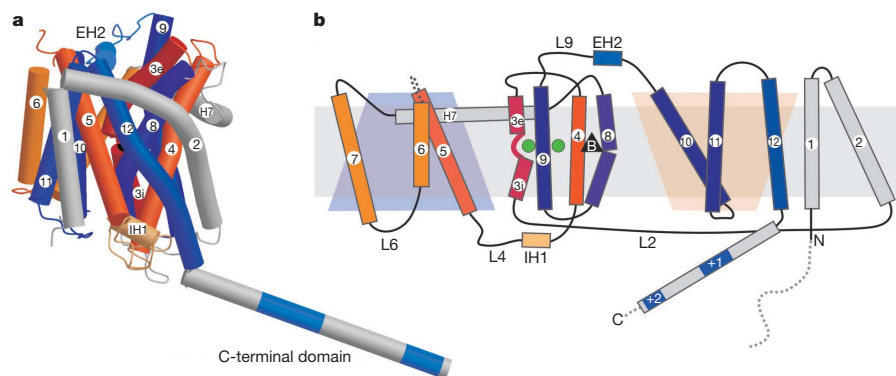


Figure 1 | Structure of an N-terminally truncated, surface-engineered BetP mutant. **a**, Side view of monomer A. Colouring and numbering of the helices (cylinders) are as in Fig. 1b. Repeat 1 (TM3–TM7) is orange, with colour intensity decreasing from the N terminus to the C terminus. The topologically related repeat 2 (TM8–TM12) is coloured blue in a similar way.

The ten C-terminal transmembrane helices contain an internal structural repeat, which is not evident in the amino-acid sequence of BetP, forming the core of the transporter. The structural repeat relates TM3–TM7 to TM8–TM12 by a pseudo-two-fold axis in the plane of the membrane (Fig. 1b). The V-shaped helix pair TM3–TM4 is closely nested with the inverted V-shaped pair TM8–TM9, forming the four-helix bundle, which is surrounded by TM5–TM7 and TM10–TM12 serving as a scaffold. The long, curved helix 7 and TM2 enclose the transporter core like a stabilizing belt.

The significant resemblance in overall architecture of the inverted structural repeats in the different Na^+ -coupled symporters BetP, LeuT_{Aa}²⁶, vSGLT²⁸ and Mhp1³⁰ is not reflected in sequence similarity. Furthermore, the similar fold provides new insights in the relation of bacterial BCCTs and eukaryotic GABA (γ -aminobutyric acid)/osmolyte transporters from the NSS family found in kidney³² and in brain³³. Most likely, they have a common ten-transmembrane-helix ancestor that evolved by gene duplication and harboured the inverted repeat, which then diverged in the course of evolution as dictated by environmental conditions³⁴.

Substrate pathway

Side chains from TM4 and TM8 contribute to the betaine-binding site (Fig. 2). As in betaine-specific binding proteins^{31,35,36}, the quaternary ammonium group is enclosed in an aromatic environment by cation– π and van der Waals interactions. In BetP, indole groups of Trp 189 and Trp 194 (TM4) and Trp 374 (TM8) form the aromatic box. The indole groups of Trp 194 and Trp 374 are almost parallel, whereas Trp 189 is

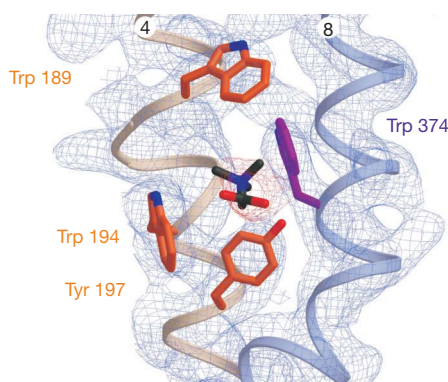


Figure 2 | The betaine-binding site. $2F_o - F_c$ map, contoured at 1σ , showing density for betaine (red) and the densities for TM4 (light brown) and TM8 (light blue) in blue. F_o and F_c are the observed and calculated structure functions, respectively. Side chains defining the tryptophan box of the betaine-binding motif are Trp 189, Trp 194, Trp 374 and Tyr 197.

TM1, TM2, helix 7 and the C-terminal domains are grey. The clusters of positive charges in the C-terminal helix are indicated in blue. **b**, Inverted repeats in the BetP topology. The substrate is represented as a black triangle and the sodium ions are green. Unresolved residues are indicated by a dotted line. Important loops are indicated as L2, L4, L6 and L9.

approximately perpendicular to both and forms a lid on the periplasmic side. The side chain of Tyr 197 makes up the fourth side of the aromatic box. Trp 194 is conserved in the BCCT family, but Trp 189, Tyr 197 and Trp 374 are only conserved in transporters of quaternary ammonium substrates, such as choline and carnitine (Supplementary Fig. 2). Replacement of Trp 189, Trp 194 and Tyr 197 in TM4 resulted in significantly reduced betaine uptake rates. Mutation of Trp 374 in TM8 leaves the transport rate unaffected (Supplementary Fig. 3), suggesting that the substrate is still accommodated, probably at a changed position, in the modified binding pocket. Removal of Trp 362, which pointed out of the substrate pathway into the periplasm, resulted in reduced activity (Supplementary Fig. 3), suggesting a role in substrate sequestration. Mutation of Trp 377 below the substrate-binding pocket inactivates BetP, but mutation of Trp 366 and Trp 371 does not affect activity (Supplementary Fig. 3). We suggest that Trp 377 may act as an additional binding site during conformational changes in the transport cycle.

In BetP and other members of the BCCT family (Supplementary Fig. 2), a total of 23 conserved aromatic side chains line the substrate pathway including the tryptophan box in the four-helix bundle (Supplementary Fig. 1b), raising the question of whether such an excessive supply is needed. According to the widely accepted alternating-access model of membrane transport³⁷, the interaction surface of the substrate and transporter need only extend to the central binding site that is switching accessibility from one side of the membrane to the other during the transport cycle. Usually, osmolytes act as co-solvents and are excluded from the first hydration shell of proteins by repulsive interaction with the protein backbone³⁸. Coating the binding site with aromatic side chains would solve this problem, by providing a surface that would, according to Tanford's transfer model³⁹, minimally repel osmolytes^{31,35,36,40}.

Functional studies²² have shown that two Na^+ ions are required to energize betaine transport in BetP, which has a Michaelis constant (K_m) for Na^+ of 39 mM (ref. 23). On the basis of the structural alignment of BetP on the LeuT_{Aa}²⁶ structure, we propose two potential Na^+ binding sites (Fig. 3a and Supplementary Fig. 4). Sodium binding in the active, osmoregulated BetP mutant used for structure determination (Supplementary Fig. 5) seems to be facilitated by main chain interactions in the flexible, glycine-rich stretch of TM3 with one Na^+ ion (Na1) coordinated by the carboxyl group of betaine, the carbonyl oxygen of Met 150 in the unwound region of TM3 and the carbonyl oxygen of Ala 148 in TM3i (Fig. 3a and Supplementary Fig. 4). The second Na^+ ion (Na2) is located in the bend between TM3e and TM3i. The carbonyl oxygen of Ala 147 in TM3i and the side chains of Ser 306 and Met 310 in TM7 coordinate Na2. Thr 467 and Ser 468 in TM10 are suggested to be additional ligands of Na1 and Na2 with an interaction probably mediated through water molecules.

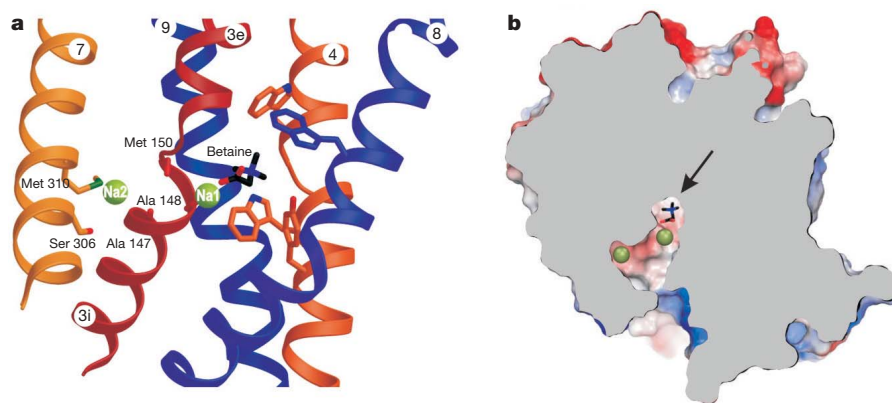


Figure 3 | The proposed sodium binding in BetP. **a**, Proposed Na^+ ion positions in BetP. Na1 is coordinated by the carboxyl group of betaine and residues in TM3i. Na2 is coordinated by residues in TM3i and TM7.

b, Accessibility of the two Na^+ ion positions and betaine (arrow) from the cytoplasm in a section through the protein volume.

Ser 468 is conserved in the BCCT family, as are the corresponding Ser 355 in the NSS family and Ser 364 or Ser 365 in the SSS family. However, the glycines flanking Met 150 in the stretch of TM3 appear only to be conserved in transporters exhibiting a 2:1 Na^+ :substrate stoichiometry (Supplementary Fig. 6). In the BCCT family, high-affinity betaine transporters (Supplementary Fig. 2) exclusively contain the conserved GxGxG motif in the segment of TM3, suggesting that BetP's specificity to betaine is related to the structure of the unwound segment upon binding of Na1.

The substrate pathway and the potential positions of the Na^+ ions are blocked from the periplasm in the BetP structure, but a narrow

funnel between TM3i, TM7, TM8 and TM10 links the putative Na sites to the cytoplasm (Fig. 3b). The funnel has an elliptical constriction defined by Ala 147 (TM3), Ile 302 and Ser 306 (TM7), Phe 380 and Phe 384 (TM8) and Ser 471 (TM10), with a major axis of ~ 4.5 Å and a minor axis of ~ 2 Å. For steric reasons and owing to the limited side-chain size of the residues involved in the constriction, the opening of the funnel will require a rearrangement of the polypeptide backbone, that is, a considerable conformational change (Fig. 4b). By also taking into account the structural symmetry of the two repeats (Supplementary Table 2), we conclude that BetP displays a unique intermediate state in the Na^+ -coupled transport cycle, which

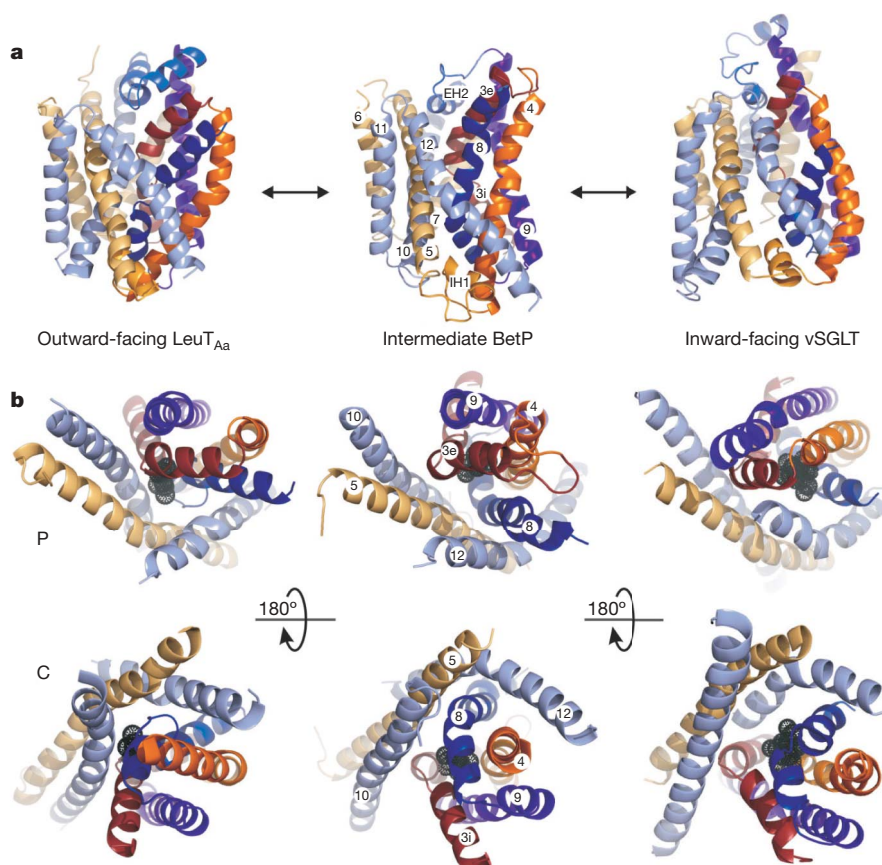


Figure 4 | Conformational changes in Na^+ -coupled transport. **a**, Side view of the four-helix bundles (TM3, TM4, TM8 and TM9) and the surrounding stabilizing scaffold (TM5–TM7 and TM10–TM12) in LeuT_{Aa}, BetP and vSGLT. Numbering of the helices is as in BetP. **b**, Top view of the four-helix

bundles and a part of the scaffold (TM5, TM10 and TM12) from the periplasm (P) and the cytoplasm (C). Grey spheres indicate the bound substrate.

differs significantly from the occluded periplasmically or cytoplasmically open states described before^{26,28,30}.

Transport mechanism

Although the available transporter structures^{26,28,30,41} support the alternating-access model of membrane transport³⁷, so far none of them show the same transporter in more than one conformation. The central question of how the different conformations interconvert to bring about membrane transport has thus remained unanswered. BetP, LeuT_{Aa}²⁶, Mhp1³⁰ and vSGLT²⁸ contain similar topologically inverted repeats that can be superimposed unambiguously (Supplementary Table 2). Structural differences among these repeats contribute to the asymmetric architecture of the outward- and inward-facing conformations of LeuT_{Aa}/Mhp1 and vSGLT, respectively (Fig. 4a)⁴².

Previous modelling studies⁴² could only exploit this asymmetry and described the change from the outward-facing conformation to the inward-facing conformation as a switching of the conformation of the two repeats. However, the occluded-intermediate state of BetP has a symmetrical architecture (Fig. 4a and Supplementary Table 2), which allows the conformational changes to be described in more detail through discussion of the periplasmically open, occluded-intermediate and cytoplasmically open conformations observed in the different transporters in terms of a single, unified transport mechanism.

The striking resemblance of the periplasmically open conformation in LeuT_{Aa} and Mhp1 suggests that the conformations observed in the different transporters are applicable to each other. Also in this context, structural alignments show a number of structurally related glycines in BetP, LeuT_{Aa}, vSGLT and Mhp1 in both repeats conserved in their respective families. Recent hydropathy-profile alignments⁴³ revealed a characteristic clustering of hydrophobic residues in transmembrane helices in transporters of the unrelated NSS, SSS and amino acid/polyamine/organocation families, confirming their similar transporter core structures.

On changing from the outward-facing conformation (LeuT_{Aa}) over an intermediate state (BetP) to the inward-facing conformation (vSGLT; Fig. 4b), a concerted, iris-like movement occurs in the four-helix bundle. The periplasmic halves of TM3, TM4 and TM9 (BetP numbering) undergo an anticlockwise rotation occluding the substrate-binding site on the periplasmic side (Fig. 4b). The concomitant movement of TM8 might be influenced by the different sizes and natures of the substrates in the three transporters. The rotation of the cytoplasmic half of the four-helix bundle moves it out of the centre of the transporter. In the scaffold surrounding the four-helix bundle, TM10 straightens and TM5 and TM12 approach TM3 and TM8 on the periplasmic side. On the cytoplasmic side, they move away from the four-helix bundle, opening a route to the substrate-binding site between TM8 and TM12. The conformational changes associated with transport can thus be described in terms of concerted movements of the four-helix bundle and the surrounding scaffold. The pivot points of these movements are located near the substrate- and ion-binding sites, close to the structurally conserved glycines as in the GxGxG motif in the stretch of TM3 and Gly301 in loop 6 (Supplementary Fig. 6). Ile302 and Ser306, both of which are involved in the occlusion of the substrate from the cytoplasm, follow Gly301. Notably, mutation of Gly301 renders BetP inactive (Supplementary Fig. 3). Therefore, this glycine might be important for the flexibility of loop 6 and, thus, for opening this pathway to the cytoplasm.

Mutagenesis studies of the LeuT_{Aa} homologue SERT reveal conformational changes during transport in the loop connecting the four-helix bundle with the C-terminal part of the scaffold^{44,45}. A comparison of the three structures indicates a major shift in the N-terminal part of this loop 9, moving out of the periplasmic vestibule in the transition to the inward-facing conformation (Fig. 4a).

In the occluded state of the BetP structure, helices adopt intermediate positions between the outward- and inward-facing conformations of

LeuT_{Aa} and vSGLT. Therefore, conformational changes during inward transport do not seem to be a mere switching motion between the two low-energy open states, as predicted by the alternating-access model, but seem to involve an additional low-energy intermediate state resulting from the concerted movement of transmembrane helices around the coupling ion-binding sites.

Trimer architecture

The three monomers labelled A, B, and C in Fig. 5a are related by a three-fold NCS axis, which run perpendicular to the membrane. The trimer has a central conical cavity (Fig. 5c, d) and is lined by 3×4 aromatic side chains (Supplementary Fig. 7). Other than in this hydrophobic cavity, the cytoplasmic surface is positively charged, whereas the periplasmic surface is negatively charged (Fig. 5d). The hydrophobic cavity is filled with non-protein density, most likely detergent or lipid. The segment of helix 7 that faces the periplasm is rich in leucines and asparagines. Therefore, it shows characteristics of a non-specific lipid interaction site⁴⁶ and may bind lipid in the central cavity to stabilize the trimer. There are deep clefts between the monomers, which are accessible from the membrane. In the membrane these would be filled with lipids, allowing the monomers in the trimer to move.

Interactions between monomers involve the C-terminal helix and the amphipathic helix 7. Helix 7 makes contact with TM2, TM3, TM9 and helix 7 of the other two monomers, and the C-terminal helix interacts with loop 2 and the C termini of the other monomers. The BetP C terminus contains two clusters of positively charged residues, from Arg 558 to Arg 568 and from Lys 581 to Lys 587 (Fig. 1a). In the BetP structure, the C-terminal helices are all differently oriented and do not obey NCS (Fig. 5b); monomer A is resolved to Arg 589, monomer B to Arg 558 and monomer C to Arg 568. The second cluster is only resolved in the C terminus of monomer A, it mediates the main crystal contacts between trimers (Supplementary Fig. 8), which contribute to the break in NCS. However, other breaks of NCS are clearly not due to crystal contacts. Arg 568 residues of monomers A and C form a salt bridge to Glu 552 of the adjacent monomer. This interaction is not found for Arg 568 of monomer B (Fig. 6).

Regulation

Alanine and proline scanning of the C-terminal helix indicate that arginines in both clusters are important for regulation⁴⁷, which is lost upon C-terminal truncation at Tyr 550²⁴. Peptide-array analysis⁴⁷ has implicated strong interactions of positively charged C-terminal domains with the negatively charged N-terminal domain. N-terminal truncation resulted in activation at higher osmolarity in *C. glutamicum* and in *Escherichia coli* polar lipid proteoliposomes (Supplementary Fig. 5), indicating that the interaction of C and N termini has an important role in regulation. When not constrained by crystal contacts, the C-terminal helix appears to have some freedom to move in a plane parallel to the membrane surface. In the BetP structure, the C terminus of monomer C points towards TM1 of monomer B, suggesting a possible interaction with the N-terminal domain, whereas the C terminus of monomer B is oriented towards TM6, suggesting to a potential interaction site with residues in loop 4 and loop 8.

The structure of BetP also reveals an important role for loop 2, which was observed by peptide-array analysis⁴⁷ to some extent. In a supposed outward-facing conformation of BetP (Fig. 4a), loop 2 would block the cytoplasmic funnel for the Na⁺ ions and the substrate. Loop 2 contains the three negatively charged residues: Asp 131, Glu 132 and Glu 135. Double mutation at Asp 131 and Glu 132 prevents expression of the *betP* gene and mutation at Glu 135 reduces transport activity (Supplementary Fig. 3). Asp 131 interacts by means of a salt bridge with Arg 558 located in the C-terminal helix of the adjacent monomer, and Glu 132 with Arg 390 in loop 8, which connects TM8 and TM9 in the four-helix bundle (Fig. 6). Loop 8 contains an additional positively charged patch of Arg 387 and Arg 392, and

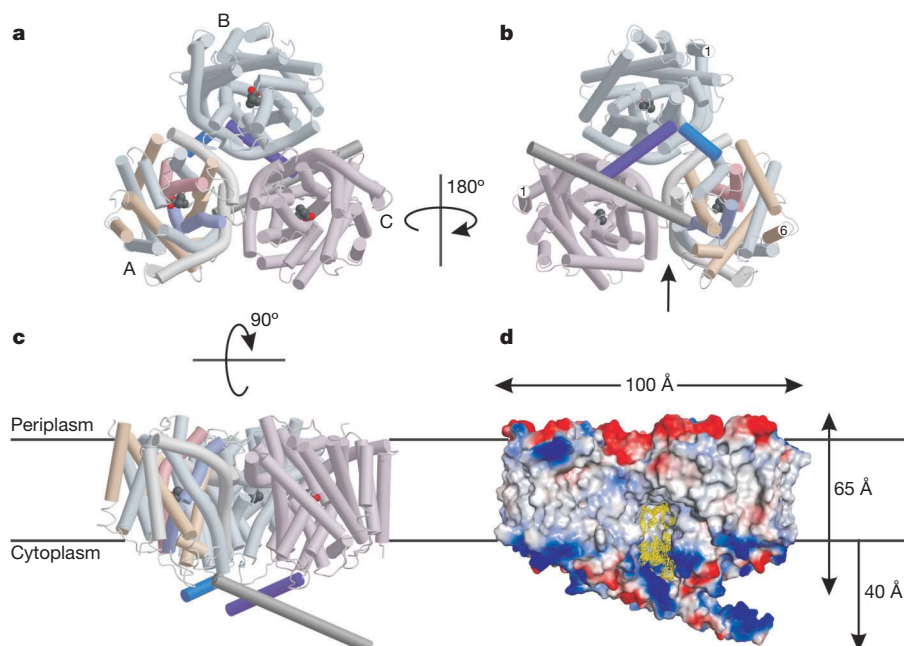


Figure 5 | Trimer architecture of BetP. **a, b**, The BetP trimer as seen from the periplasmic (**a**) and cytoplasmic (**b**) sides of the membrane. Monomers A (helices coloured as in Fig. 1, in a lighter tint), B (blue) and C (pink) are related by three-fold NCS with the exception of their C-terminal helices (darker colours). In monomers A and C in **b**, the C termini face the N termini of monomers C and B, respectively, whereas in monomer B, the C terminus points towards TM6 in monomer A. Monomers are separated by a cleft (arrow). **c**, View into the cleft between monomers A and C. The BetP trimer

protrudes from the periplasmic membrane surface by about 10 Å. On the cytoplasmic side, the α -helical C-terminal domain of monomer A extends ~ 40 Å into the cell. **d**, Surface representation of the trimer oriented as in **c**. The electrostatic surface is coloured red (negative) to blue (positive). The $F_o - F_c$ non-protein density (2σ contour level) in the hydrophobic cavity (~ 37 Å in height and ~ 30 Å in diameter) is shown in yellow. The boundaries of the lipid bilayer are indicated in **c** and **d**.

transport activity is sensitive to mutation of both arginines (Supplementary Fig. 3).

Changes in orientation of the C-terminal helix would affect the orientation of Asp 131 and, in turn, Glu 132 and hence the conformation of loop 8, and could thus regulate the transport cycle by ionic interactions. In proteoliposomes, activation of BetP in response to osmotic stress seems to be specifically triggered by high internal K^+ concentration, although the activation optimum of 220 mM (refs 23, 48) is high for a specific K^+ -binding region. In addition, the cation specificity depends on the membrane composition indicating

concomitant or competing stimuli in osmoregulation. A direct interaction of the BetP C terminus with charged lipids in the membrane as observed by surface plasmon resonance⁴⁷ could influence the accessibility of a potential regulatory K^+ -binding region. We suggest that the cation specificity most likely depends on the orientations of the C-terminal domains reflecting functionally different conformations in the activation cycle. Regulation of transport is thus a collective effect of the interactions between the three BetP monomers. Therefore, lipids in the clefts between the monomers or in the hydrophobic cavity in the centre of the trimer might affect the orientation of the C-terminal helices as well. We conclude that each monomer in the trimer activates its neighbour, taking advantage of the oligomeric architecture of BetP.

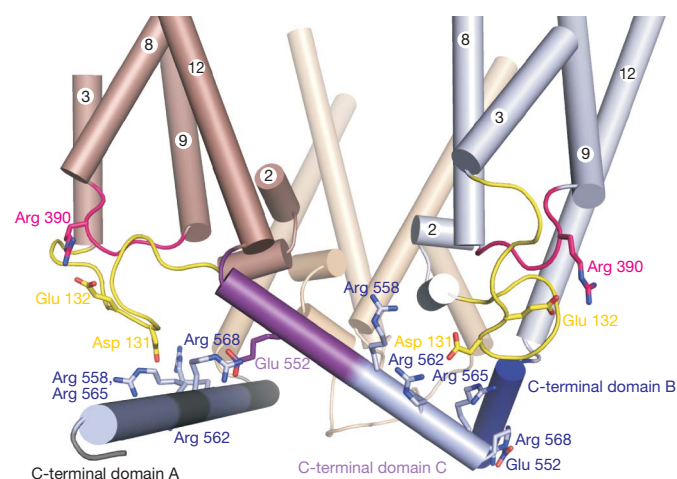


Figure 6 | Regulatory interactions mediated by the C-terminal domains. Ionic interactions of the C-terminal domains and the involved helices of monomer A (grey), monomer B (blue) and monomer C (brown-purple) with loop 2 (yellow) and loop 8 (red) on the cytoplasmic side. The two positively charged clusters in each domain are shown in light blue. Residues forming salt bridges are shown in stick representation and labelled separately.

METHODS SUMMARY

The construct of BetP Δ N29EEEE44/45/46AAA (BetP Δ N29_{Sc}) with an N-terminal StrepII tag in a IBA7 vector was used to express selenium-labelled protein in *E. coli* BL21 RIL-X cells at 37 °C, using SelenoMet media (Molecular Dimensions) containing 40 mg l⁻¹ L-selenomethionine. The protein was solubilized from isolated membranes in 2.5% (w/v) β -dodecyl-maltoside and purified by affinity and size-exclusion chromatography. BetP Δ N29_{Sc} crystals were grown by vapour diffusion at 18 °C by mixing a 1:1 volume of protein (~ 9 mg ml⁻¹) and reservoir solution containing 100 mM Na₃citrate (pH 5.55), 23% PEG 400 and 100 mM NaCl. A single-anomalous-dispersion diffraction data set to 3.3 Å was used to obtain phases from the selenium anomalous signal. The data were corrected for their strong anisotropy, and the resulting electron density was *B*-factor sharpened and averaged using the three-fold NCS operators. This resulted in an interpretable map, and the automatically built partial model was completed manually. The structure was refined to a final reliability factor $R_{\text{work}} = \sum ||F_o| - |F_c|| / \sum |F_o|$ of 25.6% and an R_{free} value (calculated for 5% of the data that were excluded from the refinement) of 26.5%. Uptake of [¹⁴C]glycine betaine by BetP and mutants was measured in *E. coli* MKH13, in *C. glutamicum* DHPF cells and in *E. coli* polar lipid proteoliposomes as described^{23,24,48}. The osmolality was adjusted to 800 mosmol kg⁻¹ by addition of sorbitol. Substrate uptake in cells or proteoliposomes was initiated by adding [¹⁴C]glycine betaine (0.1 mCi ml⁻¹) at a final concentration of 100 or 200 mM and measured as described⁴⁸.

Full Methods and any associated references are available in the online version of the paper at www.nature.com/nature.

Received 18 July 2008; accepted 21 January 2009.

- Burg, M. B. Molecular basis of osmotic regulation. *Am. J. Physiol.* **268**, F983–F996 (1995).
- Kinne, R. K. The role of organic osmolytes in osmoregulation: from bacteria to mammals. *J. Exp. Zool.* **265**, 346–355 (1993).
- Yancey, P. H. Organic osmolytes as compatible, metabolic and counteracting cytoprotectants in high osmolarity and other stresses. *J. Exp. Biol.* **208**, 2819–2830 (2005).
- Burg, M. B. & Ferraris, J. D. Intracellular organic osmolytes: function and regulation. *J. Biol. Chem.* **283**, 7309–7313 (2008).
- Wood, J. M. *et al.* Osmosensing and osmoregulatory compatible solute accumulation by bacteria. *Comp. Biochem. Physiol. A* **130**, 437–460 (2001).
- Wood, J. M. Bacterial osmosensing transporters. *Methods Enzymol.* **428**, 77–107 (2007).
- da Costa, M. S., Santos, H. & Galinski, E. A. An overview of the role and diversity of compatible solutes in Bacteria and Archaea. *Adv. Biochem. Eng. Biotechnol.* **61**, 117–153 (1998).
- Roberts, M. F. Osmoadaptation and osmoregulation in archaea. *Front. Biosci.* **5**, D796–D812 (2000).
- Pflüger, K. & Müller, V. Transport of compatible solutes in extremophiles. *J. Bioenerg. Biomembr.* **36**, 17–24 (2004).
- Blomberg, A. Osmoresponsive proteins and functional assessment strategies in *Saccharomyces cerevisiae*. *Electrophoresis* **18**, 1429–1440 (1997).
- Tuteja, N. Mechanisms of high salinity tolerance in plants. *Methods Enzymol.* **428**, 419–438 (2007).
- Beck, F. X. & Neuhofer, W. Response of renal medullary cells to osmotic stress. *Contrib. Nephrol.* **148**, 21–34 (2005).
- Lang, F. Mechanisms and significance of cell volume regulation. *J. Am. Coll. Nutr.* **26**, 613S–623S (2007).
- Lim, C. H., Bot, A. G., de Jonge, H. R. & Tilly, B. C. Osmosignaling and volume regulation in intestinal epithelial cells. *Methods Enzymol.* **428**, 325–342 (2007).
- Rösgen, J. Molecular basis of osmolyte effects on protein and metabolites. *Methods Enzymol.* **428**, 459–486 (2007).
- Garcia-Perez, A. & Burg, M. B. Importance of organic osmolytes for osmoregulation by renal medullary cells. *Hypertension* **16**, 595–602 (1990).
- Kempf, B. & Bremer, E. Uptake and synthesis of compatible solutes as microbial stress responses to high-osmolality environments. *Arch. Microbiol.* **170**, 319–330 (1998).
- Empadinhas, N. & da Costa, M. S. Diversity and biosynthesis of compatible solutes in hyper/thermophiles. *Int. Microbiol.* **9**, 199–206 (2006).
- Athawale, M. V., Dordick, J. S. & Garde, S. Osmolyte trimethylamine-N-oxide does not affect the strength of hydrophobic interactions: origin of osmolyte compatibility. *Biophys. J.* **89**, 858–866 (2005).
- Peter, H., Burkovski, A. & Krämer, R. Isolation, characterization, and expression of the *Corynebacterium glutamicum* betP gene, encoding the transport system for the compatible solute betaine. *J. Bacteriol.* **178**, 5229–5234 (1996).
- Kappes, R. M., Kempf, B. & Bremer, E. Three transport systems for the osmoprotectant betaine operate in *Bacillus subtilis*: characterization of OpuD. *J. Bacteriol.* **178**, 5071–5079 (1996).
- Farwick, M., Siewe, R. M. & Krämer, R. Betaine uptake after hyperosmotic shift in *Corynebacterium glutamicum*. *J. Bacteriol.* **177**, 4690–4695 (1995).
- Schiller, D., Krämer, R. & Mörbach, S. Cation specificity of osmosensing by the betaine carrier BetP of *Corynebacterium glutamicum*. *FEBS Lett.* **563**, 108–112 (2004).
- Peter, H., Burkovski, A. & Krämer, R. Osmo-sensing by N- and C-terminal extensions of the betaine uptake system BetP of *Corynebacterium glutamicum*. *J. Biol. Chem.* **273**, 2567–2574 (1998).
- Ziegler, C. *et al.* Projection structure and oligomeric state of the osmoregulated sodium/betaine symporter BetP of *Corynebacterium glutamicum*. *J. Mol. Biol.* **337**, 1137–1147 (2004).
- Yamashita, A., Singh, S. K., Kawate, T., Jin, Y. & Gouaux, E. Crystal structure of a bacterial homologue of Na⁺/Cl[−]-dependent neurotransmitter transporters. *Nature* **437**, 215–223 (2005).
- Chang, A. B., Lin, R., Studley, W. K., Tran, C. V. & Saier, M. H. Jr. Phylogeny as a guide to structure and function of membrane transport proteins. *Mol. Membr. Biol.* **21**, 171–181 (2004).
- Faham, S. *et al.* The crystal structure of a sodium galactose transporter reveals mechanistic insights into Na⁺/sugar symport. *Science* **321**, 810–814 (2008).
- Saier, M. H. J. Families of transmembrane sugar transport proteins. *Mol. Microbiol.* **35**, 699–710 (2000).
- Weyand, S. *et al.* Structure and molecular mechanism of a nucleobase-cation-symport-1 family transporter. *Science* **322**, 709–713 (2008).
- Schiefner, A. *et al.* Cation- π interactions as determinants for binding of the compatible solutes betaine and proline betaine by the periplasmic ligand-binding protein ProX from *Escherichia coli*. *J. Biol. Chem.* **279**, 5588–5596 (2004).
- Kempson, S. A. & Montrose, M. H. Osmotic regulation of renal betaine transport: transcription and beyond. *Pflügers Arch.* **449**, 227–234 (2004).
- Borden, L. A. GABA transporter heterogeneity: pharmacology and cellular localization. *Neurochem. Int.* **29**, 335–356 (1996).
- Rapp, M. G. E., Seppälä, S. & von Heijne, G. Identification and evolution of dual-topology membrane proteins. *Nature Struct. Mol. Biol.* **13**, 112–116 (2006).
- Schiefner, A., Holtmann, G., Diederichs, K., Welte, W. & Bremer, E. Structural basis for the binding of compatible solutes by ProX from the hyperthermophilic archaeon *Archaeoglobus fulgidus*. *J. Biol. Chem.* **279**, 48270–48281 (2004).
- Horn, C. *et al.* Molecular determinants for substrate specificity of the ligand-binding protein OpuAC from *Bacillus subtilis* for the compatible solutes betaine and proline betaine. *J. Mol. Biol.* **357**, 592–606 (2006).
- Jardetzky, O. Simple allosteric model for membrane pumps. *Nature* **211**, 969–970 (1966).
- Bolen, D. W. & Rose, G. D. Structure and energetics of the hydrogen-bonded backbone in protein folding. *Annu. Rev. Biochem.* **77**, 339–362 (2008).
- Tanford, C. Protein denaturation. C. Theoretical models for the mechanism of denaturation. *Adv. Protein Chem.* **24**, 1–95 (1970).
- Kuhlmann, S. I., Terwisscha van Scheltinga, A. C., Bienert, R., Kunte, H. J. & Ziegler, C. Osmoregulated transport of compatible solutes in the halophilic bacterium *Halomonas elongata*: 1.55 Å high-resolution structure of the periplasmic ectoine-binding protein from TRAP-transporter TeaABC. *Biochemistry* **47**, 9475–9485 (2008).
- Yernool, D., Boudker, O., Jin, Y. & Gouaux, E. Structure of a glutamate transporter homologue from *Pyrococcus horikoshii*. *Nature* **431**, 811–818 (2004).
- Forrest, L. R. *et al.* Mechanism for alternating access in neurotransmitter transporters. *Proc. Natl Acad. Sci. USA* **105**, 10338–10343 (2008).
- Lolkema, J. S. & Slotboom, D.-J. The major amino acid transporter superfamily has a similar core structure as Na⁺-galactose and Na⁺-leucine transporters. *Mol. Membr. Biol.* **25**, 567–570 (2008).
- Smicun, Y., Campbell, S. D., Chen, M. A., Gu, H. & Rudnick, G. The role of external loop regions in serotonin transport. Loop scanning mutagenesis of the serotonin transporter external domain. *J. Biol. Chem.* **274**, 36058–36064 (1999).
- Stephan, M. M., Chen, M. A., Penado, K. M. & Rudnick, G. An extracellular loop region of the serotonin transporter may be involved in the translocation mechanism. *Biochemistry* **36**, 1322–1330 (1997).
- Palsdottir, H. & Hunte, C. Lipids in membrane protein structures. *Biochim. Biophys. Acta* **1666**, 2–18 (2004).
- Ott, V., Koch, J., Späte, K., Mörbach, S. & Krämer, R. Regulatory properties and interaction of the C- and N-terminal domains of BetP, an osmoregulated betaine transporter from *Corynebacterium glutamicum*. *Biochemistry* **47**, 12208–12218 (2008).
- Schiller, D., Rübner, R., Krämer, R. & Mörbach, S. The C-terminal domain of the betaine carrier BetP of *Corynebacterium glutamicum* is directly involved in sensing K⁺ as an osmotic stimulus. *Biochemistry* **43**, 5583–5591 (2004).

Supplementary Information is linked to the online version of the paper at www.nature.com/nature.

Acknowledgements The authors thank W. Kühlbrandt and R. Krämer for support and comments on the manuscript; J. Standfuß for contributions in the early stages of the project; Ö. Yildiz, T. Barros and R. Wouts for computational support; S. Schulze, S. Mörbach, S. Nicklisch and L. Forrest for discussions; J. Hakulinen and J. Carrera for cloning; C. Perez for the reconstitution and freeze fracture experiments; and H. Volk for help with the figures. Special thanks are due to E. Pohl and the X10SA beamline staff at the Swiss Light Source, as well as the European Synchrotron Radiation Facility. This work is supported by the German Research Foundation, Collaborative Research Centre 807 'Transport and Communication across Biological Membranes'.

Author Information The coordinates for the structure reported in this work have been deposited in the Protein Data Bank under accession number 2W8A. Reprints and permissions information is available at www.nature.com/reprints. Correspondence and requests for materials should be addressed to C.Z. (christine.ziegler@mpibp-frankfurt.mpg.de).

METHODS

Purification and crystallization. The plasmid IBA7betPAN29EEE44/45/46AAA containing an N-terminal StrepII tag was constructed as described²³. For selenomethionine labelling, the plasmid was transformed into *E. coli* BL21 RIL-X cells (Stratagene). The cells were cultured in SelenoMet media (Molecular Dimensions) containing 40 mg l⁻¹ L-selenomethionine and BetPAN29EEE44/45/46AAA (BetPAN29_{Se}) was produced after induction at an absorbance at 600 nm ($A_{600\text{nm}}$) of 0.7 with 200 µg l⁻¹ anhydrotetracycline for 6 h at 37 °C. Membranes were isolated from disrupted cells and solubilized in 2.5% (w/v) β-dodecyl-maltoside (DDM, Glycon) for 40 min on ice under an N₂ stream. To minimize oxidation, 5 mM dithiothreitol and 0.5 mM EDTA were added at all subsequent steps. BetPAN29_{Se} was eluted with 5 mM desthiobiotin from the Streptactin resin (IBA GmbH) affinity column in buffer containing 25 mM Tris-HCl (pH 7.5), 200 mM NaCl, 8.7% glycerol and 0.6% Cymal-5. The protein was loaded onto a Superose 6 (GE Healthcare) size-exclusion column equilibrated with 20 mM Tris-HCl (pH 7.5), 200 mM NaCl and 0.6% Cymal-5. Purified protein was concentrated at 4 °C to ~10 mg ml⁻¹ at 3,000 g in a Vivaspinn tube (Vivascience) with a 100,000-molecular-weight cut-off.

BetPAN29 and BetPAN29_{Se} crystallized reproducibly with a reservoir solution of 100 mM Na₃citrate (pH 5.3–5.6), 14–24% PEG 400 and 100–150 mM NaCl. Crystals typically grew at 18 °C upon mixing the protein solution in 1:1 or 1:2 ratio with the reservoir solution. Addition of glycine betaine resulted in poor crystal growth, but sufficient amounts of the substrate were present in the SelenoMet medium to bind to BetP, and to remain bound during purification and crystallization. A concentration of 100 mM NaCl was necessary for well-diffracting crystals. Other salts did not produce crystals. Crystals were cryoprotected with a mixture of Paratone N and paraffin oil before freezing in liquid nitrogen. The crystals belong to orthorhombic space group $P2_12_12_1$ with cell dimensions $a = 118.1$ Å, $b = 129.4$ Å and $c = 182.9$ Å, and diffract to 2.7 Å along b^* and 3.8 Å along a^* and c^* (Supplementary Table 1).

Structure determination. X-ray diffraction data were collected on a mar225 charge-coupled device detector at the Max Planck beamline X10SA (PXII) at the Swiss Light Source in Villigen, Switzerland, processed with XDS⁴⁹ and scaled with SCALA⁵⁰. Phases were obtained by single anomalous dispersion from a data set (Supplementary Table 1) of a BetPAN29_{Se} crystal collected at the Se peak wavelength of 0.9794 Å. The program SHELXD⁵¹ was used to identify 39 Se sites related by three-fold NCS, which were used to calculate phases and complete the heavy atom model in SHARP/autoSHARP⁵². Solvent flattening and NCS averaging in both SOLOMON⁵³ and DM⁵⁴ subsequently improved phases. Anisotropy was corrected in SHARP⁵² to yield a set of phases and isotropic amplitudes, which were subsequently used in density improvement. The resulting electron density map allowed automatic building of an initial model using Buccaneer⁵⁴, which accounted for ~80% of the protein sequence. The model was manually completed and rebuilt with Coot⁵⁵ and O⁵⁶, using a three-fold symmetry-averaged map that was sharpened with a B factor of -100 Å². Tight three-fold NCS restraints were imposed throughout the refinement. Relaxation of these restraints did not result in a significant drop in R_{free} .

Refinement was initially done using BUSTER-TNT⁵⁷, followed at the final stages by alternating use of BUSTER-TNT⁵⁷ and phenix.refine⁵⁸. Phenix.refine⁵⁸ with simulated annealing and TLS refinement with nine defined TLS groups gave an overall better result in model geometry as judged by MolProbity⁵⁹. BUSTER-TNT⁵⁷ produced better guiding $F_o - F_c$ maps for model building, manifest in the improved overall refinement statistics. The final cycle of refinement was performed with BUSTER-TNT⁵⁷ (Supplementary Table 1). The model statistics resulting from MolProbity⁵⁹ are reported in Supplementary Table 1. The gap between R factors obtained during refinement for the working and test sets of reflections is surprisingly narrow. This is probably due to the strict NCS restraints used throughout the refinement and the test-set reflections being chosen randomly and not within small resolution shells.

Transport assay. Uptake of [¹⁴C]glycine betaine mediated by BetP or BetPAN29 was measured in *E. coli* MKH13, in *C. glutamicum* DHPF cells²¹ and in *E. coli* polar lipid proteoliposomes as described²³. The uptake rate was displayed relative to maximum. Absolute values are given in the legend of Supplementary Fig. 1. BetP mutants carrying the individual point mutations W194L, Y197L, W371L, W374L, W377L, P134AE135A, R210A, G301A, R387A and R392K were measured in *E. coli* MKH13²¹ cells as described²³. The BetP single point mutants W189C, W326C and W366C gave low expression yields in *E. coli* as judged by immunoblotting against the N-terminal StrepII tag and were therefore reconstituted into *E. coli* phospholipids⁴⁸ for transport measurements. The osmolality was adjusted to 800 mosmol kg⁻¹ by addition of sorbitol. Substrate uptake in cells or proteoliposomes was initiated by adding [¹⁴C]glycine betaine (0.1 mCi ml⁻¹) at a final concentration of 100 or 200 mM and measured as described⁴⁸.

49. Kabsch, W. Automatic processing of rotation diffraction data from crystals of initially unknown symmetry and cell constants. *J. Appl. Crystallogr.* **26**, 795–800 (1993).
50. Evans, P. Scaling and assessment of data quality. *Acta Crystallogr. D* **62**, 72–82 (2006).
51. Sheldrick, G. M. A short history of SHELX. *Acta Crystallogr. A* **64**, 112–122 (2008).
52. Vonrhein, C., Blanc, E., Roversi, P. & Bricogne, G. Automated structure solution with autoSHARP. *Methods Mol. Biol.* **364**, 215–230 (2007).
53. Abrahams, J. P. & Leslie, A. G. W. Methods used in the structure determination of bovine mitochondrial F₁ ATPase. *Acta Crystallogr. D* **52**, 30–42 (1996).
54. Cowtan, K. dm: An automated procedure for phase improvement by density modification. *CCP4/ESF-EACBM Newslett. Protein Crystallogr.* **31**, 34–38 (1994).
55. Emsley, P. & Cowtan, K. Coot: model-building tools for molecular graphics. *Acta Crystallogr. D* **60**, 2126–2132 (2004).
56. Jones, T. A., Zou, J.-Y., Cowan, S. W. & Kjeldgaard, M. Improved methods for the building of protein models in electron density maps and the location of errors in these models. *Acta Crystallogr. A* **47**, 110–119 (1991).
57. Blanc, E. *et al.* Refinement of severely incomplete structures with maximum likelihood in BUSTER-TNT. *Acta Crystallogr. D* **60**, 2210–2221 (2004).
58. Terwilliger, T. C. *et al.* Iterative model building, structure refinement and density modification with the PHENIX AutoBuild wizard. *Acta Crystallogr. D* **64**, 61–69 (2008).
59. Lovell, S. C. *et al.* Structure validation by C-alpha geometry: phi, psi, and C-beta deviation. *Proteins Struct. Funct. Genet.* **50**, 437–450 (2003).

A candidate sub-parsec supermassive binary black hole system

Todd A. Boroson¹ & Tod R. Lauer¹

The role of mergers in producing galaxies, together with the finding that most large galaxies harbour black holes in their nuclei¹, implies that binary supermassive black hole systems should be common. Here we report that the quasar SDSS J153636.22+044127.0 is a plausible example of such a system. This quasar shows two broad-line emission systems, separated in velocity by $3,500 \text{ km s}^{-1}$. A third system of unresolved absorption lines has an intermediate velocity. These characteristics are unique among known quasars. We interpret this object as a binary system of two black holes, having masses of $10^{7.3}$ and $10^{8.9}$ solar masses separated by ~ 0.1 parsec with an orbital period of ~ 100 years.

The present object is the first known with two broad-line systems, and builds on the recent interest in the quasar SDSS J092712.65+294344.0, which shows two sets of narrow emission lines (only one of which has associated broad lines) separated by $2,650 \text{ km s}^{-1}$ from each other^{2–6}, as well as additional emission and absorption lines at an intermediate redshift⁶. Although these characteristics might be caused by a binary black hole system, they might also be due to chance superposition of active objects or a colliding system analogous to NGC 1275⁵.

We have developed a principal components analysis technique that identifies objects having spectral characteristics inconsistent with the ensemble of quasar spectra in the SDSS (Sloan Digital Sky Survey) archive. We have applied this procedure to the rest frame spectral region $4,000\text{--}5,700 \text{ \AA}$ of $\sim 17,500$ quasars. This sample comprises all quasars having redshifts (z) less than 0.70 from the SDSS quasar catalogue, fifth release⁷ (SDSSQ5 catalogue), as well as all additional objects classified as $z < 0.70$ quasars observed for the final release (DR7). Of the 17,500 objects in the entire sample, only two objects have multiple redshift systems, SDSS J092712.65+294344.0, described above, and SDSS J153636.22+044127.0 (referred to here as J1536+0441).

J1536+0441 has SDSS point-source *ugriz* magnitudes of respectively 17.72, 17.24, 16.97, 16.80 and 16.33. The image appears stellar in SDSS images. For a redshift of 0.388 and a flat cosmology with $H_0 = 71 \text{ km s}^{-1} \text{ Mpc}^{-1}$ and $\Omega_m = 0.27$, the absolute i-band magnitude is $M_i = -24.83$. This is at the high end of the luminosity distribution for the SDSS quasar sample at this redshift. The quasar has 2MASS (Two Micron All Sky Survey) *JHK* magnitudes of respectively 15.46, 14.85 and 14.10. It was also detected by ROSAT (Röntgen satellite), with a count rate of 0.03124 s^{-1} . This is typical for SDSS quasars at this redshift. The quasar is not in the FIRST (Faint Images of the Radio Sky at Twenty Centimeters) or NVSS (NRAO VLA Sky Survey) catalogues.

The spectrum of J1536+0441 shows two broad-line emission systems and one system of narrow absorption lines. The higher redshift ‘r-system’ at $z = 0.3889$ shows broad Balmer lines ($H\alpha$, $H\beta$ and $H\gamma$) and the usual narrow lines seen in low redshift quasars. The lower redshift ‘b-system’ at $z = 0.3727$ shows broad Balmer lines ($H\alpha$ through to $H\delta$) and broad Fe II emission, seen most strongly around

$3,000 \text{ \AA}$ in the rest frame. A strong narrow absorption-line ‘a-system’ is also present, including six unresolved resonance lines, at $z = 0.38783$, which, in the quasar rest frame, is 240 km s^{-1} less than that of the r-system and $3,300 \text{ km s}^{-1}$ greater than that of the b-system. The full SDSS spectrum is shown in Fig. 1. The lines are listed in Table 1.

The r-system shows the typical features of a low-redshift quasar. The strengths and widths of the forbidden lines are normal. The somewhat larger width of the high ionization forbidden lines ([Ne V]) compared to that of the low ionization forbidden lines ([O II]) is not unusual^{8,9}. The Balmer line profiles, to the extent that they can be separated from the b-system, look normal.

The b-system has no narrow or forbidden-line emission, making it extremely unusual. An upper limit on the equivalent width of its [O III] line at $5,007 \text{ \AA}$ is $\sim 0.5 \text{ \AA}$, about 2% of the measured strength of the r-system [O III] $5,007 \text{ \AA}$ line. Although there are a few quasars known with no detectable [O III] lines, they are exclusively infrared-luminous objects that have extremely strong optical Fe II emission¹⁰. Thus, they are quite rare and show features not seen in this object.

Ultraviolet Fe II emission is unambiguously indicated by the ‘notch’ between about $3,950$ and $4,300 \text{ \AA}$. To determine to which

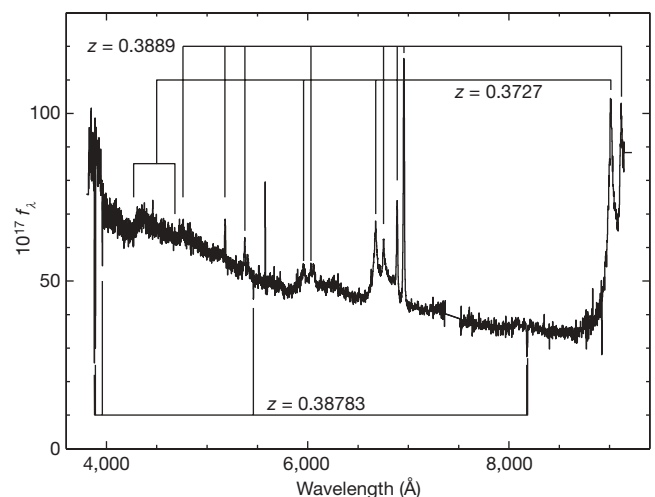


Figure 1 | The observed spectrum from the SDSS archive of the quasar SDSS J1536+0441. The three redshift systems discussed in the text are indicated with identified features marked. The r-system, at $z = 0.3889$, shows typical broad and narrow lines seen in low-redshift quasars, including the Balmer lines and the strong forbidden lines of [O II], [O III], [Ne III] and [Ne V]. The b-system, at $z = 0.3727$, shows only broad Balmer lines and ultraviolet Fe II emission. The a-system (at $z = 0.38783$) shows six unresolved absorption lines: the Mg II doublet ($2,796$ and $2,803 \text{ \AA}$), the Mg I $2,852 \text{ \AA}$ line, the Ca II K line ($3,934 \text{ \AA}$), and the Na D doublet ($5,891$ and $5,897 \text{ \AA}$). The strong unmarked emission feature is an artefact from poor subtraction of the night-sky line at $5,577 \text{ \AA}$.

¹National Optical Astronomy Observatory, Tucson, Arizona 85726, USA.

Table 1 | Spectral line properties of J1536+0441

System	Line (Å)	z	FWHM (km s ⁻¹)	EW (Å)
r-system (emission)*	H α	0.38890	ND	ND
r-system (emission)	[O III] 5,007	0.38889	550	24
r-system (emission)	[O III] 4,959	0.38889	530	8
r-system (emission)	H β	0.38894	6,000:	43
r-system (emission)	[O III] 4,363	0.38820	ND	0.8
r-system (emission)	H γ	0.38914	ND	5.1
r-system (emission)	[Ne III] 3,968	0.38941	340:	0.5
r-system (emission)	He I 3,889	0.38960	920	1.5
r-system (emission)	[Ne III] 3,869	0.38872	680	2.1
r-system (emission)	[O II] 3,727	0.38908	ND	1.8
r-system (emission)	[Ne V] 3,426	0.38912	1,030	0.9
b-system (emission)†	H α	0.37303	2,100:	165
b-system (emission)	H β	0.37247	2,400:	35
b-system (emission)	H γ	0.37253	ND	8:
b-system (emission)	H δ	0.3717:	ND	0.4:
a-system (absorption)‡	Na D 5,896	0.38782	Unresolved	0.8
a-system (absorption)	Na D 5,890	0.38794	Unresolved	1.2
a-system (absorption)	Ca II K 3,934	0.38776	Unresolved	0.4
a-system (absorption)	Mg I 2,852	0.38784	Unresolved	0.9
a-system (absorption)	Mg II 2,796	0.38781	Unresolved	2.1
a-system (absorption)	Mg II 2,803	0.38779	Unresolved	2.5

EW, equivalent width of line. Measurements marked with colon (:) are of lower precision. Entries of ND (not determined) indicate that the data quality was too low to determine a measurement.

* <z> = 0.3889.

† <z> = 0.3727.

‡ <z> = 0.38783.

system the Fe II emission should be attributed, the spectral region between 4,200 and 4,450 Å was cross-correlated with a composite quasar spectrum¹¹ (Fig. 2). It is clear that the Fe II belongs to the b-system, with a derived redshift of 0.375. Although this is slightly higher (500 km s⁻¹) than that of the b-system, Fe II emission in quasars is typically redshifted by 400 km s⁻¹ relative to the H β line¹².

The absorption line system is also atypical. The lines are unresolved in the SDSS spectra, and are almost certainly due to neutral or low-ionization gas in the line of sight rather than stars in the host galaxy. There is no evidence of stellar absorption features. Absorption such as this is very unusual in low-redshift quasars. Only 6 of the 1,000 high signal-to-noise spectra of SDSS quasars that were used for constructing the eigenspectra show Na I D absorption at the strength seen in J1536+0441, and of these, three are clearly cases of self-absorption from dense material associated with the nucleus. It is possible that this absorption arises in a gas cloud unrelated to the presence of activity in the host galaxy—even in some other object in the line of sight. It is also possible that this absorption is seen because

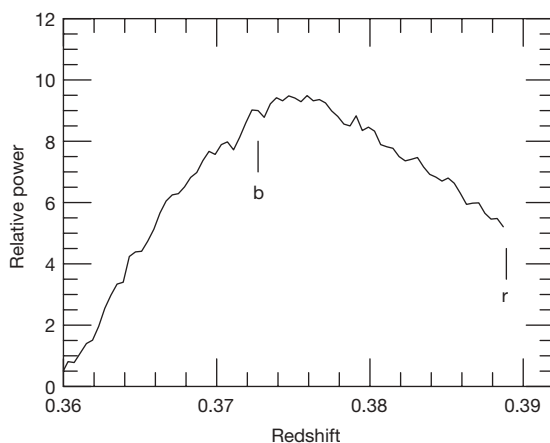


Figure 2 | Cross-correlation between the 4,200–4,450 Å region of the spectrum of J1536+0441 and the corresponding region of a composite quasar spectrum¹². The peak indicates the presence of ultraviolet Fe II at, or slightly above, the redshift of the b-system. Note that the cross-correlation is quite inconsistent with the Fe II emission being at the redshift of the r-system ($z = 0.3889$).

of the presence of the second continuum source, presumably the b-system nucleus, seen through a part of the r-system that, normally, a line of sight to the nucleus would not pass.

If the two broad-line redshifts represent broad-line emission regions around separate supermassive black holes in a single galaxy, then the simplest model would be one in which they are in a gravitationally bound system. We estimate the masses of the two black holes using the H β full-width at half-maximum (FWHM) values and assuming that a fraction, proportional to the mass, of the continuum luminosity at 5,100 Å comes from each quasar. Adopting a standard calibration¹³, we derive masses of $10^{8.9}$ and $10^{7.3}$ solar masses for the red and blue systems, respectively.

Derivation of the full orbital velocity, V , radius, R , and period, T , of the binary system depends on unknown geometrical factors. If a random circular orbit is assumed, the mean angle between the line-of-sight and the radial vector between the two black holes is 60°. Random orientation of the velocity vector implies an additional mean projection angle of 45°. The projected velocity is then $\sim 0.61V$, which gives $V \approx 6 \times 10^3$ km s⁻¹. This implies $R \approx 3 \times 10^{17}$ cm and $T \approx 100$ years. In contrast, upper limits of $T \approx 500$ years and $R \approx 9 \times 10^{17}$ cm are derived if no projection factors are assumed. In either case, the separation is approximately the size of the broad line region and very much smaller than the narrow line region. Thus, in this model, the two black holes and their broad line regions are orbiting well within a single narrow line region. It is notable that the derived characteristics of this system are similar to those proposed for OJ 287 based on its long term photometric variations^{14,15}.

For fixed black hole masses, the decay time of the binary due to gravitational radiation, t_D , is $\propto V^{-8}$, and is thus extremely sensitive to the assumed projection factors. For no projection corrections, $t_D \approx 3 \times 10^{11}$ years, whereas $t_D \approx 7 \times 10^9$ years under the model above¹⁶. This timescale is interesting, as it implies that the binary has evolved past the ‘final parsec’ scale at which decay due to energy exchange with stars becomes inefficient, but where gravitational radiation decay remains too weak to carry the evolution further¹⁷. Theoretical studies of the effects of gas dynamical friction indicate that the timescale for that process to cause the orbit to decay is much longer for such massive black holes^{18,19}, though this is an area of continuing study.

It is intriguing that the two derived black hole masses would put the systemic velocity closer to the r-system, consistent with the idea that the narrow emission lines and absorption lines are more likely to be associated with the host galaxy. Note that the masses are highly uncertain, because of both the difficulty of measuring the width of the blended lines and the uncertainty about how to split continuum flux between the two objects. This interpretation is further complicated by the fact that the narrow forbidden emission lines agree precisely with the redshift of the r-system.

A second possibility is that these are two separate quasars that are by chance seen in the same line of sight. Integrating the SDSS quasar luminosity function²⁰ yields a probability of 1.8×10^{-7} of finding a second quasar within a volume centred on a first quasar corresponding to a conservative one-arcsecond radius circle on the sky and a redshift range of $\pm 10,000$ km s⁻¹. Multiplying this by the 17,500 objects in our sample gives a probability of 3.2×10^{-3} of one chance occurrence. This calculation does not account for the possibility of an enhanced density due to the presence of a cluster of galaxies; two galaxies near the quasar on the SDSS image have photometric redshifts close to that of the quasar. The strongest, though admittedly *a posteriori*, argument against the chance superposition hypothesis is the unique lack of narrow lines in the b-system.

The most obvious interpretation of the presence of absorption at a redshift close to that of the r-system is that the b-system is background to the r-system. This would be inconsistent with an explanation involving ejection of one of the black holes, though it would be consistent with an infall interpretation, analogous with NGC 1275²¹.

In this case, however, the two broad-line systems must represent two active nuclei.

New observations could test the binary black hole hypothesis. A spectrum with higher signal-to-noise ratio may allow the detection of stellar absorption features from the host galaxy, as well as setting better limits on any narrow emission lines associated with the b-system. Detection of such features at both b- and r-system redshifts would provide compelling evidence that this is a chance superposition or a colliding pair. High spatial resolution imaging could also rule out the close binary hypothesis. Monitoring over several years could reveal changes due to the orbital motion of the system. Our simple projection model predicts a velocity change in the b-system of $\sim 10^2 \text{ km s}^{-1}$ in a single year.

Received 17 November 2008; accepted 14 January 2009.

- Magorrian, J. *et al.* The demography of massive dark objects in galaxy centers. *Astron. J.* **115**, 2285–2305 (1998).
- Komossa, S., Zhou, H. & Lu, H. A recoiling supermassive black hole in the quasar SDSS J092712.65+294344.0? *Astrophys. J.* **678**, L81–L84 (2008).
- Bogdanovic, T., Eracleous, M. & Sigurdsson, S. SDSS J092712.65+294344.0: Recoiling black hole or a sub-parsec binary candidate? Preprint at (<http://arxiv.org/abs/0809.3262>) (2008).
- Dotti, M. *et al.* SDSSJ092712.65+294344.0: A candidate massive black hole binary. Preprint at (<http://arxiv.org/abs/0809.3446>) (2008).
- Heckman, T. M., Krolik, J. H., Moran, S., Schnittman, J. & Gezari, S. SDSSJ092712.65+294344.0: NGC 1275 at $z=0.7$? Preprint at (<http://arxiv.org/abs/0810.1244>) (2008).
- Shields, G. A., Bonning, E. W. & Salviander, S. Comment on the black hole recoil candidate quasar SDSS J092712.65+294344.0. Preprint at (<http://arxiv.org/abs/0810.2563>) (2008).
- Schneider, D. P. *et al.* The Sloan Digital Sky Survey quasar catalog. IV. Fifth data release. *Astron. J.* **134**, 102–117 (2007).
- Appenzeller, I. & Wagner, S. J. Forbidden high-ionization lines in QSO spectra. *Astron. Astrophys.* **250**, 57–61 (1991).
- Moore, D. & Cohen, R. D. Narrow-line region kinematics in Seyfert nuclei. *Astrophys. J.* **433**, 602–624 (1994).
- Boroson, T. A. & Meyers, K. A. The optical properties of IR-selected and Mg II broad absorption line quasars. *Astrophys. J.* **397**, 442–451 (1992).
- Vanden Berk, D. E. *et al.* Composite quasar spectra from the Sloan Digital Sky Survey. *Astron. J.* **122**, 549–565 (2001).
- Hu, C. *et al.* A systematic analysis of Fe II emission in quasars: Evidence for inflow to the central black hole. *Astrophys. J.* **687**, 78–96 (2008).
- Denney, K. D., Peterson, B. M., Dietrich, M., Vestergaard, M. & Bentz, M. C. Systematic uncertainties in black hole masses determined from single epoch spectra. Preprint at (<http://arxiv.org/abs/0810.3234>) (2008).
- Sillanpää, A., Haarala, S., Valtonen, M. J., Sundelius, B. & Byrd, G. G. OJ 287: Binary pair of supermassive black holes. *Astrophys. J.* **325**, 628–634 (1988).
- Valtonen, M. J. *et al.* A massive binary black-hole system in OJ 287 and a test of general relativity. *Nature* **452**, 851–853 (2008).
- Peters, P. C. Gravitational radiation and the motion of two point masses. *Phys. Rev.* **136**, 1224–1232 (1964).
- Milosavljevic, M. & Merritt, D. Long term evolution of massive black hole binaries. *Astrophys. J.* **596**, 860–878 (2003).
- Gould, A. & Rix, H. Binary black hole mergers from planet-like migrations. *Astrophys. J.* **532**, L29–L32 (2000).
- Cuadra, J., Armitage, P. J., Alexander, R. D. & Begelman, M. C. Massive black hole binary mergers within sub-pc scale gas disks. *Mon. Not. R. Astron. Soc.* (in the press).
- Richards, G. T. *et al.* The Sloan Digital Sky Survey quasar survey: Quasar luminosity function from Data Release 3. *Astron. J.* **131**, 2766–2787 (2006).
- Conselice, C. J., Gallagher, J. S. & Wyse, R. F. G. On the nature of the NGC 1275 system. *Astron. J.* **122**, 2281–2300 (2001).

Acknowledgements NOAO is operated by the Association of Universities for Research in Astronomy (AURA), Inc. under cooperative agreement with the National Science Foundation (NSF). This paper has used data from the SDSS archive, the 2MASS archive, the ROSAT archive at the High Energy Astrophysics Science Archive Research Center (HEASARC), provided by NASA's Goddard Space Flight Center, the FIRST survey, and the NVSS. Funding for the SDSS and SDSS-II has been provided by the Alfred P. Sloan Foundation, the Participating Institutions, the NSF, the US Department of Energy, the National Aeronautics and Space Administration (NASA), the Japanese Monbukagakusho, the Max Planck Society, and the Higher Education Funding Council for England. The SDSS website is at <http://www.sdss.org/>. The 2MASS is a joint project of the University of Massachusetts and the Infrared Processing and Analysis Center/California Institute of Technology, funded by NASA and the NSF.

Author Information Reprints and permissions information is available at www.nature.com/reprints. Correspondence and requests for materials should be addressed to T.A.B. (tyb@noao.edu).

LETTERS

Electronic acceleration of atomic motions and disordering in bismuth

Germán Sciaini¹, Maher Harb¹, Sergei G. Kruglik¹, Thomas Payer², Christoph T. Hebeisen¹, Frank-J. Meyer zu Heringdorf², Mariko Yamaguchi¹, Michael Horn-von Hoegen², Ralph Ernstorfer^{1†} & R. J. Dwayne Miller¹

The development of X-ray and electron diffraction methods with ultrahigh time resolution has made it possible to map directly, at the atomic level, structural changes in solids induced by laser excitation^{1–8}. This has resulted in unprecedented insights into the lattice dynamics of solids undergoing phase transitions. In aluminium, for example, femtosecond optical excitation hardly affects the potential energy surface of the lattice; instead, melting of the material is governed by the transfer of thermal energy between the excited electrons and the initially cold lattice¹. In semiconductors, in contrast, exciting ~10 per cent of the valence electrons results in non-thermal lattice collapse owing to the antibonding character of the conduction band^{2–5,9,10}. These different material responses raise the intriguing question of how Peierls-distorted systems¹¹ such as bismuth¹² will respond to strong excitations. The evolution of the atomic configuration of bismuth upon excitation of its A_{1g} lattice mode, which involves damped oscillations of atoms along the direction of the Peierls distortion of the crystal, has been probed^{6–8}, but the actual melting of the material has not yet been investigated. Here we present a femtosecond electron diffraction study of the structural changes in crystalline bismuth as it undergoes laser-induced melting. We find that the dynamics of the phase transition depend strongly on the excitation intensity, with melting occurring within 190 fs (that is, within half a period of the unperturbed A_{1g} lattice mode^{6–8}) at the highest excitation. We attribute the surprising speed of the melting process to laser-induced changes in the potential energy surface of the lattice, which result in strong acceleration of the atoms along the longitudinal direction of the lattice and efficient coupling of this motion to an unstable transverse vibrational mode. That is, the atomic motions in crystalline bismuth can be electronically accelerated so that the solid-to-liquid¹³ phase transition occurs on a sub-vibrational timescale.

The crystalline structure of bismuth (Bi) is derived from a face-centred-cubic lattice rhombohedrically distorted along the body diagonal¹² by the well-known Peierls–Jones mechanism¹¹. A seminal study⁶ used time-resolved X-ray diffraction to monitor the A_{1g} mode (that is, oscillations along the direction of the Peierls distortion of Bi) and observed that after reaching a maximum, the diffraction signal decreased monotonically and subsequently reached a quasi-stationary level as the pump fluence was increased. The signal decrease was attributed to disordering caused by melting of the material, but the study did not exceed the threshold above which the process is non-reversible and, therefore, no clear information about the melting mechanism was attained. Because neither experiments nor calculations are available at photoexcitation levels above 3% of the valence

density, it remains unknown whether or not Bi can undergo a non-thermal melting transition such as that seen in semiconductors^{2–5,9,10}.

To address this question, we performed femtosecond electron diffraction (FED) studies on free-standing 30-nm-thick Bi films under non-reversible photoexcitation conditions, that is, at excitation levels where more than 3% of valence electrons are excited. The FED experiments were carried out in transmission mode. As the Bi films were [111] oriented and the electron beam diffracts from planes which are practically parallel to it, this geometry ensures that the diffraction signal is not sensitive to the coherent A_{1g} oscillations ($\langle 111 \rangle$ direction). The Bi films were excited using 200-fs laser pulses at a wavelength of 775 nm over a wide range of pump laser fluences below and above the melting point, and their structure probed using FED at increasingly longer delay times after the laser excitation. The sample was moved to a new spot between laser shots, because each laser shot led to disintegration of the sample at the irradiated area. For each time point, the diffraction signal was integrated over 4–12 shots. The number of shots per time point was limited by the total area of the sample. (For further details, see Methods.)

Measurements below the damage threshold of the Bi films were performed to extract the lattice heating dynamics at lower excitation levels and to obtain the absorbed energy as a function of incident pump fluence *in situ*. Figure 1a shows the difference in radially averaged diffracted intensity obtained at different delay times, for a pump fluence of 0.84 mJ cm^{–2}. The signal due to inelastic scattering, between the (1–10) and (–211) peaks, serves as a signature of lattice heating and is recorded as a function of the time delay (Fig. 1b). The characteristic time constant for this process was found to be 2–3 ps (Fig. 1d), which corresponds to the decay time constants of 2–4 ps obtained for the different diffraction peaks (Fig. 1c). Figure 1e shows the increase in lattice temperature, $\Delta T_l = T_{l,eq} - T_{l,R}$, as a function of incident laser fluence. Here $T_{l,R}$ and $T_{l,eq}$ are the lattice temperatures before excitation (room temperature, ~294 K) and after carrier-phonon equilibration, respectively. The value of $T_{l,eq}$ was calculated from the Debye–Waller model¹⁴, which gives the dependence of the diffracted intensity on lattice temperature as

$$\frac{I_s(T_{l,eq})}{I_s(T_{l,R})} = \exp \left\{ -\frac{s^2}{2} (B(T_{l,eq}) - B(T_{l,R})) \right\}$$

where I_s is the diffracted intensity, s is the scattering vector modulus and B is the Debye–Waller factor (a function of temperature obtained from a parameterization¹⁴). $I_s(T_{l,eq})/I_s(T_{l,R})$ was extracted from the amplitude decays of the exponential fits of the data (Fig. 1c).

We note that a linear regression fits the data in Fig. 1e, reflecting the fact that the excitation levels are in the linear-absorption regime.

¹Institute for Optical Sciences and Departments of Chemistry and Physics, University of Toronto, 80 St George Street, Toronto, Ontario M5S 3H6, Canada. ²Fachbereich Physik and Center for Nanointegration Universität Duisburg-Essen, 47057 Duisburg, Germany. [†]Present address: Physik Department E11, Technische Universität München, 85747 Garching, Germany.

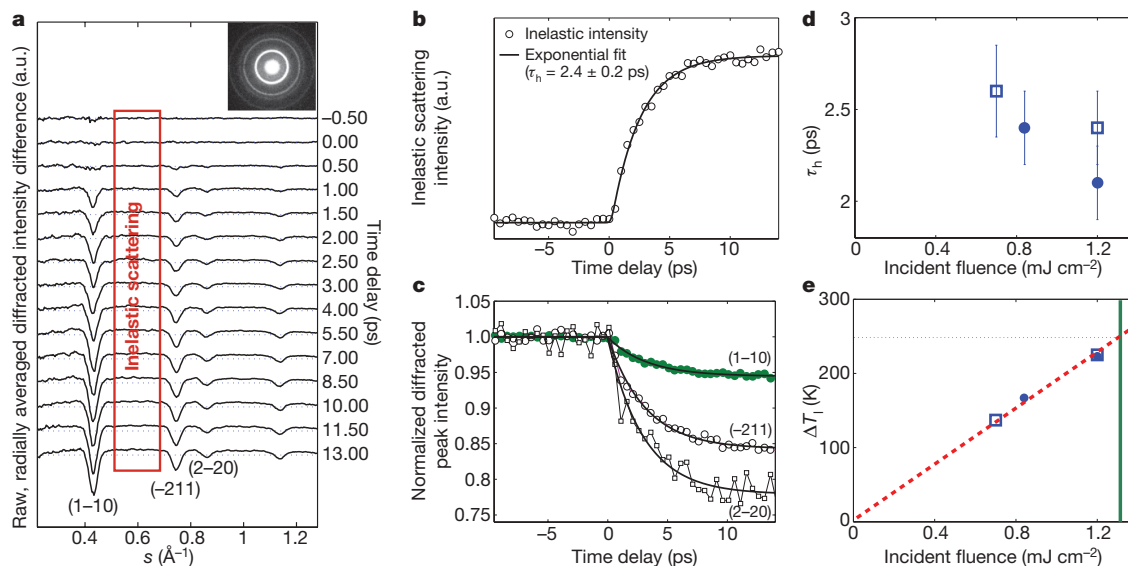


Figure 1 | FED data below the melting point (reversible conditions). **a**, Raw, radially averaged diffracted intensity difference between images at different time delays and a reference image (inset) taken without pump laser excitation (sample 2; see Methods). a.u., arbitrary units. **b**, Circles, rise of inelastic scattering obtained by integrating the intensity between the (1-10) and (-211) peaks (red box in **a**); trace, exponential fit of the data convolved with a Gaussian instrumental response of 400 fs (full width at half maximum). **c**, Normalized, radially averaged intensity decays of the (1-10),

(-211) and (2-20) peaks; traces, exponential fits. Incident fluence was 0.84 mJ cm^{-2} . **d**, Time constants, τ_h , obtained for the rise of the inelastic scattering as a function of incident fluence. Error bars, standard error (s.e.m.) obtained from the fits. Squares represent sample 1 and circles represent sample 2. **e**, Increase in lattice temperature as a function of the incident laser fluence. The dashed line gives the linear fit of the data and the vertical, solid line delineates the melting threshold (see text for details).

We also note that extrapolation of the incident fluence to the value required to reach the melting point of Bi gives $\sim 1.3 \text{ mJ cm}^{-2}$ (Fig. 1e), in agreement with the observed damage threshold, $\sim 1.4 \text{ mJ cm}^{-2}$. The minimum incident fluence, F_m , that ensures the total melting of the probed volume was estimated from the slope, a , of the fit shown in Fig. 1e ($a = 183 \text{ K mJ}^{-1} \text{ cm}^2$) according to

$$F_m = \frac{C_l \Delta T_{l,m} + \Delta_{\text{fus}} H}{a C_l}$$

Here C_l , the heat capacity of solid Bi ($25.52 \text{ J mol}^{-1} \text{ K}^{-1}$)¹⁵, multiplied by a represents the amount of absorbed energy per incident fluence, $\Delta T_{l,m}$ is the increase in lattice temperature ($\sim 250 \text{ K}$) needed to reach the melting point from room temperature¹⁵, and $\Delta_{\text{fus}} H$ is the enthalpy of fusion of Bi ($\sim 11.14 \times 10^3 \text{ J mol}^{-1}$)¹⁵. This estimate gives a value for F_m of 3.9 mJ cm^{-2} , and experiments of Bi melting were therefore performed at excitation levels above this value (incident fluence range, 6–23 mJ cm^{-2}).

Figure 2 shows the results obtained for an incident fluence of 18 mJ cm^{-2} . Diffraction patterns obtained by averaging single-shot measurements without and with laser excitation, at a time delay of +1 ps, are shown in Fig. 2a and Fig. 2b, respectively. At this time delay after laser excitation, the 1-10 reflection of the unperturbed, crystalline Bi has mostly disappeared and a diffuse ring at smaller scattering angles emerges. The radially averaged intensities of the two diffraction patterns (Fig. 2c) clearly reflect that laser excitation has caused the collapse of the crystalline structure of solid Bi and the emergence of a new phase, whose structure factor agrees with that of liquid Bi (ref. 13). Information on the evolution of the order-to-disorder process is obtained by studying, as functions of the time delay, the decay of the (1-10) peak of crystalline Bi and the increase of the diffracted intensity in the $0.23\text{--}0.34 \text{ \AA}^{-1}$ range, which corresponds to lattice disordering and liquid-phase dynamics (Fig. 2d). We note that the rise of the liquid-phase pattern roughly follows the decay of the (1-10) peak; this behaviour is observed for all excitation fluences used.

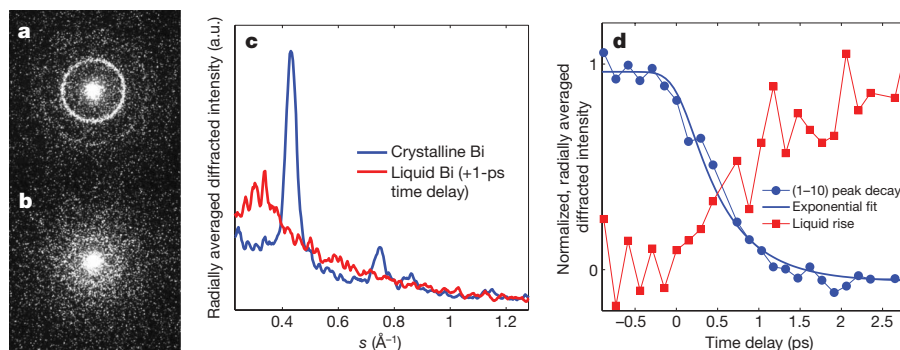


Figure 2 | Typical results obtained using FED above the melting point (averaged single-shot measurements). Excitation fluence was 18 mJ cm^{-2} . **a**, **b**, Diffraction patterns recorded without (**a**) and with (**b**) pump laser excitation, at +1-ps time delay (20 shots averaged). **c**, Radially averaged intensity profiles of the diffraction patterns shown in **a** (blue trace) and **b** (red

trace). **d**, Blue, decay of the (1-10) peak; red, rise of the integrated intensity in the range $0.23\text{--}0.34 \text{ \AA}^{-1}$ (four shots averaged). The thicker blue trace is an exponential fit convolved with the instrumental response that gives a decay time constant of $530 \pm 130 \text{ fs}$ (s.e.m.).

Figure 3 summarizes the results of experiments involving total melting of the probed Bi sample. The percentage of excited valence electrons is calculated, as a first-order approximation, by extrapolating the linear relationship between incident laser fluence and excitation level that was found in experiments conducted below the damage threshold (see Methods for details). The data show that the characteristic times for the lattice collapse, τ_c , are substantially shorter than those of the lattice heating, τ_h , determined below the damage threshold (Fig. 1b, d), indicating that Bi melts non-thermally. However, this non-thermal melting is very different from that of semiconductors, where the decay time constants for disordering show a much weaker dependence on the pump laser fluence and reach a plateau when the excitation intensity is increased^{4,5}.

Insights into the non-thermal melting of Bi can be gained by considering the laser-induced evolution of the potential energy surface (PES) of crystalline Bi along the direction of the Peierls distortion. Such PES changes have been mapped⁷ by time-resolved X-ray diffraction for excited carrier densities <2% and calculated¹⁶ using a constrained density functional approach for excitation levels of up to 3% of the valence electrons. The calculations found that the excitation of ~1% of the valence carriers shifts the PES minima, and that the Peierls barrier decreases¹⁶. The atoms, initially at the equilibrium position of the electronic ground state, r_{eq} , therefore experience a net force along the A_{1g} mode coordinate due to the increase of the potential energy gradient, $|\nabla E_{pot}|_{r_{eq}}$. The overall result is the launching of atomic motions by a displacive excitation mechanism¹⁷. When the excitation level reaches ~2.5% of the valence electrons, the Peierls barrier completely flattens and $|\nabla E_{pot}|_{r_{eq}}$ increases further¹⁶, leading to stronger displacive forces; at an excitation level of 3% of the valence electrons, the two minima have already converged to one, and the phonon mode has stiffened. Other density functional calculations up to an excitation level of 1.5% of the valence density were carried out in a two-dimensional configuration space, that is, along the A_{1g} mode coordinate and perpendicular to that direction (that is, along the E_g mode coordinate)^{18,19}. In addition to the earlier observations¹⁶, these studies found that the PES gets flatter along the E_g direction when the excited carrier density is increased, with the coupling between the modes strongly depending on pump fluence.

Our experiments summarized in Fig. 3 probe the evolution of the PES of solid Bi at excitation levels exceeding 3% of the valence electrons. We note that on the timescale that disordering is taking place, that is, a few hundred femtoseconds, heat exchange between the initially photoexcited electron-hole plasma and the lattice system can be neglected. As a result, the electron gas and the atomic lattice

are only coupled through the exchange of mechanical work⁹; that is, the initial laser-induced change in the PES is translated into kinetic energy through the atomic displacements leading to disorder. Figure 4 illustrates the changes in the PES of crystalline Bi on increasing electronic excitation, in agreement with our observations: the higher the excitation fluence, the greater the potential energy gradient and the more intense the displacive forces¹⁷ that act on the atoms along the longitudinal direction and thus result in an increasingly faster collapse of the lattice. This effect is manifested by the strong dependence of the lattice-collapse time constants on the laser fluence (Fig. 3a), with the linear trend indicating that the speed of the atomic motions is not saturating down to the time-resolution limit of our experiment. At the highest excitation level (15% of the valence density), the lattice collapses unexpectedly quickly—within 190 fs, which is only half a period of the unperturbed A_{1g} lattice mode^{6–8}. However, the concerted appearance of an isotropic liquid phase, where correlations with long-range order have disappeared, is more surprising. The mechanism by which an initially well-directed motion might lead to a liquid phase on such short timescale is not obvious. For several semiconductors such as GaAs, Si (ref. 9) and InSb (ref. 10), it has been theoretically predicted that at excitation levels of >9% of the valence carriers, a transverse acoustic mode becomes unstable. Therefore, a saddle point along the longitudinal PES minimum is generated and can lead to motions in the transverse direction as a consequence of the anharmonic coupling between the modes.

The lattice dynamics we observe at the highest excitation level are too fast to involve a multiple-collision process and instead indicate very efficient coupling between longitudinal and transverse lattice modes. That is, strong anharmonic coupling between the initially activated A_{1g} mode and the E_g optical mode or a transverse acoustic mode²⁰ that becomes unstable provides the shear motion necessary to produce an isotropic liquid phase. According to the PES evolution illustrated in Fig. 4, the initial longitudinal atomic motion should indeed move very quickly on a ‘downhill’ path to reach the saddle point in about a quarter of a period of the nascent A_{1g} phonon mode⁶, and then be further accelerated along the transverse direction. We also note that when considering that the number of nearest-neighbour atoms in liquid Bi is just one or two greater than that in the crystalline phase¹³, once the longitudinal motion couples to the transverse direction, only a few collisions are, in principle, needed to reach the liquid structure. The solid-to-liquid phase transition in Bi, occurring in less time than a period of the unperturbed A_{1g} lattice mode, illustrates the driven nature of the atomic motions in this Peierls-distorted solid and the importance of the electron–lattice correlation effects present.

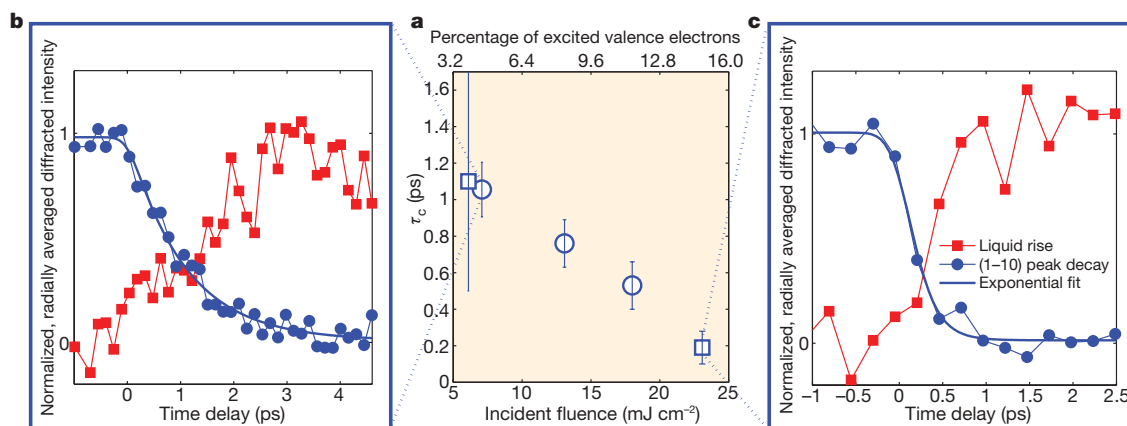


Figure 3 | Fluence dependence of the lattice disordering process. **a**, Decay time constants of the (1–10) peak, τ_c , obtained from exponential fits convolved with the instrumental response. Error bars, s.e.m. obtained from the fits. **b**, Decay of the (1–10) peak ($\tau_c = 1,060 \pm 150$ fs (s.e.m.)) and rise of

the liquid-phase scattering for an incident fluence of 7 mJ cm^{-2} . **c**, Same as **b**, but for an incident fluence of 23 mJ cm^{-2} ($\tau_c = 190 \pm 90$ fs (s.e.m.)). Squares, sample 1; circles, sample 2.

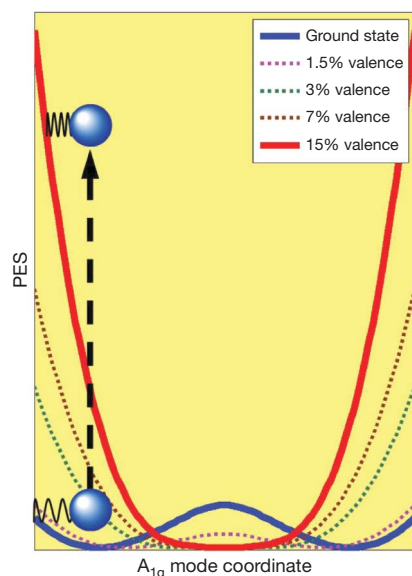


Figure 4 | Sketch of photoinduced changes of the PES of crystalline Bi upon electronic excitation. For clearness, only the A_{1g} phonon mode coordinate is shown to depict the disappearance of the Peierls distortion with electronic excitation. The spring represents the increasing potential energy force or PES gradient that drives the system towards the disordered phase. For illustrative purposes, the relative offset among the curves was subtracted. In the perpendicular or transverse direction (not shown), an unstable E_g or acoustic transverse mode giving rise to a saddle point is expected to develop. The PES at the highest excitation is shown to be highly anharmonic to illustrate the necessarily enhanced coupling to other lattice modes with increased excitation.

METHODS SUMMARY

In the FED experiments, we scattered ~ 350 -fs electron pulses²¹ containing $\sim 10^4$ electrons with a kinetic energy of 55 keV off the Bi sample to monitor the photo-induced changes initiated by 775-nm, 200-fs pump pulses. The 30-nm-thick crystalline Bi films were epitaxially grown on two different substrates^{22,23}, salt (sample 1) and carbon-coated mica (sample 2), then floated off the substrates at a water–air interface and picked up using a host silicon mesh. Both samples showed the same main grain orientation and dynamics upon photoexcitation.

Full Methods and any associated references are available in the online version of the paper at www.nature.com/nature.

Received 11 August 2008; accepted 13 January 2009.

1. Siwick, B. J., Dwyer, J. R., Jordan, R. E. & Miller, R. J. D. An atomic-level view of melting using femtosecond electron diffraction. *Science* **302**, 1382–1385 (2003).

2. Harb, M. *et al.* Electronically driven structure changes of Si captured by femtosecond electron diffraction. *Phys. Rev. Lett.* **100**, 155504 (2008).
3. Siders, C. W. *et al.* Detection of nonthermal melting by ultrafast X-ray diffraction. *Science* **286**, 1340–1342 (1999).
4. Lindenberg, A. M. *et al.* Atomic-scale visualization of inertial dynamics. *Science* **308**, 392–395 (2005).
5. Hillyard, P. B. *et al.* Carrier-density-dependent lattice stability in InSb. *Phys. Rev. Lett.* **98**, 125501 (2007).
6. Sokolowski-Tinten, K. *et al.* Femtosecond X-ray measurement of coherent lattice vibrations near the Lindemann stability limit. *Nature* **422**, 287–289 (2003).
7. Fritz, D. M. *et al.* Ultrafast bond softening in bismuth: Mapping a solid's interatomic potential with X-rays. *Science* **315**, 633–636 (2007).
8. Johnson, S. L. *et al.* Nanoscale depth-resolved coherent femtosecond motion in laser-excited bismuth. *Phys. Rev. Lett.* **100**, 155501 (2008).
9. Stampfli, P. & Bennemann, K. H. Theory for laser-induced femtosecond phase transition of silicon and GaAs. *Appl. Phys. A* **60**, 191–196 (1995).
10. Zijlstra, E. S., Tatarinova, L. L. & Garcia, M. E. Anharmonic noninertial lattice dynamics during ultrafast nonthermal melting of InSb. *Phys. Rev. Lett.* **101**, 135701 (2008).
11. Peierls, R. E. *More Surprises in Theoretical Physics* 24–26 (Princeton Univ. Press, 1991).
12. Madelung, O., Rössler, U. & Schulz, M. in *Semiconductors Vol. 41C, Non-Tetrahedrally Bonded Elements and Binary Compounds I 1–3* (Springer, 1990).
13. Sharrah, P. C., Petz, J. I. & Kruh, R. F. Determination of atomic distributions in liquid lead-bismuth alloys by neutron and X-ray diffraction. *J. Chem. Phys.* **32**, 241–246 (1960).
14. Gao, H. X. & Peng, L.-M. Parameterization of the temperature dependence of the Debye-Waller factors. *Acta Crystallogr. A* **55**, 926–932 (1999).
15. Lide, D. R. (ed.) *CRC Handbook of Chemistry and Physics* 88th edn, Sec. 4, 127, 133, Sec. 6, 110 (CRC, 2007).
16. Murray, É. D., Fritz, D. M., Wahlstrand, J. K., Fahy, S. & Reis, D. A. Effect of lattice anharmonicity on high-amplitude phonon dynamics in photoexcited bismuth. *Phys. Rev. B* **72**, 060301(R) (2005).
17. Zeiger, H. J. *et al.* Theory for dispersive excitation of coherent phonons. *Phys. Rev. B* **45**, 768–778 (1992).
18. Zijlstra, E. S., Tatarinova, L. L. & Garcia, M. E. Laser-induced phonon-phonon interactions in bismuth. *Phys. Rev. B* **74**, 220301(R) (2006).
19. Zijlstra, E. S., Tatarinova, L. L. & Garcia, M. E. Ab-initio study of coherent phonons excited by femtosecond laser pulses in Bismuth. *Proc. SPIE* **6261**, 62610R (2006).
20. Wu, X. & Xu, X. Coherent phonon excitation in bismuth. *Appl. Surf. Sci.* **253**, 6301–6304 (2007).
21. Hebeisen, C. T. *et al.* Grating enhanced ponderomotive scattering for visualization and full characterization of femtosecond electron pulses. *Opt. Express* **16**, 3334–3341 (2008).
22. Kammiller, M. & Horn-von Hoegen, M. Low energy electron diffraction of epitaxial growth of bismuth on Si(111). *Surf. Sci.* **576**, 56–60 (2005).
23. Payer, Th *et al.* Ultrathin epitaxially grown bismuth (111) membranes. *Appl. Phys. Lett.* **93**, 093102 (2008).

Acknowledgements We thank A.-A. Dhirani for the use of his deposition chamber. We acknowledge financial support provided by the Natural Science and Engineering Research Council and the Deutsche Forschungsgemeinschaft within the SFB 616, Energy Dissipation at Surfaces. R.E. thanks the Alexander-von-Humboldt foundation for financial support.

Author Information Reprints and permissions information is available at www.nature.com/reprints. Correspondence and requests for materials should be addressed to R.J.D.M. (dmiller@lphys.chem.utoronto.ca).

METHODS

FED experiment. The main challenge in FED is dealing with the temporal broadening of the electron pulses owing to space charge. Our approach has been to minimize the effects of space charge by using a compact gun design, with 3 cm of propagation between photocathode and sample. In the present study, we used ~ 350 -fs electron pulses containing $\sim 10^4$ electrons with a kinetic energy of 55 keV, and focused to a 150- μm spot. The experimental conditions have sufficient electrons per pulse to ensure good enough signal-to-noise ratio in a few shots per time delay. The electron pulse duration was characterized using a recently developed electron/laser-pulse cross-correlation method based on ponderomotive scattering²¹. Photoinduced changes in Bi were initiated using 775-nm, 200-fs pump pulses focused to 500 μm . The spatial overlap between the electron beam (z direction) and the pump beam at the sample position was ensured within 20 μm (x and y directions). A centring window located at the sample plane was used for this purpose and the electron beam transmission and pump beam reflection were monitored as a function of x (or y). Taking the duration of the optical pump pulse into account, the overall instrumental response was ~ 400 fs (full width at half maximum). The tip-tilt of the sample plane was characterized using optical methods, ensuring a temporal mismatch between pump and probe of < 50 fs over the whole sample area. The measurements carried out below the damage threshold were performed at a frequency of 500 Hz and the laser excited area was found to reach the initial room temperature within the 2 ms between laser shots. Control studies with just the electron beam showed no detectable change in the sample for periods of days.

Sample preparation. The Bi films were grown epitaxially in a dedicated, ultra-high-vacuum deposition system. Film thickness was monitored *in situ* with a quartz rate monitor that was calibrated *ex situ* using atomic force microscopy. The 30-nm-thick, crystalline Bi films were grown on two different substrates, NaCl and carbon-coated mica. After growth, the films were floated off the substrate at a water–air interface and were then picked up with an optically flat silicon mesh. The film grown on salt (sample 1) provided a [111]-oriented sample with two main grain domains rotated by 90° relative to each other. Diffraction from this film showed the expected 12-fold symmetry^{22,23} as a consequence of the hexagonal crystalline symmetry around the $\langle 111 \rangle$ axis. The film grown on carbon-coated mica (sample 2) had the same main grain orientation; however, it showed a ring feature in the diffraction patterns, reflecting a higher grain dislocation around the $\langle 111 \rangle$ rotational axis. Apart from these differences, both samples showed, as expected, the same order-to-disorder dynamics upon photoexcitation.

Calculation of the fraction of excited carriers. The fraction of excited valence electrons was calculated as

$$\frac{N_{\text{val}}^{\text{exc}}}{N_{\text{val}}^{\text{tot}}} = \frac{N_{\text{ph}}^{\text{abs}}}{5N_{\text{at}}} = \frac{C_1 \Delta T_1}{5h\nu} = 3.3 \times 10^{-5} \Delta T_1 = 6.1 \times 10^{-3} F$$

where ΔT_1 is measured in kelvin and F is measured in millijoules per square centimetre. Here $N_{\text{ph}}^{\text{abs}}$ is the number of absorbed photons, N_{at} is the number of atomic sites in the excitation volume, $N_{\text{val}}^{\text{exc}}$ is the number of excited carriers and $N_{\text{val}}^{\text{tot}}$ is the total number of valence carriers; C_1 is the heat capacity of solid Bi ($25.52 \text{ J mol}^{-1} \text{ K}^{-1}$); $h\nu$ is the photon energy ($1.54 \times 10^5 \text{ J mol}^{-1}$); and F is the incident fluence. The formula takes into account the fact that there are five valence electrons per atomic site and the fact that $N_{\text{ph}}^{\text{abs}}$ equals $N_{\text{val}}^{\text{exc}}$. The relation between ΔT_1 and F was obtained from the slope of the plot in Fig. 1e. This equation was derived from energy conservation, assuming that, after photon absorption, radiative processes are negligible in comparison with non-radiative ones, which is a fair approximation considering the small band gap of Bi.

LETTERS

Temperature-induced A–B intersite charge transfer in an A-site-ordered $\text{LaCu}_3\text{Fe}_4\text{O}_{12}$ perovskite

Y. W. Long¹, N. Hayashi², T. Saito¹, M. Azuma¹, S. Muranaka² & Y. Shimakawa¹

Changes of valence states in transition-metal oxides often cause significant changes in their structural and physical properties^{1,2}. Chemical doping is the conventional way of modulating these valence states. In ABO_3 perovskite and/or perovskite-like oxides, chemical doping at the A site can introduce holes or electrons at the B site, giving rise to exotic physical properties like high-transition-temperature superconductivity and colossal magnetoresistance^{3,4}. When valence-variable transition metals at two different atomic sites are involved simultaneously, we expect to be able to induce charge transfer—and, hence, valence changes—by using a small external stimulus rather than by introducing a doping element. Materials showing this type of charge transfer are very rare, however, and such externally induced valence changes have been observed only under extreme conditions like high pressure^{5,6}. Here we report unusual temperature-induced valence changes at the A and B sites in the A-site-ordered double perovskite $\text{LaCu}_3\text{Fe}_4\text{O}_{12}$; the underlying intersite charge transfer is accompanied by considerable changes in the material's structural, magnetic and transport properties. When cooled, the compound shows a first-order, reversible transition at 393 K from $\text{LaCu}^{2+}_3\text{Fe}^{3.75+}_4\text{O}_{12}$ with $\text{Fe}^{3.75+}$ ions at the B site to $\text{LaCu}^{3+}_3\text{Fe}^{3+}_4\text{O}_{12}$ with rare Cu^{3+} ions at the A site. Intersite charge transfer between the A-site Cu and B-site Fe ions leads to paramagnetism-to-antiferromagnetism and metal-to-insulator isostructural phase transitions. What is more interesting in relation to technological applications is that this above-room-temperature transition is associated with a large negative thermal expansion.

A-site-ordered double perovskites with the general chemical formula $\text{A}'\text{A}_3\text{B}_4\text{O}_{12}$ have received much attention owing to their special ordered structures and wide variety of physical properties such as colossal magnetoresistance under weak fields, giant dielectric constant over a wide temperature range and ferrimagnetic transitions above room temperature^{7–12}. As shown in Fig. 1, these compounds crystallize with an $\text{Im}\bar{3}$ cubic lattice in which the A'- and A-site cations are at the originally 12-fold-coordinated A site in a simple ABO_3 perovskite. Because of the special cation ordering and the heavy tilting of corner-sharing BO_6 octahedra, high pressure is often needed to stabilize the $\text{A}'\text{A}_3\text{B}_4\text{O}_{12}$ perovskite structure. Unlike the A site in the simple ABO_3 perovskite, the A site in $\text{A}'\text{A}_3\text{B}_4\text{O}_{12}$ accommodates transition-metal ions like Jahn–Teller-distorted Cu^{2+} and Mn^{3+} . Owing to the presence of valence-variable transition-metal ions at both the A site and the B site, $\text{A}'\text{A}_3\text{B}_4\text{O}_{12}$ perovskites provide opportunities to study the unusual A–B intersite charge transfer and resultant changes in structural and physical properties.

$\text{LaCu}_3\text{Fe}_4\text{O}_{12}$ prepared at 10 GPa and 1,400 K crystallized as an A-site-ordered double perovskite in which all of the A' and A sites are respectively occupied by La and Cu ions. (See the high-resolution

synchrotron X-ray diffraction (SXRD) pattern at 300 K and the corresponding Rietveld-analysis result in Supplementary Fig. 1.) The oxygen content was proved to be stoichiometric from thermogravimetry (Supplementary Fig. 2). By analogy with other A-site-ordered perovskites like $\text{La/Bi}^{3+}\text{Cu}^{2+}_3(\text{Mn}^{3+}\text{Mn}^{4+}_3)\text{O}_{12}$ (refs 10, 13), the nominal composition with oxygen stoichiometry implies a simple ionic formula with a mixed valence at the B site: $\text{La}^{3+}\text{Cu}^{2+}_3(\text{Fe}^{3+}\text{Fe}^{4+}_3)\text{O}_{12}$. Bond-valence sum¹⁴ calculations from the result of structure refinement with SXRD data (Supplementary Table 1), however, give valences of +2.90 for Cu ions and +3.05 for Fe ions (Supplementary Table 2). Furthermore, the ^{57}Fe Mössbauer spectrum at room temperature confirms the Fe^{3+} state with a high-spin configuration ($S = 5/2$) as shown in Fig. 2a, where a magnetic sextuplet is seen and the isomer shift of 0.34 mm s^{-1} relative to $\alpha\text{-Fe}$ is a typical value for an Fe^{3+} ion in octahedral coordination^{15,16}. These results strongly suggest a charge combination of $\text{La}^{3+}\text{Cu}^{3+}_3\text{Fe}^{3+}_4\text{O}_{12}$ at room temperature. We note that the instability of Cu^{3+} ions makes Cu oxides with Cu^{3+} very rare, and it is the high-pressure synthesis of the present compound that stabilizes this unusual high-oxidation state of Cu.

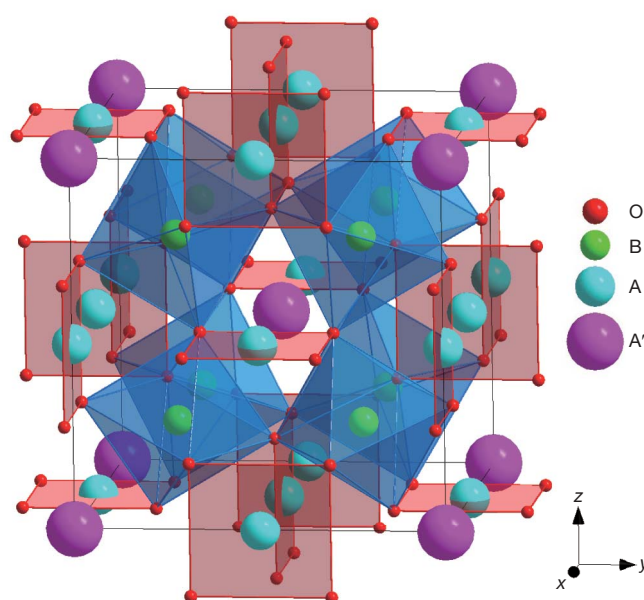


Figure 1 | Crystal structure of the A-site-ordered $\text{A}'\text{A}_3\text{B}_4\text{O}_{12}$ double perovskite. The space group is $\text{Im}\bar{3}$, and the atomic positions are $2a(0, 0, 0)$, for A'; $6b(0, 0.5, 0.5)$, for A; $8c(0.25, 0.25, 0.25)$, for B and $24g(x, y, 0)$, for O. The A-site ions make square-planar coordinated and isolated AO_4 units and the B-site ions form corner-sharing BO_6 octahedra.

¹Institute for Chemical Research, Kyoto University, Uji, Kyoto 611-0011, Japan. ²Graduate School of Human and Environmental Studies, Kyoto University, Sakyo, Kyoto 606-8501, Japan.

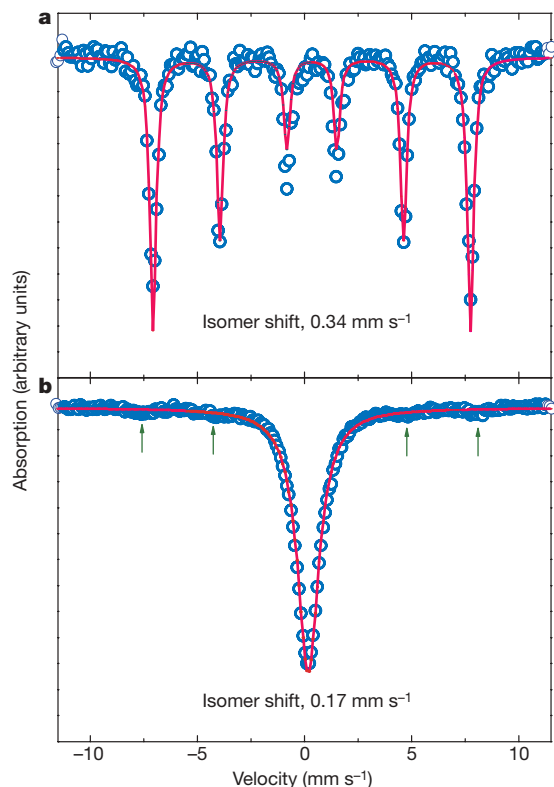


Figure 2 | Temperature dependence of Mössbauer data. **a**, Mössbauer spectrum at room temperature (298 K). **b**, Mössbauer spectrum at 423 K. The solid curves are the fits. The spectrum from a small amount of $\alpha\text{-Fe}_2\text{O}_3$ impurity is marked with arrows.

With increasing temperature, the X-ray diffraction patterns of $\text{LaCu}_3\text{Fe}_4\text{O}_{12}$ show the gradual shifts expected from the lattice expansion, but between 373 and 423 K there is an anomalous jump to a larger angle (Fig. 3a). As can be seen in Fig. 3b, the unit-cell volume of $\text{LaCu}_3\text{Fe}_4\text{O}_{12}$ abruptly decreases by $\sim 1.0\%$ around 400 K, which is consistent with the temperature, $T_c = 393$ K, at which a sharp peak was observed in a differential thermal analysis measurement (Supplementary Fig. 2). Because no symmetrical change is discernable, the anomaly at 393 K should be a first-order isostructural phase transition. Moreover, our SXRD measurements confirmed that this transition was completely reversible.

Despite the absence of symmetrical variation in the crystal structure, analysis of the structure of the high-temperature phase revealed notable changes in the bond lengths of both Cu–O in the A-site squares and Fe–O in the B-site octahedra (Supplementary Table 1). The bond-valence sum calculations give valences of $+2.06$ for the Cu ions and $+3.44$ for the Fe ions in the high-temperature phase (Supplementary Table 2). In addition, the Mössbauer spectrum at 423 K (Fig. 2b) is very different from that at room temperature. A singlet with an isomer shift of $\sim 0.17 \text{ mm s}^{-1}$ suggests an unusual high-oxidation state for Fe ions. Because the typical isomer shifts for Fe^{3+} and Fe^{4+} in octahedral coordination are respectively ~ 0.35 and 0.07 mm s^{-1} (refs 15–18), the observed isomer shift at 423 K implies that the Fe ions in the present compound are in a valence state intermediate between Fe^{3+} and Fe^{4+} . These results indicate, on the basis of a simple ionic valence calculation, that the high-temperature phase should be $\text{La}^{3+}\text{Cu}^{2+}_3\text{Fe}^{3.75+}_4\text{O}_{12}$. The charge combination above T_c is therefore the same as that of the A-site-ordered perovskites $\text{La}^{3+}\text{Cu}^{2+}_3\text{Mn}^{3.75+}_4\text{O}_{12}$ and $\text{Bi}^{3+}\text{Cu}^{2+}_3\text{Mn}^{3.75+}_4\text{O}_{12}$ (refs 10, 13).

These results strongly suggest that at $T_c = 393$ K there is an unusual charge transfer between the A-site Cu ions and the B-site Fe ions. Simultaneous valence changes ($3\text{Cu}^{2+} - 3e^- \rightarrow 3\text{Cu}^{3+}$ and $4\text{Fe}^{3.75+} + 3e^- \rightarrow 4\text{Fe}^{3+}$) lead to the isomorphous phase transition from

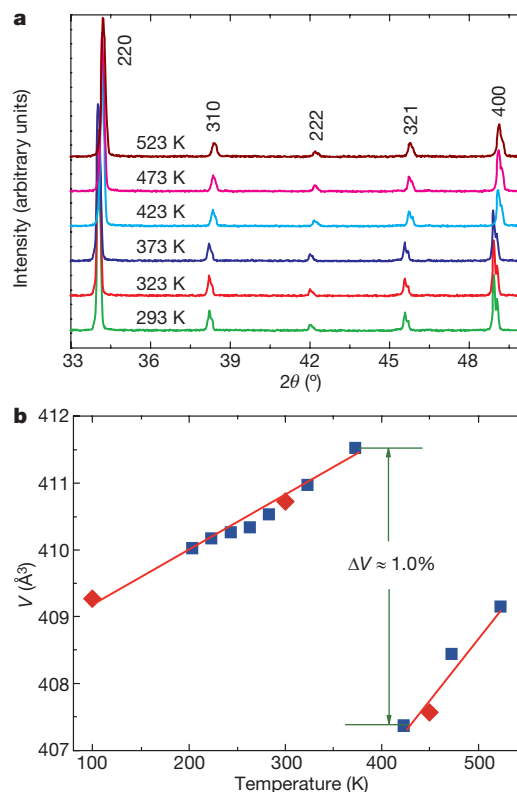


Figure 3 | Anomalous changes in structural data. **a**, Changes in X-ray diffraction patterns with the isostructural phase transition between 373 and 423 K. 2θ , diffraction angle. **b**, Temperature dependence of unit-cell volume, V . The solid lines are guides for the eye. The error bars for the V are smaller than the symbols. The data were obtained from Cu $K\alpha$ X-ray diffraction (squares) and SXRD (diamonds).

the high-temperature $\text{LaCu}^{2+}_3\text{Fe}^{3.75+}_4\text{O}_{12}$ to the low-temperature $\text{LaCu}^{3+}_3\text{Fe}^{3+}_4\text{O}_{12}$. The unusually high $\text{Fe}^{3.75+}$ state instability at low temperature is thus resolved by the A–B intersite charge transfer. This charge transfer contrasts sharply with the charge disproportionation from Fe^{4+} to Fe^{3+} and Fe^{5+} ($2\text{Fe}^{4+} \rightarrow \text{Fe}^{3+} + \text{Fe}^{5+}$) found in an isostructural double perovskite, $\text{CaCu}^{2+}_3\text{Fe}^{4+}_4\text{O}_{12}$ (ref 19), and a simple perovskite, $\text{CaFe}^{4+}\text{O}_3$ (ref. 18). In those compounds, the unusual high-valence state Fe^{4+} is stabilized by the disproportionation of charges accompanying a rock-salt-type ordered arrangement of aliovalent species in the ground states. A similar charge disproportionation has been observed even in $\text{Sr}_{1-x}\text{La}_x\text{FeO}_3$ ($x \approx 0.1\text{--}0.6$) with an intermediate-valence high-oxidation state Fe (ref. 20). In the present compound, $\text{LaCu}_3\text{Fe}_4\text{O}_{12}$, however, both the X-ray diffraction and Mössbauer spectra confirm the absence of charge disproportionation at temperatures down to 4.2 K. It is interesting that the replacement of the A'-site cation—that is, the substitution of La^{3+} for Ca^{2+} in $\text{CaCu}_3\text{Fe}_4\text{O}_{12}$, which corresponds to substitution at only one-quarter of the A sites in a simple perovskite—leads to the completely different ground state. Again, Cu^{3+} with the square-planar coordination of oxygen ions seldom exists, and this unusual ground state should be stabilized by the special A-site-ordered perovskite structure.

The ilmenite FeTiO_3 and the perovskite BiNiO_3 are two rare compounds that exhibit an intersite charge transfer, but only under high pressure. The pressure-induced charge transfer in the former is indicated by an irreversible change in $\text{Fe}^{3+}/\text{Fe}^{2+}$ ratio from ~ 0.2 to 0.45 (ref. 5). The unusually charge-disproportionated $\text{Bi}^{3+}_{0.5}\text{Bi}^{5+}_{0.5}\text{Ni}^{2+}\text{O}_3$ changes to $\text{Bi}^{3+}\text{Ni}^{3+}\text{O}_3$ at around 4 GPa as a result of the charge transfer from Bi^{5+} to Ni^{2+} , which is accompanied by a structural transition from triclinic to monoclinic⁶. The present A–B intersite charge transfer, by contrast, occurs when temperature changes at ambient pressure and does not change the crystal symmetry. Both $\text{Fe}^{3.75+}$ and Cu^{3+} are in

unusually high-valence states that are stabilized by the special ordered crystal structure. Their energy levels should be comparable, and the delicate balance between the two states can be modified by changing temperature. In the A-site-ordered perovskite structure, all oxygen atoms are shared by the FeO_6 octahedra and CuO_4 square-planar units. If the unusual $\text{Fe}^{3.75+}$ ($d^{4.25}$) and Cu^{3+} (d^8) high-oxidation states are respectively considered $d^5(\text{Fe}^{3+})\bar{L}^{0.75}$ and $d^9(\text{Cu}^{2+})\bar{L}$ with ligand holes \bar{L} (ref. 21), the simultaneous valence change should be mediated by 'double charge transfers' between the Fe ions and the O ions and between the Cu ions and the O ions. Thus, the orbital hybridization and correlation effects play a key role in the A–B intersite charge transfer.

The intersite charge transfer gives rise to significant changes in magnetic and transport properties. As seen in Fig. 4a in the temperature dependence of the isomer shift and hyperfine field obtained from the Mössbauer spectrum data, the isomer shift of $\sim 0.17 \text{ mm s}^{-1}$ for high-temperature $\text{LaCu}_{2+3}\text{Fe}^{3.75+}_4\text{O}_{12}$ abruptly changes to $\sim 0.30 \text{ mm s}^{-1}$ at T_c . Correspondingly, a magnetic splitting appears in the Mössbauer spectrum and the hyperfine field increases to $\sim 40 \text{ T}$. These results suggest that for $T < T_c$ there is a magnetic-ordered state due to the Fe^{3+} magnetic species produced by the A–B intersite charge transfer. As shown in the inset of Fig. 4b, the observed linear relationship between magnetization and magnetic field

indicates antiferromagnetic ordering below T_c , and a decrease in susceptibility at T_c is consistent with the change from a paramagnetic state to an antiferromagnetic state (Fig. 4b). In the antiferromagnetic $\text{LaCu}_{2+3}\text{Fe}^{3+}_4\text{O}_{12}$, Cu^{3+} ions with square-planar coordination are non-magnetic because of the considerable energy splitting between $d_{3z^2-r^2}$ and $d_{x^2-y^2}$ orbitals, as seen in $\text{MCu}^{3+}\text{O}_2$ (M, alkaline metal), and they do not contribute to the magnetic properties^{22,23}. The magnetic ordering is therefore ascribed to the B-site $\text{Fe}^{3+}\text{O}\text{--}\text{Fe}^{3+}$ antiferromagnetic superexchange interactions. This is completely different from the B-site $\text{Fe}^{3+}\text{O}\text{--}\text{Fe}^{5+}$ ferromagnetic coupling in the charge-disproportionated $\text{CaCu}_3(\text{Fe}^{3+}_2\text{Fe}^{5+}_2)\text{O}_{12}$ (ref. 19).

As seen from the temperature dependence of normalized resistivity (Fig. 4c), the A–B intersite charge transfer also causes a metal-to-insulator transition. The thermal hysteresis and the jump in the resistivity are consistent with the first-order nature of the transition, as shown by the large change in cell volume. Because of the spatial isolation of CuO_4 units (Fig. 1), the electronic configuration of Fe ions dominates the conductivity behaviour. In the high-temperature paramagnetic $\text{LaCu}_{2+3}\text{Fe}^{3.75+}_4\text{O}_{12}$ phase, the intermediate valence state of Fe ($d^5\bar{L}^{0.75}$) makes the material metallic. In the antiferromagnetic $\text{LaCu}_{2+3}\text{Fe}^{3+}_4\text{O}_{12}$ phase, by contrast, a high-resistivity insulating state appears and, as shown in the inset of Fig. 4c, the temperature dependence of resistivity is well fitted by a three-dimensional variable-range hopping model. We emphasize that the observed metal-to-insulator transition caused by the A–B intersite charge transfer in $\text{LaCu}_3\text{Fe}_4\text{O}_{12}$ is essentially different from the resistivity changes induced by the charge disproportionation in the isostructural $\text{CaCu}_3\text{Fe}_4\text{O}_{12}$ and the charge ordering in the isostructural $(\text{NaMn}^{3+}_3)(\text{Mn}^{3+}_2\text{Mn}^{4+}_2)\text{O}_{12}$ (refs 19, 24).

We point out that the isotropic volume contraction by as much as $\sim 1.0\%$ that occurs at T_c as temperature increases is a negative thermal expansion (NTE) like that reported in antiperovskite manganese nitrides^{25,26}. Materials showing NTE are technologically important, but only a very small number of such materials are known²⁷. Furthermore, a characteristic feature of the present charge-transfer-induced NTE in the cubic $\text{LaCu}_3\text{Fe}_4\text{O}_{12}$ is that it is associated with simultaneous transitions in magnetic and electric properties. This implies that the NTE could be controlled by external stimuli such as magnetic field and electric current above room temperature, which would be useful for applications such as elasticity-tuned sensors and switching devices.

METHODS SUMMARY

$\text{LaCu}_3\text{Fe}_4\text{O}_{12}$ was prepared at 10 GPa and 1,400 K with a cubic-anvil-type high-pressure apparatus. The starting materials were La_2O_3 , CuO and Fe_2O_3 , and KClO_4 was used as an oxidizing agent. The residual KCl and a small amount of impurities were washed out using a dilute acid solution. The $\text{LaCu}_3\text{Fe}_4\text{O}_{12}$ structure was studied by X-ray diffraction with $\text{Cu K}\alpha$ radiation and high-resolution SXRD at beamline BL02B2 at Japan's SPring-8 synchrotron facility (wavelength, $\lambda = 0.77747 \text{ \AA}$). The GSAS program was used to refine the structural parameters²⁸. ^{57}Fe Mössbauer spectra were obtained using a $^{57}\text{Co}/\text{Rh}$ source and a control absorber consisting of $\alpha\text{-Fe}$. The susceptibility and magnetization data were collected with a superconducting quantum interference device magnetometer, and the resistance was measured using a conventional method.

Full Methods and any associated references are available in the online version of the paper at www.nature.com/nature.

Received 17 November 2008; accepted 22 January 2009.

- Imada, M., Fujimori, A. & Tokura, Y. Metal-insulator transitions. *Rev. Mod. Phys.* **70**, 1039–1263 (1998).
- Goto, T. & Luthi, B. Charge ordering, charge fluctuations and lattice effects in strongly correlated electron systems. *Adv. Phys.* **52**, 67–118 (2003).
- Lee, P. A., Nagaosa, N. & Wen, X. G. Doping a Mott insulator: physics of high-temperature superconductivity. *Rev. Mod. Phys.* **78**, 17–85 (2006).
- Salamon, M. B. & Jaime, M. The physics of manganites: structure and transport. *Rev. Mod. Phys.* **73**, 583–628 (2001).
- Seda, T. & Hearne, G. R. Pressure induced $\text{Fe}^{2+} + \text{Ti}^{4+} \rightarrow \text{Fe}^{3+} + \text{Ti}^{3+}$ intervalence charge transfer and the $\text{Fe}^{3+}/\text{Fe}^{2+}$ ratio in natural ilmenite (FeTiO_3) minerals. *J. Phys. Condens. Matter* **16**, 2707–2718 (2004).

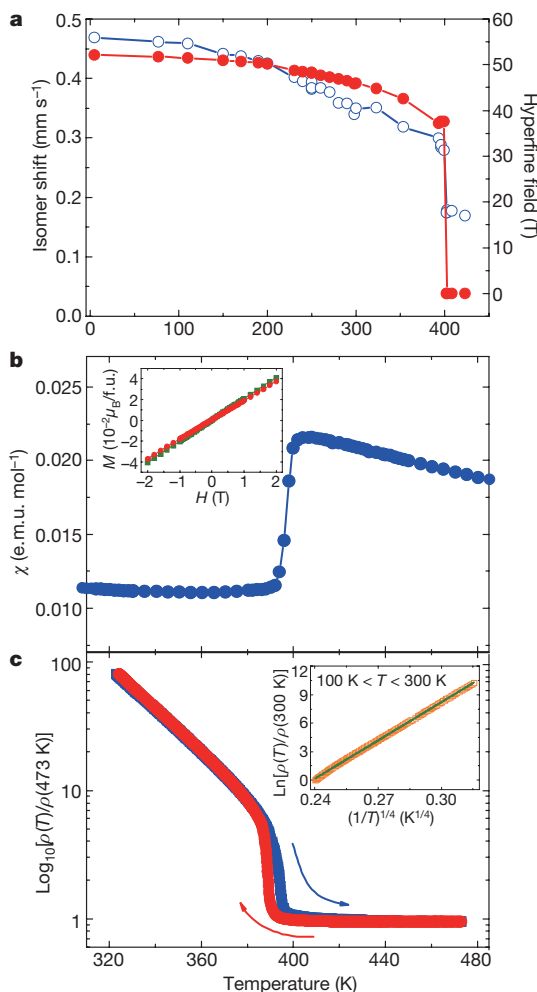


Figure 4 | Temperature dependence of isomer shift and hyperfine field, susceptibility (χ) and normalized resistivity. **a**, The isomer shift (blue) and hyperfine field (red) obtained from the Mössbauer data. **b**, Magnetic susceptibility measured at a magnetic field of $H = 0.1 \text{ T}$. The inset shows magnetization (M) behaviour at 300 K (circles) and 200 K (squares). $\mu_B/\text{f.u.}$, Bohr magnetons per formula unit. **c**, Normalized resistivity (ρ). The inset shows the result of fitting to a three-dimensional variable-range hopping model with the formula $\rho(T) = \rho_0 \exp(T_0/T)^{1/4}$.

6. Azuma, M. *et al.* Pressure-induced intermetallic valence transition in BiNiO_3 . *J. Am. Chem. Soc.* **129**, 14433–14436 (2007).
7. Zeng, Z., Greenblatt, M., Subramanian, M. A. & Croft, M. Large low-field magnetoresistance in perovskite-type $\text{CaCu}_3\text{Mn}_4\text{O}_{12}$ without double exchange. *Phys. Rev. Lett.* **82**, 3164–3167 (1999).
8. Subramanian, M. A., Li, D., Duan, N., Reisner, B. A. & Sleight, A. W. High dielectric constant in $\text{ACu}_3\text{Ti}_4\text{O}_{12}$ and $\text{ACu}_3\text{Ti}_3\text{FeO}_{12}$ phases. *J. Solid State Chem.* **151**, 323–325 (2000).
9. Homes, C. C., Vogt, T., Shapiro, S. M., Wakimoto, S. & Ramirez, A. P. Optical response of high-dielectric-constant perovskite-related oxide. *Science* **293**, 673–676 (2001).
10. Takata, K. *et al.* Magnetoresistance and electronic structure of the half-metallic ferrimagnet $\text{BiCu}_3\text{Mn}_4\text{O}_{12}$. *Phys. Rev. B* **76**, 024429 (2007).
11. Sánchez-Benítez, J. *et al.* Preparation, crystal and magnetic structure, and magnetotransport properties of the double perovskite $\text{CaCu}_{2.5}\text{Mn}_{4.5}\text{O}_{12}$. *Chem. Mater.* **15**, 2193–2200 (2003).
12. Shimakawa, Y. A-site-ordered perovskites with intriguing physical properties. *Inorg. Chem.* **47**, 8562–8570 (2008).
13. Alonso, J. A. *et al.* Enhanced magnetoresistance in the complex perovskite $\text{LaCu}_3\text{Mn}_4\text{O}_{12}$. *Appl. Phys. Lett.* **83**, 2623–2625 (2003).
14. Brown, I. D. & Altermatt, D. Bond-valence parameters obtained from a systematic analysis of the Inorganic Crystal Structure Database. *Acta Crystallogr. B* **41**, 244–247 (1985).
15. Li, X. *et al.* Mössbauer spectroscopic study on nanocrystalline LaFeO_3 materials. *Hyperfine Interact.* **69**, 851–854 (1991).
16. Blaaup, C. & van der Woude, F. Magnetic and structural properties of BiFeO_3 . *J. Phys. Chem.* **6**, 1422–1431 (1973).
17. Kawasaki, S., Takano, M. & Takeda, Y. Ferromagnetic properties of $\text{SrFe}_{1-x}\text{Co}_x\text{O}_3$ synthesized under high pressure. *J. Solid State Chem.* **121**, 174–180 (1996).
18. Takano, M. *et al.* Charge disproportionation in CaFeO_3 studied with the Mössbauer effect. *Mater. Res. Bull.* **12**, 923–928 (1977).
19. Yamada, I. *et al.* A perovskite containing quadrivalent iron as a charge-disproportionated ferrimagnet. *Angew. Chem. Int. Ed.* **47**, 7032–7035 (2008).
20. Takano, M., Kawachi, J., Nakanishi, N. & Takeda, Y. Valence state of the Fe ions in $\text{Sr}_{1-x}\text{La}_x\text{FeO}_3$. *J. Solid State Chem.* **39**, 75–84 (1981).
21. Bocquet, A. E. *et al.* Electronic structure of $\text{SrFe}^{4+}\text{O}_3$ and related Fe perovskite oxides. *Phys. Rev. B* **45**, 1561–1570 (1992).
22. Riesemeier, H., Gärtner, S., Lüders, K., Schmalz, M. & Schöllhorn, R. Susceptibility and NQR investigations on NaCuO_2 . *J. Phys. Chem. Solids* **55**, 613–615 (1994).
23. Imai, K. *et al.* Preparation, crystal structure, and magnetic property of a new compound LiCuO_2 . *J. Phys. Soc. Jpn* **61**, 1819–1820 (1992).
24. Prodi, A. *et al.* Charge, orbital and spin ordering phenomena in the mixed valence manganite $(\text{NaMn}^{3+}_3)(\text{Mn}^{3+}_2\text{Mn}^{4+}_2)\text{O}_{12}$. *Nature Mater.* **3**, 48–52 (2004).
25. Takenaka, K. & Takagi, H. Giant negative thermal expansion in Ge-doped antiperovskite manganese nitrides. *Appl. Phys. Lett.* **87**, 261902 (2005).
26. Takenaka, K., Asano, K., Misawa, M. & Takagi, H. Negative thermal expansion in Ge-free antiperovskite manganese nitrides: Tin-doping effect. *Appl. Phys. Lett.* **92**, 011927 (2008).
27. Sleight, A. W. Isotropic negative thermal expansion. *Annu. Rev. Mater. Sci.* **28**, 29–43 (1998).
28. Larson, A. C. & von Dreele, R. B. *General Structure Analysis System (GSAS)*. Report No. LAUR 86-748 (Los Alamos National Laboratory, 1994).

Supplementary Information is linked to the online version of the paper at www.nature.com/nature.

Acknowledgements We thank K. Nishimura and K. Oka for help with the high-pressure synthesis and magnetic measurements, and we thank K. Jungeun for help with the SXRD experiments. Thanks are also due to M. Takano for discussions. This work was partly supported by Grants-in-Aid for Scientific Research (19GS0207, 18350097, 17038014, 19014010 and 19340098), by the Global COE Program 'International Center for Integrated Research and Advanced Education in Materials Science' and by a grant for the Joint Project of Chemical Synthesis Core Research Institutions from the Ministry of Education, Culture, Sports, Science and Technology of Japan.

Author Contributions Y.W.L. and Y.S. designed the study; Y.W.L. synthesized the sample and performed X-ray diffraction, thermogravimetric, magnetic and electrical measurements with the help of M.A. and T.S.; N.H. carried out Mössbauer measurements with the help of S.M.; all of the authors discussed the results; and Y.W.L. and Y.S. wrote the manuscript.

Author Information Reprints and permissions information is available at www.nature.com/reprints. Correspondence and requests for materials should be addressed to Y.W.L. (ywlong@msk.kuicr.kyoto-u.ac.jp) or Y.S. (shimak@scl.kyoto-u.ac.jp).

METHODS

Raw oxide materials La_2O_3 , CuO and Fe_2O_3 in the mole ratio 1:6:4 were used to prepare the A-site-ordered perovskite $\text{LaCu}_3\text{Fe}_4\text{O}_{12}$. The mixture of the starting materials was put into a platinum capsule with an oxidizing agent (KClO_4) and was treated at 10 GPa and 1,400 K for 1 h with a cubic-anvil-type high-pressure apparatus. The residual KCl and a small amount of unreacted reagents were washed from the product using dilute acid.

The high-resolution SXRD was performed with the large Debye–Scherrer camera with an imaging plate detector installed at beamline BL02B2 at SPring-8. The powder sample was put into a glass capillary tube with an inner diameter of 0.1 mm and was rotated during the measurements. The wavelength used was 0.77747 Å. The SXRD data were collected at 100, 300 and 450 K in a 2θ range from 1° to 75° with a 0.01° resolution and were analysed by the Rietveld method using the GSAS software²⁸. Conventional X-ray diffraction was performed, using a Rigaku X-ray diffractometer, with $\text{Cu K}\alpha$ radiation (40 kV, 300 mA) at temperatures from 173 to 523 K to see changes in the lattice parameters and the phase transition.

Thermogravimetric measurements were made, using a Rigaku TG-DTA 8120 system, from room temperature to 1,200 K in air with a heating rate of 10 K min^{-1} . The oxide products of $\text{LaCu}_3\text{Fe}_4\text{O}_{12}$ decomposition were identified by X-ray diffraction. The ^{57}Fe Mössbauer spectra were obtained in transmission geometry using a $^{57}\text{Co/Rh}$ γ -ray source in combination with a constant-acceleration spectrometer. The source velocity was calibrated by using pure α -Fe. The obtained spectra were fitted by a least-squares method with Lorentzian functions. Magnetic susceptibility and magnetization were measured using a Quantum Design superconducting quantum interference device magnetometer in a zero-field cooling mode. The susceptibility measurements were made at 0.1 T in the temperature range from 5 to 500 K. The magnetization in the magnetic ordered state was measured at 200 and 300 K under field strengths between -2 and 2 T. The electrical resistance of the sample was measured using a conventional four-probe method. Thermal hysteresis of the resistance around the transition temperature was measured while heating and cooling at 0.5 K min^{-1} .

LETTERS

Shallow fault-zone dilatancy recovery after the 2003 Bam earthquake in Iran

Eric J. Fielding¹, Paul R. Lundgren¹, Roland Bürgmann² & Gareth J. Funning³

Earthquakes radiate from slip on discrete faults, but also commonly involve distributed deformation within a broader fault zone, especially near the surface. Variations in rock strain during an earthquake are caused by heterogeneity in the elastic stress before the earthquake, by variable material properties and geometry of the fault zones, and by dynamic processes during the rupture^{1,2}. Stress changes due to the earthquake slip, both dynamic and static, have long been thought to cause dilatancy in the fault zone that recovers after the earthquake^{3–5}. Decreases in the velocity of seismic waves passing through the fault zone due to coseismic dilatancy have been observed⁶ followed by postseismic seismic velocity increases during healing^{5,7,8}. Dilatancy and its recovery have not previously been observed geodetically. Here we use interferometric analysis of synthetic aperture radar images to measure postseismic surface deformation after the 2003 Bam, Iran, earthquake and show reversal of coseismic dilatancy in the shallow fault zone that causes subsidence of the surface. This compaction of the fault zone is directly above the patch of greatest coseismic slip at depth. The dilatancy and compaction probably reflects distributed shear and damage to the material during the earthquake that heals afterwards. Coseismic and postseismic deformation spread through a fault zone volume may resolve the paradox of shallow slip deficits for some strike-slip fault ruptures⁹.

Several seismic studies have found that the ratio of the velocities of S waves to P waves decreases with time after an earthquake, in addition to an overall velocity increase, reflecting a postseismic increase in the Poisson's ratio of fault zone material; this increase in Poisson's ratio is interpreted as an increase in the fraction of pore space filled with liquid^{6,7} as the fault zone contracts. These postseismic changes reverse the coseismic velocity changes due to dilatancy in the fault zone. Seismic waves are relatively insensitive to the depth of the anomalies, but the damaged fault zone may be confined to the top 3–4 km of the crust and possibly to very shallow (~200 m) depths⁸.

Fault zone dilatancy is caused by pervasive damage where small cracks open up within the deformed rocks, increasing the porosity and volume^{3–5}. It has been difficult to measure the predicted coseismic dilatancy and postseismic volume decrease in earthquake fault zones geodetically, because dilatancy occurs within a very narrow damage zone along the earthquake rupture and many other postseismic processes also cause deformation of the Earth's surface.

Geodetic measurements of far-reaching postseismic deformation for many large earthquakes have been modelled as a combination of viscous relaxation in the lower crust and upper mantle and with aseismic afterslip on a deep continuation of the fault that ruptured¹⁰. Postseismic deformation in the upper crust has been explained by pore-pressure transients^{11,12} and by afterslip both immediately surrounding coseismic slip patches and up-dip from the coseismic rupture^{13–15}, which can overwhelm the deformation from dilatancy

recovery. We exploit interferometric synthetic aperture radar (InSAR) to measure negative volume change in the fault zone after a large earthquake in Iran.

Here we analyse 3.5 years of postseismic deformation after the M_w (moment magnitude) 6.6 earthquake that devastated the city of Bam, Iran, on 26 December 2003, using synthetic aperture radar from the European Space Agency Envisat satellite. The earthquake primarily ruptured a buried strike-slip fault that extends under the city of Bam and beneath a broad alluvial plain to the south^{16–21}. This fault is part of a broad system of north–south oriented, right-lateral shear in eastern Iran¹⁹. Because the first synthetic aperture radar image was acquired 12 days after the earthquake, we cannot separate the earliest phase of postseismic deformation from the coseismic deformation. The stable surface around Bam provides optimal InSAR coherence¹⁸ for mapping deformation during and after the earthquake. The surface rupture from coherence and field mapping^{16,18} propagated from the south towards Bam¹⁹. Inversion of the surface deformation measured by InSAR^{9,17}, cross-correlation of optical imagery, and levelling data^{20,21} require slip >2 m at depths of 4–5 km on the main fault, with less near the surface and little slip north of Bam. Maximum offsets across the surface ruptures were 0.25 m (refs 16, 18, 19), but total shear across a zone about 1 km wide is >1 m (refs 17, 21). A less pronounced shallow slip deficit has also been found for some other large strike-slip earthquakes⁹. We concentrate on surface displacement features with spatial scales less than 10 km that can resolve deformation in roughly the upper 8 km of the crust, because atmospheric effects mask InSAR signals at larger scales²².

Two features stand out in the postseismic deformation, with different spatial scales and temporal behaviour. We examine the hypotheses that these are caused by (1) afterslip, (2) localized poroelastic rebound at a restraining bend of the coseismic rupture, and (3) localized compaction of material that dilated during the earthquake. The first major feature in the postseismic pattern is two lobes of line-of-sight (LOS) change near the south end of the main coseismic rupture with positive LOS motion (towards the satellite locations) to the east of the rupture (A1 and A2 on Fig. 1 and Supplementary Fig. 5) and alternating zones of positive and negative LOS motion that have much lower amplitude, but similar spatial extent, about 10 km further north. The descending track (no. 120) is dominated by strong positive LOS motion (towards the satellite locations) to the southeast of the rupture (A1), whereas the ascending tracks (nos 156 and 385) have a smaller area of positive amplitude to the east combined with negative LOS motion to the west (A2), requiring a substantial eastward component of displacement. The combination of these features is consistent with afterslip above and to the south of the main coseismic asperity that ruptured during the 2003 earthquake. The time series shows that the afterslip rate decayed with a time constant of ~335 days if an exponential time function is assumed (Fig. 2a).

¹Jet Propulsion Laboratory, California Institute of Technology, 4800 Oak Grove Drive, Pasadena, California 91109, USA. ²Department of Earth and Planetary Science, University of California, Berkeley, California 94720, USA. ³Department of Earth Sciences, University of California, Riverside, California 92521, USA.

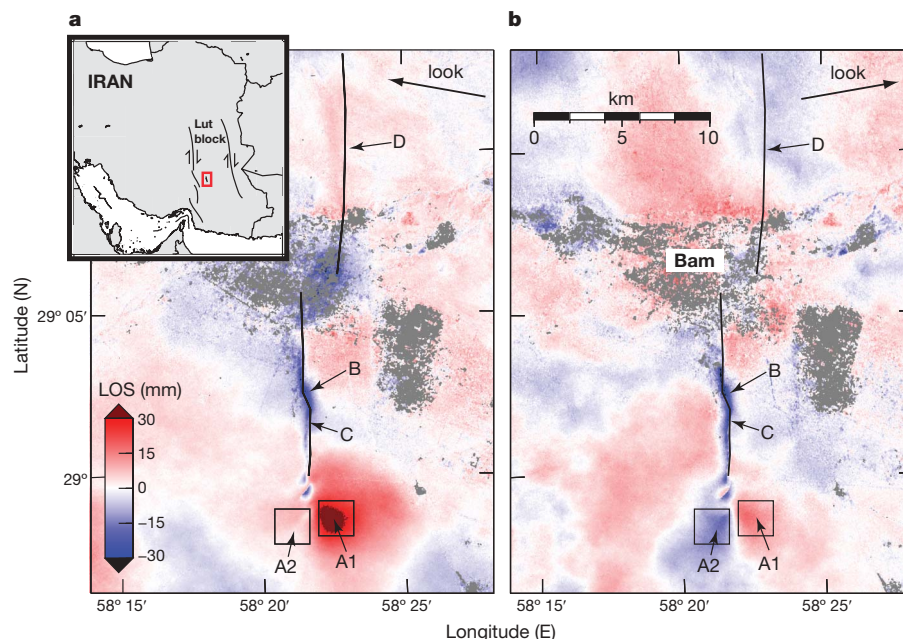
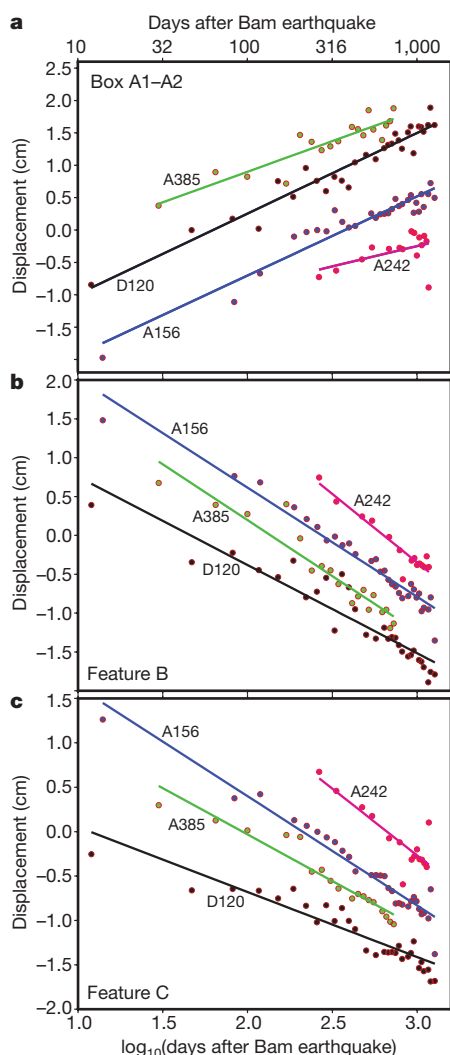


Figure 1 | Postseismic surface deformation after the Bam, Iran, earthquake. **a, b,** Maps from two Envisat tracks in radar lines-of-sight (LOS); fits to each time series have been converted to estimates of total displacement between 12 and 1,097 days after the 26 December 2003 earthquake. Black lines, locations of coseismic fault ruptures mapped from

InSAR¹⁸. Difference of boxes A1 and A2, used for Fig. 2a, measures afterslip at 2–3 km depth. Subsidence at B is poroelastic and at C is recovery of dilatancy. D is minor uplift on northern fault. **a,** Descending track no. 120. **b,** Ascending track no. 156. Horizontal components of look vectors shown with arrows. Inset, location of Bam in southeast Iran.



Second, the spatial pattern (see Fig. 1) includes a narrow zone of >20 mm subsidence combined with horizontal motion towards the coseismic surface ruptures observed south of the city of Bam^{16,18}. Subsidence is strongest near a left bend of the right-lateral fault (feature B in Fig. 1) and continues along a roughly 500-m-wide zone north and south of the bend (feature C). This zone continued to subside for at least 3.5 years after the earthquake (Fig. 2b, c). We advocate that this subsidence has both poroelastic (feature B) and dilatancy recovery (feature C) components.

Readjustment of pore fluid pressure (poroelastic rebound) in the crust can cause volume changes following earthquakes, resulting in postseismic subsidence over areas of coseismic pressure increase and vice versa. The widest and strongest subsidence south of Bam is where the left bend caused compression (feature B on Figs 1 and 3) and coseismic uplift of at least 60 mm (Supplementary Fig. 6). A large part of the postseismic subsidence there is probably due to a poroelastic response reflecting partial deflation of the coseismic uplift due to fluid flow away from the compressed fault bend. Early relaxation in the first 12 days after the earthquake is included in the coseismic interferogram and cannot be measured. The Bam fault-bend subsidence has a nearly log-linear rate out to the end of the 3.5 years we analysed; the relaxation time for an exponential decay fit is 1.7 years.

The postseismic subsidence along the rupture zone south of Bam, however, extends >2 km to the north and >4 km south of the left bend in the fault (C in Fig. 3); this requires another process in addition to poroelastic rebound in the restraining bend, as the rest of the zone experienced no measurable coseismic compression. To the south of the bend, the surface ruptures mapped in the field^{16,18}

Figure 2 | Postseismic deformation of features as function of time. **a,** Time series of difference between range change of boxes A1 and A2 (see Fig. 1) plotted versus the logarithm of the time in days since the earthquake, for four Envisat tracks. Lines show least squares fits with the $\log(t)$ function; line colour is keyed to data. Prefixes A and D denote respectively ascending and descending tracks. **b,** Subsidence in fault bend due to poroelastic rebound from difference between polygon B and boxes to east and west (see Fig. 3). **c,** Subsidence south of fault bend (difference between polygon C and two adjacent boxes, see Fig. 3) interpreted as recovery of coseismic dilatancy in the shallow fault zone.

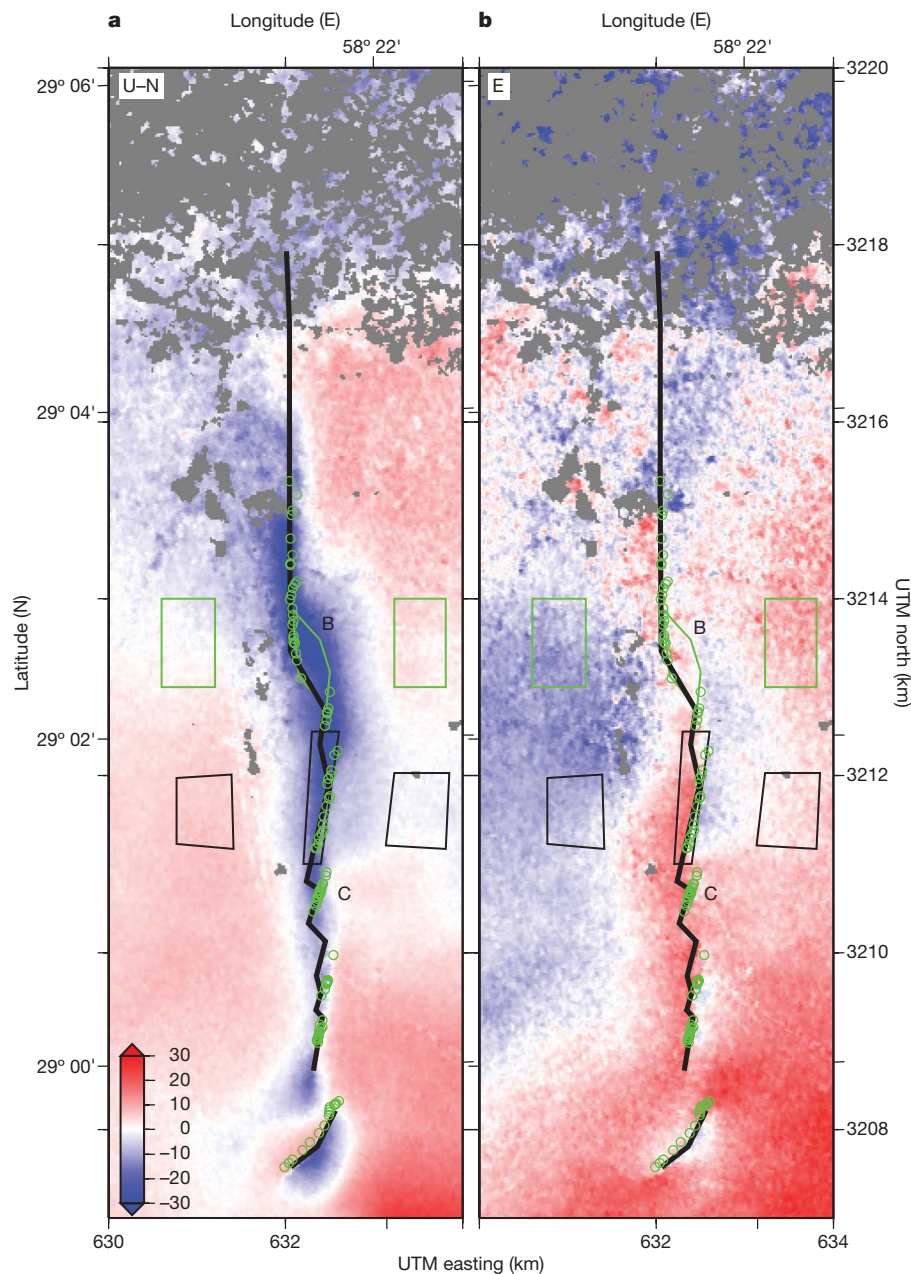


Figure 3 | Transformed components of total displacement from tracks 120 and 156. **a, b,** Components in mm (colour scale) for the area of the main coseismic rupture south of Bam, showing the narrow zone of subsidence along the fault: **a**, 'up' minus $0.1 \times$ 'north' ($U - N$); **b**, 'east' (E). Black lines, locations of coseismic rupture from InSAR; green circles, locations of

coseismic rupture mapped in the field¹⁸. Boxes B and C used for time series plots of Fig. 2b and c, respectively. On left, labelled and unlabelled tickmarks show respectively latitude and UTM (universal transverse Mercator projection, zone 40) north; and vice versa for tickmarks on right.

included a small opening component, indicating east–west coseismic expansion in the surface layer, which is also reflected in the coseismic InSAR^{17,18}. The postseismic InSAR shows that there is a net motion of the surface on both sides of the fault towards the fault south of the bend (see Fig. 3b), which suggests that there was coseismic dilation or damage in the fault zone that subsequently relaxed. The material that compacted after the earthquake apparently did not have enough fluid flowing inward to fill the dilated pore space created during the earthquake to counteract the compaction and subsidence. There is no indication of dilatancy recovery along the rupture segment north of Bam (feature D in Fig. 1), where a small amount of postseismic uplift indicates different material properties or stress conditions of the shallow fault zone.

To explore the processes and kinematics of the postseismic transients that cause the surface deformation features, we utilize elastic

half-space dislocation models. We model the afterslip using the two planar faults of the coseismic model: a near-vertical right-lateral strike-slip fault and an oblique-slip (fixed rake 151°) thrust dipping 64° to the west¹⁷. The preferred afterslip distribution on these faults has 100–136 mm of afterslip above and to the south of the large coseismic slip area on the main fault, and also has afterslip on the secondary fault just below the afterslip on the main fault (Supplementary Fig. 7). The peak afterslip is at about 3 km depth in the south and shallower than 2 km depth to the north. We explored alternative fault geometries, but few aftershocks were located in the area south of the main coseismic rupture to provide constraints on the fault geometry²³. None of the afterslip models explain the narrow zone of subsidence along the main fault.

Broad-scale surface rebound due to pore-pressure relaxation after the coseismic stress change can be approximated by taking the difference

between surface deformation fields of undrained and drained elastic models²⁴. The predicted deformation is opposite in sign from coseismic displacements and from postseismic deformation (see Fig. 1 and Supplementary Fig. 9). We cannot rule out a small amount (<10 mm) of broad-scale poroelastic rebound in the first two months after the Bam earthquake because longer-wavelength atmospheric effects are particularly strong in the two Envisat scenes acquired in early January 2004, obscuring deformation at scales greater than about 5 km.

We model the compaction of the fault zone with a grid of regularly spaced contracting Mogi point sources in an elastic half-space. This simple approximation allows efficient computations, but does not directly model the physical process that must involve a more continuous contracting volume. We performed an inversion with both the contracting Mogi source array and afterslip on the main rupture to determine an optimum joint distribution of deformation sources. The afterslip in the joint model is similar to the two-fault afterslip model, and the contraction sources are concentrated in a band that is deeper and stronger in the northern part (see Fig. 4c). The vertical extent of the contraction band depends on the amount of smoothing applied in the inversion, but the depth is constrained by the width of the observed subsidence. This model fits the measured subsidence and horizontal contraction (Figs 3 and 4). Our data only resolve contraction in the upper kilometre of the fault zone (with a total volume decrease of $8.4 \times 10^4 \text{ m}^3$); however, $2 \times 10^5 \text{ m}^3$ of dilatancy recovery could have occurred on the remaining coseismic slip zone below 1 km depth without producing significant surface deformation. Because the magnitude of coseismic dilatancy and its recovery is likely to be reduced at greater depths and confining pressures²⁵, dilatancy processes may have occurred at greater depths but are not resolved by geodetic data.

The restricted spatial extent and the three years of increasing subsidence in the fault zone south of Bam is very different from the broad-scale elevation changes of 1–2 months duration interpreted as pore-pressure transients after a similar earthquake in Iceland¹¹. The Bam poroelastic response has a much longer time constant (Fig. 2b) than the relaxation time of 0.75 years estimated for Landers²⁴ and about 2 months for the Iceland earthquake¹¹. The >1.7 year relaxation time for the Bam fault-bend subsidence (feature B) implies that the poroelastic rock volume has lower permeability.

The zone of strong postseismic contraction in the fault zone (Fig. 3, feature C) is directly above the largest coseismic slip^{9,17}, where the coseismic surface ruptures were widest and had the largest offsets in InSAR and field mapping¹⁸. This is also where coseismic optical and synthetic aperture radar pixel offsets show ~ 1 m of right-lateral shear over about 1 km centred on the fault^{17,21}. It is impossible to determine from the surface displacements alone what part of the shear is elastic versus inelastic deformation, but theoretical models of deformation of porous media predict that shear at shallow depths is likely to involve damage with a dilatancy component²⁵. The postseismic contraction occurred in the area where coseismic fault zone shear and hence damage were strongest. The depth of the contraction probably reflects the distribution of coseismic dilatancy; this is controlled by material strength variations and by distribution of water in the shallow crust, both modulated by stress.

We conclude that the localized postseismic subsidence over the Bam fault zone is only partly due to poroelastic rebound in a prominent restraining bend in the rupture; this subsidence is dominated by healing and compaction of coseismic dilatation and damage in the upper ~ 1 km of the fault zone outside of the bend²⁵. The postseismic compaction at

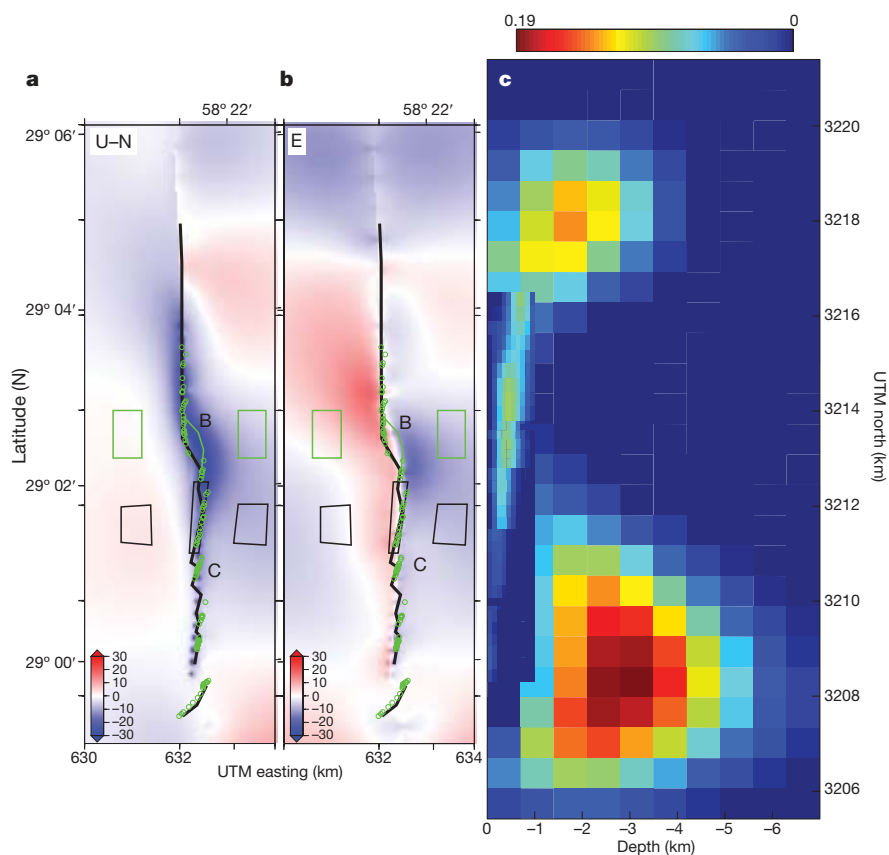


Figure 4 | Shallow fault zone contraction and main fault afterslip combined model results. Maps of predicted deformation in mm (colour scale) for the same area as Fig. 3; **a**, 'up' minus $0.1 \times$ 'north' (U-N), and **b**, 'east' (E). **c**, Model source strength shown in north-south profile aligned with maps.

Depth in km on horizontal axis. Shallow fault zone volume decrease (in 10^4 m^3) is shown as colour of small rectangles; main fault afterslip magnitude (in m) is shown as colour of large squares (same colour scale). Some afterslip patches are hidden behind the shallow fault zone.

Bam is approximately logarithmic in time, consistent with measurements of changes in the velocities of seismic waves in fault zones^{5–8}.

METHODS SUMMARY

We formed 342 full-resolution interferograms from 94 Envisat ASAR (advanced synthetic aperture radar) scenes on four different satellite tracks acquired between 7 January 2004 and 22 June 2007 (Supplementary Tables 1–4 and Supplementary Figs 1–4) using the JPL/Caltech ROI_pac²⁶ and Stanford SNAPHU²⁷ software. We calculated time series of line-of-sight (LOS) deformation for each track using a modified small baseline subset algorithm²⁸ (see Supplementary Information for full Methods description). The LOS vectors for the four tracks are nearly coplanar, so the north component of ground motion is poorly constrained (Supplementary Table 5). The temporal resolution is determined by the 35-day repeat cycle of the Envisat orbit and the spatial resolution is approximately 20×20 m on the ground.

We mitigate atmospheric errors by computing the total LOS-change maps from a number of independent measurements. Long-wavelength errors due to atmospheric effects and imprecise orbit knowledge were reduced by fitting and removing a planar phase gradient from a 40×40 km subset of each date's solution (Fig. 1, Supplementary Fig. 5). This also removes any long-wavelength deformation signal, so we cannot resolve postseismic deformation due to viscoelastic relaxation or afterslip in the lower crust or mantle.

For efficient model parameter optimization, we selected about 1,000 samples from estimated total deformation for the target area (Fig. 1, Supplementary Fig. 5) from each of the four tracks using a source-dependent sampling method²⁹ with the main coseismic rupture planes¹⁷ as the sources. Green's functions relating dislocations (shear or tensile) on fault patches to deformation at the surface were calculated with the Poly3D program³⁰. We optimized the distribution of dislocation magnitudes on fixed-geometry surfaces with a non-negative least squares procedure including a smoothing constraint. In the joint source modelling, we used a shallow fault extending to 2 km depth along the main coseismic rupture to optimize the sampling. Details are in Supplementary Information.

Received 6 July 2008; accepted 9 January 2009.

- Mai, P. M. & Beroza, G. C. A spatial random field model to characterize complexity in earthquake slip. *J. Geophys. Res.* **107**, 2308, doi:10.1029/2001JB000588 (2002).
- Ben-Zion, Y. & Sammis, C. G. Characterization of fault zones. *Pure Appl. Geophys.* **160**, 677–715 (2003).
- Nur, A. Effects of stress on velocity anisotropy in rocks with cracks. *J. Geophys. Res.* **76**, 2022–2034 (1971).
- Scholz, C. H. Post-earthquake dilatancy recovery. *Geology* **2**, 551–554 (1974).
- Vidale, J. E. & Li, Y.-G. Damage to the shallow Landers fault from the nearby Hector Mine earthquake. *Nature* **421**, 524–526 (2003).
- Li, Y.-G., Chen, P., Cochran, E. S., Vidale, J. E. & Burdette, T. Seismic evidence for rock damage and healing on the San Andreas Fault associated with the 2004 M 6.0 Parkfield earthquake. *Bull. Seismol. Soc. Am.* **96**, S349–S363 (2006).
- Schaff, D. P. & Beroza, G. C. Coseismic and postseismic velocity changes measured by repeating earthquakes. *J. Geophys. Res.* **109**, B10302, doi:10.1029/2004JB003011 (2004).
- Peng, Z. G. & Ben-Zion, Y. Temporal changes of shallow seismic velocity around the Karadere-Düzce branch of the North Anatolian Fault and strong ground motion. *Pure Appl. Geophys.* **163**, 567–600 (2006).
- Fialko, Y., Sandwell, D., Simons, M. & Rosen, P. A. Three-dimensional deformation caused by the Bam, Iran, earthquake and the origin of shallow slip deficit. *Nature* **435**, 295–299 (2005).
- Bürgmann, R. & Dresen, G. Rheology of the lower crust and upper mantle: Evidence from rock mechanics, geodesy and field observations. *Annu. Rev. Earth Planet. Sci.* **36**, 531–567 (2008).
- Jónsson, S., Segall, P., Pedersen, R. & Björnsson, G. Post-earthquake ground movements correlated to pore-pressure transients. *Nature* **424**, 179–183 (2003).
- Peltzer, G., Rosen, P., Rogez, F. & Hudnut, K. Postseismic rebound in fault step-overs caused by pore fluid-flow. *Science* **273**, 1202–1204 (1996).
- Johanson, I. A., Fielding, E. J., Rolandone, F. & Bürgmann, R. Coseismic and postseismic slip of the 2004 Parkfield earthquake from geodetic data. *Bull. Seismol. Soc. Am.* **96**, S269–S282 (2006).

- Langbein, J., Murray, J. R. & Snyder, H. A. Coseismic and initial postseismic deformation from the 2004 Parkfield, California, earthquake, observed by global positioning system, electronic distance meter, creepmeters, and borehole strainmeters. *Bull. Seismol. Soc. Am.* **96**, S304–S320 (2006).
- Hsu, Y. J. *et al.* Frictional afterslip following the 2005 Nias-Simeulue earthquake, Sumatra. *Science* **312**, 1921–1926 (2006).
- Talebian, M. *et al.* The 2003 Bam (Iran) earthquake: Rupture of a blind fault. *Geophys. Res. Lett.* **31**, L11611, doi:10.1029/2004GL020058 (2004).
- Funing, G. J., Parsons, B. E., Wright, T. J., Jackson, J. A. & Fielding, E. J. Surface displacements and source parameters of the 2003 Bam (Iran) earthquake from Envisat advanced synthetic aperture radar imagery. *J. Geophys. Res.* **110**, B09406, doi:10.1029/2004JB003338 (2005).
- Fielding, E. J. *et al.* Surface ruptures and building damage of the 2003 Bam, Iran, earthquake mapped by satellite synthetic aperture radar interferometric correlation. *J. Geophys. Res.* **110**, B03302, doi:10.1029/2004JB003299 (2005).
- Jackson, J. A. *et al.* Seismotectonic, rupture-process, and earthquake-hazard aspects of the 26 December 2003 Bam, Iran, earthquake. *Geophys. J. Int.* **166**, 1270–1292 (2006).
- Motagh, M. *et al.* Combination of precise leveling and InSAR data to constrain source parameters of the Mw = 6.5, 26 December 2003 Bam earthquake. *Pure Appl. Geophys.* **163**, 1–18 (2006).
- Peyret, M. *et al.* The source motion of 2003 Bam (Iran) earthquake constrained by satellite and ground-based geodetic data. *Geophys. J. Int.* **169**, 849–865 (2007).
- Bürgmann, R., Rosen, P. A. & Fielding, E. J. Synthetic aperture radar interferometry to measure Earth's surface topography and its deformation. *Annu. Rev. Earth Planet. Sci.* **28**, 169–209 (2000).
- Sadeghi, H., Aghda, S. M. F., Suzuki, S. & Nakamura, T. 3-D velocity structure of the 2003 Bam earthquake area (SE Iran): Existence of a low-Poisson's ratio layer and its relation to heavy damage. *Tectonophysics* **417**, 269–283 (2006).
- Peltzer, G., Rosen, P., Rogez, F. & Hudnut, K. Poroelastic rebound along the Landers 1992 earthquake surface rupture. *J. Geophys. Res.* **103**, 30131–30145 (1998).
- Hamiel, Y., Lyakhovsky, V. & Agnon, A. Coupled evolution of damage and porosity in poroelastic media: Theory and applications to deformation of porous rocks. *Geophys. J. Int.* **156**, 701–713 (2004).
- Rosen, P. A., Hensley, S., Peltzer, G. & Simons, M. Updated repeat orbit interferometry package released. *Eos* **85**, 47 (2004).
- Chen, C. W. & Zebker, H. A. Network approaches to two-dimensional phase unwrapping: Intractability and two new algorithms. *J. Opt. Soc. Am. A* **17**, 401–414 (2000).
- Berardino, P., Fornaro, G., Lanari, R. & Sansosti, E. A new algorithm for surface deformation monitoring based on small baseline differential SAR interferograms. *IEEE Trans. Geosci. Rem. Sens.* **40**, 2375–2383 (2002).
- Lohman, R. B. & Simons, M. Some thoughts on the use of InSAR data to constrain models of surface deformation: Noise structure and data downsampling. *Geochem. Geophys. Geosyst.* **6**, Q01007, doi:10.1029/2004GC000841 (2005).
- Thomas, A. L. Poly3D: A Three-Dimensional, Polygonal Element, Displacement Discontinuity Boundary Element Computer Program with Applications to Fractures, Faults, and Cavities in the Earth's Crust. M.Sc. Thesis, Stanford Univ. (1993).

Supplementary Information is linked to the online version of the paper at www.nature.com/nature.

Acknowledgements Envisat data are copyright 2004–07 European Space Agency and were provided under AOE project 668. We thank R. Lohman for the use of data resampling programs and discussions. We thank J. Jackson, M. Talebian, D. McKenzie, J.-P. Avouac, Z. Liu, Z.H. Li, E. Cochran, F. Horowitz, G. Peltzer, Y. Ben-Zion and E. Hearn for discussions. Part of this research was performed at the Jet Propulsion Laboratory, California Institute of Technology, under contract with the National Aeronautics and Space Administration.

Author Contributions E.J.F. performed the data analysis, interpretation and modelling. P.R.L. wrote the time series analysis and modelling framework programs, and contributed to interpretation. R.B. and G.J.F. contributed to modelling and interpretation. E.J.F. and R.B. wrote the manuscript with contributions from all authors.

Author Information Reprints and permissions information is available at www.nature.com/reprints. Correspondence and requests for materials should be addressed to E.J.F. (Eric.J.Fielding@jpl.nasa.gov).

Phytoplankton in the ocean use non-phosphorus lipids in response to phosphorus scarcity

Benjamin A. S. Van Mooy¹, Helen F. Fredricks¹, Byron E. Pedler^{1†}, Sonya T. Dyhrman², David M. Karl³, Michal Koblížek^{4,5}, Michael W. Lomas⁶, Tracy J. Mincer¹, Lisa R. Moore⁷, Thierry Moutin⁸, Michael S. Rappé⁹ & Eric A. Webb¹⁰

Phosphorus is an obligate requirement for the growth of all organisms; major biochemical reservoirs of phosphorus in marine plankton include nucleic acids and phospholipids^{1–3}. However, eukaryotic phytoplankton and cyanobacteria (that is, ‘phytoplankton’ collectively) have the ability to decrease their cellular phosphorus content when phosphorus in their environment is scarce^{1,4,5}. The biochemical mechanisms that allow phytoplankton to limit their phosphorus demand and still maintain growth are largely unknown. Here we show that phytoplankton, in regions of oligotrophic ocean where phosphate is scarce, reduce their cellular phosphorus requirements by substituting non-phosphorus membrane lipids for phospholipids. In the Sargasso Sea, where phosphate concentrations were less than 10 nmol l^{-1} , we found that only $1.3 \pm 0.6\%$ of phosphate uptake was used for phospholipid synthesis; in contrast, in the South Pacific subtropical gyre, where phosphate was greater than 100 nmol l^{-1} , plankton used $17 \pm 6\%$ (ref. 6). Examination of the planktonic membrane lipids at these two locations showed that classes of sulphur- and nitrogen-containing membrane lipids, which are devoid of phosphorus, were more abundant in the Sargasso Sea than in the South Pacific. Furthermore, these non-phosphorus, ‘substitute lipids’ were dominant in phosphorus-limited cultures of all of the phytoplankton species we examined. In contrast, the marine heterotrophic bacteria we examined contained no substitute lipids and only phospholipids. Thus heterotrophic bacteria, which compete with phytoplankton for nutrients in oligotrophic regions like the Sargasso Sea, appear to have a biochemical phosphorus requirement that phytoplankton avoid by using substitute lipids. Our results suggest that phospholipid substitutions are fundamental biochemical mechanisms that allow phytoplankton to maintain growth in the face of phosphorus limitation.

Linkages between phosphorus availability and phytoplankton productivity in the ocean have received renewed attention in recent years^{7–11}, yet there remains little direct evidence for instantaneous phosphorus limitation of primary production. For example, in the oligotrophic eastern Mediterranean Sea, where phosphate concentrations are sub-nanomolar and phosphate turnover times are only a few hours, a large-scale phosphorus-addition experiment did not stimulate net phytoplankton growth or the rate of total community photosynthesis¹¹. A similar lack of stimulation by phosphate alone was recently reported in the oligotrophic Sargasso Sea¹², where the concentrations of phosphate are also quite low⁷. These observations are indicative of phytoplankton communities that are highly adapted to

phosphorus scarcity and can simultaneously maintain both low cellular phosphorus requirements and effective rates of photosynthesis.

Phytoplankton communities in oligotrophic regions of the ocean are generally dominated by cyanobacteria⁸, or, at times, small eukaryotic phytoplankton¹³. Phosphate is typically the preferred form of dissolved phosphorus for these organisms^{8,14,15}, but recent work has shown that many phytoplankton species can supplement their phosphorus demand by accessing dissolved organic phosphorus^{16–18}. It has also been shown that phytoplankton have the ability to lower their physiological phosphorus demand by as much as 50% in response to phosphorus limitation^{1,4,5}. This latter strategy is important because it essentially allows phytoplankton in oligotrophic marine environments to maintain growth in the face of phosphorus limitation. The physiological mechanisms for maintaining growth while lowering overall phosphorus demand are unknown, but the options are basically limited to reducing either nucleic-acid or phospholipid synthesis rates. Unlike nucleic acids, there are alternative, non-phosphorus membrane lipid molecules that may be substituted for phospholipids. These ‘substitute lipids’ have the same ionic charge as phospholipids, and thus serve similar biochemical purposes within cells^{19,20}. Although it has been hypothesized that phytoplankton in the environment might synthesize substitute lipids in response to phosphorus limitation^{2,19,20}, this hypothesis has yet to be tested outside of cultures of a few model organisms.

To understand whether phytoplankton use phospholipid substitutions as a strategy to mitigate phosphorus limitation in the ocean, we examined the synthesis of phospholipids in the Sargasso Sea, a setting where phytoplankton appear to be stressed¹⁶ by low concentrations of phosphate⁷. Our study sampled a mode water eddy, which is a physical oceanographic feature that can support very high rates of phytoplankton growth¹³. We found that the cycling of phosphorus was also particularly rapid: the turnover time of phosphate in surface waters ($n = 21$) was $1.4 \pm 1.0 \text{ h}$ (mean \pm s.d.), which is nearly a factor of three shorter than previously reported²¹. This rapid turnover, compounded by concentrations that averaged $7.9 \pm 2.4 \text{ nmol l}^{-1}$, indicated that phytoplankton were experiencing conditions where phosphate was scarce. We measured total community phospholipid synthesis rates, and found that they constituted only $1.3 \pm 0.6\%$ of the total phosphate uptake rate (Fig. 1). These observations contrast markedly with those we made in the surface waters of the oligotrophic North Pacific subtropical gyre ($n = 12$) and South Pacific subtropical gyre ($n = 18$), where the total planktonic community supported phospholipid synthesis rates that contributed $12 \pm 8\%$

¹Department of Marine Chemistry and Geochemistry, Woods Hole Oceanographic Institution, Woods Hole, Massachusetts 02543, USA. ²Department of Biology, Woods Hole Oceanographic Institution, Woods Hole, Massachusetts 02543, USA. ³Department of Oceanography, University of Hawaii, Honolulu, Hawaii, USA. ⁴Institute of Microbiology, Czech Academy of Sciences, Třeboň, Czech Republic. ⁵Institute of Physical Biology, University of South Bohemia, Nové Hrad, Czech Republic. ⁶Bermuda Institute of Ocean Sciences, St. George, Bermuda. ⁷Department of Biological Sciences, University of Southern Maine, Portland, Maine, USA. ⁸Laboratoire d’Océanographie Physique et Biogéochimique, Centre d’Océanologie de Marseille, Aix-Marseille University, France. ⁹Hawaii Institute of Marine Biology, University of Hawaii, Kaneohe, Hawaii, USA. ¹⁰Department of Biological Sciences, University of Southern California, Los Angeles, California, USA. [†]Present address: Scripps Institution of Oceanography, University of California at San Diego, La Jolla, California, USA.

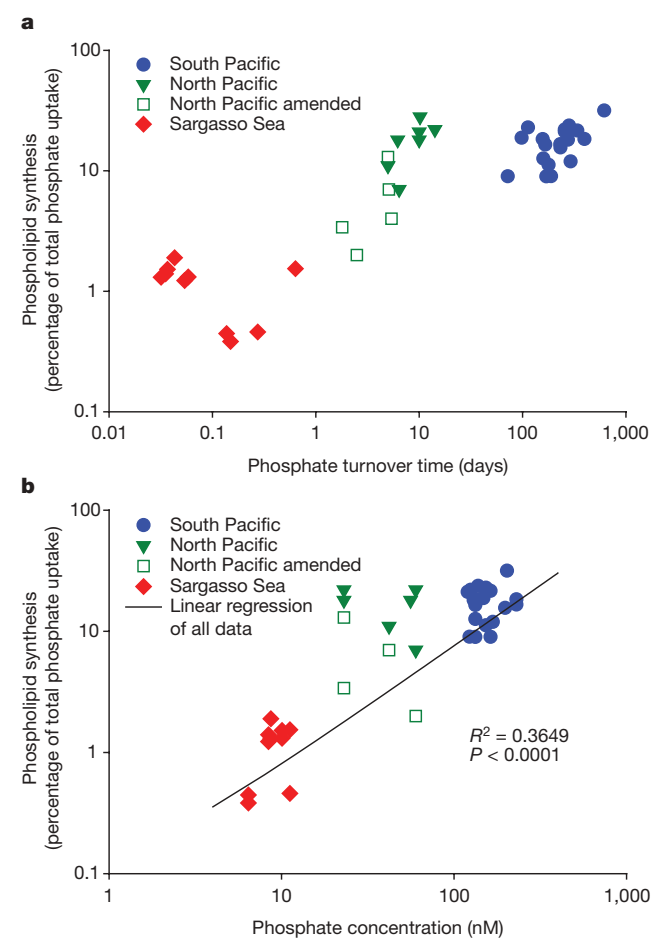


Figure 1 | Relationships between phosphate and phospholipid synthesis. Percentages of total phosphate uptake allocated to phospholipid synthesis and their relationships with phosphate turnover times (a) and phosphate concentrations (b). Solid symbols for South and North Pacific are data from refs 2, 6 and 22. Open symbols for the North Pacific are data from incubations, which were amended with NH_4^+ at a final concentration of 50 nmol l^{-1} (see ref. 3; ambient concentrations are generally of the order of 30 nmol l^{-1}) in an attempt to increase rates of phosphate uptake. The linear regression in the bottom plot indicates that 36% of the variation in the use of phosphate for phospholipid synthesis can be explained by the variation in phosphate concentrations. This suggests there is a strong, fundamental and global-scale control on phosphate allocation within the planktonic communities in response to variations in phosphorus availability.

and $17 \pm 6\%$ of total phosphate uptake, respectively^{2,6} (Fig. 1). In the North Pacific and South Pacific, phosphate concentrations averaged 44.9 ± 19.9 and $151.2 \pm 36.3 \text{ nmol l}^{-1}$, respectively, and phosphate turnover times averaged 6.8 ± 3.6 and 239 ± 74 days, respectively^{14,22}, which indicates that phosphate was much more readily available in these two environments than in the Sargasso Sea. Thus, our data unequivocally show a fundamental relationship between the availability of phosphorus and its biochemical allocation within planktonic cells on large geographic scales.

We also conducted a series of laboratory experiments with batch cultures of representative cyanobacteria and eukaryotic phytoplankton under phosphorus-replete and phosphorus-depleted conditions. Using a common approach, we grew these organisms in high- and low-phosphate media, and then harvested the cells once we observed a clear difference in growth rates under the two conditions. During these experiments we observed that non-phosphorus membrane lipids were substituted for phospholipids in all cases (Table 1). Cyanobacteria of the genera *Synechococcus*, *Prochlorococcus*, *Crocospaera* and *Trichodesmium* all showed the ability to substitute the non-phosphorus membrane lipid sulphoquinovosyldiacylglycerol (SQDG; Supplementary Fig. 1) for the phospholipid phosphatidylglycerol (Supplementary Fig. 1) under conditions of phosphorus limitation (Table 1); both of these membrane lipids are anionic in the pH range of seawater and to a certain extent these lipids are biochemically equivalent¹⁹. The SQDG/phosphatidylglycerol ratios in phosphorus-limited cultures of *Synechococcus* and *Prochlorococcus* were higher than nitrogen-fixing *Trichodesmium* and *Crocospaera*; this lack of biochemical flexibility on the part of the nitrogen-fixing genera is consistent with the observed susceptibility of these organisms to phosphorus limitation^{9–11,18}. From the measured cellular phosphatidylglycerol content of *Synechococcus* and *Prochlorococcus* we determined that the substitution of SQDG for phosphatidylglycerol spared 0.3×10^6 to 5.2×10^6 atoms of phosphorus per cell, which, depending on the strain, equates to 10–86% of the phosphorus in their genomic DNA (Supplementary Table 1). Because the genes involved in SQDG synthesis²³ only contain about 5×10^3 phosphorus atoms, this metabolic pathway unequivocally confers a net phosphorus-sparing capability. Given that genomic DNA composes more than half of the total cellular phosphorus in phosphorus-limited cultures of *Synechococcus* and *Prochlorococcus*⁴, we calculate that the ability to synthesize SQDG in place of phosphatidylglycerol spares an amount of phosphorus equivalent to 5–43% of their total cellular phosphorus demand.

In the phosphorus-limited cultures of eukaryotic phytoplankton, we observed that non-phosphorus ‘betaine’ lipids were substituted for phosphatidylcholine (Table 1 and Supplementary Fig. 1). There are three structurally related types of betaine lipid molecule (Supplementary Fig. 1), and, like phosphatidylcholine, they are all

Table 1 | Ratios of substitute lipids to phospholipids in phytoplankton cultures and environmental samples

	SQDG/PG ratio, P-replete	SQDG/PG ratio, P-limited	BL/PC ratio, P-replete	BL/PC ratio, P-limited
Cyanobacteria				
<i>Synechococcus</i> WH8102	9.9 ± 2.0	120.5 ± 7.1	0†	0†
<i>Synechococcus</i> WH7803	10.3 ± 0.3	61.6 ± 15.4	0†	0†
<i>Synechococcus</i> WH5701	6.2 ± 0.5	132.0 ± 31.0	0†	0†
<i>Prochlorococcus</i> MED4	20.0 ± 1.3	34.1 ± 1.6	0†	0†
<i>Crocospaera watsonii</i>	4.0	5.8	0†	0†
<i>Trichodesmium erythreum</i>	7.8 ± 1.0	18.5 ± 4.9	0†	0†
Eukaryotic phytoplankton				
<i>Thalassiosira pseudonana</i>	3.0 ± 0.9	394.8 ± 48.2	<0.01‡	>500§
<i>Chaetoceros affinis</i>	10.5 ± 3.6	26.3 ± 9.0	0.9 ± 0.2	27.8 ± 8.3
<i>Emiliania huxleyi</i>	<0.01*	<0.01*	0.7	1.3
Communities				
South Pacific	3.6 ± 0.8	NA	3.6 ± 1.7	NA
Sargasso Sea	NA	4.5 ± 1.1	NA	13.1 ± 4.0

Bold type indicates significant differences between phosphorus-replete and phosphorus-limited conditions as indicated by directional Mann–Whitney U-tests ($P \leq 0.05$). Cultures were analysed in triplicate or greater except for *C. watsonii* and *E. huxleyi*, which were analysed once. In the South Pacific, five discrete samples of the total planktonic community ($>0.2 \mu\text{m}$) were collected and analysed; there were six samples from the Sargasso Sea. NA, not applicable; BL, betaine lipid; PC, phosphatidylcholine; SQDG, sulphoquinovosyldiacylglycerol; PG, phosphatidylglycerol. *SQDG not detected; analytical sensitivity is given. †BLs not detected and are not known to be produced by cyanobacteria. ‡BLs not detected; analytical sensitivity is given. §PC not detected; analytical sensitivity is given.

zwitterionic in the pH range of seawater. Furthermore, both phosphatidylcholine and betaine lipids contain one atom of nitrogen per molecule, and thus the substitution of betaine lipids for phosphatidylcholine does not require additional cellular nitrogen. Phosphorus-limited cultures of the diatom *Thalassiosira pseudonana* used betaine lipids to the complete exclusion of phosphatidylcholine. This substitution spared them $16 \pm 8\%$ of their total phosphorus demand compared with cells grown under phosphorus-replete conditions. The diatom *Chaetoceros affinis* and coccolithophorid *Emiliania huxleyi* also used betaine lipids, and we estimate that this substitution spared them approximately 10–30% of total phosphorus demand. Furthermore, as was observed in cyanobacteria, *T. pseudonana* and *C. affinis* also substituted SQDG for phosphatidylglycerol.

Based on the lipids we observed in phosphorus-limited cultures, we hypothesized that substitute lipids would be more prevalent in the Sargasso Sea than in the South Pacific. Indeed, we found that betaine lipids were the most abundant intact membrane lipids in the Sargasso Sea, reaching an average combined concentration of $2.4 \pm 0.2 \mu\text{g l}^{-1}$. In contrast, the concentration of betaine lipids was only $0.2 \pm 0.1 \mu\text{g l}^{-1}$ in the South Pacific. Furthermore, the betaine lipid/phosphatidylcholine ratio was 13.1 ± 4.0 in the Sargasso Sea, which is almost a factor of 4 higher than the 3.6 ± 1.7 we observed in the South Pacific (Table 1). Betaine lipids and phosphatidylcholine are by no means exclusive to the domain Eukarya (see ref. 26, and references therein), but they have yet to be reported in any cyanobacterium (see also Table 1), and, as discussed below, they do not appear to be abundant in heterotrophic bacteria from oligotrophic environments. Concentrations of SQDG were also higher in the Sargasso Sea than in the South Pacific (0.8 ± 0.3 compared with $0.3 \pm 0.1 \mu\text{g l}^{-1}$), and this was reflected in the higher SQDG/phosphatidylglycerol ratios in the Sargasso Sea (Table 1). However, phosphatidylglycerol is not derived from phytoplankton alone but is also synthesized by heterotrophic bacteria², which confounds the interpretation of community SQDG/phosphatidylglycerol ratios; given the contribution of phosphatidylglycerol by heterotrophic bacteria, it is striking that we were able to observe a higher SQDG/phosphatidylglycerol ratio in the Sargasso Sea, the expected response of phytoplankton to lower phosphorus availability.

An additional class of non-phosphorus lipids, ornithine lipids, has been reported in lineages of aerobic anoxygenic phototrophic (AAP) bacteria. However, with the exception of two samples from the South Pacific, we did not detect ornithine lipids in any of our samples from the field. We examined the AAP bacterium *Roseobacter* sp. strain COL2P originating from the oligotrophic Mediterranean Sea and found that although ornithine lipids were more prevalent in phosphorus-limited cultures, they did not appear to function as substitutes for phospholipids in this species (Supplementary Fig. 2). Given this observation, and the relatively low abundance of AAP bacteria in the oligotrophic North Atlantic²⁴, the absence of ornithine lipids in the Sargasso Sea is not particularly surprising.

Bacteria of the SAR11 clade dominate the heterotrophic bacterial community of the Sargasso Sea^{8,25}. We found that a representative of this clade, *Pelagibacter ubique*, synthesized only the phospholipids phosphatidylglycerol and phosphatidylethanolamine. These results are consistent with those from marine bacteria isolated by classical methods². The sum of these phospholipids in *P. ubique* amounted to 1.5×10^6 atoms of phosphorus per cell, which, for comparison, is 10 times more than the phospholipids in phosphorus-limited *Synechococcus* sp. strain WH8102 cells (0.16×10^6 atoms of phosphorus per cell). We were not able to examine *P. ubique* in phosphorus-limited cultures. However, known bacterial genes for SQDG²³, betaine lipid²⁶ and ornithine lipid²⁷ synthesis are absent from the *P. ubique* genome. The absence of these genes, which encode pathways that could spare *P. ubique* an amount of cellular phosphorus equivalent to almost half their entire genome, is a puzzling potential side effect of genome streamlining in this organism²⁸.

We tracked the lipid composition of resident heterotrophic bacteria from the Sargasso Sea ($n = 3$) in regrowth incubations²⁹, which are designed to allow heterotrophic bacteria to grow exponentially in the absence of other plankton. Even though concentrations of phosphate decreased from 6.4 ± 2.0 to $1.7 \pm 1.2 \text{ nmol l}^{-1}$ during the course of growth, we observed marked increases in phosphatidylglycerol and phosphatidylethanolamine only (Supplementary Fig. 3), whereas concentrations of substitute lipids decreased or remained low (Supplementary Fig. 4). Furthermore, the phospholipid content per cell of heterotrophic bacteria remained nearly constant throughout the incubation at $1.7 \pm 0.2 \times 10^6$ atoms of phosphorus per cell, which is essentially the same value we observed for *P. ubique* under phosphorus-replete conditions (Supplementary Fig. 5). Thus heterotrophic bacteria in the Sargasso Sea appeared not to use substitute lipids, which suggests that this group of organisms has a lipid-based requirement for phosphorus that could put them at a disadvantage against phytoplankton when phosphorus is scarce (Fig. 2). Indeed, phosphorus availability has been shown to play a role in affecting the growth rates of heterotrophic bacteria in the Sargasso Sea³⁰ and in the aforementioned phosphorus-addition experiment in the eastern Mediterranean Sea¹¹.

Phospholipid substitutions appear to be an important biochemical mechanism for cyanobacteria and eukaryotic phytoplankton to maintain photosynthesis in environments where phosphorus is scarce. Our data from the Sargasso Sea demonstrate that betaine-lipid-rich eukaryotic phytoplankton use this strategy to great effect in response to phosphorus-depleted conditions, and we hypothesize that this could contribute to the recent observation that phytoplankton in this environment are biologically nitrogen-limited¹² despite the chemical oceanographic observations suggesting otherwise^{7,21}. However, it is important to recognize that eukaryotic phosphatidylcholine and betaine lipids both contain one nitrogen atom per molecule, whereas

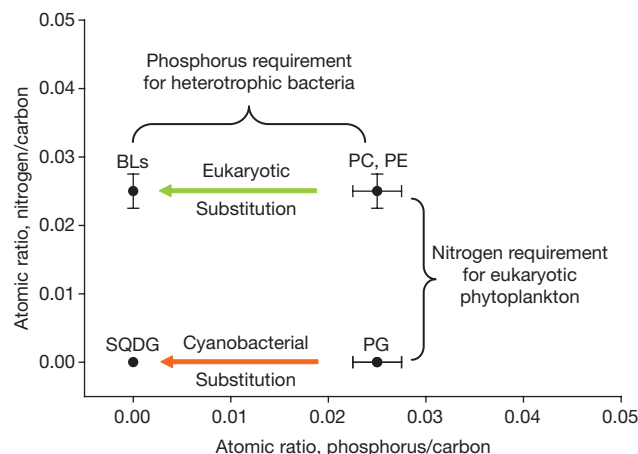


Figure 2 | Relative phosphorus and nitrogen contents of membrane lipids expressed as atomic ratios to carbon. Both cyanobacteria and eukaryotic phytoplankton have the ability to substitute non-phosphorus-containing lipids for phospholipids, whereas heterotrophic bacteria do not. Thus, heterotrophic bacteria are burdened with a phosphorus requirement for membrane lipid synthesis. In addition, betaine lipids and phosphatidylcholine contain nitrogen whereas SQDG and phosphatidylglycerol do not. Thus we posit that eukaryotic phytoplankton are burdened with an obligate lipid-based nitrogen requirement for membrane lipid synthesis; our data with nitrogen-limited *E. huxleyi* indicate that these nitrogen-containing lipids are not substituted with any other lipid (B.A.S.V.M. and S.T.D., unpublished observations). There is no evidence for the ability of heterotrophic bacteria to substitute phosphatidylglycerol for phosphatidylethanolamine in the data from the regrowth incubations (Supplementary Fig. 3). Error bars indicate the approximate range of carbon atoms in the indicated classes of lipid molecules. BLs, betaine lipids; PC, phosphatidylcholine; PE, phosphatidylethanolamine; SQDG, sulphoquinovosyldiacylglycerol; PG, phosphatidylglycerol.

cyanobacterial SQDG and phosphatidylglycerol do not. Thus eukaryotic phytoplankton, in contrast to cyanobacteria, appear to be burdened with a nitrogen requirement associated with membrane lipid synthesis (Fig. 2). We hypothesize that this difference could be a contributing factor to the dominance of cyanobacteria in all three of the oligotrophic regions of the ocean we studied, where, in addition to phosphorus, nitrogen is also scarce.

METHODS SUMMARY

Environmental samples were collected from the surface mixed layer (depth less than 60 m) using Niskin bottles. South Pacific stations were occupied during the BIOSOPE campaign approximately along 30° S between 110° and 90° W in November 2004; exact dates and locations have been described⁶. The Sargasso Sea cruise was conducted in April 2007 at approximately 31° N 63° W. The North Pacific data are from HOT cruises to 22° 45' N 158° W (ref. 2). To determine the percentage phosphate incorporation into phospholipids, seawater samples were incubated with [³³P]phosphate, and lipids were extracted as previously described^{2,6}. Membrane lipid molecules were extracted and analysed by high-performance liquid chromatography–mass spectrometry (HPLC–MS) as previously described². Authentic standards for quantification of SQDG and betaine lipids (Supplementary Fig. 1) were isolated from phosphorus-limited cultures of *Synechococcus* sp. strain WH8102 and *C. affinis*, respectively, using preparative HPLC². Phytoplankton were grown in batch cultures using standard methods and media (Supplementary Table 2); cells were harvested as soon as cultures in phosphorus-depleted media showed an attenuation in the increase in cell numbers or chlorophyll fluorescence compared with cultures in phosphorus-replete media. Cultures of *P. ubique* were grown in supplemented seawater as described²⁵. Heterotrophic bacteria regrowth incubations were conducted as described²⁹ where seawater was filtered through acid-cleaned 0.2 µm pore-size membranes, re-inoculated with a 10% volume of whole seawater, and incubated in the dark at *in situ* temperatures. Total cellular phosphorus of *T. pseudonana* was determined after combusting cells in the presence of magnesium sulphate; the resultant phosphate was dissolved in dilute hydrochloric acid and quantified using a standard molybdate method. Total cellular phosphorus and lipid phosphorus of *E. huxleyi* and *C. affinis* were estimated based on data from ref. 1 and references therein. Mann–Whitney *U*-tests were applied to identify significant differences (*P* < 0.05) between samples because sample sizes were too small to assume normal distributions.

Received 18 June; accepted 20 November 2008; corrected 5 March (details online).
Published online 1 February 2009.

- Geider, R. J. & La Roche, J. Redfield revisited: variability of C:N:P in marine microalgae and its biochemical basis. *Eur. J. Phycol.* **37**, 1–17 (2002).
- Van Mooy, B. A. S., Rocap, G., Fredricks, H. F., Evans, C. T. & Devol, A. H. Sulfolipids dramatically decrease phosphorus demand by picocyanobacteria in oligotrophic marine environments. *Proc. Natl Acad. Sci. USA* **103**, 8607–8612 (2006).
- Van Mooy, B. A. S. & Devol, A. H. Assessing nutrient limitation of *Prochlorococcus* in the North Pacific subtropical gyre by using an RNA capture method. *Limnol. Oceanogr.* **53**, 78–88 (2008).
- Bertilsson, S., Berglund, O., Karl, D. M. & Chisholm, S. W. Elemental composition of marine *Prochlorococcus* and *Synechococcus*: implications for the ecological stoichiometry of the sea. *Limnol. Oceanogr.* **48**, 1721–1731 (2003).
- Krauk, J. M., Villareal, T. A., Sohm, J. A., Montoya, J. P. & Capone, D. G. Plasticity of N:P ratios in laboratory and field populations of *Trichodesmium* spp. *Aquat. Microb. Ecol.* **42**, 243–253 (2006).
- Van Mooy, B. A. S., Moutin, T., Duhamel, S., Rimmelin, P. & Van Wambeke, F. Phospholipid synthesis rates in the eastern subtropical South Pacific Ocean. *Biogeosciences* **5**, 133–139 (2008).
- Wu, J., Sunda, W., Boyle, E. A. & Karl, D. M. Phosphate depletion in the western North Atlantic Ocean. *Science* **289**, 759–762 (2000).
- Zubkov, M. V. *et al.* Microbial control of phosphate in the nutrient-depleted North Atlantic subtropical gyre. *Environ. Microbiol.* **9**, 2079–2089 (2007).
- Sanudo-Wilhelmy, S. A. *et al.* Phosphorus limitation of nitrogen fixation by *Trichodesmium* in the central Atlantic Ocean. *Nature* **411**, 66–69 (2001).
- Mills, M. M., Ridame, C., Davey, M. & La Roche, J. Iron and phosphorus co-limit nitrogen fixation in the eastern tropical North Atlantic. *Nature* **429**, 292–294 (2004).
- Thingstad, T. F. *et al.* Nature of phosphorus limitation in the ultraoligotrophic eastern Mediterranean. *Science* **309**, 1068–1071 (2005).
- Moore, C. M. *et al.* Relative influence of nitrogen and phosphorus availability on phytoplankton physiology and productivity in the oligotrophic sub-tropical North Atlantic Ocean. *Limnol. Oceanogr.* **53**, 291–305 (2008).
- McGillcuddy, D. J. Jr *et al.* Eddy/wind interactions stimulate extraordinary mid-ocean plankton blooms. *Science* **316**, 1021–1026 (2007).

- Björkman, K. & Karl, D. M. Bioavailability of dissolved organic phosphorus in the euphotic zone at station ALOHA, North Pacific subtropical gyre. *Limnol. Oceanogr.* **48**, 1049–1057 (2003).
- Moore, L. R., Ostrowski, M., Scanlan, D. J., Feren, K. & Sweetsir, T. Ecotypic variation in phosphorus-acquisition mechanisms within marine picocyanobacteria. *Aquat. Microb. Ecol.* **39**, 257–269 (2005).
- Lomas, M. W., Swain, A., Shelton, R. & Ammerman, J. W. Taxonomic variability of phosphorus stress in Sargasso Sea phytoplankton. *Limnol. Oceanogr.* **49**, 2302–2310 (2004).
- Dyhrman, S. T. *et al.* Phosphonate utilization by the globally important marine diazotroph *Trichodesmium*. *Nature* **439**, 68–71 (2006).
- Webb, E., Jakuba, R., Moffet, J. & Dyhrman, S. Molecular assessment of phosphorus and iron physiology in *Trichodesmium* populations from the western central and western South Atlantic. *Limnol. Oceanogr.* **52**, 2221–2232 (2007).
- Benning, C., Beatty, J. T., Prince, R. C. & Somerville, C. R. The sulfolipid sulfoquinovosyldiacylglycerol is not required for photosynthetic electron transport in *Rhodospirillum rubrum* but enhances growth under phosphate limitation. *Proc. Natl Acad. Sci. USA* **90**, 1561–1565 (1993).
- Sato, N., Hagio, M., Wada, H. & Tsuzuki, M. in *Recent Advances in the Biochemistry of Plant Lipids* (eds Harwood, J. L. & Quinn, P. J.) (Portland Press, 2000).
- Ammerman, J. W., Hood, R. R., Case, D. A. & Cotner, J. B. Phosphorus deficiency in the Atlantic: an emerging paradigm in oceanography. *Eos* **84**, 165–170 (2003).
- Moutin, T. *et al.* Phosphate availability and the ultimate control of new nitrogen input by nitrogen fixation in the tropical Pacific Ocean. *Biogeosciences* **5**, 95–109 (2008).
- Güller, S., Essigmann, B. & Benning, C. A cyanobacterial gene, *sqdX*, required for biosynthesis of the sulfolipid sulfoquinovosyldiacylglycerol. *J. Bacteriol.* **182**, 543–545 (2000).
- Koblížek, M., Mašín, M., Ras, J., Poulton, A. J. & Prášil, O. Rapid growth rates of aerobic anoxygenic phototrophs in the ocean. *Environ. Microbiol.* **9**, 2401–2406 (2007).
- Rappé, M. S., Connon, S. A., Vergin, K. L. & Giovannoni, J. Cultivation of ubiquitous SAR11 marine bacterioplankton clade. *Nature* **418**, 630–633 (2002).
- Riekhof, W. R., Andre, C. & Benning, C. Two enzymes, BtaA and BtaB, are sufficient for betaine lipid biosynthesis in bacteria. *Arch. Biochem. Biophys.* **441**, 96–105 (2005).
- Weissenmayer, B., Gao, J.-L. I. M. L.-L., & Geiger, O. Identification of a gene required for the biosynthesis of ornithine-derived lipids. *Mol. Microbiol.* **45**, 721–733 (2002).
- Giovannoni, S. J. *et al.* Genome streamlining in a cosmopolitan oceanic bacterium. *Science* **309**, 1242–1245 (2005).
- Carlson, C. A., Ducklow, H. W. & Sleeter, T. D. Stocks and dynamics of bacterioplankton in the northwestern Sargasso Sea. *Deep-Sea Res.* **43**, 491–515 (1996).
- Mills, M. M. *et al.* Nitrogen and phosphorus co-limitation of bacterial productivity and growth in the oligotrophic subtropical North Atlantic. *Limnol. Oceanogr.* **53**, 824–834 (2008).

Supplementary Information is linked to the online version of the paper at www.nature.com/nature.

Acknowledgements We thank the captains and crews of the RVs *L'Atalante*, *Atlantic Explorer*, *Kilo Moana* and *Ka'imikai-o-Kanaloa*. J. Dacey, R. Johnson, N. Levine, T. Gregory, D. Sadler, H. Claustre and A. Sciandra provided access and logistical support for our cruises. K. Björkman and P. Rimmelin provided phosphate data. N. Trowbridge, M. Brandon, S. Haley, E. Orchard and K. Roache-Johnson assisted with cultures. D. Glover provided input on data treatment and presentation. This research was supported by grants from the National Science Foundation (OCE-0646944 to B.A.S.V.M., OCE-0451419 to S.T.D., OCE-0326616 to D.M.K., OCE-0453023 to M.W.L., OCE-0453019 to L.R.M. and DEB-0207085 to M.S.R.), the Office of Naval Research (N00014-06-1-0134 to B.A.S.V.M.) and Czech Republic research grants (GACR-206/07/0241 and GAAV-1QS500200570 to M.K.). The BIOSOPE campaign was a contribution of the French LEFE-CYBER program funded by the Centre National de la Recherche Scientifique and the Institut des Sciences de l'Univers. Funding was also provided by the Gordon and Betty Moore Foundation, the Center for Microbial Oceanography: Research and Education, the Woods Hole Oceanographic Institution Ocean Life Institute and the Woods Hole Oceanographic Institution Mary Sears Travel Fund.

Author Contributions B.A.S.V.M. designed the study, conducted experiments and collected samples at sea, and wrote the manuscript. All of the other authors made essential, substantive contributions to the original and/or revised manuscripts. In addition, H.F.F. analysed lipids by mass spectrometry. B.E.P. assisted with lipid analyses and prepared samples in the laboratory and at sea. S.T.D., M.K., L.R.M., M.S.R. and E.A.W. each contributed to the design of the study and conducted experiments with cultures under phosphorus-limiting and -replete conditions. D.M.K., M.W.L. and T.M. provided data from the cruises and facilitated the work at sea.

Author Information Reprints and permissions information is available at www.nature.com/reprints. Correspondence and requests for materials should be addressed to B.A.S.V.M. (bvanmooy@whoi.edu).

Sleep and sensorimotor integration during early vocal learning in a songbird

Sylvan S. Shank¹ & Daniel Margoliash^{1,2}

Behavioural studies widely implicate sleep in memory consolidation in the learning of a broad range of behaviours^{1–4}. During sleep, brain regions are reactivated^{5,6}, and specific patterns of neural activity are replayed^{7–10}, consistent with patterns observed in previous waking behaviour. Birdsong learning is a paradigmatic model system for skill learning^{11–14}. Song development in juvenile zebra finches (*Taeniopygia guttata*) is characterized by sleep-dependent circadian fluctuations in singing behaviour, with immediate post-sleep deterioration in song structure followed by recovery later in the day¹⁵. In sleeping adult birds, spontaneous bursting activity of forebrain premotor neurons in the robust nucleus of the arcopallium (RA) carries information about day-time singing¹⁶. Here we show that, in juvenile zebra finches, playback during the day of an adult ‘tutor’ song induced profound and tutor-song-specific changes in bursting activity of RA neurons during the following night of sleep. The night-time neuronal changes preceded tutor-song-induced changes in singing, first observed the following day. Interruption of auditory feedback greatly reduced sleep bursting and prevented the tutor-song-specific neuronal remodelling. Thus, night-time neuronal activity is shaped by the interaction of the song model (sensory template) and auditory feedback, with changes in night-time activity preceding the onset of practice associated with vocal learning. We hypothesize that night-time bursting induces adaptive changes in premotor networks during sleep as part of vocal learning. By this hypothesis, adaptive changes driven by replay of sensory information at night and by evaluation of sensory feedback during the day interact to produce the complex circadian patterns seen early in vocal development.

To explore the role of sleep in the early phases of song learning, we characterized the properties of single RA neurons in head-fixed, sleeping juvenile zebra finches during nights before and after the onset of tutor song exposure. Sleep was defined on the basis of behavioural and electroencephalographic criteria (see Supplementary Information)¹⁷. During sleep, RA neurons tended to discharge irregularly or ‘burst’, as seen in distributions of inter-spike intervals (ISIs; Fig. 1a, black curve)¹⁶. Starting on the night after the first day of exposure to the tutor song, there was a sharp increase in the amount of high-frequency spiking activity (Fig. 1a, red curve). Across all birds, we quantified the effect of tutor song exposure as a normalized change in the percentage of ISIs ≤ 40 ms, which showed a significant increase starting on the night after the first day of tutor song exposure and persisted thereafter (Fig. 1b). A significant result was also obtained considering firing rates that were normalized by linearly scaling the ISIs for each cell ($P = 0.02$, repeated measures analysis of variance (ANOVA), $\alpha = 0.05$; Fig. 1b, open circles). This verified that the increase in high-frequency activity was not dependent on changes in mean spike rates after tutoring, but was the result of a specific increase in high-frequency activity including bursting.

Within each bird there was some variation in the amount of high-frequency activity of RA cells on nights after the onset of song learning, but the tendency towards shorter ISIs was apparent in most cells (Fig. 1c).

Emerging RA bursting activity, furthermore, was shaped by the specific tutor song that a bird heard. Nightly mean ISI distributions were calculated for all RA neurons recorded for each bird after tutor song exposure (which showed little difference from night to night; Fig. 2c), and nightly mean distributions were averaged together to generate one mean curve per bird. For the resulting post-exposure curves, within the high-frequency range (ISIs ≤ 40 ms), the shapes—as assessed using Pearson correlation coefficients—were more similar in birds hearing the same tutor song than in birds hearing different tutor songs (see Supplementary Information). This grouping of ISI distribution shapes by tutor song can be visualized by comparing the average ISI distributions for individual birds on nights before tutor song exposure to those on nights after tutor song exposure (Fig. 2a, black and coloured lines, respectively). The differences between groups can be visualized by comparing global average ISI distributions—one for each group of birds hearing a given tutor song (Fig. 2b).

Once a bird was exposed to a tutor song, a prototypical post-exposure ISI distribution shape was quickly obtained and then maintained. To quantify this, we compared (using Pearson correlations) the nightly ISI distributions (≤ 40 ms) for each bird before and after song exposure to the corresponding global mean curve (Fig. 2b), excluding data from the bird being analysed from the global mean distributions. Before tutor song exposure, both the within- and between-group comparisons (Fig. 2d, black and grey dots, respectively) had large variability and were not significantly different from each other on any night ($P = 0.25$ to $P = 0.73$). By the first night after tutor song exposure, ISI distributions had already assumed their post-exposure shape, showing increased Pearson correlations with much lower variability (Fig. 2d, red dots), whereas the across-group correlations did not increase (Fig. 2d, pink dots). These differences were statistically significant starting from the first night ($P = 0.0082$, two-tailed t -test, $\alpha = 0.05$), and continued to show a significant difference throughout the post-exposure period ($P < 0.05$ for 8 out of 11 post-exposure nights; see also Supplementary Fig. 2), emphasizing that stable changes in ISI distributions were rapidly achieved and then maintained in the days after tutor song exposure.

Zebra finches begin singing as early as 25 days of age¹⁸, so our ~ 40 -day-old birds had extensive sensorimotor experience before neural recordings were performed. To explore the influence of singing and auditory feedback on the structure of RA neuronal bursting, we performed two additional experiments. We prevented singing by surgically muting two birds (a third bird, M2, sang in spite of the surgery), and raised a second group of four birds in continuous 100 dB white noise environments to suppress auditory feedback.

¹Department of Psychology, ²Department of Organismal Biology and Anatomy, University of Chicago, Chicago, Illinois 60637, USA.

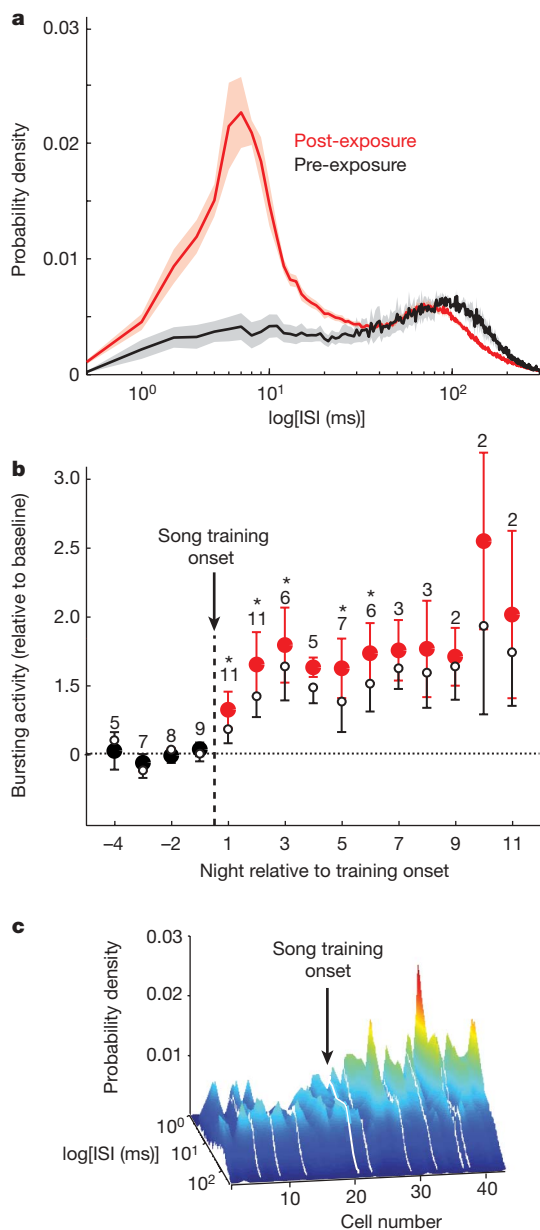


Figure 1 | High-frequency bursting in RA. **a**, ISI distributions for all cells for each night from bird S6 were averaged; each curve (\pm s.e.m.) shows the global average of all nights before tutor song exposure (black; $n = 19$ cells, 3 nights, PHD 43–47) and after exposure (red; $n = 59$ cells, 12 nights, PHD 49–62). **b**, The tutor song triggered an increase in high-frequency bursting (13 birds, $n = 489$ cells, 37.4 ± 56.4 min per cell, 5.6 cells per bird per night). The number of birds contributing to each point is shown above each point. $*P < 0.05$ by sign test comparing mean pre- and post-exposure values within birds, $\alpha = 0.05$. Filled circles: untransformed data (\pm s.e.m.); open circles: spike-rate normalized data ($-$ s.e.m.; see Methods and Supplementary Information). **c**, ISI distributions for all 44 consecutively recorded cells from bird S9. White lines indicate daytime.

All seven birds cued tutor song playback; for birds in the white noise environments, this also briefly eliminated the masking noise. A noise-cancellation technique allowed us to qualitatively assess the amount of singing in white noise conditions (Fig. 3e).

The absence of auditory feedback had large effects on RA sleep bursting. Even before the onset of tutor song exposure, experimental birds showed notably reduced levels of bursting activity compared to birds with intact auditory feedback. ISI distributions showed suppressed short-duration ISIs for all six feedback-deprived birds (that is, excluding M2; 14 nights, 65 cells; Fig. 3a, lower black line)

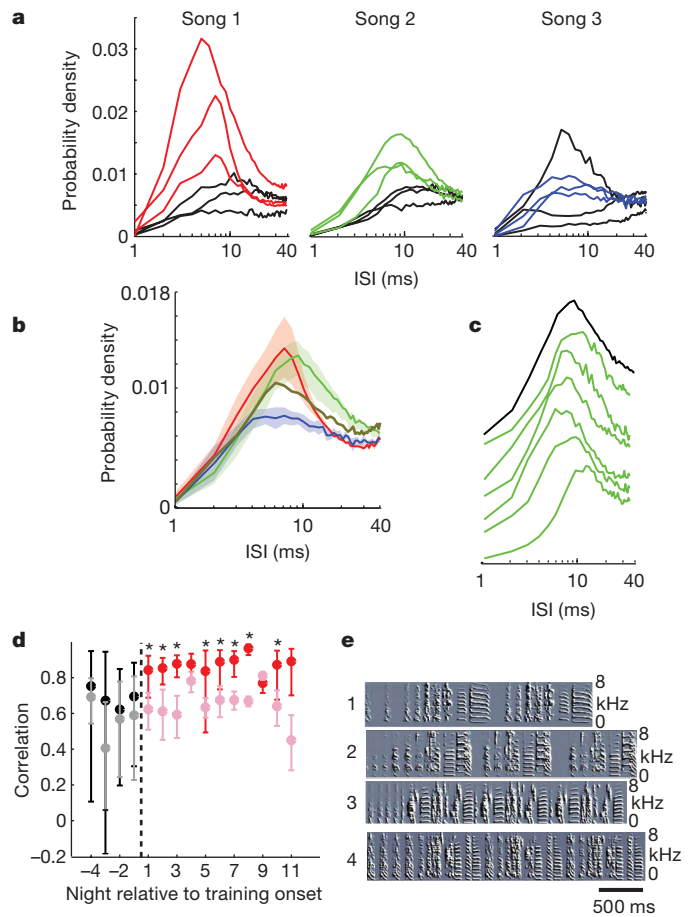


Figure 2 | Tutor songs shape RA bursting. **a**, ISI distributions averaged across all post-exposure nights, one per bird, by tutor song. Black lines, pre-exposure; coloured lines, post-exposure. Song 1, $n = 3$ birds, 59 cells (only a representative 3 out of 7 birds are shown to reduce clutter, see Supplementary Fig. 4 for all birds); song 2, $n = 3$ birds, 85 cells; song 3, $n = 3$ birds, 38 cells. **b**, Global mean (\pm s.e.m.) ISI distributions after tutor song exposure; each curve is the average for each tutor song group. For song 1, two birds with the largest high frequency peaks were removed from the average so that curves have comparable peak heights. The brown line is the single song 4 bird. **c**, Green lines are averages for each of the six post-exposure nights in one bird; the black line is the song 2 global mean (from **b**). **d**, ISI distributions change on exposure to tutor song. Shown are Pearson correlation coefficients comparing nightly curves for a given bird with global post-exposure means (see text). Nightly means (\pm s.d.) comparing birds hearing the same (pre- and post-exposure, black and red dots, respectively) or different (grey and pink dots, respectively) tutor songs are plotted. **e**, Tutor song spectrographs.

compared to birds with normal feedback ($n = 13$ birds, 38 nights, 163 cells; Fig. 3a, upper black line). Considering ISIs ≤ 40 ms, these differences were significant ($P = 0.03$, two-tailed t -test on arcsin-transformed data, $\alpha = 0.05$).

The absence of feedback also disrupted the changes in RA induced by sensory exposure. In feedback-deprived birds, tutor song exposure did not induce an increase in bursting activity (comparing ISIs ≤ 40 ms before to those after exposure, $P = 0.45$, two-tailed t -test on arcsin-transformed data, $\alpha = 0.05$, $n = 6$ birds, 31 nights, 151 cells). Furthermore, on the nights after tutor song exposure, high-frequency bursting was greatly suppressed in feedback-deprived birds ($n = 6$ birds, 18 nights, 98 cells; Fig. 3b, lower red line) compared with normal birds (Fig. 3b, upper red line; $P = 0.04$, two-tailed t -test on arcsin-transformed data, $\alpha = 0.05$).

Subsequent recovery of sensorimotor feedback released RA neurons to rapidly recover to normal patterns. After exposure to 'song 1', but before cessation of the masking noise, the four birds in the white noise environment showed suppressed high-frequency activity compared to

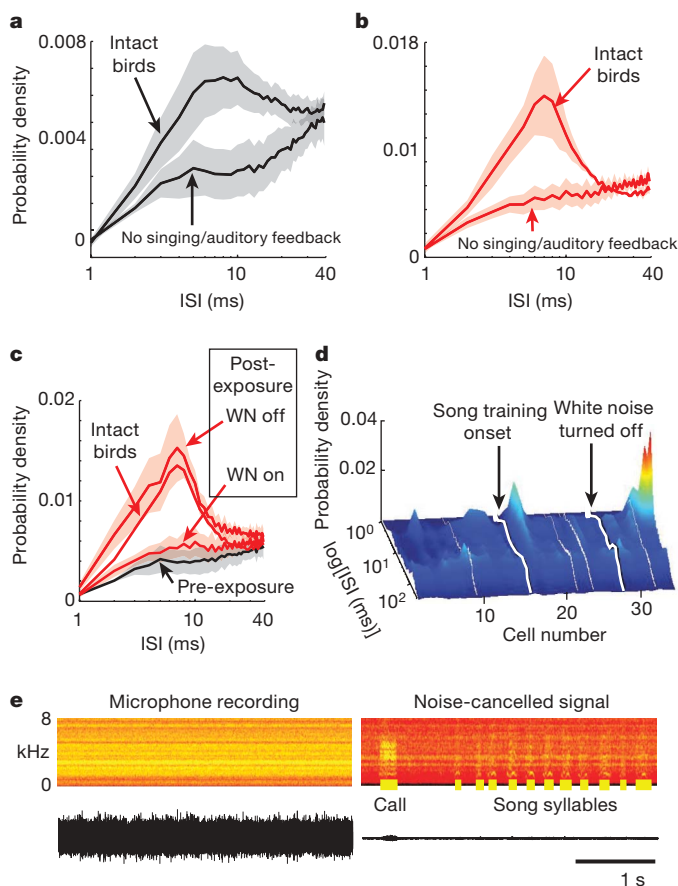


Figure 3 | RA sleep activity in absence of auditory feedback (white noise or muted). **a**, ISI distributions before tutor song exposure, averaged across two muted birds and four birds raised in white noise (lower black line), and averaged (for comparison) across 13 birds with normal feedback (upper black line). **b**, Birds exposed to white noise and those that were muted fail to show tutor-song-specific ISI distributions after song exposure. Lower red line: mean post-exposure distribution from muted birds and those exposed to white noise (5 out of 6 birds heard song 1). Upper red line: mean distribution from intact song 1 birds (same as in Fig. 2c). **c**, Bursting returns when feedback is restored. Birds exposed to white noise ($n = 4$) both pre-exposure (black line) and post-exposure but in white noise (lower red line) show suppression of bursting; bursting recovers after white noise (WN) is turned off (upper red line). Compare with distribution for intact song 1 birds (middle red line). **d**, Profound suppression of bursting for all cells in a bird exposed to white noise. White lines represent daytime. **e**, Recording of singing in the presence of 100 dB white noise without and with noise cancellation (left and right, respectively). Right, bold yellow lines mark vocalizations.

birds with normal access to their feedback (comparing ISIs ≤ 40 ms, $P = 0.04$, two-tailed t -test on arcsin-transformed data, $\alpha = 0.05$, $n = 12$ nights, 56 cells), with similar ISI distributions to those observed before tutor song exposure ($n = 8$ nights, 44 cells; Fig. 3c, black curve). The white noise was turned off for a portion of the fourth day of tutor song exposure (turned off for the first three hours, $n = 2$ birds; turned off for the last five hours, $n = 2$ birds) and then turned off completely starting on the fifth day. In two birds that sang robustly during white noise exposure (one released from white noise at the start of the day, the other at the end of the day), during sleep on the night after the fourth day of exposure, the expected tutor-song-specific ISI distributions were observed in the activity of RA neurons for the first time. A third robust singer also showed the expected shift, but only on the following night (Fig. 3d). Singing was suppressed in the fourth bird (white noise (WN)4) throughout the period of white noise exposure and showed a robust increase only by the fourth day after white noise was turned off. Concomitantly, sleep bursting of RA neurons also

remained suppressed for those three additional nights, and then on the night after that first day of singing RA neurons expressed bursting with an ISI distribution appropriate for song 1 ($r = 0.92 \pm 0.04$, -0.08 within-group on the two nights post-singing onset versus $r = 0.16 \pm 0.39$, -0.46 for the three nights before singing onset). The mean ISI curve for all four birds ($n = 17$ nights, 84 cells), representing only the data collected after white noise was turned off ($n = 3$ birds) or after white noise was turned off and singing had commenced (for WN4), was typical of birds exposed to song 1 with normal feedback (Fig. 3c, upper red curve).

Analysis of the fine structure of vocal development further demonstrated the tight temporal correlation between song development and night-time bursting. We examined the entropy variance—a measure of song complexity that shows an upward developmental trend tracking song learning¹⁵—for all song segments each bird sang each day. By this measure, songs gained structure in a saltatory manner on the second day of tutor song exposure ($P = 0.006$, repeated measures ANOVA, $\alpha = 0.05$; Fig. 4a)¹⁹. The increase in entropy variance on the second day of training was not present with the first vocalizations of that day. Instead, the increase seen on the second day was achieved across singing in the early part of the day. On days before tutor song exposure and on the first day of exposure, there was no significant increase in entropy variance across morning singing (Fig. 4b, c, see Supplementary Information for statistical analysis). However, starting on the second day of exposure and on the days thereafter, birds showed a clear increase in entropy variance across the early part of the day (Fig. 4b, c), similar to what has been reported previously^{15,20}, and this was significant (see Supplementary Information). Because birds vocalized on the first day of song tutoring before and after they cued tutor song playback, however, this could confound the implications of changes in night-time RA bursting if the birds modified their songs on the first day but only after tutor song exposure, and this was not reflected in mean changes for that day. Analysis of singing at the end of the day, analysis of the most complex songs and analysis of singing immediately after tutoring, however, all failed to support this alternative explanation (Supplementary Information).

In birdsong learning, memories of conspecific songs are acquired early in development and act as a referent to guide subsequent auditory-feedback-dependent sensorimotor learning^{12–14,21–24}. In an influential account of this process, the acquired memory of song was envisioned to act as a ‘sensory template’, directly matching auditory feedback arising from singing with the sensory representation of the memorised song guiding changes in vocal output^{13,25}. We found that the effects of tutor song exposure were immediate, profound and distributed—expressed as rapid, fundamental and long-lasting changes in song-specific high-frequency spiking activity in a fore-brain nucleus one synapse from the motor nucleus innervating the syrinx. The isolation rearing our birds experienced before tutor song exposure is likely to have enhanced the magnitude of these effects beyond what would otherwise be seen in normally raised birds²⁶. Nevertheless, the timing and song-type specificity of the changes are consistent with the action of a song (sensory) memory influencing the functional organization of a motor circuit²⁷, although a causal link has yet to be established. The rapidity of changes in RA sleep activity and its subsequent stability bolsters the idea that the sensory representation was quickly established, opening a ‘gate’ or enabling a dormant circuit, and that song development proceeded with the sensory representation expressed at night guiding changes in daytime premotor patterns. This motivates a new hypothesis: sensory memories can act indirectly (offline) on sensorimotor performance by means of spontaneous activity.

We speculate that during sleep, changes in the RA network (‘consolidation’) reflect updating of sensory memories. Night-time changes would establish a new configuration in the RA network. The following morning, plastic responses released by singing subsequent to night-time reconfiguration might first drive the network away from stability before it recovers stability with additional iterations; this could explain

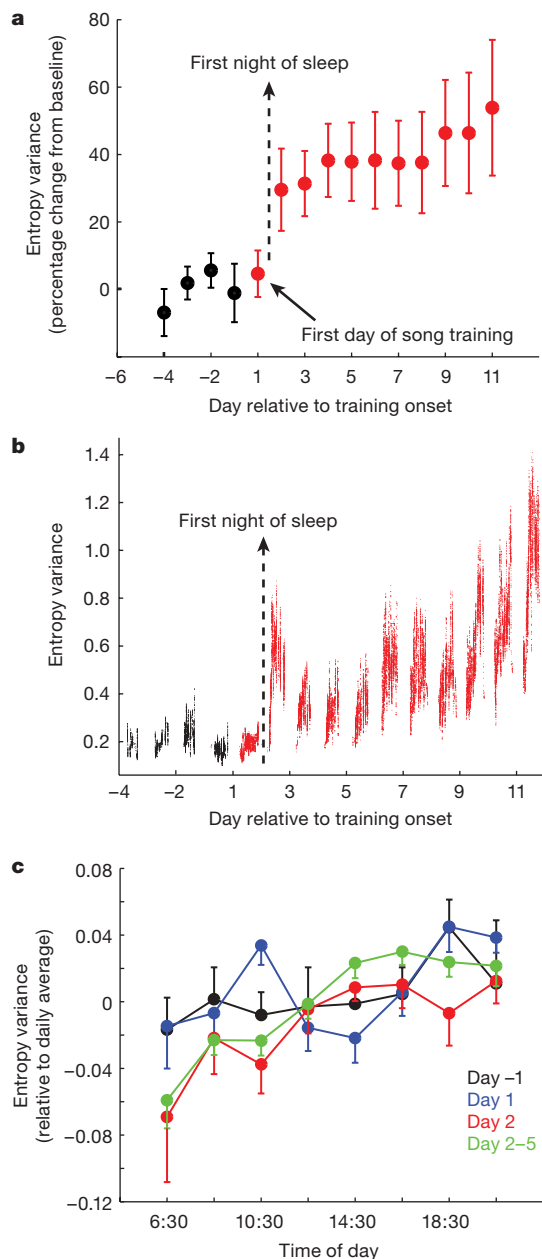


Figure 4 | Entropy variance changes after a night of sleep. **a**, Mean daily entropy variance for bird vocalizations. Data for each bird were normalized by dividing within-day means by the mean of the four nights preceding exposure. **b**, Entropy variance of all sounds produced by one bird across 15 days, smoothed by 40 data points within each day. The entropy variance increase across the second day of training is achieved across morning singing. **c**, Entropy variance daily trends, averaged across all (non-manipulated) birds in two-hour bins (\pm s.e.m.) for the day before training onset (black), the first day of training (blue), the second day of training (red) and the average of the second to the fifth day of training (green).

the non-monotonic changes in singing observed each morning during development¹⁵. A larger magnitude of non-monotonic singing behaviour—which is positively correlated with the eventual degree of song copying¹⁵—would result from stronger or more accurate sensory influences on premotor networks. Because the differences between sensory (night time) and motor (daytime) network configurations decrease during development (improved sensorimotor integration), the magnitude of the circadian singing patterns would decrease, as is actually observed¹⁵. The plastic changes that we have described are released by the confluence of two sensory signals: the model and feedback. We further speculate this could occur at the level of RA itself,

which receives inputs from the descending motor pathway and from the cortico-basal ganglia pathway.

Spontaneous activity guides early development of the nervous system. Here, high-frequency burst-mode firing, a common feature of vertebrate forebrain neurons, is structured by sleep-mediated learning mechanisms, emerging strikingly late in development as the organism experiences appropriate environmental cues. It remains to be seen whether bursting sleep activity represents the activation of sensory traces in other forms of skill learning, and perhaps more generally. Structured spontaneous discharge is observed broadly in the forebrain during sleep²⁸, and has been associated with recall^{29,30}.

METHODS SUMMARY

Birds were bred in-house in sound-isolation boxes, and were female-raised to isolate them from adult male song beginning on or before post-hatch-day (PHD) 15. Males ($n = 21$) were isolated in individual sound-isolation boxes between PHD 30 and PHD 35, and received a preparatory surgery between PHD 37 and PHD 40. Song was recorded continuously starting on or before the first day post-surgery until at least PHD 90, and neural recordings began two to three days later. Birds were permitted to self-elicited song playback by pulling a string in the cage after 3.3 ± 1.6 nights of neuronal recordings.

Bursting increase. We quantified the increase in high-frequency neuronal activity as a normalized change in the percentage of the ISI distribution ≤ 40 ms, which captures short intervals associated with bursting in these juvenile birds and the difference in bursting before and after song exposure (Fig. 1a). Nightly values were calculated by first taking the mean ISI distribution across cells for a given night for a given bird. The proportion of the mean distribution ≤ 40 ms was found and nightly values were normalized within birds by the mean from the four nights preceding tutor song exposure onset (Fig. 1b). We also performed the same calculation but first applying a linear transformation of ISIs so that the mean spike rate was the same for all cells before and after tutor song exposure, finding a similar increase in bursting after song exposure (Fig. 1b, open circles).

Correlation coefficients. For statistical analysis of Pearson correlation coefficients, Fisher's r -to- z transformation was performed on the correlation values. Where the transformed data are plotted (Fig. 2d), the r values have asymmetrical standard deviations because the transformation yields values between -1 and 1 .

Full Methods and any associated references are available in the online version of the paper at www.nature.com/nature.

Received 11 June; accepted 31 October 2008.

Published online 14 December 2008.

- Karni, A., Tanne, D., Rubenstein, B. S., Askenasy, J. J. & Sagi, D. Dependence on REM sleep of overnight improvement of a perceptual skill. *Science* **265**, 679–682 (1994).
- Fenn, K. M., Nusbaum, H. C. & Margoliash, D. Consolidation during sleep of perceptual learning of spoken language. *Nature* **425**, 614–616 (2003).
- Wagner, U., Gais, S., Haider, H., Verleger, R. & Born, J. Sleep inspires insight. *Nature* **427**, 352–355 (2004).
- Walker, M. P. & Stickgold, R. Sleep, memory, and plasticity. *Annu. Rev. Psychol.* **57**, 139–166 (2006).
- Peigneux, P. *et al.* Are spatial memories strengthened in the human hippocampus during slow wave sleep? *Neuron* **44**, 535–545 (2004).
- Rasch, B., Buchel, C., Gais, S. & Born, J. Odor cues during slow-wave sleep prompt declarative memory consolidation. *Science* **315**, 1426–1429 (2007).
- Ji, D. & Wilson, M. A. Coordinated memory replay in the visual cortex and hippocampus during sleep. *Nature Neurosci.* **10**, 100–107 (2007).
- Qin, Y. L., McNaughton, B. L., Skaggs, W. E. & Barnes, C. A. Memory reprocessing in corticocortical and hippocampocortical neuronal ensembles. *Phil. Trans. R. Soc. Lond. B* **352**, 1525–1533 (1997).
- Nadasdy, Z., Hirase, H., Czurko, A., Csicsvari, J. & Buzsáki, G. Replay and time compression of recurring spike sequences in the hippocampus. *J. Neurosci.* **19**, 9497–9507 (1999).
- Hennevin, E., Huetz, C. & Edeline, J. M. Neural representations during sleep: from sensory processing to memory traces. *Neurobiol. Learn. Mem.* **87**, 416–440 (2007).
- Marler, P. & Tamura, M. Culturally transmitted patterns of vocal behavior in sparrows. *Science* **146**, 1483–1486 (1964).
- Marler, P. A comparative approach to vocal learning: song development in white-crowned sparrows. *J. Comp. Physiol. Psychol.* **71**, 1–25 (1970).
- Konishi, M. The role of auditory feedback in the control of vocalization in the white-crowned sparrow. *Z. Tierpsychol.* **22**, 770–783 (1965).
- Zeigler, H. P. & Marler, P. R. (eds) *Behavioral Neurobiology of Birdsong* (Ann. NY Acad. Sci., 2004).

15. Derégnaucourt, S., Mitra, P. P., Feher, O., Pytte, C. & Tchernichovski, O. How sleep affects the developmental learning of bird song. *Nature* **433**, 710–716 (2005).
16. Dave, A. S. & Margoliash, D. Song replay during sleep and computational rules for sensorimotor vocal learning. *Science* **290**, 812–816 (2000).
17. Low, P. S., Shank, S. S., Sejnowski, T. J. & Margoliash, D. Mammalian-like features of sleep structure in zebra finches. *Proc. Natl Acad. Sci. USA* **105**, 9081–9086 (2008).
18. Roper, A. & Zann, R. The onset of song learning and song tutor selection in fledgling zebra finches. *Ethology* **112**, 458–470 (2006).
19. Tchernichovski, O., Mitra, P. P., Lints, T. & Nottebohm, F. Dynamics of the vocal imitation process: how a zebra finch learns its song. *Science* **291**, 2564–2569 (2001).
20. Crandall, S. R., Adam, M., Kinnischtzke, A. K. & Nick, T. A. HVC neural sleep activity increases with development and parallels nightly changes in song behavior. *J. Neurophysiol.* **98**, 232–240 (2007).
21. Marler, P. & Peters, S. Sparrows learn adult song and more from memory. *Science* **213**, 780–782 (1981).
22. Hultsch, H. & Todt, D. Memorization and reproduction of songs in nightingales (*Luscinia megarhynchos*): evidence for package formation. *J. Comp. Physiol. A* **165**, 197–203 (1989).
23. Funabiki, Y. & Konishi, M. Long memory in song learning by zebra finches. *J. Neurosci.* **23**, 6928–6935 (2003).
24. Leonardo, A. & Konishi, M. Decrystallization of adult birdsong by perturbation of auditory feedback. *Nature* **399**, 466–470 (1999).
25. Konishi, M. in *Perception and Experience* (eds Walk, R. D. & Pick, H. L. J.) 105–118 (Plenum, 1978).
26. Adret, P. & Margoliash, D. Metabolic and neural activity in the song system nucleus robustus archistriatalis: effect of age and gender. *J. Comp. Neurol.* **454**, 409–423 (2002).
27. Nick, T. A. & Konishi, M. Neural song preference during vocal learning in the zebra finch depends on age and state. *J. Neurobiol.* **62**, 231–242 (2005).
28. Evarts, E. V., Bental, E., Bihari, B. & Huttenlocher, P. R. Spontaneous discharge of single neurons during sleep and waking. *Science* **135**, 726–728 (1962).
29. Pastalkova, E., Itskov, V., Amarasingham, A. & Buzsáki, G. Internally generated cell assembly sequences in the rat hippocampus. *Science* **321**, 1322–1327 (2008).
30. Gelbard-Sagiv, H., Mukamel, R., Harel, M., Malach, R. & Fried, I. Internally generated reactivation of single neurons in human hippocampus during free recall. *Science* **322**, 96–101 (2008).

Supplementary Information is linked to the online version of the paper at www.nature.com/nature.

Acknowledgements We thank M. Fukushima for extensive discussions, and J.-M. Ramirez, H. C. Nusbaum, S. M. Sherman and M. Konishi for comments on the manuscript. A. S. Dave and M.F. designed and implemented the white noise recording/cancellation environment.

Author Contributions S.S.S. performed the experimental work.

Author Information Reprints and permissions information is available at www.nature.com/reprints. Correspondence and requests for materials should be addressed to D.M. (dan@bigbird.uchicago.edu).

METHODS

Birds were maintained on a reverse light schedule (light, 6:30 p.m.–10:30 a.m.; light:dark, 16 h:8 h) to permit experiments during daytime hours. Around PHD 38, subjects received a single surgery, including implantation of a head-restraint pin and dural EEG electrodes, and, for some birds, muting.

Neural recordings began two to three days after the surgery, in the same boxes that housed the birds. Birds were wrapped in a cloth and the head was immobilized, connectors were attached to EEG electrode leads, and a high-impedance electrode was lowered into the brain above RA. The box was then closed for the duration of the eight-hour night. Birds were illuminated with infrared light, and EEG signals and video were recorded for the duration of the night while single-cell recordings in RA were obtained. Birds experienced normal levels of rapid eye movement (REM) and non-REM sleep as that which has been reported in songbirds previously^{17,31}, and brief periods of wakefulness. RA was identified stereotactically and by the readily identifiable activity patterns of RA neurons.

After 3.3 ± 1.6 nights in the recording apparatus (range 1–6 nights), when sufficient pre-exposure data had been obtained (2.6 ± 1.1 nights of successful recordings; range 1–5 nights), birds were allowed to self-elicited playback of a song model by pulling a string, until PHD 90. Birds were limited to ten renditions of the tutor song during each morning and afternoon training session. Neuronal recordings were collected over 5–16 nights (except one bird for which we only succeeded in collecting data for nights –2, –1 and 1 relative to song exposure).

Because clearly identifiable repeated syllables do not begin to emerge until several days after tutor song exposure onset¹⁵, rather than try to cluster song elements in proto-syllables, we examined the entropy variance of all song elements produced to assess daily trends before and after the onset of tutor song exposure. Data collection and analysis used Sound Analysis Pro, Matlab, and in-house software.

Surgical muting. For some birds, a muting procedure³² was performed at the time of the surgery. A small opening was made into the interclavicular air sac. A small fenestra was made in the trachea just rostral to the syrinx and in the bronchi immediately caudal to the syrinx within the interclavicular air sac. The external opening was sutured closed. This procedure probably eliminates the ability to generate pressure across the syrinx. Birds M1 and M3 were successfully muted but bird M2 continued to vocalize immediately after the surgery (presumably, the vocal tract holes sealed). Both muted birds eventually recovered the ability to sing. On days 9 and 11 post-surgery, M1 and M3 began making very sparse, soft vocalizations composed of simple harmonic stacks of various length. Over the following few weeks, birds developed normal plastic song and both eventually achieved a final copy that showed learning in the range of the non-devocalized birds.

White noise cancellation. White noise was played continuously, during the subjective day, starting on the day before the first night of neural recordings. To assess whether birds were singing, we used an active noise cancellation technique³³. In brief, probe auditory signals were played and recorded to estimate the transfer function of the recording chamber. Using the known input to the speaker and the transfer function, the white noise signal broadcast from the speaker was subtracted from the overall signal reaching the microphone, allowing us to observe song (albeit with low fidelity). On the basis of this technique we observed that birds WN1, WN2 and WN3 sang frequently while exposed to continuous white noise (and they also sang immediately after the white noise was turned off). Bird WN4 failed to sing in white noise and also only recovered singing four days after white noise exposure was terminated.

Song similarity measures. The similarity of a bird's song to its tutor song was computed as described previously^{15,19,34} using Sound Analysis Pro software. In brief, means and variances of acoustic features, principally duration, pitch, Weiner entropy and mean frequency, were calculated for each syllable produced by each bird. Similarity between a given song and the tutor song a bird heard was computed by a quantitative comparison of this array of acoustic features.

31. Rattenborg, N. C. *et al.* Migratory sleeplessness in the white-crowned sparrow (*Zonotrichia leucophrys gambelii*). *PLoS Biol.* **2**, E212 (2004).

32. Pytte, C. L. & Suthers, R. A. A bird's own song contributes to conspecific song perception. *Neuroreport* **10**, 1773–1778 (1999).

33. Leonardo, A. Experimental test of the birdsong error-correction model. *Proc. Natl Acad. Sci. USA* **101**, 16935–16940 (2004).

34. Tchernichovski, O., Nottebohm, F., Ho, C. E., Pesaran, B. & Mitra, P. P. A procedure for an automated measurement of song similarity. *Anim. Behav.* **59**, 1167–1176 (2000).

LETTERS

Innate immune recognition of infected apoptotic cells directs T_H17 cell differentiation

Miriam Beer Torchinsky¹, Johan Garaude¹, Andrea P. Martin¹ & J. Magarian Blander¹

Adaptive immune responses rely on differentiation of CD4 T helper cells into subsets with distinct effector functions best suited for host defence against the invading pathogen. Interleukin (IL)-17-producing T helper cells (T_H17) are a recently identified subset, separate from the T helper type 1 (T_H1) and T helper type 2 (T_H2) subsets¹. Synergy between the cytokines transforming growth factor- β and IL-6 *in vitro* induces development of T_H17 cells in mouse^{1–5} and human⁶ systems, whereas IL-23 supports expansion of these cells^{2,4,5}. However, it is not known which conditions *in vivo* would induce this combination of cytokines. Furthermore, it is enigmatic that a combination of pro-inflammatory and anti-inflammatory cytokines would be required to generate an effector T_H17 response. Here we show that the relevant physiological stimulus triggering this combination of cytokines is the recognition and phagocytosis of infected apoptotic cells by dendritic cells. Phagocytosis of infected apoptotic cells uniquely triggers the combination of IL-6 and transforming growth factor- β through recognition of pathogen-associated molecular patterns⁷ and phosphatidylserine exposed on apoptotic cells⁸, respectively. Conversely, phagocytosis of apoptotic cells in the absence of microbial signals induces differentiation of the closely related regulatory T cells, which are important for controlling autoimmunity⁹. Blocking apoptosis during infection of the mouse intestinal epithelium with the rodent pathogen *Citrobacter rodentium*¹⁰, which models human infections with the attaching and effacing enteropathogenic and enterohaemorrhagic *Escherichia coli*, impairs the characteristic T_H17 response in the lamina propria. Our results demonstrate that infected apoptotic cells are a critical component of the innate immune signals instructing T_H17 differentiation, and point to pathogens particularly adept at triggering apoptosis that might preferentially induce T_H17-mediated immunity. Because T_H17 cells have been correlated with autoimmune diseases¹, investigation of the pathways of innate recognition of infected apoptotic cells might lead to improved understanding of the causative defects in autoimmunity.

We asked which innate immune recognition events trigger simultaneous synthesis of transforming growth factor- β (TGF- β) and IL-6. Whereas phagocytosis of apoptotic cells induces TGF- β synthesis⁸, IL-6 is induced when microbial structures activate pattern-recognition receptors such as Toll-like receptors (TLRs)^{7,11}. Concomitant ligation of TLRs during phagocytosis of infected apoptotic cells might, therefore, constitute a scenario where IL-6 and TGF- β are induced together. We used either apoptotic neutrophils isolated following peritoneal injection of *E. coli* (*E. coli*-infected neutrophils) or apoptotic B cells carrying the TLR4 ligand lipopolysaccharide (LPS-blasts). Dendritic cells (DCs) that phagocytosed apoptotic LPS-blasts secreted more IL-23 and TGF- β than DCs treated with free LPS, and importantly only TGF- β made in response to infected or uninfected apoptotic cells was biologically active (Fig. 1a and

Supplementary Fig. 1). Despite similar IL-6 levels, the level of IL-12 produced following phagocytosis of apoptotic LPS-blasts was lower than that in response to free LPS (Fig. 1a), which may also favour T_H17 over T_H1 development in response to apoptotic LPS-blasts. Quantitative polymerase chain reaction with reverse transcription (RT-qPCR) analyses of RNA from DCs further showed induction of *Il6*, *Il23a* (encodes IL-23p19), *Il12a* (IL-12p35), *Il12b* (IL-12p40), *Il10* and *Tnfrsf15* (TNF family member TL1A), which promotes T_H17 proliferation¹², in response to apoptotic LPS-blasts and apoptotic *E. coli*-infected neutrophils (Supplementary Fig. 2). These transcripts were not induced in response to uninfected apoptotic B cells or apoptotic neutrophils.

To test whether the cytokine milieu created by these conditions is conducive for T_H17 induction, we cultured naive (CD25[−]CD62L^{high}CD44^{low}) CD4 T cells in conditioned medium (CM) derived from DCs that phagocytosed apoptotic LPS-blasts. Naive CD4 T cells cultured with this CM (DCCM-apoptotic LPS-blasts) secreted IL-17A (referred to as IL-17 from hereon), indicating differentiation into the T_H17 lineage (Fig. 1b, filled bars). Published T_H17 differentiation protocols that use antigen-presenting cells require neutralization of the antagonistic effects of the cytokine interferon- γ (IFN- γ)^{1,2,4}. Furthermore, TLR ligands are classically considered to induce T_H1 cells producing IFN- γ . Whereas IFN- γ neutralization allowed some induction of IL-17-secreting (IL-17⁺) CD4 T cells by CM from DCs treated with free LPS, anti-IFN- γ was not required for IL-17 secretion by T cells activated in DCCM-apoptotic LPS-blasts (Fig. 1b, open bars), indicating that DC stimulation by TLR ligands within the context of apoptotic cells creates particularly efficient conditions for generation of IL-17⁺ CD4 T cells. No IL-17 was detected when naive CD4 T cells were cultured with CM from DCs that phagocytosed necrotic cells (Supplementary Fig. 3), or with CM from DCs that phagocytosed apoptotic B cells not carrying TLR ligands (DCCM-apoptotic B cells; Fig. 1b). Supplementing this latter CM with IL-6 restored IL-17 secretion, indicating that TLR ligation during recognition of apoptotic LPS-blasts elicits IL-6 production that complements TGF- β induced by apoptotic cells (Fig. 1b).

RT-qPCR showed high induction of *Rorc*, which encodes the T_H17-lineage-specific transcription factor ROR γ ¹³, and *Il17a* when sorted naive CD4 T cells were activated in the presence of DCCM-apoptotic LPS-blasts or DCCM-apoptotic B cells supplemented with IL-6 (Fig. 1c). Notably, *Il22*, which encodes the IL-10 family cytokine IL-22, the synthesis of which is induced by IL-23 (refs 14 and 15), was induced in response to DCCM-apoptotic LPS-blasts (Fig. 1c), consistent with the ability of apoptotic LPS-blasts, but not apoptotic cells, to promote IL-23 synthesis (Fig. 1a). None of the T cells, except those activated in the presence of IL-12, expressed the T_H1-lineage-specific transcription factor T-BET (also known as TBX21)³ (Fig. 1c). Thus, IL-17⁺ CD4 T cells generated in response to phagocytosis of TLR-ligand-containing apoptotic cells were bona fide T_H17 cells.

¹Immunology Institute, Department of Medicine, Mount Sinai School of Medicine, 1425 Madison Avenue, New York, New York 10029, USA.

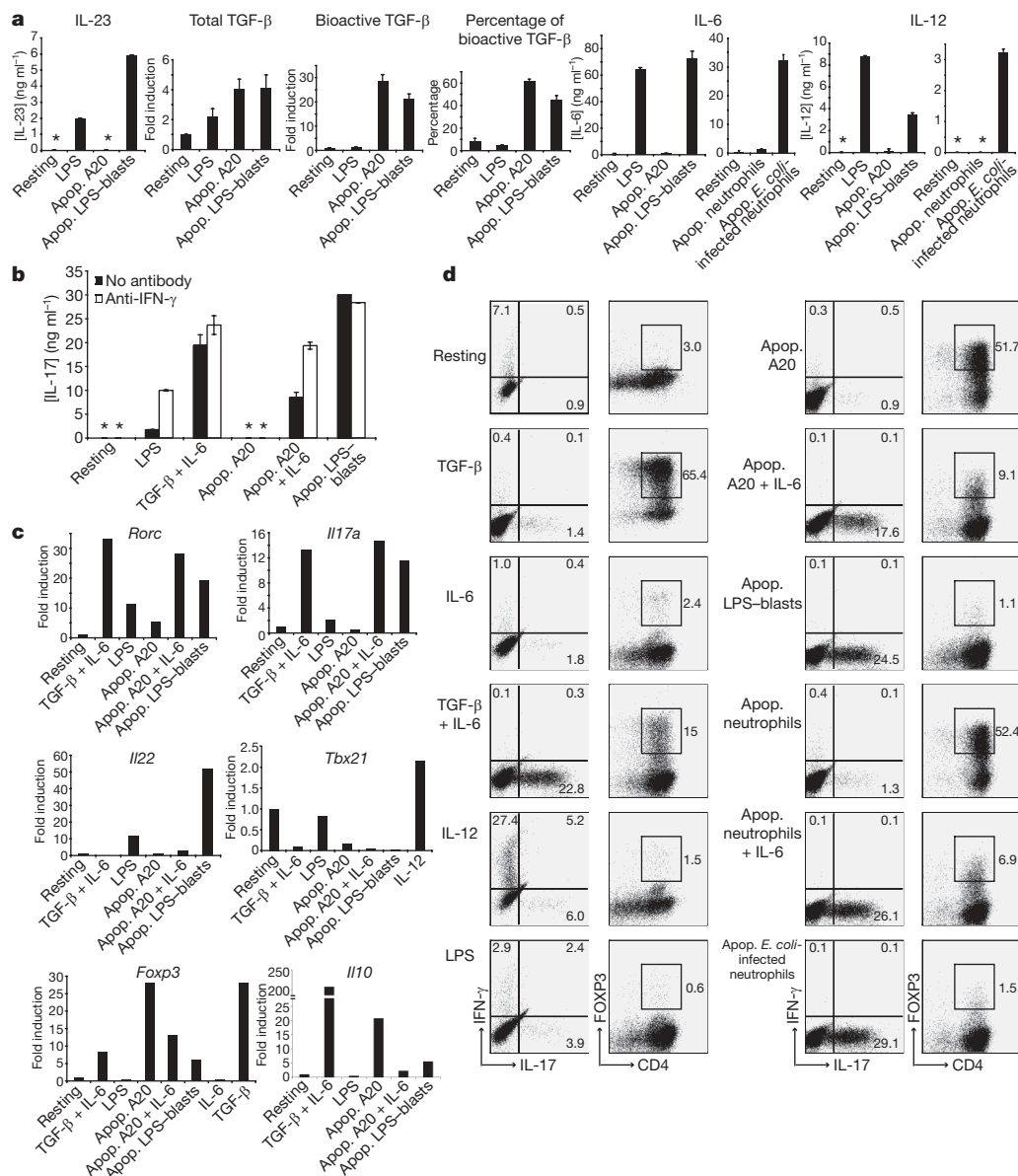


Figure 1 | Phagocytosis of infected and TLR-ligand-carrying apoptotic cells induces conditions optimal for development of T_H17 cells. Bone-marrow-derived dendritic cells (BMDCs) were stimulated with lipopolysaccharide (LPS) or phagocytic cargo as indicated. A20 is a B cell line. Apop., apoptotic. **a**, Cytokine levels measured in BMDC conditioned medium (DCCM) collected at 18 h. **b–d**, Naive CD4 T cells activated in the presence of various DCCM with or without anti-IFN- γ antibody and added cytokines

Reciprocal development of regulatory T (T_{reg}) and T_H17 cells², combined with DC production of bioactive TGF- β , but not IL-23 (ref. 16), IL-6 or IL-12 following phagocytosis of apoptotic cells (Fig. 1a and Supplementary Fig. 2), led us to examine expression of FOXP3, a transcription factor unique to regulatory T cells (T_{reg})^{2,3}. In contrast to T_H17 development in response to DCCM-apoptotic LPS-blasts and DCCM-apoptotic *E. coli*-infected neutrophils, FOXP3-expressing but not IL-17-producing cells developed in response to DCCM-apoptotic B cells and DCCM-apoptotic neutrophils (Fig. 1d). Addition of IL-6 to the latter DCCM impaired FOXP3 expression and restored IL-17 production (Fig. 1d). RT-qPCR showed *Foxp3* induction inversely mirrored that of *Rorc*, with highest induction when T cells were activated with DCCM-apoptotic B cells or TGF- β (Fig. 1c). *Foxp3* induction was impaired when IL-6 was added (consistent with previous reports²) and when T cells were activated with DCCM-apoptotic LPS-blasts (Fig. 1c), which contain IL-6 (Fig. 1a).

(IL-6 + TGF- β added to medium). **b**, Secreted IL-17 measured at 48 h following re-stimulation with anti-CD3. **c**, Fold induction of indicated transcripts 48 h post stimulation. **d**, Intracellular cytokines detected 4 h post re-stimulation with phorbol 12-myristate 13-acetate (PMA)/ionomycin (except for FOXP3). Flow cytometry plots gated on CD4⁺ cells. Numbers in quadrants indicate the percentage of positively stained cells. Error bars, s.d.; asterisks, not detected. Data represent four independent experiments.

Persistence of *Foxp3* transcripts and FOXP3-expressing cells (Figs 1c and 1d, respectively) in the TGF- β plus IL-6 conditions (in contrast to previous reports²) may be a consequence of the comparatively higher levels of TGF- β (5 ng ml⁻¹) that we used to approximate the average concentrations of TGF- β present in DCCM-apoptotic B cells or DCCM-apoptotic LPS-blasts (Supplementary Fig. 1).

T_H17 development in the presence of DCCM-apoptotic LPS-blasts was severely compromised upon inclusion of the pan-caspase inhibitor Q-VD-OPH during induction of apoptosis in LPS-blasts (Fig. 2a; apoptosis inhibition, Supplementary Fig. 4). IL-17 secretion was impaired in a dose-dependent manner when neutralizing antibody to TGF- β was present, with no synergistic inhibition with a neutralizing antibody to the p19 subunit of IL-23 (Fig. 2b). Neutralizing p19 alone still permitted emergence of IL-17⁺ cells, consistent with a role for IL-23 in expanding but not initiating development of these cells (Fig. 2b). Neutralizing IL-6 strongly inhibited

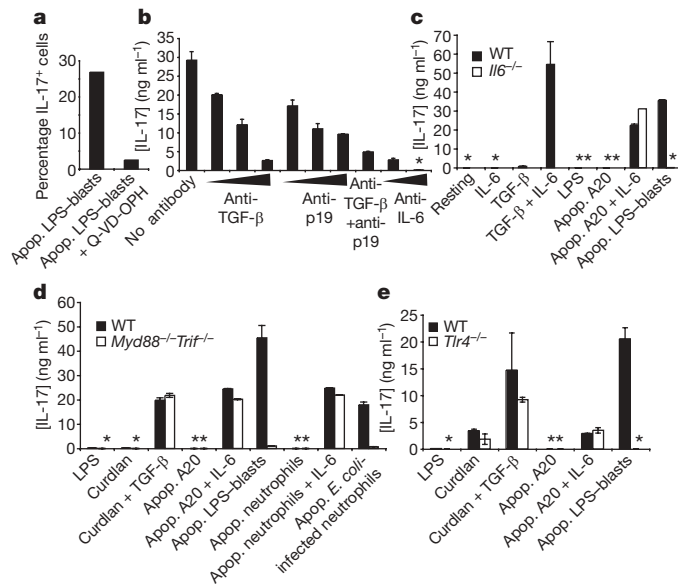


Figure 2 | Development of T_H17 cells in response to infected and TLR-ligand-carrying apoptotic cells requires TGF- β and IL-6 synthesis as well as TLR signalling by DCs. **a**, **b**, Naive CD4 T cells activated in the presence of DCCM-apoptotic LPS-blasts. **a**, Percentage IL-17 $^{+}$ cells among CD4 $^{+}$ T cells stained intracellularly 4 h post re-stimulation with PMA/ionomycin. LPS-blasts induced to undergo apoptosis in the presence or absence of Q-VD-OPH, a pan-caspase inhibitor. **b**–**e**, Secreted IL-17 measured at 48 h following re-stimulation with anti-CD3. **b**, Neutralizing antibodies added in primary cultures with DCCM-apoptotic LPS-blasts. **c**–**e**, DCCM from wild-type (WT), *Il6* $^{-/-}$, *Myd88* $^{-/-}$ *Trif* $^{-/-}$ or *Tlr4* $^{-/-}$ BMDCs. Curdlan is a β -glucan component of fungal cell walls. In **c**, IL-6, TGF- β or IL-6 + TGF- β were added to the medium. Error bars, s.d.; asterisks, not detected. Data represent three independent experiments.

IL-17 secretion (Fig. 2b). Furthermore, *Il6* $^{-/-}$ DCCM-apoptotic LPS-blasts failed to support T_H17 development (Fig. 2c; *Il6* $^{-/-}$ DC cytokines, Supplementary Fig. 5). Addition of IL-6 to DCCM-apoptotic B cells from either wild-type or *Il6* $^{-/-}$ DCs led to similar IL-17 secretion from activated naive CD4 T cells (Fig. 2c).

We next asked whether T_H17 development requires TLR signalling within DCs during phagocytosis of apoptotic *E. coli*-infected neutrophils or apoptotic LPS-blasts. Under these conditions, CM from DCs derived from *Myd88* $^{-/-}$ *Trif* $^{-/-}$ mice (Fig. 2d, where absence of signalling adaptors MyD88 and TRIF (also known as TICAM1) abrogates responses through all TLRs¹¹) or *Tlr4* $^{-/-}$ mice (Fig. 2e, where absence of TLR4 abrogates responses to LPS¹¹) did not support T_H17 but instead supported T_{reg} development (Supplementary Fig. 6). However, consistent with a lack of TLR involvement in recognition of apoptotic cells *per se*, generation of T_H17 cells was unaffected by absent TLR signalling when DCCM-apoptotic B cells or DCCM-apoptotic neutrophils were supplemented with IL-6 (Fig. 2d, e). Furthermore, DCs derived from *Myd88* $^{-/-}$ *Trif* $^{-/-}$ and *Tlr4* $^{-/-}$ mice directed induction of IL-17 $^{+}$ CD4 T cells when stimulated with curdlan, a fungal β -glucan that activates DCs independently of TLRs and induces T_H17 development when TGF- β is concomitantly present (Fig. 2d, e)¹⁷.

Given that infected apoptotic cells can drive development of T_H17 cells, a subset implicated in autoimmunity¹, could this process be accompanied by induction of a regulatory component? Twenty-five per cent of the IL-17 $^{+}$ CD4 T cells induced by DCCM-apoptotic LPS-blasts also produced IL-10, an anti-inflammatory cytokine¹⁸ (Fig. 3a). Distinct IL-10-producing (IL-10 $^{+}$) CD4 T cells that did not produce IL-17 were also induced. Similar 'IL-10 $^{+}$ ' and 'dual IL-10 $^{+}$ IL-17 $^{+}$ ' cells were induced in response to DCCM-apoptotic B cells supplemented with IL-6 (Fig. 3a). *Il10* transcripts were upregulated in response to DCCM-apoptotic B cells (Fig. 1c), although we could

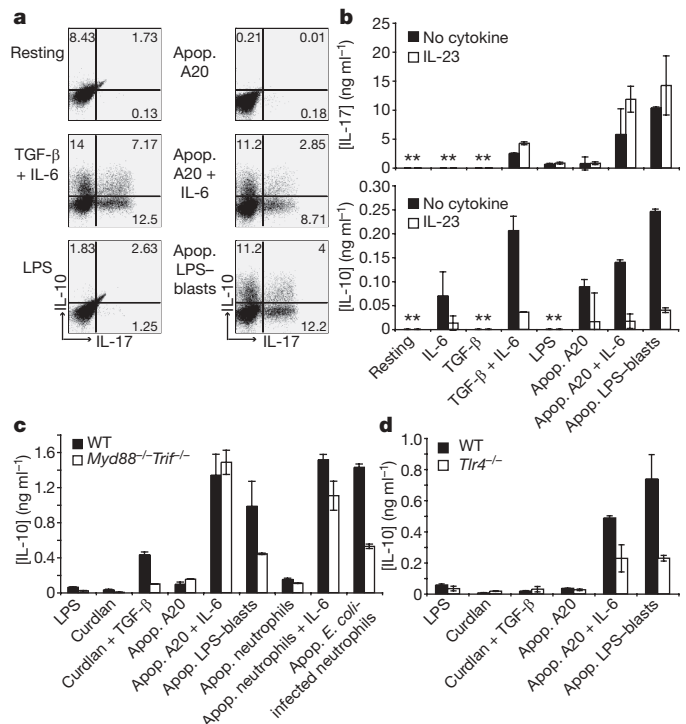


Figure 3 | Development of T_H17 cells in response to infected and TLR-ligand-carrying apoptotic cells is accompanied by production of the immunoregulatory cytokine IL-10. **a**–**d**, Naive CD4 T cells activated in the presence of the indicated DCCM from wild-type (WT) C57BL/6J, *Myd88* $^{-/-}$ *Trif* $^{-/-}$ or *Tlr4* $^{-/-}$ BMDCs. **a**, Intracellular cytokines detected 4 h post re-stimulation with PMA/ionomycin. Flow cytometry plots gated on CD4 $^{+}$ cells. **b**–**d**, Secreted IL-17 and IL-10 were measured at 48 h following re-stimulation with anti-CD3 (for **b**, IL-23 was added to secondary cultures). IL-6, TGF- β and IL-6 + TGF- β in **a** and **b** were added in primary cultures to medium. Error bars, s.d.; asterisks, not detected. Data represent three independent experiments.

not detect IL-10 $^{+}$ CD4 T cells in response to apoptotic cells alone by staining (Fig. 3a). Consistent with previous reports^{19,20}, TGF- β plus IL-6 also induced 'IL-17 $^{+}$ ', 'IL-10 $^{+}$ ' and 'dual IL-10 $^{+}$ IL-17 $^{+}$ ' CD4 T cells (Fig. 3a). Thus, unlike the reported inhibitory effects of IL-23 on IL-10 production upon reactivation of T_H17 cells¹⁹, IL-23 produced in response to apoptotic LPS-blasts (Fig. 1a) did not inhibit IL-10 production during initial generation of T_H17 cells from naive T cells. Indeed, neutralizing IL-23 in primary cultures had no appreciable effect on IL-10 $^{+}$ cells (Supplementary Fig. 7).

IL-23 only slightly increased secreted IL-17 during re-stimulation of IL-17 $^{+}$ CD4 T cells, consistent with the role of IL-23 in expanding T_H17 cells^{2,4,5} (Fig. 3b, top). However, as reported¹⁹, IL-23 markedly impaired IL-10 secretion upon reactivation (Fig. 3b, bottom). Unlike IL-17, appreciable IL-10 remained in response to DCCM-apoptotic LPS-blasts or DCCM-*E. coli*-infected neutrophils when TLR signalling was absent in the phagocytic DCs (Fig. 3c, d), and was confined to 'IL-10 $^{+}$ ' cells (Supplementary Fig. 8). As expected, all three populations were intact in response to *Myd88* $^{-/-}$ *Trif* $^{-/-}$ DCCM-apoptotic plus IL-6 compared to wild-type DCCM-apoptotic plus IL-6 (Supplementary Fig. 8). Thus, T_H17 development upon recognition of infected apoptotic cells is accompanied by IL-10 induction, which may limit inflammatory responses mediated by these cells during infections¹⁸.

We investigated whether blockade of apoptosis impairs T_H17 development *in vivo* during bacterial infections known to trigger T_H17 responses. Orogastric infection with *Citrobacter rodentium* results in massive apoptosis in intestinal epithelial cells^{21,22} (shown as TUNEL-positive cells in Fig. 4a, left panels; quantification, Supplementary Fig. 9). Moreover, IL-17 $^{+}$ CD4 T cells are increased

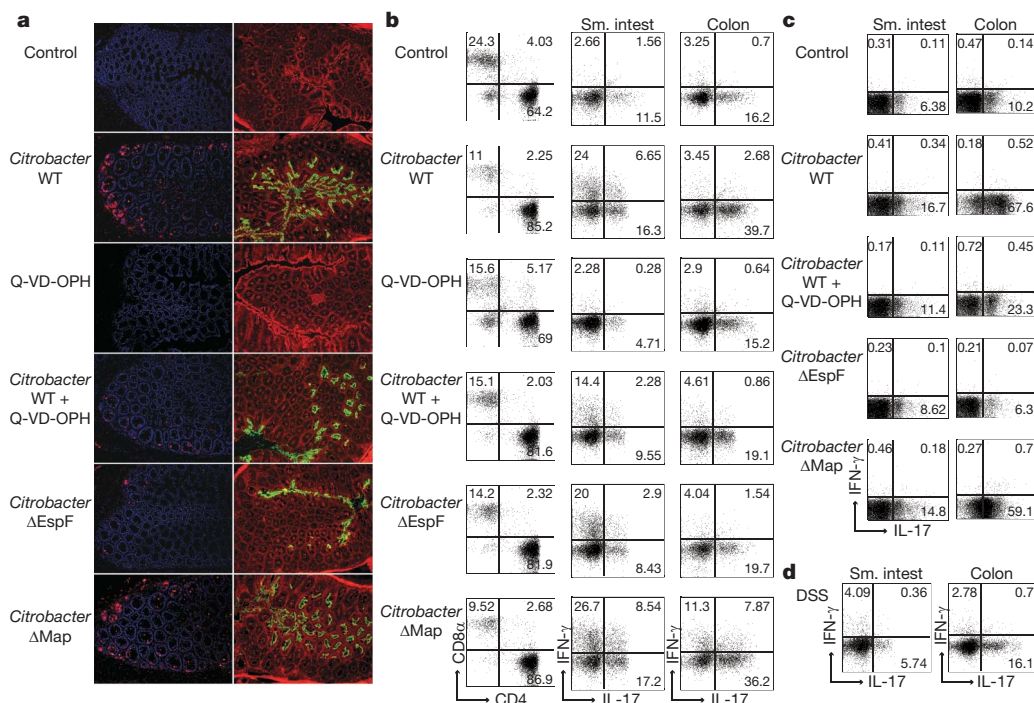


Figure 4 | Blocking apoptosis during *C. rodentium* infection impairs development of a T_H17 immune response. **a**, Immunofluorescence analyses of C3H/HeOuJ colonic sections on day 6 post-infection and/or Q-VD-OPH as indicated. Left panels, TUNEL (red), DAPI (blue). Right panels, enteropathogenic *Escherichia coli* (EPEC) LPS O-antigen (green), phalloidin (red). **b–d**, Detection of intracellular cytokine production by C57BL/6J

lamina propria lymphocytes (LPL) on day 9 (**b, d**) and C3H/HeOuJ LPL on day 6 (**c**) post indicated treatments. Intracellular cytokine staining performed 4 h post LPL re-stimulation with PMA/ionomycin. Flow cytometry plots gated on $CD3^+$ cells (**b**, left panels) or $CD4^+$ cells (**b**, middle and right panels, **c** and **d**). Control, uninfected. Data represent three independent experiments.

in number and predominate within the small intestinal and colonic lamina propria^{4,14} of *C. rodentium*-infected C57BL/6J mice (Fig. 4b and Supplementary Fig. 10; other tissues, Supplementary Fig. 11) and the more susceptible C3H/HeOuJ mice²² (Fig. 4c).

To inhibit apoptosis, we treated *C. rodentium*-infected mice with Q-VD-OPH, which effectively decreased TUNEL-positive cells (Fig. 4a; quantification, Supplementary Fig. 9) and markedly diminished $IL-17^+$ $CD4^+$ T cells, in C57BL/6J mice to levels similar to those in uninfected mice (Fig. 4b, c). Q-VD-OPH did not affect T-cell expansion and proliferation (Supplementary Fig. 12a, b), DC function or T_H1/T_H17 differentiation (Supplementary Figs 12c and 13). Thus, blockade of apoptosis in a relevant model of infection *in vivo* profoundly interfered with the T_H17 response.

We next tested the requirement for apoptosis in T_H17 induction by a fundamentally different approach using a mutant strain of *C. rodentium* incapable of inducing apoptosis. EspF (EPEC-secreted protein F) and Map (mitochondrial-associated protein) are effectors encoded by the locus of enterocyte effacement pathogenicity island in attaching and effacing pathogenic *E. coli*²³. Despite similar colonization (Fig. 4a, right panels), shedding in stool and colonic hyperplasia (see Supplementary Methods for references), only wild type and ΔMap mutants induce apoptosis and tight junction disruption *in vitro* and *in vivo*, whereas ΔEspF mutants fail to do so^{21,22,24,25}. This is indicated by increased TUNEL-positive cells in the distal colon of wild-type- and ΔMap-infected but not ΔEspF-infected mice compared to uninfected mice (Fig. 4a, left panels; quantification, Supplementary Fig. 9). We thus assessed T_H17 development in the intestinal lamina propria in response to infection with these *C. rodentium* mutants. Equivalent numbers of CD4 and CD8 T cells were present in the lamina propria of all wild-type-, ΔEspF- and ΔMap-infected C57BL/6J (Fig. 4b, leftmost panels) and C3H/HeOuJ mice (not shown). Infections with either wild-type or ΔMap *C. rodentium* resulted in considerable increases in $IL-17^+$ $CD4^+$ T cells in the colonic lamina propria (Fig. 4b, c), and more modest increases in the small

intestinal lamina propria (Fig. 4b, c). In contrast, no such increases were observed during infection with ΔEspF *C. rodentium*, for which percentages of $IL-17^+$ $CD4^+$ T cells were similar to those in uninfected controls (Fig. 4b, c).

Percentages of $IFN-\gamma^+$ $CD4^+$ T cells were similar in the small intestinal lamina propria of C57BL/6J mice infected with wild-type, ΔEspF and ΔMap *C. rodentium* (Fig. 4b), consistent with intact expression of the bacterial protein intimin, which drives T_H1 responses in *C. rodentium* infections^{4,10}. No such $IFN-\gamma^+$ $CD4^+$ T cells were detected in infected C3H/HeOuJ mice, which may relate to the increased susceptibility of these mice to *C. rodentium* infection compared to C57BL/6J mice. Percentages of FOXP3-expressing CD4 T cells were similar in all infected and uninfected groups of either C57BL/6J or C3H/HeOuJ mice (Supplementary Fig. 14). We could not detect $IL-10^+$ $CD4^+$ T cells in either strain (not shown).

Because ΔEspF can neither induce apoptosis nor disrupt tight junctions, it remained possible that tight junction disruption *per se* could drive the observed T_H17 response. However, despite reducing apoptosis, Q-VD-OPH has no effect on *Citrobacter* infection-induced barrier dysfunction²⁵. Furthermore, dextran-sulphate-sodium-induced damage of the intestinal epithelium did not increase $IL-17^+$ $CD4^+$ T cells over uninfected controls (Fig. 4d). These results argue against a role for disruption of intestinal epithelium integrity as a stimulus for T_H17 development.

Cell death results in immunological consequences determined by molecular components intrinsic to dying cells and specific to the nature of the trigger for cell death²⁶. Our findings illustrate how the immunosuppressive nature of apoptotic cell clearance²⁷ can coexist with the necessarily inflammatory nature of infection, and assign an important role to phagocytosis of apoptotic cells in contributing signals which, in combination with TLR engagement, induce tailored immunity to bacterial infection through development of T_H17 cells. Apoptosis in the absence of TLR engagement leads to tolerance through development of T_{reg} cells.

Our results also explain why some but not all microbial pathogens induce T_H17 cells, and indicate the importance of examining apoptosis induction by these pathogens. Tissue repair processes uniquely associated with effector functions of T_H17 cells^{3,14,28} would aid the host response against pathogens that cause significant apoptosis and tissue damage. How these results relate to induction of T_H17 cells after stimulating TLR5 on a distinct lamina propria DC subset²⁹, and via ATP derived from gut commensals³⁰, are questions to be resolved.

METHODS SUMMARY

Naïve CD4 T cells from C57BL/6J mice were cultured with 4 µg 48-well-plate-bound anti-CD3, 2 µg ml⁻¹ anti-CD28 and 1:500 anti-IL-4 ascites in the presence and absence of DCCM. Where indicated, cytokines were added to T-cell cultures as follows: 50 ng ml⁻¹ IL-6, 5 ng ml⁻¹ TGF-β, 10 ng ml⁻¹ IL-12, and 10 ng ml⁻¹ IL-23. The following neutralizing antibodies were used: anti-IFN-γ, 5 µg ml⁻¹; anti-TGF-β, 1, 5 and 10 µg ml⁻¹; anti-IL-23p19, 5, 10 and 20 µg ml⁻¹; anti-IL-6, 1 and 5 µg ml⁻¹. Cytokines were measured by ELISA. Bioactive TGF-β was measured using *Tgfb1*^{-/-} reporter mouse embryonic fibroblasts transfected with SMAD-binding elements coupled to secreted alkaline phosphatase, whereas total TGF-β was determined after acidification/neutralization. For ELISA measurements of IL-17 or IL-10, T cells were re-stimulated at 96 h with 96-well-plate-bound 1 µg anti-CD3. Before intracellular cytokine staining, T cells were re-stimulated at 72 h for 4 h with phorbol 12-myristate 13-acetate (PMA)/ionomycin plus brefeldin A (except before FOXP3 staining). T-cell RNA was prepared at 48 h following primary stimulation and RT-qPCR performed using primer pairs and Fam-BHQ-1 probes (Biosearch Technologies) or Applied Biosystems TaqMan gene expression assays. Samples were normalized to HPRT or β-actin and 'fold-inductions' of transcripts calculated using the ΔΔC_t method relative to T cells activated with anti-CD3 under neutral conditions. After starvation, mice were infected by orogastric administration of 2.5 × 10⁸ (C3H/HeOuj) or 2 × 10⁹ (C57BL/6J) *C. rodentium*. 0.4 mg Q-VD-OPH (SM Biochemicals) was injected intraperitoneally at 90 min, 24 h and 48 h after inoculation. C3H/HeOuj mice were additionally injected on days 3 and 5, and C57BL/6J on days 4, 6 and 8. Dextran sulfate sodium (DSS) was administered in drinking water at 2.5 mg ml⁻¹ for 7 days.

C. rodentium mutants were provided by B. B. Finlay, TGF-β reporter cells by T. Wyss-Coray, *Tlr4*^{-/-} and *Myd88*^{-/-} *Trif*^{-/-} mice by S. Akira and *Il-6*^{-/-} mice by R. Medzhitov, and C57BL/6J and C3H/HeOuj mice were purchased from the Jackson Laboratory. Animal care and experimentation were performed in accordance with approved MSSM Institutional Animal Care and Use Committee protocols. Full methods are found in Supplementary Information.

Received 11 August 2008; accepted 14 January 2009.

- Weaver, C. T., Hatton, R. D., Mangan, P. R. & Harrington, L. E. IL-17 family cytokines and the expanding diversity of effector T cell lineages. *Annu. Rev. Immunol.* **25**, 821–852 (2007).
- Bettelli, E. *et al.* Reciprocal developmental pathways for the generation of pathogenic effector T_H17 and regulatory T cells. *Nature* **441**, 235–238 (2006).
- Dong, C. T_H17 cells in development: an updated view of their molecular identity and genetic programming. *Nature Rev. Immunol.* **8**, 337–348 (2008).
- Mangan, P. R. *et al.* Transforming growth factor-β induces development of the T_H17 lineage. *Nature* **441**, 231–234 (2006).
- Veldhoen, M., Hocking, R. J., Atkins, C. J., Locksley, R. M. & Stockinger, B. TGFβ in the context of an inflammatory cytokine milieu supports *de novo* differentiation of IL-17-producing T cells. *Immunity* **24**, 179–189 (2006).
- O'Garra, A., Stockinger, B. & Veldhoen, M. Differentiation of human T_H17 cells does require TGF-β. *Nature Immunol.* **9**, 588–590 (2008).
- Medzhitov, R. Recognition of microorganisms and activation of the immune response. *Nature* **449**, 819–826 (2007).
- Serhan, C. N. & Savill, J. Resolution of inflammation: the beginning programs the end. *Nature Immunol.* **6**, 1191–1197 (2005).
- Sakaguchi, S. Naturally arising CD4⁺ regulatory T cells for immunologic self-tolerance and negative control of immune responses. *Annu. Rev. Immunol.* **22**, 531–562 (2004).

- Kaper, J. B., Nataro, J. P. & Mobley, H. L. Pathogenic *Escherichia coli*. *Nat. Rev. Microbiol.* **2**, 123–140 (2004).
- Kawai, T. & Akira, S. TLR signaling. *Semin. Immunol.* **19**, 24–32 (2007).
- Pappu, B. P. *et al.* TL1A–DR3 interaction regulates Th17 cell function and Th17-mediated autoimmune disease. *J. Exp. Med.* **205**, 1049–1062 (2008).
- Ivanov, I. I. *et al.* The orphan nuclear receptor RORγt directs the differentiation program of proinflammatory IL-17⁺ T helper cells. *Cell* **126**, 1121–1133 (2006).
- Zheng, Y. *et al.* Interleukin-22 mediates early host defense against attaching and effacing bacterial pathogens. *Nature Med.* **14**, 282–289 (2008).
- Zheng, Y. *et al.* Interleukin-22, a T_H17 cytokine, mediates IL-23-induced dermal inflammation and acanthosis. *Nature* **445**, 648–651 (2007).
- Stark, M. A. *et al.* Phagocytosis of apoptotic neutrophils regulates granulopoiesis via IL-23 and IL-17. *Immunity* **22**, 285–294 (2005).
- LeibundGut-Landmann, S. *et al.* Syk- and CARD9-dependent coupling of innate immunity to the induction of T helper cells that produce interleukin 17. *Nature Immunol.* **8**, 630–638 (2007).
- Couper, K. N., Blount, D. G. & Riley, E. M. IL-10: the master regulator of immunity to infection. *J. Immunol.* **180**, 5771–5777 (2008).
- McGeachy, M. J. *et al.* TGF-β and IL-6 drive the production of IL-17 and IL-10 by T cells and restrain T_H17 cell-mediated pathology. *Nature Immunol.* **8**, 1390–1397 (2007).
- Stumhofer, J. S. *et al.* Interleukins 27 and 6 induce STAT3-mediated T cell production of interleukin 10. *Nature Immunol.* **8**, 1363–1371 (2007).
- Nagai, T., Abe, A. & Sasakawa, C. Targeting of enteropathogenic *Escherichia coli* EspF to host mitochondria is essential for bacterial pathogenesis: critical role of the 16th leucine residue in EspF. *J. Biol. Chem.* **280**, 2998–3011 (2005).
- Vallance, B. A., Deng, W., Jacobson, K. & Finlay, B. B. Host susceptibility to the attaching and effacing bacterial pathogen *Citrobacter rodentium*. *Infect. Immun.* **71**, 3443–3453 (2003).
- Deng, W. *et al.* Dissecting virulence: systematic and functional analyses of a pathogenicity island. *Proc. Natl Acad. Sci. USA* **101**, 3597–3602 (2004).
- Nougayre, J. P. & Donnenberg, M. S. Enteropathogenic *Escherichia coli* EspF is targeted to mitochondria and is required to initiate the mitochondrial death pathway. *Cell. Microbiol.* **6**, 1097–1111 (2004).
- Viswanathan, V. K., Wehlen, A., Koutsouris, A., Roxas, J. L. & Hecht, G. Enteropathogenic *E. coli*-induced barrier function alteration is not a consequence of host cell apoptosis. *Am. J. Physiol. Gastrointest. Liver Physiol.* **294**, G1165–G1170 (2008).
- Zitvogel, L. & Kroemer, G. Introduction: the immune response against dying cells. *Curr. Opin. Immunol.* **20**, 501–503 (2008).
- Voll, R. E. *et al.* Immunosuppressive effects of apoptotic cells. *Nature* **390**, 350–351 (1997).
- Laurence, A., O'Shea, J. J. & Watford, W. T. Interleukin-22: a sheep in wolf's clothing. *Nature Med.* **14**, 247–249 (2008).
- Uematsu, S. *et al.* Regulation of humoral and cellular gut immunity by lamina propria dendritic cells expressing Toll-like receptor 5. *Nature Immunol.* **9**, 769–776 (2008).
- Atarashi, K. *et al.* ATP drives lamina propria T_H17 cell differentiation. *Nature* **455**, 808–812 (2008).

Supplementary Information is linked to the online version of the paper at www.nature.com/nature.

Acknowledgements We are grateful to R. Medzhitov, L. Mayer and D. Amsen for advice and critical reading of the manuscript, S. Lira for use of cryostat and microscope, B. B. Finlay and W. Deng for *Citrobacter* mutants, former Blander laboratory members H. Pêche and B. Trinité for technical assistance and discussions, S. Mehrotra for advice with caspase inhibitors, and I. George and M. Grisotto for cell sorting. We are indebted to B. Brown, H. Xiong, G. Frankel, C. Dong, K. Schluns, M. Kamanaka, S. Yu, P. Arnaboldi, M. Bogunovic, B. M. Baker, S. L. Fishman, M. Blander and S. J. Blander for technical advice, assistance and support. J.G. is supported by the Fondation pour la Recherche Médicale, and J.M.B. is supported by NIH grant A1073899 and the Kinship Foundation Searle Scholar Award.

Author Contributions M.B.T. and J.M.B. designed experiments and wrote the manuscript. M.B.T. performed all experiments. J.G. performed RT-qPCRs, bioactive TGF-β assays, and helped with tissue staining. A.P.M. performed tissue sectioning, staining and quantification. J.M.B. initiated and directed the study.

Author Information Reprints and permissions information is available at www.nature.com/reprints. Correspondence and requests for materials should be addressed to J.M.B. (julie.blander@mssm.edu).

Type II fatty acid synthesis is not a suitable antibiotic target for Gram-positive pathogens

Sophie Brinster^{1,2}, Gilles Lamberet³, Bart Staels⁴, Patrick Trieu-Cuot⁵, Alexandra Gruss³ & Claire Poyart^{1,2,5,6}

Antimicrobial drugs targeting the reportedly essential type II fatty acid synthesis (FASII) pathway^{1–5} have been recently acclaimed for their efficacy against infections caused by multiresistant Gram-positive bacteria^{6–8}. Our findings show that the strategy for antibiotic development based on FASII pathway targets is fundamentally flawed by the fact that exogenous fatty acids fully bypass inhibition of this pathway in both *in vitro* and *in vivo* conditions. We demonstrate that major Gram-positive pathogens—such as streptococci, pneumococci, enterococci and staphylococci—overcome drug-induced FASII pathway inhibition when supplied with exogenous fatty acids, and human serum proves to be a highly effective source of fatty acids. For opportunist pathogen *Streptococcus agalactiae*, growth in serum leads to an overall decrease of FASII gene expression. No antibiotic inhibitor could have a stronger effect than the inactivation of the target gene, so we challenged the role of FASII using deletion mutants. Our results unequivocally show that the FASII target enzymes are dispensable *in vivo* during *S. agalactiae* infection. The results of this study largely compromise the use of FASII-based antimicrobials for treating sepsis caused by Gram-positive pathogens.

The bacterial FASII pathway is considered a promising target for the development of novel antimicrobial drugs^{1–5}. The recently described drugs platensimycin and platencin, which were shown to target key FASII enzymes FabB/F and/or FabH, displayed potent activities against Gram-positive cocci including *Staphylococcus aureus*, *Enterococcus faecalis*, *Enterococcus faecium*, and *Streptococcus pneumoniae*^{4,6,7}. Success in the use of FASII as antimicrobial target has further stimulated efforts to identify natural and synthetic inhibitors of this pathway (see refs 4, 5, 8 and 9 for reviews). However, there are numerous reports of Gram-positive bacteria—such as *S. aureus*, *Lactococcus lactis*, and different lactobacilli—that incorporate exogenous fatty acids in their membranes, some of which were shown to display optimal growth after fatty acid addition^{10–12}. In *S. agalactiae*, a major pathogen responsible for neonatal meningitis, exogenously added oleic acid was incorporated directly into bacterial membranes and overcame a fatty acid biosynthesis defect due to NADH oxidase deficiency¹³. Added unsaturated fatty acids also overcame genetic fatty acid biosynthetic defects in a *fabB* mutant of *Escherichia coli*¹⁴, a *fabH* mutant of *L. lactis*¹⁵, and *fabM* mutants of *S. pneumoniae* and *Streptococcus mutans*^{1,16,17}.

The use of FASII pathway enzymes as antimicrobial targets in previous reports seemed incongruous to us in view of bacterial and host properties: as human serum is an extremely rich source of fatty acids (~3 g l⁻¹), with abundant amounts of C18 unsaturated fatty acids¹⁸, we hypothesized that it might complement a bacterial fatty acid biosynthetic defect, and thereby render FASII-blocking drugs ineffective for *in vivo* bacterial inhibition. This hypothesis concerns the basic common steps in the FASII synthesis cycle, which is used in

several major low-GC Gram-positive pathogens. It would not concern bacteria with requirements for fatty acids missing in serum, or drugs that target subsequent activities, for example, those involved in phospholipid or lipid A synthesis (see refs 8 and 19).

Clinical isolates of Gram-positive pathogens *S. aureus*, *E. faecalis*, *E. faecium*, *S. pneumoniae*, *Streptococcus pyogenes* and *S. agalactiae*, including singly or multiply drug resistant strains, were tested for sensitivity to FASII inhibitors. We chose two commercially available anti-FASII drugs: cerulenin, which like platensimycin and platencin inhibits FabB/F, and triclosan, which targets FabI and other FASII components^{8,20}. Bacteria were challenged with these drugs in the presence or absence of exogenous fatty acids (Supplementary Table 1). In standard medium lacking fatty acids, all streptococci, enterococci and staphylococci tested were sensitive to cerulenin and triclosan within minimal inhibitory concentration (MIC) ranges similar to those reported for previously tested species^{11,20}. However, sensitivity to cerulenin and triclosan was alleviated in all strains, regardless of their antibiotic resistance profiles, by supplying fatty acids via Tween 80 or human serum.

The predominant fatty acids in human serum, comprising ~80% of the total fatty acids, are the unsaturated linoleic (C18:2n-6) and oleic (C18:1n-9) acids, and the saturated palmitic (C16:0) and stearic acids (C18:0)¹⁸. They were individually tested for their capacity to overcome cerulenin inhibition of *S. agalactiae* strain NEM316, which was used as the model (Supplementary Table 2). The unsaturated fatty acids each fully alleviated *S. agalactiae* growth inhibition by cerulenin. In contrast, neither saturated fatty acid restored *S. agalactiae* growth. Addition of a neutral detergent that makes micelles (Brij58 0.01% v/v) to a *S. agalactiae* culture had no impact on cerulenin sensitivity (data not shown). This demonstrates that the ability of human serum to overcome cerulenin inhibition of *S. agalactiae* can be explained by unsaturated fatty acid availability.

This remarkable effect of serum overcoming FASII pathway inhibition led us to perform quantitative polymerase chain reaction with reverse transcription (RT-PCR) to determine its effects on expression of the *fab* genes in *S. agalactiae*. Serum addition provoked a 3- to 40-fold decrease in expression of the eight FASII genes tested (Fig. 1a). This result further indicates that the FASII pathway requirement is alleviated in fatty-acid-rich serum.

The challenge test for the FASII requirement is to remove FASII genes from the bacterial genome. Our goal was to inactivate drug target candidates, so we constructed *S. agalactiae* strains with deletions in *fabF* (*gbs0336*), *fabM* (*gbs0329*), and *fabMF* (see complete Methods and Supplementary Fig. 1; ref. 21). Remarkably, a quintuple mutant defective in *fabMKDGF* (*gbs329* and *gbs0333* through *gbs0336*) could also be established, despite the potentially broad impact of such an extensive deletion. Growth of all these mutants was severely defective in standard Todd Hewitt (TH) medium. In contrast, they all grew like the wild-type (WT) strain in serum, or

¹Institut Cochin, Université Paris Descartes, CNRS (UMR 8104), Paris, France. ²INSERM, U567, Paris, France. ³INRA, UR888, Unité Bactéries Lactiques et Pathogènes Opportunistes, F-78350, Jouy en Josas, France. ⁴Institut Pasteur de Lille, INSERM UMR545, Université Lille 2, Lille, France. ⁵Institut Pasteur, Unité de Biologie des Bactéries Pathogènes à Gram Positif, URA CNRS 2172, Paris, France. ⁶Assistance Publique Hôpitaux de Paris, Centre National de Référence des Streptocoques, Hôpital Cochin, Paris, France.

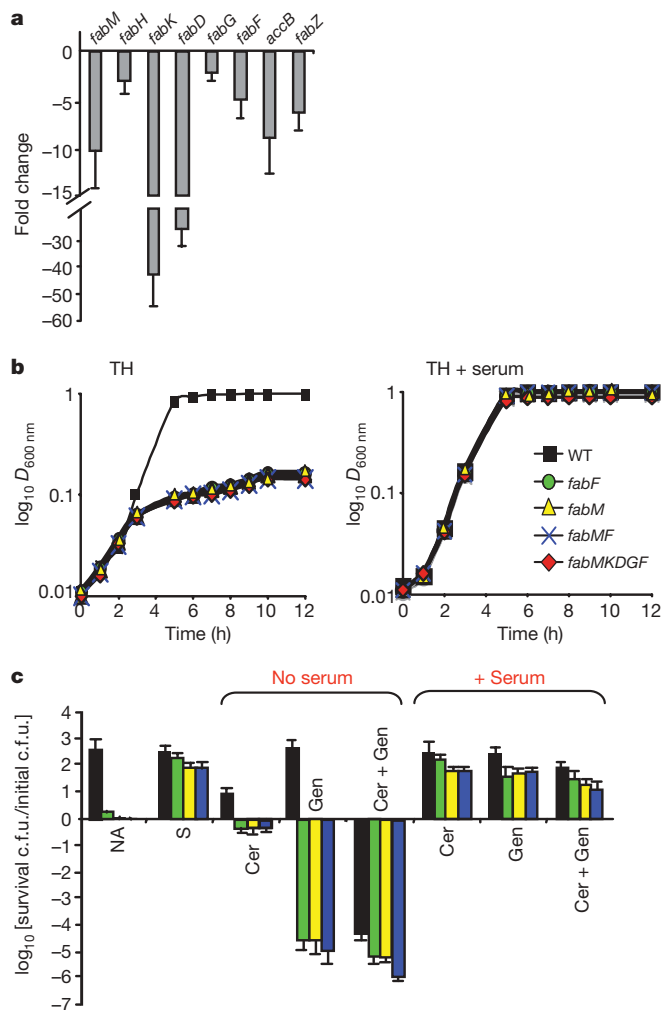


Figure 1 | Impact of serum addition on *S. agalactiae* FASII gene expression and growth. **a**, The expression of eight FASII genes was quantified by qRT-PCR in *S. agalactiae* WT cells grown to exponential phase in TH with or without serum (50%). Values are presented as a ratio of expression in TH relative to expression in TH plus serum (average \pm s.d., $n = 3$). **b**, Growth of WT, *fabM*, *fabF*, *fabMF* and *fabMKDGF* strains in TH medium versus serum ($n \geq 3$, <10% variation). **c**, Bacterial activity of cerulenin (Cer) alone and in combination with gentamicin (Gen) in TH medium with and without serum (average \pm s.d., $n = 6$). NA, no addition; S, 50% serum. Bacterial strains are coloured as in **b**. See Supplementary Fig. 1 for *S. agalactiae* NEM316 *fab* gene nomenclature.

with added oleic acid or linoleic acid (Fig. 1b and Supplementary Fig. 1b). The above results strongly suggest that serum can effectively take over the role of the FASII pathway.

Robust growth of *fab* mutant strains implies that available fatty acids reconstitute the defective cells. We examined this effect in detail for the *fabM*, *fabF* and *fabMF* mutants, which encode distinct functions in the FASII pathway: elongation (FabF) and unsaturated fatty acid synthesis (FabM)^{8,9}. Fatty acid composition was analysed from the WT, *fabM*, *fabF* and *fabMF* cultures after growth in TH medium with or without Tween 80 (0.1%), or in human serum (100%) (Fig. 2a and Supplementary Table 3). The WT profile in TH medium without added fatty acids presumably corresponds to its fatty acid biosynthetic capacity. Growth in Tween 80 led to high proportions of cellular oleic acid (Supplementary Table 3), which integrates directly into membranes, as previously reported¹³.

Significantly, serum, which sustained equivalent robust growth of WT and the *fabM*, *fabF* and *fabMF* mutant strains, resulted in comparable cellular fatty acid profiles that were enriched in serum-specific fatty acids (Fig. 2a and Supplementary Table 3). Although

neither linoleic (C18:2n-6) nor arachidonic (C20:4n-6) acid is synthesized by *S. agalactiae*, both are prominent in serum-grown strains. Extractions performed after three hours of growth in serum (data not shown) contained markedly less serum-specific fatty acids than after 12 hours, indicating that adaptation to environmental fatty acids is gradual. Assimilation of saturated as well as unsaturated fatty acids might suggest that fatty-acid-binding serum components such as albumin facilitate uptake of these moieties²². These results demonstrate that exogenous fatty acid sources have the remarkable effect of effacing the observable differences between WT and *fab* mutant fatty acid profiles (Fig. 2a and Supplementary Table 3). Human whole blood also proved to be an effective fatty acid source (data not shown). We conclude that the host environment is a major and privileged source of fatty acids that fully compensates a *S. agalactiae* FASII defect.

We tested for synergistic effects when combining a FASII inhibitor and an aminoglycoside provided in the absence or presence of added fatty acids. Although monotherapy using aminoglycosides is poorly effective against Streptococcaceae, it is well known that these protein synthesis inhibitors act synergistically with cell-wall inhibitors such as β -lactams or glycopeptides²³. We thus asked whether bacterial membrane modifications induced by FASII inhibitors enable gentamicin to reach its target, and whether exogenous fatty acids abolish its effect. In fatty-acid-free medium (Fig. 1c), gentamicin alone did not affect growth of the WT strain but was active against *fabF*, *fabM*, and *fabMF* (10^5 -fold reduction of colony-forming units, c.f.u.), indicative of a barrier defect in these mutants. No growth was observed for any cultures containing cerulenin. In contrast, a combination of gentamicin plus cerulenin at MIC values was synergistic on the WT strain, leading to a 10^4 -fold c.f.u. reduction. Addition of serum fully abolished the synergy on the WT, and on all tested strains, providing further evidence that membrane defects due to FASII-directed antibiotics or *fab* gene mutations are alleviated by exogenous fatty acids.

To respond to the main question addressed here—that is, whether FASII inhibitors could be active *in vivo*—we examined whether inhibition of FASII might be overcome *in vivo* in models for systemic *S. agalactiae* infection. The virulence capacity of WT, *fabM*, *fabF* and *fabMF* strains was compared in a neonatal rat infection model. Two-day-old rat pups were infected by intraperitoneal injection with 5×10^6 c.f.u. of each strain (Fig. 2b). Mortality caused by WT and the *fab* mutants was the same over the 120-hour period after injection, indicating that functions assured by *fabM* and *fabF* genes are dispensable for *S. agalactiae* virulence in this model.

Infectivity of FASII-defective mutants was further examined in a mouse adult infection model (Fig. 2c). To exclude any possibility that serum fatty acid variations might be a factor in determining the bacterial FASII requirement, experiments included a group of mice treated with fenofibrate, a hypolipidemic drug currently used to treat hypertriglyceridemia and known to decrease plasma triglycerides both in humans and rodents^{24,25}. The serum of the fenofibrate-treated group had lower triglyceride and free fatty acid levels (73% and 29%, respectively) than the untreated group (Supplementary Fig. 2). Six-week-old mice were infected with 5×10^7 c.f.u. of WT, *fabF* or *fabMF* mutants, and animals were killed and dissected at 3, 24 and 48 hours after infection. Bacterial counts in blood, brain, and liver of the WT and *fab* mutant strains were superimposable, as seen in non-treated and fenofibrate-treated groups (Fig. 2c). These results show unequivocally that the FASII bacterial pathway is not required for *S. agalactiae* septicemic infection models, even in the presence of the most efficacious lipid-lowering treatment widely used in human medicine.

Drug discovery is very costly, and recent studies point out that bacterial responses to drugs may be dramatically affected by *in vivo* conditions²⁶. The effect of serum on drug efficacy was mentioned in recent studies of the FASII-targeted drugs platensimycin and platenicin^{6,7}. In those studies, a fourfold increase in MIC of *S. aureus* by serum addition *in vitro* was considered minor compared to the inhibitory effects of the tested drugs, a conclusion not consistent with our

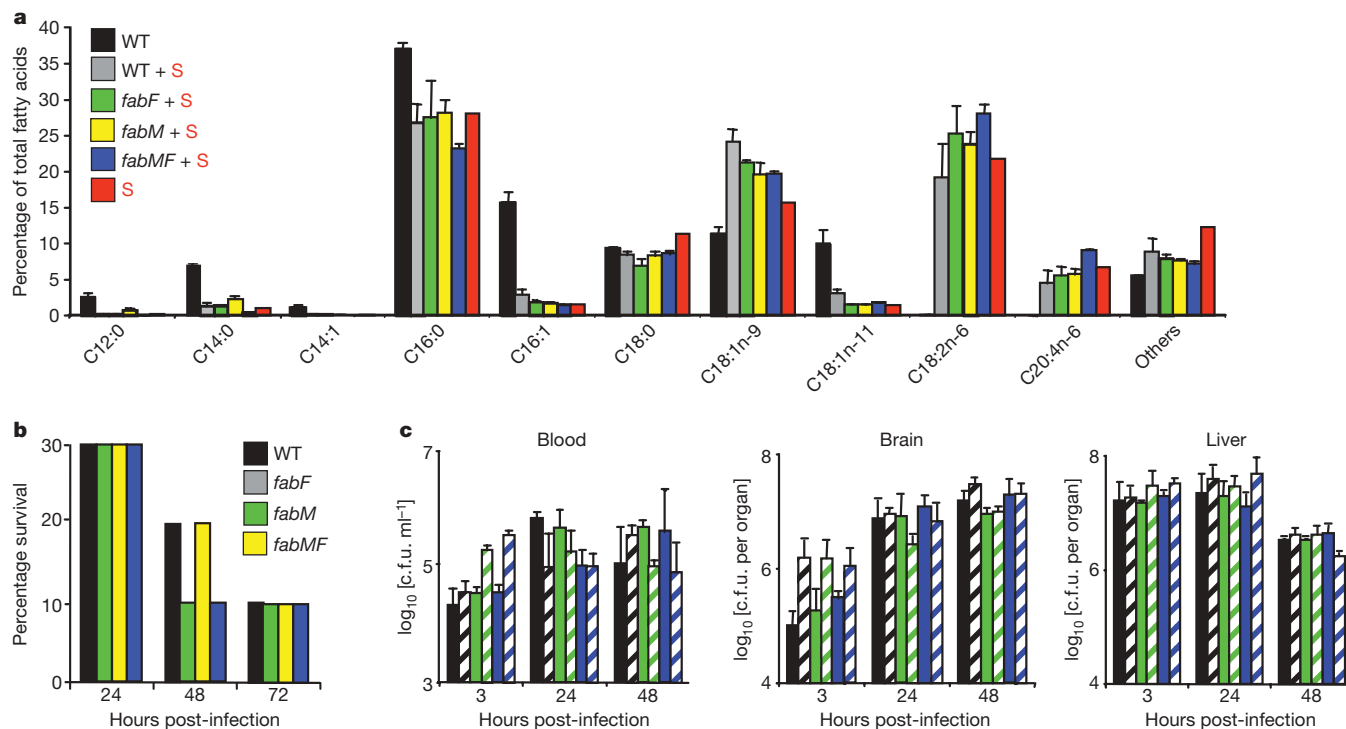


Figure 2 | Cellular fatty acid composition and *in vivo* virulence assays.

a, Fatty acid composition as a function of medium fatty acid content. WT, *fabM*, *fabF* and *fabMF* strains were precultured in TH medium supplemented with 0.1% Tween 80, washed extensively, and then resuspended for growth in TH medium, TH plus 0.1% Tween 80, or 100% serum (S) (average \pm s.d., $n = 3$). Full data are in Supplementary Table 3. Red bars correspond to serum analysis (average $n = 2$) used for bacterial

growth. **b**, Neonatal rat model for WT, *fabM*, *fabF* and *fabMF* virulence ($n = 10$ per strain). **c**, Infection of mice treated or not with fenofibrate. WT, *fabM* and *fabMF* strains were used to infect C57BL/6 mice that received fenofibrate (striped bars) or not (filled colour bars, bacterial strains are coloured as in **b**; average \pm s.d., $n = 3-4$ per strain and per point). Inocula were 5×10^6 c.f.u. for **b**, and 5×10^7 c.f.u. for **c**.

results. However, serum concentrations used in those reports were not specified, and it is conceivable that they were lower than those used here, as we observed suppression of the inhibitory effect of cerulenin on *S. aureus* in undiluted serum (Supplementary Table 1). Moreover, conditions used to test *in vivo* efficacy of the antibiotics did not mimic real infection and treatment. In the previous work⁶, a kidney infection model was used with an inoculum of 10^3 c.f.u., followed 30 minutes later by intravenous continuous antibiotic treatment (that is, before bacterial adaptation to the host and infection were established). The success of the treatment was based on a single 24-hour follow-up of kidneys. These conditions, though frequently used, differ from more stringent tests designed to confront real infection conditions (for example, generally higher inoculum, and importantly, the time interval between infection and antibiotic administration, and a longer post-infection follow-up²⁷). These factors might explain the apparent success of the antibiotic challenge. However, our results strongly predict that FASII-directed drugs would be ineffective under natural infection conditions. The decreased virulence of a *S. mutans fabM* strain was observed in a murine dental caries model¹⁷. The low amounts of fatty acids in saliva (20 mg l^{-1}) as compared to serum (3 g l^{-1})^{18,28} probably explain why the FASII pathway would be needed for *S. mutans* virulence in a caries model, but dispensable for septicemic infection.

Our data show that major Gram-positive pathogens overcome growth inhibition by antimicrobials targeting the FASII pathway when environmental fatty acids, particularly unsaturated fatty acids, are available. These findings indicate that FASII-targeted antimicrobials are unsuitable for the treatment of septicemic infections caused by these pathogens. They also raise new questions about the consequences of fatty acid assimilation in the colonized or infected host with respect to gene expression, drug and stress sensitivity, and host-bacterial interactions.

METHODS SUMMARY

The complete methods are presented in the Supplementary Information. All bacterial strains were cultured at 37°C . The MICs of the FASII biosynthesis inhibitors cerulenin and triclosan were tested on three isolates of six pathogenic species in TH medium without or with added Tween 80 or filtered human serum (referred to as serum) using standard assays. An antibacterial combination assay on *S. agalactiae* parental and mutant strains was performed using gentamicin and cerulenin. The test medium was TH or TH plus 10% serum. Fatty acid composition was determined on *S. agalactiae* WT, *fabM*, *fabF* and *fabMF* strains pre-cultured in 0.1% Tween 80, then grown under three conditions: TH; TH plus 0.1% Tween 80 (positive control); and 100% serum. Bacterial fatty acid composition was analysed as described¹³, with minor modifications (see Supplementary Methods). Plasma triglyceride and free fatty acid concentrations were measured by commercially available reagents (bioMérieux and Wako Chemicals, respectively). *S. agalactiae* in-frame deletions in *gbs0329* (*fabM*), *gbs0336* (*fabF*) and *gbs0333* (*fabK*) to *gbs0336* (*fabF*) were constructed using standard methods (see Supplementary Methods and Supplementary Table 4), except that transformants were plated on agar medium supplemented with 0.1% Tween 80. Quantitative real-time PCR (qRT-PCR) analysis was performed as described²⁹ using primers listed in Supplementary Table 4. *In vivo* virulence studies on parental and *fab* mutant strains for mortality studies used two-day-old neonatal Sprague-Dawley rat pups injected intraperitoneally (survival was followed over four days), and to follow bacterial development in specific organs, three-week-old C57BL/6 mice (Charles River), treated or not for two weeks with fenofibrate (Sigma). Mice were then infected intravenously with *S. agalactiae* strains, and after 3, 24 and 48 h, groups of three to four mice were killed and bacterial counts in blood and homogenates of liver and brain were determined by plating serial dilutions on TH agar containing 0.1% Tween 80.

Full Methods and any associated references are available in the online version of the paper at www.nature.com/nature.

Received 7 July 2008; accepted 13 January 2009.

- Altabe, S., Lopez, P. & de Mendoza, D. Isolation and characterization of unsaturated fatty acid auxotrophs of *Streptococcus pneumoniae* and *Streptococcus mutans*. *J. Bacteriol.* **189**, 8139–8144 (2007).

2. Marrakchi, H., Zhang, Y. M. & Rock, C. O. Mechanistic diversity and regulation of Type II fatty acid synthesis. *Biochem. Soc. Trans.* **30**, 1050–1055 (2002).
3. Price, A. C. *et al.* Inhibition of beta-ketoacyl-acyl carrier protein synthases by thiolactomycin and cerulenin. Structure and mechanism. *J. Biol. Chem.* **276**, 6551–6559 (2001).
4. Wright, H. T. & Reynolds, K. A. Antibacterial targets in fatty acid biosynthesis. *Curr. Opin. Microbiol.* **10**, 447–453 (2007).
5. Zhang, Y. M., White, S. W. & Rock, C. O. Inhibiting bacterial fatty acid synthesis. *J. Biol. Chem.* **281**, 17541–17544 (2006).
6. Wang, J. *et al.* Platensimycin is a selective FabF inhibitor with potent antibiotic properties. *Nature* **441**, 358–361 (2006).
7. Wang, J. *et al.* Discovery of platencin, a dual FabF and FabH inhibitor with *in vivo* antibiotic properties. *Proc. Natl Acad. Sci. USA* **104**, 7612–7616 (2007).
8. Zhang, Y. M. & Rock, C. O. Membrane lipid homeostasis in bacteria. *Nat. Rev. Microbiol.* **6**, 222–233 (2008).
9. Campbell, J. W. & Cronan, J. E. Jr. Bacterial fatty acid biosynthesis: targets for antibacterial drug discovery. *Annu. Rev. Microbiol.* **55**, 305–332 (2001).
10. Johnsson, T., Nikkila, P., Toivonen, L., Rosenqvist, H. & Laakso, S. Cellular fatty acid profiles of *Lactobacillus* and *Lactococcus* strains in relation to the oleic acid content of the cultivation medium. *Appl. Environ. Microbiol.* **61**, 4497–4499 (1995).
11. Altenbern, R. A. Cerulenin-inhibited cells of *Staphylococcus aureus* resume growth when supplemented with either a saturated or an unsaturated fatty acid. *Antimicrob. Agents Chemother.* **11**, 574–576 (1977).
12. Kankaanpää, P., Yang, B., Kallio, H., Isolauri, E. & Salminen, S. Effects of polyunsaturated fatty acids in growth medium on lipid composition and on physicochemical surface properties of lactobacilli. *Appl. Environ. Microbiol.* **70**, 129–136 (2004).
13. Yamamoto, Y. *et al.* The group B streptococcus NADH oxidase Nox-2 is involved in fatty acid biosynthesis during aerobic growth and contributes to virulence. *Mol. Microbiol.* **62**, 772–785 (2006).
14. Campbell, J. W. & Cronan, J. E. Jr. *Escherichia coli* FadR positively regulates transcription of the *fabB* fatty acid biosynthetic gene. *J. Bacteriol.* **183**, 5982–5990 (2001).
15. Lai, C. Y. & Cronan, J. E. Beta-ketoacyl-acyl carrier protein synthase III (FabH) is essential for bacterial fatty acid synthesis. *J. Biol. Chem.* **278**, 51494–51503 (2003).
16. Fozo, E. M. & Quivey, R. G. Jr. The *fabM* gene product of *Streptococcus mutans* is responsible for the synthesis of monounsaturated fatty acids and is necessary for survival at low pH. *J. Bacteriol.* **186**, 4152–4158 (2004).
17. Fozo, E. M., Scott-Anne, K., Koo, H. & Quivey, R. G. Jr. Role of unsaturated fatty acid biosynthesis in virulence of *Streptococcus mutans*. *Infect. Immun.* **75**, 1537–1539 (2007).
18. Nakamura, T. *et al.* Serum fatty acid levels, dietary style and coronary heart disease in three neighbouring areas in Japan: the Kumihama study. *Br. J. Nutr.* **89**, 267–272 (2003).
19. Raetz, C. R., Reynolds, C. M., Trent, M. S. & Bishop, R. E. Lipid A modification systems in gram-negative bacteria. *Annu. Rev. Biochem.* **76**, 295–329 (2007).
20. Bhargava, H. N. & Leonard, P. A. Triclosan: applications and safety. *Am. J. Infect. Control* **24**, 209–218 (1996).
21. Glaser, P. *et al.* Genome sequence of *Streptococcus agalactiae*, a pathogen causing invasive neonatal disease. *Mol. Microbiol.* **45**, 1499–1513 (2002).
22. Hamilton, J. A. How fatty acids bind to proteins: the inside story from protein structures. *Prostaglandins Leukot. Essent. Fatty Acids* **67**, 65–72 (2002).
23. Moellering, R. C. Jr & Weinberg, A. N. Studies on antibiotic synergism against enterococci. II. Effect of various antibiotics on the uptake of 14 C-labeled streptomycin by enterococci. *J. Clin. Invest.* **50**, 2580–2584 (1971).
24. Berger, J. & Moller, D. E. The mechanisms of action of PPARs. *Annu. Rev. Med.* **53**, 409–435 (2002).
25. Staels, B., Maes, M. & Zambon, A. Fibrates and future PPARalpha agonists in the treatment of cardiovascular disease. *Nature Clin. Pract. Cardiovasc. Med.* **5**, 542–553 (2008).
26. Scotti, M. *et al.* Coexpression of virulence and fosfomycin susceptibility in *Listeria*: molecular basis of an antimicrobial *in vitro-in vivo* paradox. *Nature Med.* **12**, 515–517 (2006).
27. Gill, C. J. *et al.* *In vivo* activity and pharmacokinetic evaluation of a novel long-acting carbapenem antibiotic, MK-826 (L-749,345). *Antimicrob. Agents Chemother.* **42**, 1996–2001 (1998).
28. Tomita, Y., Miyake, N. & Yamanaka, S. Lipids in human parotid saliva with regard to caries experience. *J. Oleo Sci.* **57**, 115–121 (2008).
29. Yamamoto, Y. *et al.* Respiration metabolism of group B streptococcus is activated by environmental haem and quinone and contributes to virulence. *Mol. Microbiol.* **56**, 525–534 (2005).

Supplementary Information is linked to the online version of the paper at www.nature.com/nature.

Acknowledgements We are grateful to I. Tardieux, P. Bouloc and L. Gutmann for critical reading and discussion of the manuscript, and P. Gaudu and Y. Yamamoto for discussion. We thank A. Bouaboud for technical assistance, and C. Fievet and N. Hennuye for mouse serum fatty acid analyses and advice. This work was supported by research funding from the French Agence Nationale de la Recherche (ANR, StrepRespire Project), INSERM, INRA, Université Paris Descartes, and the Institut Pasteur. S.B. was a recipient of a post-doctoral fellowship from the ANR StrepRespire Project.

Author Contributions S.B. performed MIC experiments, genetic constructions, phenotypic characterization of the mutants. G.L. performed fatty acid determination. C.P. and S.B. conducted *in vivo* experiments. B.S. participated in the design of *in vivo* triglyceride and fatty acid depletion experiments. C.P., P.T.-C. and A.G. conceptualized and designed the study. C.P. and A.G. wrote the manuscript with contributions from S.B., G.L. and P.T.-C.

Author Information Reprints and permissions information is available at www.nature.com/reprints. Correspondence and requests for materials should be addressed to C.P. (claire.poyart@cch.aphp.fr) or A.G. (alexandra.gruss@jouy.inra.fr).

METHODS

Fatty acid biosynthesis inhibitor and antibacterial assay. MICs were determined in TH broth in 96-well microplates by a dilution method. Exponential bacterial cultures (2×10^6 c.f.u.) were added to wells containing increasing concentrations of cerulenin or triclosan. Plates were incubated at 37 °C overnight and the MIC was defined as the lowest antibiotic concentration that inhibited visible growth. An antibacterial combination assay on *S. agalactiae* strains was performed at the following drug concentrations: gentamicin $8 \mu\text{g ml}^{-1}$ and cerulenin $8 \mu\text{g ml}^{-1}$. Medium was TH or TH plus 10% filtered human serum. Viable counts were determined at 12 h by plating appropriate dilutions on solid TH medium containing 0.1% Tween 80. Synergy was defined as ≥ 100 -fold decrease in c.f.u. ml^{-1} for the combination compared to the active single agent alone. At least three independent experiments were performed with samples in duplicate.

Determination of fatty acid composition. *S. agalactiae* WT, *fabM*, *fabF*, and *fabMF* cultures were propagated in TH broth containing 0.1% Tween 80, and grown to $D_{600\text{ nm}}$ of ~ 0.7 . Cells were washed three times in TH, concentrated 100-fold, and used to inoculate fresh cultures under three conditions: TH; TH plus 0.1% Tween 80 (positive control); and 100% filtered human serum. Cells were harvested after 12 h growth in static conditions at 37 °C, and were washed three times in 0.9% NaCl containing 0.01% Triton X-100, followed by two washes in 0.9% NaCl. Procedures for cell growth and preparation and for cellular and serum fatty acid determinations are also in the Supplementary Table 2 legend.

Bacterial fatty acid composition was analysed as described¹³, with minor modifications. Briefly, washed wet cells (approximately 2–5 mg) were treated with MeOHNa, and fatty acid methyl esters were extracted by adding 200 μl of heptane containing methyl 10-undecenoate (~ 0.22 mM) (Sigma-Aldrich) as internal standard. Serum fatty acid composition was determined on a 200 μl lyophilized sample, which was esterified overnight in 500 μl MeOH plus 50 μl undiluted H_2SO_4 to which 200 μl heptane was added as internal standard. Analyses were carried out on an Autosystem XL gas chromatograph (Perkin Elmer) equipped with a DB-Wax (F&W Scientific) column (30 m \times 0.25 mm \times 0.25 μm). The initial temperature of the on-column injector was 50 °C; the injector was warmed after 0.4 min to 200 °C at $240^\circ\text{C min}^{-1}$, and maintained for 20 min. The temperature of the flame ionization detector was 260 °C. Chromatography was performed at an initial temperature of 50 °C (held for 1 min). The temperature was then increased by $10^\circ\text{C min}^{-1}$ up to 130 °C, followed by 4°C min^{-1} up to 230 °C (held for 10 min). The carrier gas (H_2) flow rate was 20 ml min^{-1} . Results were collected and treated by Turbochrom system (Perkin Elmer). Samples from at least two independent experiments were analysed in duplicate.

Lipid measurements. Plasma triglyceride concentrations were measured by an enzymatic assay adapted to microtitre plates using a commercially available

reagent from bioMérieux (triglycerides PAP 1000). Free fatty acid concentrations were measured using a commercially available reagent from WAKO Chemicals (NEFA-HR 2).

Construction of deletion mutant strains and qRT-PCR analysis. In-frame deletions in *gbs0329* (*fabM*), *gbs0336* (*fabF*), and *gbs0333* (*fabK*) to *gbs0336* (*fabF*) were constructed by using splicing-by-overlap-extension PCR as previously described³⁰ using the oligonucleotides listed in Supplementary Table 4. To carry out chromosomal gene inactivation, PCR fragments were cloned into the thermosensitive shuttle plasmid pG+host1 (ref. 31). Electroporation of GBS strains and allelic exchange were performed as described³⁰ except that transformants were grown in TH supplemented with 0.1% Tween 80. In-frame deletions were confirmed by PCR and sequence analysis. Combined mutants *fabMF* or *fabMKDGF* were constructed by successive allelic exchanges.

qRT-PCR analysis was performed as described²⁹ using primers listed in Supplementary Table 4 (Invitrogen). For each gene, triplicate reactions were performed on RNA samples isolated from at least two independent experiments. The relative fold change of each gene was calculated from $2^{-\Delta\Delta\text{Ct}}$ by using *gyrA* as an internal control gene.

In vivo virulence studies. Exponential *S. agalactiae* cultures grown in TH containing 0.1% Tween 80 were washed three times in 0.9% NaCl, resuspended in RPMI, and incubated without fatty acids for 3 h. Cells were then washed twice and resuspended in 0.9% NaCl. Two-day-old neonatal Sprague-Dawley rat pups were used for mortality studies. Randomized groups of 12 rat pups were inoculated intraperitoneally with 5×10^6 c.f.u. and their survival was studied over a 4-day period.

Adult animal infection tests were performed on C57BL/6 mice (Charles River), treated or not with fenofibrate (Sigma). Three-week-old C57BL/6 female were given a normal diet SAFE-A03 chow of 3.2 kcal g^{-1} metabolizable energy (SAFE). Mice were divided in two groups: One received chow with fenofibrate added (0.2% w/w corresponding to $400 \text{ mg kg}^{-1} \text{ day}^{-1}$) and the other was maintained on the regular chow. Blood was collected before treatment and at days 8 (data not shown) and 15 after a 4-h fasting period to measure serum triglyceride and fatty acid levels. The treatment period lasted two weeks and animals were then inoculated intravenously with 5×10^7 c.f.u. of bacteria, prepared as above. At 3, 24 and 48 h, groups of 3 to 4 mice were sacrificed and bacterial counts in blood and homogenates of liver and brain were determined by plating serial dilutions on TH agar plates supplemented with 0.1% Tween 80. Animal studies were performed at the Pasteur Institute, in compliance with the animal research ethics standards and regulations.

30. Dramsi, S. *et al.* Assembly and role of pili in group B streptococci. *Mol. Microbiol.* **60**, 1401–1413 (2006).

31. Maguin, E., Prevost, H., Ehrlich, S. D. & Gruss, A. Efficient insertional mutagenesis in lactococci and other gram-positive bacteria. *J. Bacteriol.* **178**, 931–935 (1996).

The rate of N-WASP exchange limits the extent of ARP2/3-complex-dependent actin-based motility

Ina Weisswange¹, Timothy P. Newsome^{1†}, Sibylle Schleich¹ & Michael Way¹

Understanding cell motility will require detailed knowledge not only of the localization of signalling networks regulating actin polymerization, but also of their dynamics. Unfortunately, many signalling networks are not amenable to such analysis, as they are frequently transient and dispersed. By contrast, the signalling pathways used by pathogens undergoing actin-based motility are highly localized and operate in a constitutive fashion^{1–5}. Taking advantage of this, we have analysed the dynamics of neuronal Wiskott–Aldrich syndrome protein (N-WASP), WASP-interacting protein (WIP), GRB2 and NCK, which are required to stimulate actin-related protein (ARP)2/3-complex-dependent actin-based motility of vaccinia virus^{6–9}, using fluorescence recovery after photobleaching. Here we show that all four proteins are rapidly exchanging, albeit at different rates, and that the turnover of N-WASP depends on its ability to stimulate ARP2/3-complex-mediated actin polymerization. Conversely, disruption of the interaction of N-WASP with GRB2 and/or the barbed ends of actin filaments increases its exchange rate and results in a faster rate of virus movement. We suggest that the exchange rate of N-WASP controls the rate of ARP2/3-complex-dependent actin-based motility by regulating the extent of actin polymerization by antagonizing filament capping.

During infection, vaccinia virus enhances its cell-to-cell spread by stimulating ARP2/3-complex-dependent actin polymerization beneath the extracellular enveloped virus by locally activating Src- and Abl-dependent signalling cascades^{6,10–12} consisting of GRB2, NCK, WIP and N-WASP^{6–9,13} (Fig. 1a). To obtain insights into the dynamics of this signalling network, we examined the turnover rates of green fluorescent protein (GFP)-tagged GRB2, NCK, WIP and N-WASP recruited to the tips of virus-induced actin tails (Fig. 1b and Supplementary Figs 1, 2), using fluorescence recovery after photobleaching (FRAP). We found that all four GFP-tagged proteins rapidly recover to nearly pre-bleach values, suggesting that they do not form a stable complex beneath the virus (Fig. 1c and Supplementary Fig. 3). Similar results were also observed for GFP-tagged NCK and N-WASP in cell lines lacking endogenous NCK or N-WASP (Supplementary Figs 2, 3). Unexpectedly, the recovery of N-WASP is ~3.5 times slower than that of NCK and WIP, although they are thought to be responsible for the recruitment of N-WASP^{6–8,13}. The similar recovery rates of NCK and WIP suggest that these proteins may be functioning together as a complex. However, NCK is still recruited by the virus independently of WIP in N-WASP-null cells (Fig. 1d, e). Our data suggest that WIP and N-WASP are recruited to the virus as a complex in a NCK-dependent fashion.

Our previous observations indicate that the recruitment of GRB2, which is dependent on phosphorylation of tyrosine 132 of A36R and the presence of N-WASP (Fig. 1a, d), results in the formation of more

actin tails than in its absence⁹. To determine whether GRB2 promotes actin tail formation by stabilizing the actin tail-nucleating complex, we examined the exchange rate of NCK, WIP and N-WASP, which are recruited to actin tails in the absence of tyrosine-132 phosphorylation (Fig. 2a). The A36R–Y132F virus, which does not recruit GRB2, formed fewer actin tails than the Western Reserve (WR) strain (Supplementary Fig. 4). Moreover, FRAP analyses reveal that the absence of GRB2 results in a significant increase in the rate of recovery, not only of N-WASP but also NCK and WIP (Fig. 2b, c and Supplementary Figs 4, 5). A role for GRB2 in stabilization of the complex is also consistent with the increased rate of recovery of GFP–NCK in the absence of GRB2, WIP and N-WASP recruitment in N-WASP-null cells (Fig. 1e and Supplementary Fig. 3).

To confirm our observations obtained using the A36R–Y132F virus, we examined the effects of RNA interference (RNAi)-mediated depletion of GRB2. FRAP analyses on RNAi-treated cells reveal that loss of GRB2 also increases the rates of recovery for NCK, WIP and N-WASP (Fig. 2d, e and Supplementary Fig. 5). These effects are specific to the loss of GRB2, as expressing cyan fluorescent protein (CFP)–GRB2-res, which is resistant to RNAi, results in NCK, WIP and N-WASP exchange rates that are similar to the control values (Fig. 2d, e and Supplementary Fig. 5). Taken together, our data show that GRB2 is acting as a secondary adaptor to help stabilize the vaccinia actin-tail-nucleating complex.

Even in the absence of GRB2, the rate of recovery of N-WASP did not approach that of NCK or WIP. One possible explanation is that N-WASP is stabilized by an additional interaction. Recent observations have shown that the WASP-homology 2 (WH2) domains of N-WASP, or actin bound to these domains, can interact with free barbed ends of growing actin filaments¹⁴. To test whether this interaction might explain why N-WASP turns over more slowly than NCK and WIP, we expressed GFP-tagged N-WASP–R410A/R438A (RA/RA), which has a 30-fold-lower affinity for actin monomers than the wild-type protein¹⁴, in N-WASP-null cells (Fig. 3a and Supplementary Fig. 6). N-WASP-null cells expressing GFP–N-WASP–RA/RA that were infected with WR or A36R–Y132F viruses had significantly fewer actin tails than those complemented with N-WASP (Supplementary Fig. 6). The loss of GRB2 recruitment and/or N-WASP–RA/RA also resulted in significantly shorter actin tails (Fig. 3b and Supplementary Fig. 6). FRAP analysis revealed that N-WASP–RA/RA has a faster exchange rate than N-WASP in WR-infected cells (Fig. 3c, d and Supplementary Fig. 6). Interactions between WH2 and actin thus help to stabilize N-WASP during ARP2/3-complex-mediated actin polymerization. However, this interaction cannot explain why the dynamics of N-WASP–RA/RA is slower than that of NCK and WIP even in the absence of GRB2.

We therefore wondered whether an interaction between N-WASP and the ARP2/3 complex responsible for nucleating actin polymerization

¹Cell Motility Laboratory, Cancer Research UK, London Research Institute, 44 Lincoln's Inn Fields, London WC2A 3PX, UK. †Present address: School of Molecular and Microbial Biosciences, G08 - Biochemistry and Microbiology, University of Sydney, New South Wales 2006, Australia.

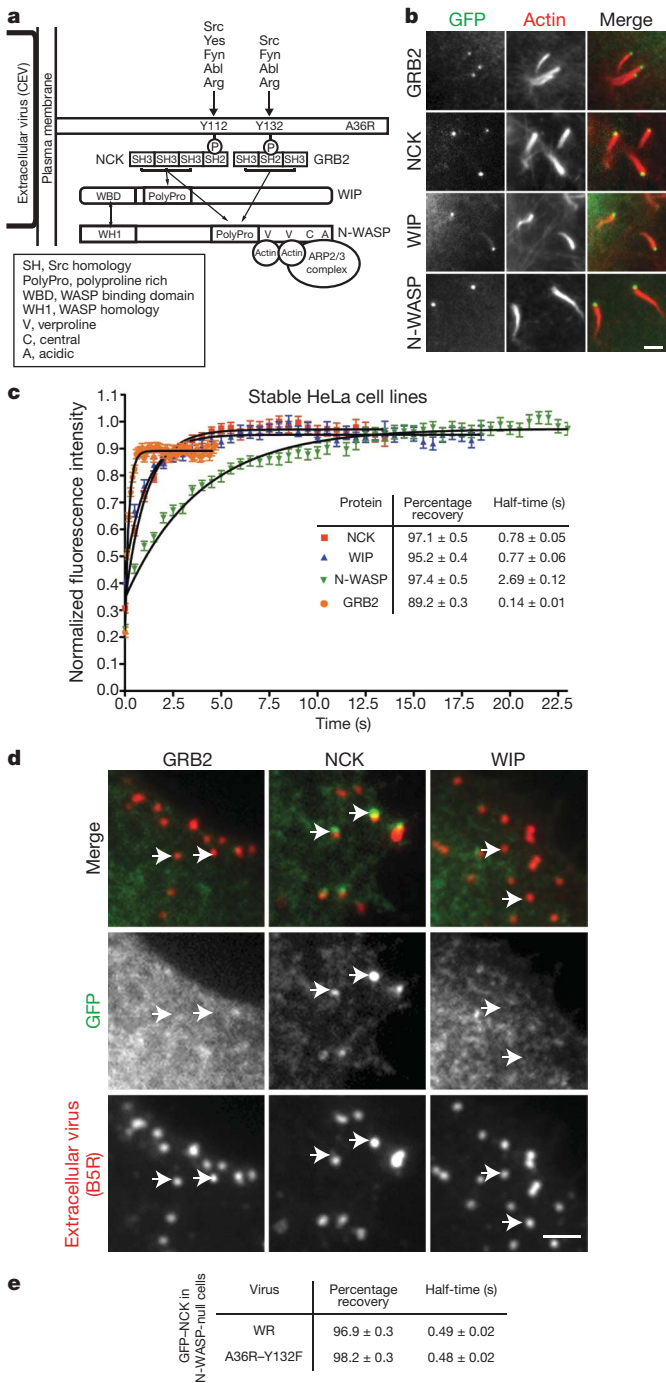


Figure 1 | Components of the vaccinia actin-nucleating complex are highly dynamic. **a**, Sketch indicating the interactions between the proteins recruited beneath extracellular virus particles that are responsible for stimulating ARP2/3-mediated actin tail formation. Src- and Abl-family kinases known to phosphorylate tyrosine 112 or 132 of A36R are indicated together with motifs and domains. **b**, Immunofluorescence images demonstrating that GFP-tagged NCK, GRB2, WIP and N-WASP (green) are recruited to the tips of virus-induced actin tails (red) in infected HeLa cells. Scale bar, 2.5 μm. **c**, The recovery kinetics of the indicated GFP-tagged protein on the tips of actin tails after photobleaching. Error bars, s.e.m. with $n = 52$. The values for the percentage and half-time of recovery for each protein are indicated. **d**, GFP-tagged NCK, but not GRB2 or WIP, is recruited beneath extracellular virus particles (B5R, red) in N-WASP-null cells. Scale bar, 2.5 μm. **e**, Values derived from 52 fitted recovery curves together with the s.e.m. for the percentage and half-time of recovery of GFP-NCK in N-WASP-null cells infected with the indicated virus.

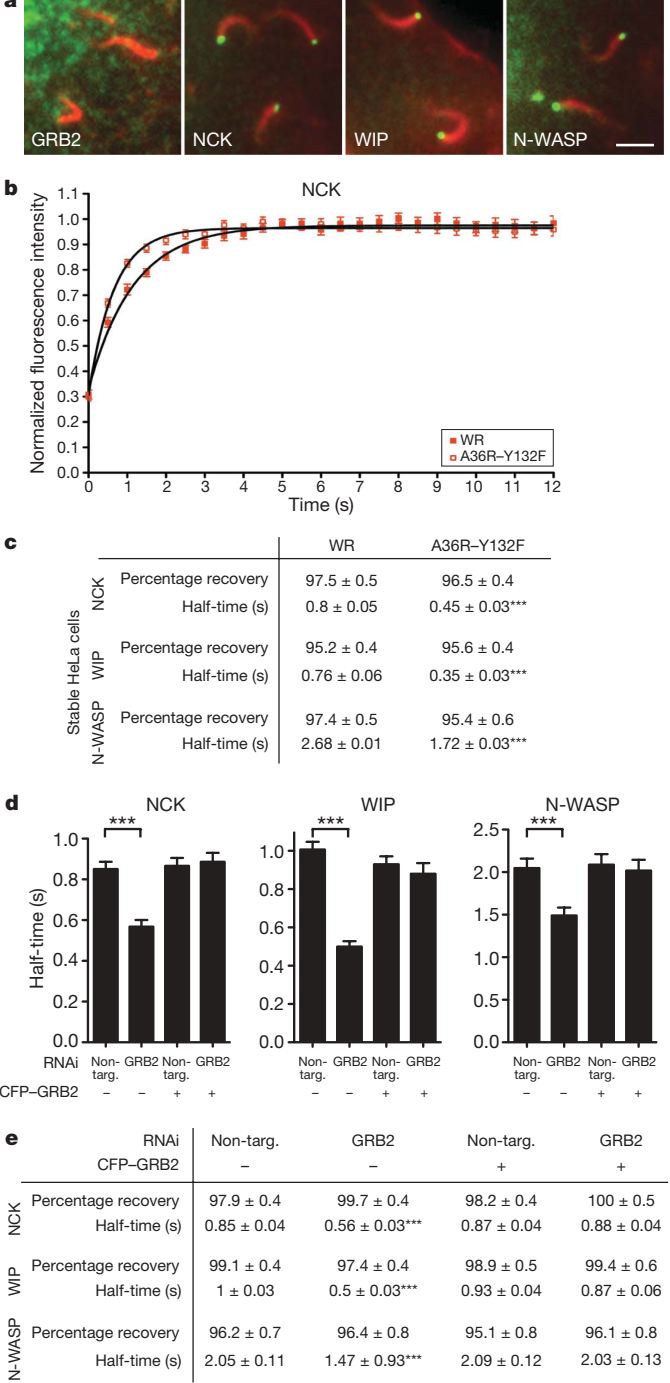


Figure 2 | GRB2 stabilizes the vaccinia actin-nucleating complex. **a**, Immunofluorescence images demonstrating that GFP-tagged NCK, WIP and N-WASP, but not GRB2, are recruited to the tips of actin tails induced by the A36R-Y132F virus. Scale bar, 2.5 μm. **b**, The recovery kinetics of GFP-NCK on the tips of actin tails after photobleaching in WR- and A36R-Y132F-infected HeLa cells. Error bars, s.e.m.; $n = 52$. **c**, Values derived from 52 fitted recovery curves for the percentage and half-time of recovery together with the s.e.m. of the indicated GFP-tagged protein in HeLa cells infected with WR and A36R-Y132F viruses. **d**, The half-time of recovery of GFP-tagged NCK, WIP and N-WASP on the tips of actin tails in HeLa cells treated with the indicated RNAi, GRB2-specific or non-targeting control (non-targ.), with or without expression of RNAi-resistant CFP-GRB2. Error bars, s.e.m.; $n = 52$. **e**, Values derived from 52 fitted recovery curves together with the s.e.m. of the percentage and half-time of recovery for the indicated GFP-tagged proteins in HeLa cells treated with the indicated RNAi. *** $P < 0.001$.

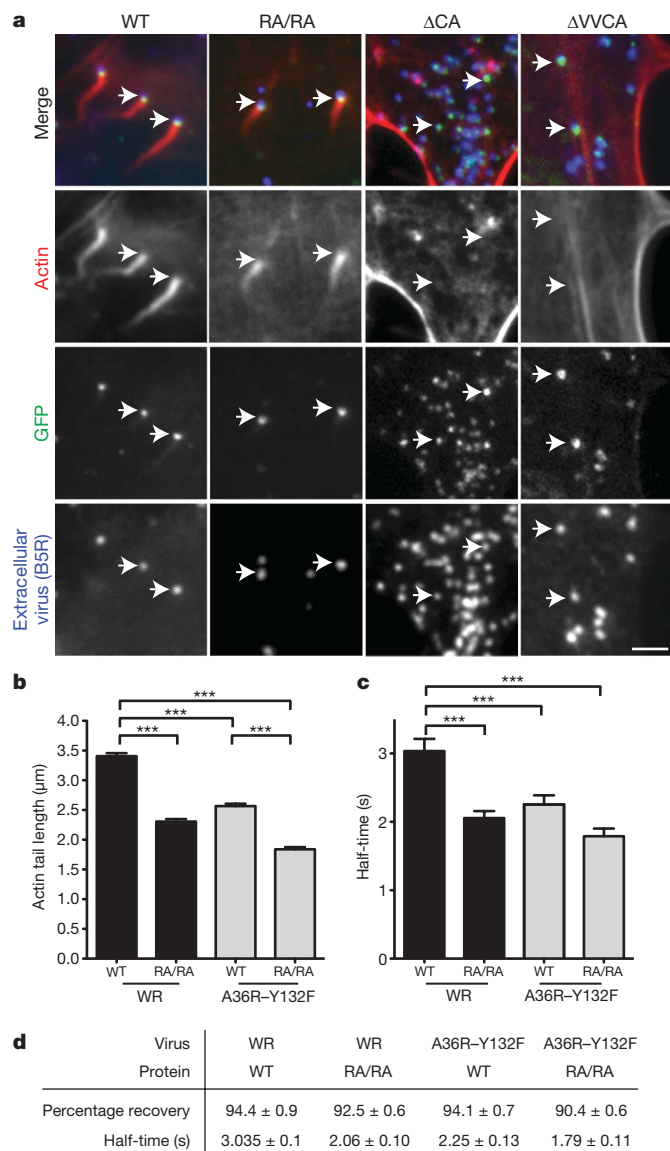


Figure 3 | WH2:actin filament interactions contribute to N-WASP stability. **a**, Immunofluorescence images demonstrating that GFP-tagged wild-type (WT), RA/RA, ΔCA and ΔVVCA N-WASP are recruited beneath extracellular virus particles (B5R, blue) in the N-WASP-null cells. Only GFP-tagged N-WASP and RA/RA mutant are able to rescue actin tail formation (red) in the N-WASP-null cells. Scale bar, 2.5 μm. **b**, The length of actin tails induced by WR and A36R-Y132F viruses in rescued N-WASP-null cells expressing GFP-tagged N-WASP or N-WASP-RA/RA. Error bars, s.e.m. with $n = 450$. **c**, The half-time of recovery of GFP-tagged N-WASP and N-WASP-RA/RA in WR- and A36R-Y132F-infected cells. Error bars, s.e.m. with $n = 52$. **d**, Values derived from 52 fitted recovery curves together with the s.e.m. for GFP-tagged N-WASP or N-WASP-RA/RA in N-WASP-null cells infected with the indicated virus. *** $P < 0.001$.

might also contribute to its stability. The turnover rate of N-WASP with WH2, central and acidic regions deleted, N-WASP-ΔVVCA, which is unable to promote ARP2/3-complex-dependent actin tail formation, was examined (Fig. 1a)⁷. GFP-N-WASP-ΔVVCA was recruited beneath virus particles but was unable to promote their movement, as it cannot stimulate actin tail formation in N-WASP-null cells (Fig. 3a and Supplementary Fig. 6). Unexpectedly, we found that after bleaching, GFP-N-WASP-ΔVVCA did not recover (Fig. 4a and Supplementary Fig. 7). GFP-N-WASP with central and acidic regions deleted, GFP-N-WASP-ΔCA, which can still bind actin monomers but is unable to interact with the ARP2/3 complex, was also recruited beneath the virus and did not turn over (Figs 3a and 4a).

The lack of recovery of these mutants would suggest that the turnover of N-WASP is dependent on active actin polymerization. We therefore examined the turnover rate of N-WASP in the presence of cytochalasin D, a potent inhibitor of actin polymerization¹⁵. Cytochalasin D inhibited actin tail formation and virus movement, although GRB2, NCK, WIP and N-WASP were still recruited (Fig. 4b, data not shown and Supplementary Fig. 8). The ARP2/3 complex (anti-ARPC5) and actin were also still recruited to the virus, albeit at reduced levels in the presence of the drug (Supplementary Fig. 9). Moreover, the recovery of GFP-tagged N-WASP and WIP was severely reduced (Fig. 4c and Supplementary Fig. 8). By contrast, NCK was able to recover, albeit at a slower rate, consistent with its ability to be recruited independently of WIP and N-WASP. The turnover rate of GRB2 remained essentially unchanged (Fig. 4c). One possible explanation for our observations is that interaction of N-WASP with the ARP2/3 complex and stimulation of actin polymerization promotes its dissociation from WIP. This dissociation would allow both proteins to act independently of each other, consistent with their different rates of exchange.

An actin filament nucleated by the ARP2/3 complex will polymerize until a capping protein blocks the growing barbed end. An interaction of the growing barbed end with the WH2 domains of N-WASP would also effectively limit filament extension. The association of N-WASP with the barbed end of a growing actin filament as well as the ARP2/3 complex nucleating a new actin filament could explain why N-WASP has a slower exchange rate than NCK and WIP. Ultimately however, this interaction may limit the overall rate of virus movement, as it competes with the addition of actin monomers to the growing barbed end of filaments beneath the virus. The turnover of N-WASP is therefore required for actin-based motility of the virus, and at the same time active actin polymerization is required to promote turnover of the molecule. This hypothesis is consistent with recent observations demonstrating that release of N-WASP from actin and the ARP2/3 complex is required for actin-based motility of functionalized giant unilamellar vesicles¹⁶.

Our model predicts that the stability of N-WASP beneath the virus, which is dependent on GRB2 and active actin polymerization, will determine how fast the virus moves, as it will regulate the overall rate of actin polymerization in the actin tail. To examine if this is the case, we measured the rate of actin-based virus movement in the absence of GRB2 and in cells only expressing N-WASP-RA/RA (Fig. 4d). We found that loss of the stabilizing influence of GRB2 on N-WASP results in significantly faster rate of movement for the A36R-Y132F virus ($0.33 \pm 0.01 \mu\text{m s}^{-1}$ versus $0.28 \pm 0.01 \mu\text{m s}^{-1}$). Disruption of the interaction of N-WASP with the barbed end of actin filaments also promoted a similar increase in speed ($0.34 \pm 0.01 \mu\text{m s}^{-1}$). An increase in the rate of movement of lipid-coated beads is also observed in *in vitro* motility assays when the WH2 domains of N-WASP are disrupted¹⁴. The fastest rate of virus movement ($0.37 \pm 0.01 \mu\text{m s}^{-1}$) was observed in A36R-Y132F-infected cells only expressing N-WASP-RA/RA (Fig. 4d).

Our results indicate that the reduced stability of N-WASP enhances virus motility even though the actin tails get shorter (Fig. 3b). The formation of shorter tails suggests that reducing N-WASP-barbed end interactions does not actually lead to more extensive growth of individual actin filaments. It could, however, result in increased capping of barbed ends by capping proteins because of reduced competition with N-WASP beneath the virus. Consistent with this, previous observations in reconstituted *in vitro* motility assays have shown that increased capping of barbed ends also increases the rate of *Listeria* motility, although actin tail lengths get shorter¹⁷. Our suggestion is further supported by recent observations demonstrating that capping protein enhances actin-based motility by promoting actin filament nucleation by the ARP2/3 complex¹⁸.

In conclusion, we suggest that in the steady state, it is the stability of N-WASP association beneath the extracellular virus that determines how fast it moves, by virtue of its ability to regulate actin

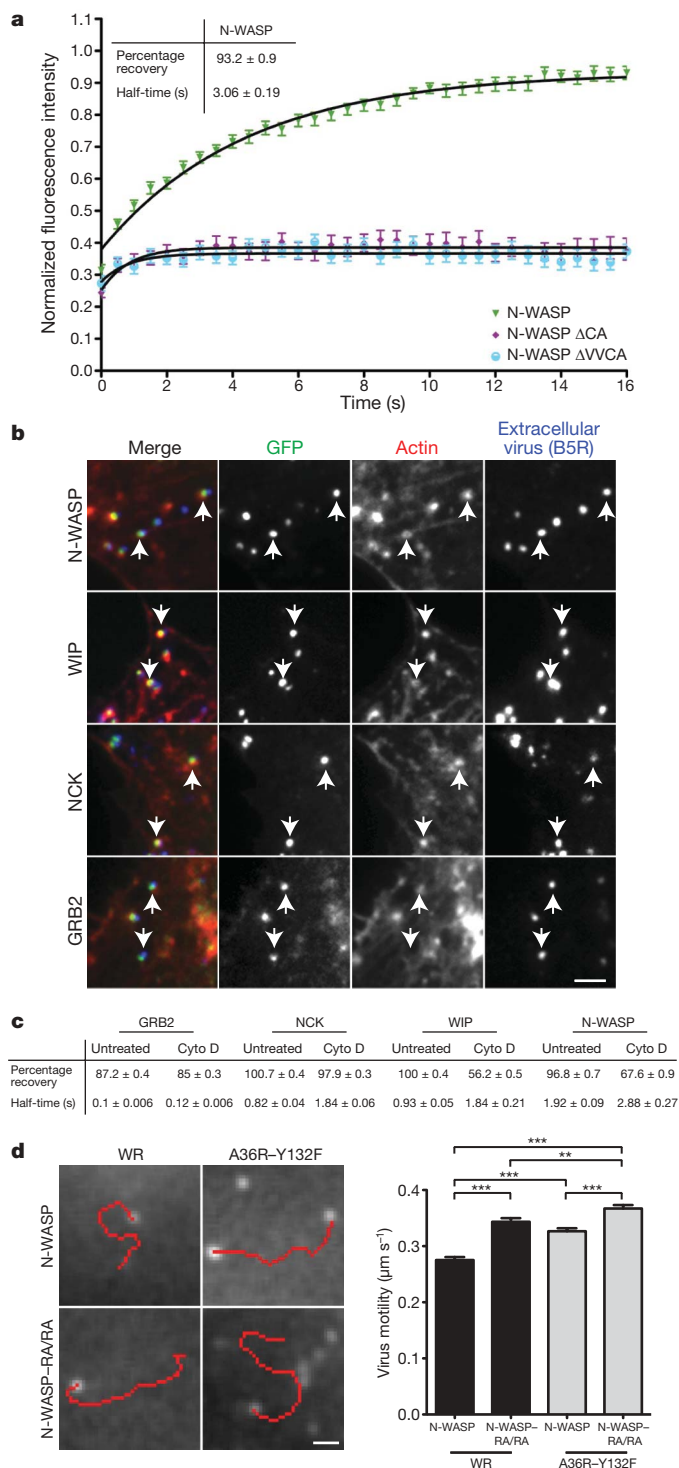


Figure 4 | Virus movement and N-WASP turnover is dependent on actin polymerization. **a**, The recovery kinetics of GFP-tagged N-WASP, Δ CA and Δ VVCA after photobleaching, together with the fitted data for N-WASP. Error bars, s.e.m. with $n = 52$. **b**, GFP-tagged NCK, GRB2, WIP and N-WASP are recruited by extracellular virus particles (B5R, blue) but are unable to induce actin tails in the presence of cytochalasin D. Scale bar, 2.5 μ m. **c**, The percentage and half-time of recovery derived from 52 fitted recovery curves for the indicated proteins in the presence or absence of cytochalasin D (cyto D). **d**, Images illustrating the movement of WR and A36R-Y132F viruses over 1 min (red line) in N-WASP-null cells expressing GFP-tagged N-WASP or N-WASP-RA/RA. Scale bar, 1 μ m. The graph shows the average speed of virus movements ($n = 120$ –150) over 1 min. $**P < 0.01$, $***P < 0.001$.

filament growth by antagonizing capping proteins. Furthermore, the inverse relationship between the rate of N-WASP exchange and the number of actin tails suggests that there is also a critical balance between the stability of N-WASP, barbed-end capping and ARP2/3-complex-dependent actin filament nucleation. Future studies will be aimed at understanding the relationship between these parameters as well as the organization of filaments within virus-induced actin tails.

METHODS SUMMARY

Cell lines, infection and immunofluorescence. Stable cell lines expressing GFP-tagged GRB2, NCK1, WIP, N-WASP and N-WASP mutants were created using recombinant lentiviruses and isolated by fluorescence-activated cell sorting (FACS) as described previously¹⁹. Cells were infected with WR and A36R-Y132F strains of vaccinia virus and processed for immunofluorescence analysis to reveal extracellular virus particles, the actin cytoskeleton and GFP signals as described previously²⁰. Actin tail formation was quantified as previously described⁹.

Live cell imaging and FRAP analysis. Live cell imaging of vaccinia-infected cells at 37 °C was performed using a Plan-Apochromat $\times 63/1.4$ objective on a Zeiss Axiovert 200 equipped with a Photometrics Cascade II camera controlled by Metamorph. The motion of the GFP-N-WASP signal associated with 120–150 red fluorescent protein (RFP)-tagged viruses at the tip of actin tails was tracked for 1 min using Metamorph to calculate the average speed in micrometres per second.

All FRAP experiments were performed using a Zeiss LSM 510 META system with a Plan-Apochromat $\times 63/1.4$ objective at 37 °C. The GFP signal associated with moving virus particles was bleached using two iterations of the 488-nm laser at 80% power followed by image acquisition every 300 ms (except in the case of GRB2, where there was no delay) with laser power settings of 4% for 488 nm (GFP) and 8% for 568 nm (RFP) using an open pinhole. The recovery of the GFP signal associated with the virus was measured using Metamorph. The resulting background-subtracted data was then normalized to the first pre-bleached image and fitted using the Prism software and the equation $Y_{(t)} = (Y_{\max} - Y_{\min})(1 - e^{-kt}) + Y_{\min}$ (ref. 21), where $Y_{(t)}$ is the intensity of fluorescence at time t , Y_{\max} and Y_{\min} are respectively the maximum and minimum intensities of fluorescence post-bleaching and k is the rate constant of recovery. In all cases, the percentage, the rate constant and the half-time of recovery were derived from 52 fitted recovery curves together with the s.e.m. and significance where appropriate.

Full Methods and any associated references are available in the online version of the paper at www.nature.com/nature.

Received 23 October 2008; accepted 12 January 2009.

1. Frischknecht, F. & Way, M. Surfing pathogens and the lessons learned for actin polymerization. *Trends Cell Biol.* **11**, 30–38 (2001).
2. Munter, S., Way, M. & Frischknecht, F. Signaling during pathogen infection. *Sci. STKE* 2006, doi: 10.1126/stke.3352006re5 (2006).
3. Bhavsar, A. P., Guttman, J. A. & Finlay, B. B. Manipulation of host-cell pathways by bacterial pathogens. *Nature* **449**, 827–834 (2007).
4. Pawson, T. & Warner, N. Oncogenic re-wiring of cellular signaling pathways. *Oncogene* **26**, 1268–1275 (2007).
5. Backert, S., Feller, S. M. & Wessler, S. Emerging roles of Abl family tyrosine kinases in microbial pathogenesis. *Trends Biochem. Sci.* **33**, 80–90 (2008).
6. Frischknecht, F. *et al.* Actin based motility of vaccinia virus mimics receptor tyrosine kinase signalling. *Nature* **401**, 926–929 (1999).
7. Moreau, V. *et al.* A complex of N-WASP and WIP integrates signalling cascades that lead to actin polymerization. *Nature Cell Biol.* **2**, 441–448 (2000).
8. Snapper, S. B. *et al.* N-WASP deficiency reveals distinct pathways for cell surface projections and microbial actin-based motility. *Nature Cell Biol.* **3**, 897–904 (2001).
9. Scaplehorn, N. *et al.* Grb2 and Nck act cooperatively to promote actin-based motility of vaccinia virus. *Curr. Biol.* **12**, 740–745 (2002).
10. Newsome, T. P., Scaplehorn, N. & Way, M. SRC mediates a switch from microtubule- to actin-based motility of vaccinia virus. *Science* **306**, 124–129 (2004).
11. Reeves, P. M. *et al.* Disabling poxvirus pathogenesis by inhibition of Abl-family tyrosine kinases. *Nature Med.* **11**, 731–739 (2005).
12. Newsome, T. P., Weisswange, I., Frischknecht, F. & Way, M. Abl collaborates with Src family kinases to stimulate actin-based motility of vaccinia virus. *Cell. Microbiol.* **8**, 233–241 (2006).
13. Zettl, M. & Way, M. The WH1 and EVH1 domains of WASP and Ena/VASP family members bind distinct sequence motifs. *Curr. Biol.* **12**, 1617–1622 (2002).
14. Co, C., Wong, D. T., Gierke, S., Chang, V. & Taunton, J. Mechanism of actin network attachment to moving membranes: barbed end capture by N-WASP WH2 domains. *Cell* **128**, 901–913 (2007).

15. Kueh, H. Y., Charras, G. T., Mitchison, T. J. & Brieher, W. M. Actin disassembly by cofilin, coronin, and Aip1 occurs in bursts and is inhibited by barbed-end cappers. *J. Cell Biol.* **182**, 341–353 (2008).
16. Delatour, V. *et al.* Arp2/3 controls the motile behavior of N-WASP-functionalized GUVs and modulates N-WASP surface distribution by mediating transient links with actin filaments. *Biophys. J.* **94**, 4890–4905 (2008).
17. Pantaloni, D., Boujemaa, R., Didry, D., Gounon, P. & Carlier, M.-F. The Arp2/3 complex branches filament barbed ends: functional antagonism with capping proteins. *Nature Cell Biol.* **2**, 385–391 (2000).
18. Akin, O. & Mullins, R. D. Capping protein increases the rate of actin-based motility by promoting filament nucleation by the Arp2/3 complex. *Cell* **133**, 841–851 (2008).
19. Arakawa, Y., Cordeiro, J. V. & Way, M. F11L-mediated inhibition of RhoA-mDia signaling stimulates microtubule dynamics during vaccinia virus infection. *Cell Host Microbe* **1**, 213–226 (2007).
20. Arakawa, Y., Cordeiro, J. V., Schleich, S., Newsome, T. & Way, M. The release of vaccinia virus from infected cells requires RhoA-mDia modulation of cortical actin. *Cell Host Microbe* **1**, 227–240 (2007).
21. Shewan, A. M. *et al.* Myosin 2 is a key Rho kinase target necessary for the local concentration of E-cadherin at cell-cell contacts. *Mol. Biol. Cell* **16**, 4531–4542 (2005).

Supplementary Information is linked to the online version of the paper at www.nature.com/nature.

Acknowledgements We would like to thank T. Pawson and S. Snapper for NCK- and N-WASP-null cell lines and the FACS laboratory (Cancer Research UK, London) for help sorting stable cell lines. We are also very grateful to the members of the Way laboratory, J. Beaudouin, M.-F. Carlier, H. Gerhardt, B. Mayer, K. Rottner, M. Rosen and M. Welch for discussions and comments on the manuscript. T.P.N. was funded in part by a fellowship from the Human Frontier Science Program (HFSP). This work was funded by Cancer Research UK.

Author Information Reprints and permissions information is available at www.nature.com/reprints. Correspondence and requests for materials should be addressed to M.W. (michael.way@cancer.org.uk).

METHODS

Generation of stable GFP cell lines and western-blot analysis. NCK 1/2^{-/-} (ref. 22) and N-WASP^{-/-} (ref. 8) cells were provided by T. Pawson and S. Snapper, respectively. Inserts corresponding to GRB2, NCK, WIP, N-WASP and N-WASP-ΔVCA were isolated from previously described vectors^{6,7,9} and cloned into the NotI/EcoRI site of a modified pLL3.7-GFP vector^{19,23}. N-WASP-RA/RA and N-WASP-ΔCA mutants were created by PCR using GFP-N-WASP as a template. N-WASP-RA/RA and N-WASP-ΔCA were cloned into the NotI/EcoRI sites of the pE/L-GFP and pLL3.7-GFP vectors. The fidelity of all clones was confirmed by sequencing.

Lentiviruses for each of the GFP-tagged proteins were produced using the Lentivirus system^{19,23}. Cells were infected with lentiviruses and stable lines expressing the various GFP-tagged proteins isolated using FACS. The following cell lines expressing the indicated GFP-tagged protein were created: HeLa (GRB2, NCK, WIP and N-WASP); N-WASP^{-/-} (N-WASP, N-WASP-ΔVCA and N-WASP-ΔCA, and N-WASP-RA/RA) and NCK 1/2^{-/-} (NCK1).

Western-blot analysis of GFP-stable cell lines and short interfering RNA (siRNA)-treated cells was performed using the following primary antibodies: GFP 3E1 (Cancer Research UK); actin (Ac74), α -actinin (BM 7.52) and α -tubulin (DM14) (Sigma-Aldrich); NCK rabbit polyclonal (Upstate Biotech), GRB2 (81) (Transduction Laboratories); WIP (H224) (Santa Cruz) and N-WASP⁷. The following secondary antibodies were used: goat HRP conjugates to rabbit, rat and mouse IgG (Bio-Rad Laboratories).

Infections, immunofluorescence and actin tails. Cells were infected with WR or A36R-Y132F viruses at a multiplicity of infection of 0.5 and immunofluorescence analyses performed at 8 h post-infection for HeLa cells and 10 h post-infection for knockout cells as previously described^{9,20}. Virus particles were labelled with an antibody against B5R (19C2 rat monoclonal)²⁴ and F-actin was stained using Alexa 568- or Alexa 488-phalloidin (Molecular Probes). The ARP2/3 complex was detected using anti-ARPC5 (p16-Arc) (323H3 mouse monoclonal, Synaptic Systems). Actin tail formation was quantified by counting 100 cells on three independent days as previously described⁹. Only B5R positive, that is, infected cells where virus particles had reached the cell periphery, were analysed. Actin tail length was assessed in N-WASP^{-/-} cells stably expressing GFP-N-WASP or GFP-N-WASP-RA/RA 10 h after infection with WR or A36R-Y132F. The lengths of actin tails was determined from fixed images of ten individual cells in three independent experiments. For each of the four conditions, at least 450 actin tails were measured.

Construction of recombinant RFP-A3L vaccinia virus. A fragment of genomic WR DNA corresponding to 200 base pairs upstream of A3L was amplified by PCR and cloned into the KpnI site of pEL-RFP-A3L to create the targeting LA-RFP-A3L in pBS SKII. The RFP-A3L targeting vector was transfected into WR- and A36R-Y132F-infected cells. The viruses encoding RFP-A3L were isolated by successive rounds of plaque purification and the fidelity of the final recombinant viruses was confirmed by sequencing, immunofluorescence, plaque size comparison and re-infection assays as described previously²⁰.

Live-cell imaging, FRAP and data analysis. All live-cell imaging was performed on cells infected with WR and A36R-Y132F viruses that also encode RFP-A3L within their genome to ensure that the analysed GFP signal corresponds to a virus particle. Virus particle motility was analysed in N-WASP^{-/-} cells stably expressing GFP-tagged N-WASP or N-WASP-RA/RA 10 h post-infection. The GFP signal was recorded every 5 s for a period of 3 min using a Plan-Apochromat 63/1.40 Oil Ph3 lens on a Zeiss Axiovert 200 equipped with a Cascade II (Photometrics) under the control of Metamorph (Molecular Devices). The motion of the GFP signal, which corresponds to the tip of an actin tail, was tracked using Metamorph over a period of 1 min to calculate the speed in micrometres per second. Imaging was performed on three independent days and more than 40 virus particles in at least ten different cells were analysed on each day.

All FRAP experiments were performed on a LSM 510 META system using a Plan-Apochromat 63/1.40 Oil Ph3 lens (Zeiss). Infected cells to be imaged were first identified under low-light fluorescence using the eyepiece. The particle to

bleach was aligned live on the computer screen to a saved region of interest (ROI) for bleaching. Two pre-bleached images were acquired before the GFP signal was bleached using two iterations of the 488-nm laser at 80% power followed by acquisition of images with laser powers described above. Images were recorded with laser power settings of 4% for 488 nm (GFP) and 8% for 568 nm (RFP) using an open pinhole. The time interval between acquisitions was set to 300 ms, except in the case of GRB2, where there was no delay.

The fluorescence intensity of the bleached virus particle was determined using a fixed-size ROI, which was moved by hand to ensure it always remained centred over the moving virus particle, with Metamorph. The fluorescence intensity in a fixed ROI immediately adjacent to the virus was measured and an average value for the whole movie was subtracted from the virus signal to correct for background fluorescence. As the area imaged was small and virus particles were moving, it was not possible to correct for photo-damage because a reference non-bleached particle was not available in each movie. The resulting background-subtracted data was then normalized to the first pre-bleached image.

Kinetic modelling was performed using the Prism software and the equation $Y(t) = (Y_{\max} - Y_{\min})(1 - e^{-kt}) + Y_{\min}$ (ref. 21). The rate constant of recovery (k) and the maximum recovery compared with the first pre-bleached image (percentage recovery) were calculated from the fitted curves. The rate constant of recovery was used to calculate the half-time ($t_{1/2} = \ln 2/k$). Each curve represents an average of 52 virus particles that were acquired over three consecutive days in which between 15 and 20 viruses were bleached in at least five different cells. Data in the graphs are presented as mean and standard error of the mean.

RNAi treatments. HeLa cells were transfected with 20 pmol of a SMARTpool of four oligonucleotide duplexes against GRB2 (UGAAUGAGCUGGUGGAUUA UU, AGGCAGAGCUUAAUGGAAAUU, CGAAGAAUGUGAUCAGAACUU, GAAAGGAGCUUGCCACGGGUU) or the non-targeting SMARTpool 2 (Dharmacon) using the Lipofectamine RNAi Max kit (Invitrogen) according to the manufacturer's protocol. Two days post-transfection, cells were infected with WR and processed for FRAP analysis, immunofluorescence or western-blot analysis 8 h later. To rescue the RNAi effect on GRB2, an RNAi-resistant GRB2 was cloned Not/EcoRI into the pE/L-CFP vector. The following primers were used to introduce silent mutations into the codons encoding the indicated amino acids in GRB2: Glu 30, Cys 32, Gln 34; Ala 39, Leu 41, Gly 43; Asn 129, Leu 131, Asp 133; Gly 196, Cys 198, His 199. The clone was verified by sequence analysis. RNAi-treated HeLa cells were infected with WR and transfected with the CFP-GRB2-res, which is resistant to RNAi, 4 h later using Effectene (Qiagen) according to the manufacturer's protocol. Two hours post-transfection, cells were washed and allowed to recover for 2 h before imaging was started. Before analysing a cell the expression of CFP-GRB2-res in each cell was checked.

Cytochalasin D treatments. Cells were plated on fibronectin-coated coverslips or MatTek dishes to a confluency of around 70% the day before the experiment. Cells were infected for 8 h before cytochalasin D (Sigma-Aldrich) was added to the medium at a final concentration of 1 μ M as described previously²⁰. Cells were treated for 30 min before fixation or directly used for FRAP experiments.

Statistical analysis. The data in the graphs are presented as mean and standard error of the mean. The data were analysed by analysis of variance followed by Newman-Keuls multiple comparison test or Student's t -test using Prism 5.0 (GraphPad Software). Statistical analysis of fitted FRAP data was performed using the "Do the best fit values of selected parameters differ between data sets" function in Prism 5.0. A P value of <0.05 is considered statistically significant. A single asterisk indicates $P < 0.05$, a double asterisk indicates $P < 0.01$ and a triple asterisk indicates $P < 0.001$.

22. Bladt, F. *et al.* The murine Nck SH2/SH3 adaptors are important for the development of mesoderm-derived embryonic structures and for regulating the cellular actin network. *Mol. Cell. Biol.* **23**, 4586–4597 (2003).
23. Robinson, D. A. *et al.* A lentivirus-based system to functionally silence genes in primary mammalian cells, stem cells and transgenic mice by RNA interference. *Nature Genet.* **33**, 401–406 (2003).
24. Hiller, G. & Weber, K. Golgi-derived membranes that contain an acylated viral polypeptide are used for vaccinia virus envelopment. *J. Virol.* **55**, 651–659 (1985).

LETTERS

Casein kinase 1 α governs antigen-receptor-induced NF- κ B activation and human lymphoma cell survival

Nicolas Bidère^{1,4*}, Vu N. Ngo^{2*}, Jeansun Lee¹, Cailin Collins², Lixin Zheng¹, Fengyi Wan¹, R. Eric Davis², Georg Lenz², D. Eric Anderson³, Damien Arnoult⁴, Aimé Vazquez⁴, Keiko Sakai^{1†}, Jun Zhang¹, Zhaojing Meng⁵, Timothy D. Veenstra⁵, Louis M. Staudt^{2*} & Michael J. Lenardo^{1*}

The transcription factor NF- κ B is required for lymphocyte activation and proliferation as well as the survival of certain lymphoma types^{1,2}. Antigen receptor stimulation assembles an NF- κ B activating platform containing the scaffold protein CARMA1 (also called CARD11), the adaptor BCL10 and the paracaspase MALT1 (the CBM complex), linked to the inhibitor of NF- κ B kinase complex^{3–12}, but signal transduction is not fully understood¹. We conducted parallel screens involving a mass spectrometry analysis of CARMA1 binding partners and an RNA interference screen for growth inhibition of the CBM-dependent ‘activated B-cell-like’ (ABC) subtype of diffuse large B-cell lymphoma (DLBCL)¹². Here we report that both screens identified casein kinase 1 α (CK1 α) as a bifunctional regulator of NF- κ B. CK1 α dynamically associates with the CBM complex on T-cell-receptor (TCR) engagement to participate in cytokine production and lymphocyte proliferation. However, CK1 α kinase activity has a contrasting role by subsequently promoting the phosphorylation and inactivation of CARMA1. CK1 α has thus a dual ‘gating’ function which first promotes and then terminates receptor-induced NF- κ B. ABC DLBCL cells required CK1 α for constitutive NF- κ B activity, indicating that CK1 α functions as a conditionally essential malignancy gene—a member of a new class of potential cancer therapeutic targets.

For a better understanding of signal regulation by the CBM complex, we performed a mass spectrometry proteomic screen after CARMA1 immunoprecipitation. Sixteen peptides covering 54% of the length of CK1 α were isolated from an excised band (Fig. 1a and Supplementary Fig. 1). CK1 α belongs to the CK1 family of serine/threonine protein kinases, which regulates developmental and homeostatic processes including the Wnt/ β -catenin pathway and circadian rhythm¹³. Co-immunoprecipitations in HEK293T cells showed that haemagglutinin (HA)-tagged CK1 α interacted with V5-CARMA1 (Fig. 1b). CARMA1, BCL10 and MALT1 associated with CK1 α after TCR stimulation in Jurkat T lymphocytes, and in BJAB B cells stimulated with phorbol 12-myristate 13-acetate (PMA) and ionomycin (Fig. 1c–e). Notably, phosphorylated forms of BCL10 and ubiquitinated species of MALT1, modifications due to signalling¹⁴, associated with CK1 α . Moreover, MALT1 and BCL10 precipitations revealed TCR-induced recruitment of CK1 α concomitantly with inhibitor of NF- κ B kinase (IKK)- β and phosphorylated IKK- β (p-IKK- β ; Fig. 1d and data not shown). Also, cytosolic CK1 α reorganized into punctate structures that co-localized with CD3 clusters on TCR activation (Fig. 1f), suggesting an association with CBM components within membrane microdomains^{2,15}. In contrast to

TCR agonists, tumour necrosis factor- α (TNF- α), which does not use the CBM, induced no interaction between CK1 α and CBM constituents (Supplementary Fig. 2). Finally, antibody depletion of CK1 α from cell lysates removed nearly the entire active CBM complex (Supplementary Fig. 3). Hence, CK1 α is a new component selectively entering the active CBM complex after antigen receptor stimulation.

CK1 α harbours a short and unique carboxy-terminal portion attached to the conserved kinase domain¹³ (Fig. 1a). Removing this region (Δ 283–337) abolished CK1 α binding to CARMA1 (Fig. 1g). In addition, the human (residues 283–337) and mouse (283–325) CK1 α C-terminal domains were sufficient, with Y292 and D293 as the key residues, for CARMA1 association (Fig. 1h and Supplementary Fig. 4a, b). We also found that both the coiled-coil (CC) and linker regions (CCL) of CARMA1 together were critical for CK1 α binding (Fig. 1i and Supplementary Fig. 4c).

The CBM complex is an obligate gateway from lymphocyte antigen receptors to NF- κ B activation^{1,3,8–11}. To define the functional importance of CK1 α , we first decreased its endogenous levels by RNA interference in primary human T cells. CK1 α (also called *CSNK1A1*) silencing reduced TCR-induced interleukin-2 (IL-2) production as did silencing of messenger RNA for NF- κ B p65 (*RELA*) and *BCL10* (Fig. 2a). This was accompanied by diminished IL-2 receptor (CD25) upregulation, and reduced proliferation (Fig. 2b). In Jurkat cells, CK1 α knockdown with small interfering RNAs (siRNAs) decreased the TCR induction of an NF- κ B luciferase reporter as efficiently as a *BCL10* siRNA (Fig. 2c). Again, TNF- α -mediated NF- κ B was unaffected, underscoring the selective involvement of CK1 α in the TCR–NF- κ B pathway. Accordingly, CK1 α -silenced primary T cells and Jurkat cells also displayed diminished p65 NF- κ B nuclear translocation after TCR, but not TNF- α , stimulation (Supplementary Fig. 5a–c). By contrast, NF- κ B activation proceeded normally when levels of CK1 δ or CK1 ϵ were reduced (Supplementary Fig. 6). Thus, among the CK1s, CK1 α provides an essential, non-redundant function in regulating TCR-induced NF- κ B activation.

To achieve a better knockdown, single Jurkat clones stably expressing a small hairpin RNA (shRNA) against CK1 α were generated. As expected, NF- κ B activation was markedly reduced on stimulation, as I κ B α phosphorylation and degradation were inhibited (Fig. 2d–f). Other early TCR signalling events, such as ERK1/2 phosphorylation, overall tyrosine phosphorylation, calcium mobilization and NF-AT activation occurred normally (Fig. 2e and Supplementary Fig. 5d–f). Of note, NF- κ B activity was restored when CK1 α -silenced cells were

¹Molecular Development Section, Laboratory of Immunology, National Institute of Allergy and Infectious Diseases. ²Metabolism Branch, Center for Cancer Research, National Cancer Institute. ³Proteomics and Mass Spectrometry Facility, National Institute of Diabetes and Digestive and Kidney Diseases, National Institutes of Health, Bethesda, Maryland 20892, USA. ⁴U542, INSERM, Université Paris-Sud, Hôpital Paul Brousse, Villejuif 94800, France. ⁵Laboratory of Proteomics and Analytical Technologies (LPAT), National Cancer Institute, Frederick, Maryland 21702, USA. [†]Present address: Division of Viral Immunology, Center for AIDS Research, Kumamoto University, 2-2-1 Honjoh, Kumamoto-shi, Kumamoto-ken 860-0811, Japan.

*These authors contributed equally to this work.

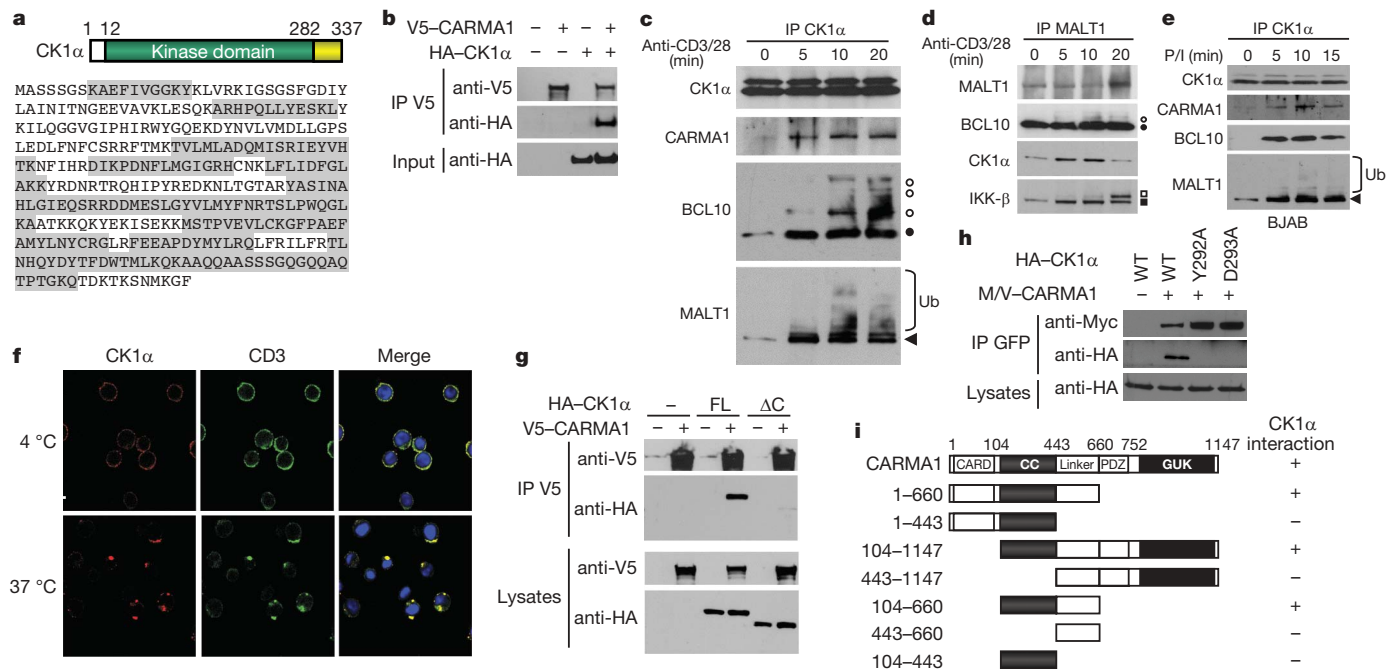


Figure 1 | Identification of CK1α as a CARMA1-binding partner.

a, Schematic and sequence of CK1α. Peptides identified by a mass spectrometry analysis of CARMA1-containing complexes are highlighted in grey. **b**, Interaction between HA-CK1α and V5-CARMA1 in HEK293T cells by immunoprecipitation (IP) and immunoblot (IB).

c–e, Immunoprecipitation/immunoblot, as indicated, in Jurkat T lymphocytes stimulated with $1 \mu\text{g ml}^{-1}$ anti-CD3 and anti-CD28 (**c**, **d**), and in BJBAB cells stimulated with 20 ng ml^{-1} PMA and 300 ng ml^{-1} ionomycin (**e**). Filled and open symbols indicate non-phosphorylated and phosphorylated forms, respectively. Ub, ubiquitin. **f**, Confocal images of

CD3 and CK1α after CD3 crosslinking in Jurkat T lymphocytes. Nuclei counterstaining is shown in blue. **g**, Immunoprecipitation/immunoblot of V5-CARMA1 binding to HA-tagged full-length (FL) CK1α or CK1α lacking residues 283–337 (ΔC) in HEK293T cells. **h**, Myc/Venus (M/V)-tagged CARMA1 association with HA-CK1α mutants in HEK293T cells by immunoprecipitation/immunoblot. **i**, Mapping of the minimal CK1α-binding domain of CARMA1 by immunoprecipitation/immunoblot in HEK293T cells expressing HA-CK1α and M/V-CARMA1 truncation mutants.

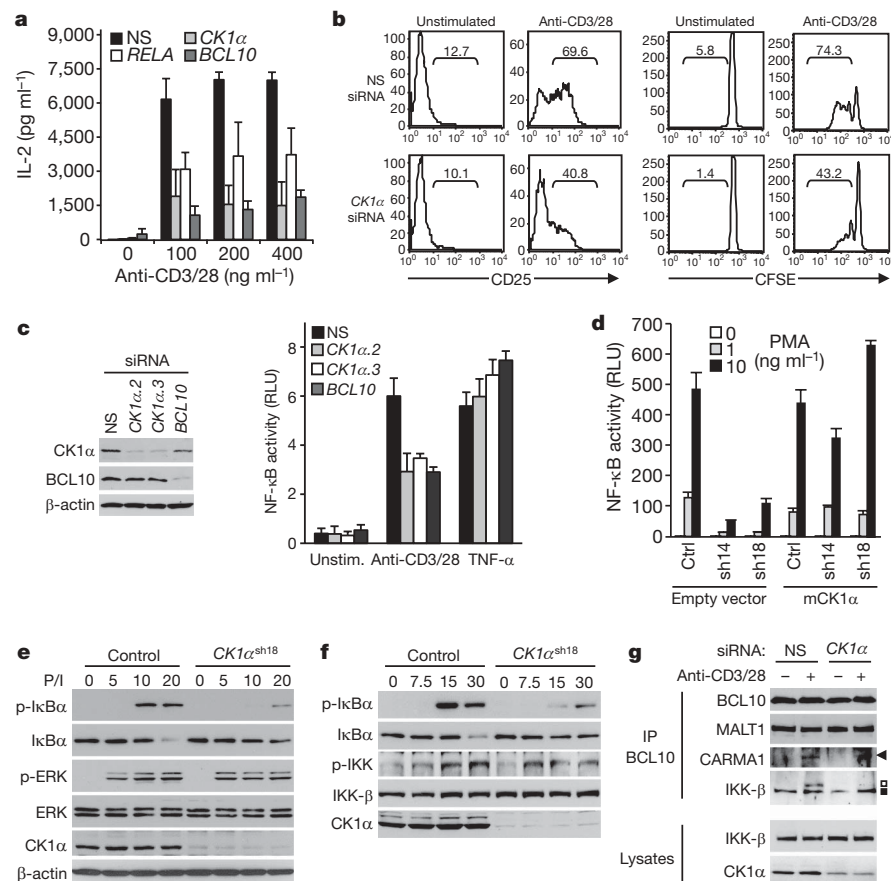


Figure 2 | Requirement of CK1α for NF-κB activation and proliferation in lymphocytes.

a, **b**, Human peripheral blood T lymphocytes were transfected with siRNA for CK1α, NF-κB p65 (RELA), BCL10, or scrambled nonspecific (NS) siRNA. IL-2 secretion (mean and s.d. of triplicate measurements) and CD25 induction 12 h after stimulation is shown.

Carboxyfluorescein succinimidyl ester (CFSE) dilution was assessed after 96 h. The percentage of CD25-positive cells, and of dividing cells, is shown. **c**, NF-κB luciferase assay (mean and s.d. of triplicate experiments) of Jurkat cells transfected with CK1α (CK1α.2 and CK1α.3), BCL10 or NS siRNA, and stimulated with $1 \mu\text{g ml}^{-1}$ anti-CD3 and anti-CD28, or with 25 ng ml^{-1} TNF-α. Left panel: immunoblot for CK1α, BCL10 and β-actin. RLU, relative light units. **d**, NF-κB luciferase assay of Jurkat cells stably expressing CK1α shRNA (sh14 and sh18) reconstituted with a control vector or with mouse CK1α (mCK1α), stimulated with PMA and 100 ng ml^{-1} ionomycin, and analysed as in **c**. **e**, **f**, Immunoblot of control and CK1α shRNA (sh18) expressing Jurkat cells exposed to 10 ng ml^{-1} PMA and 100 ng ml^{-1} ionomycin.

g, Immunoprecipitation/immunoblot of NS- and CK1α-silenced Jurkat cells stimulated with $1 \mu\text{g ml}^{-1}$ anti-CD3 and anti-CD28 for 20 min. Arrowhead indicates CARMA1; black and open squares indicate IKK-β and phosphorylated IKK-β, respectively.

rescued with ectopic mouse CK1 α (mCK1 α), but not with mCK1 α mutants lacking CARMA1 binding ability, indicating that CK1 α function requires association with CARMA1 (Fig. 2d and Supplementary Fig. 7). Hence, CK1 α is selectively required for optimal physiological activation of NF- κ B on TCR stimulation in normal lymphocytes.

Promptly following TCR ligation, protein kinase C (PKC)- θ phosphorylates CARMA1 and unleashes its adaptor functions^{16,17}. CARMA1 then promotes I κ B α phosphorylation by recruiting signalling molecules, including BCL10, MALT1 and IKK^{17,18}. Although IKK was phosphorylated after stimulation of CK1 α -silenced cells, p-IKK- β was no longer recruited to the CBM complex (Fig. 2f, g). This parallels previous observations in CARMA1- and BCL10-deficient cells¹⁹. Hence, the recruitment of p-IKK and consequent alterations of I κ B α are defective without CK1 α . Nonetheless, CK1 α still associated with CARMA1 in PKC- θ - or BCL10-silenced cells, or after treatment with the PKC inhibitor rottlerin, although BCL10/MALT1 recruitment to CK1 α /CARMA1 and NF- κ B activation were diminished (Supplementary Fig. 8). Thus, CK1 α associates with CARMA1 independently of PKC- θ and BCL10, and does not require PKC- θ -dependent modifications of CARMA1.

To investigate the role of CK1 α enzyme activity, we generated kinase-dead CK1 α by introducing point mutations in the ATPase domain (K46R, D136N, or D136A)^{20,21}. In CK1 α -silenced Jurkat cells, mCK1 α (D136N) markedly enhanced TCR-induced NF- κ B activation, surpassing the response in cells reconstituted with wild-type CK1 α (Fig. 3a). Human K46R, D136N and D136A CK1 α mutants gave similar results (Supplementary Fig. 9a). Accordingly, I κ B α phosphorylation and degradation was augmented in mCK1 α (D136N) expressing cells compared with wild-type mCK1 α (Fig. 3b). The CK1 α (D136N) synergistic effect was abolished in BCL10-silenced cells, or when mCK1 α (D136N/D293A) was used (Supplementary Fig. 9d, e), suggesting that enhanced NF- κ B activity requires BCL10 and binding to CARMA1. Thus, CK1 α kinase activity has a negative role in TCR-induced NF- κ B activation, in addition to the positive signalling role of CK1 α in the CBM complex.

By analogy with IKK- β , which marks BCL10 for degradation by phosphorylation²², we inferred that CK1 α might phosphorylate a substrate to downregulate the CBM complex. CARMA1, which binds CK1 α , was an attractive candidate. We observed that wild-type CK1 α , but not CK1 α (D136N), retarded the electrophoretic migration of CARMA1 in a λ -phosphatase-dependent manner, suggesting that CK1 α phosphorylates it (Fig. 3c and Supplementary Fig. 10). Because CARMA1 contains 142 potential phospho-acceptors, we used truncation mutants to identify CK1 α phosphorylation sites. In HEK293T cells, CARMA1-CCL(104–660) existed as two species, and wild-type CK1 α , but not CK1 α (D136N), shifted essentially all the CARMA1-CCL to the slow-migrating, λ -phosphatase-sensitive species (Fig. 3d and Supplementary Fig. 10a, b). CARMA1-CCL(104–616) was the shortest CK1 α -sensitive construct, as a mutant lacking residues 606–616 was not modified (Fig. 3e). The substitution to alanine of serines S603, S607 and S608 showed that only S608A and S603A/S608A (2SA) were insensitive to CK1 α , suggesting that S608 might be the key CK1 α phosphorylation site (Fig. 3f). NF- κ B enhancement was observed in CARMA1-deficient Jurkat cells¹¹ reconstituted with CARMA1(2SA) and CARMA1(S608A) (Fig. 3g and Supplementary Fig. 10c, d). This evidence indicates that CK1 α specifically phosphorylates CARMA1 at S608, which impairs its ability to activate NF- κ B.

Using a doxycycline-inducible shRNA retroviral library, we conducted a systematic screen for essential survival genes for two molecularly and clinically distinct lymphoma types, ABC and GCB (germinal centre B-cell-like) DLBCL^{12,23,24}. ABC, but not GCB, DLBCL cells rely on constitutive NF- κ B activation for proliferation and survival²⁵. Previously, this screen identified CARMA1, BCL10 and MALT1 as critical components for ABC DLBCL cell survival¹². Additional screening uncovered two CK1 α shRNAs that were

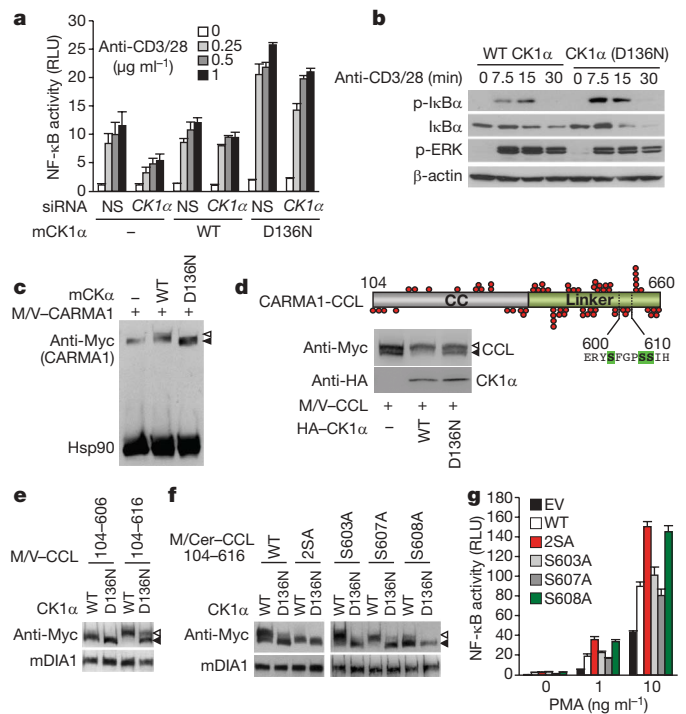


Figure 3 | CK1 α kinase activity contributes to the negative feedback control of the CBM complex and NF- κ B activation. **a**, NF- κ B luciferase assay (mean and s.d. of triplicate experiments) of nonspecific (NS)- and CK1 α -silenced Jurkat cells reconstituted with an empty vector (–), wild-type CK1 α (WT) or a D136N mutant mouse CK1 α (mCK1 α). RLU, relative luciferase units. **b**, Immunoblot of Jurkat cells expressing wild-type CK1 α or mCK1 α (D136N) stimulated with 1 μ g ml⁻¹ anti-CD3 and anti-CD28. **c**, Immunoblot of HEK293T cells expressing Myc/Venus (M/V)-CARMA1 together with an empty vector (–), wild-type CK1 α , or mCK1 α (D136N). Filled and open triangles indicate CARMA1 and its shifted form, respectively; Hsp90, loading control. **d**, Schematic of CARMA1 coiled-coil linker region (CARMA1-CCL(104–660)). Red circles indicate serine/threonine residues. An immunoblot of HEK293T cells overexpressing a vector alone (–), wild-type CK1 α , or CK1 α (D136N) with M/V-CARMA1-CCL(104–660) is shown. Open and filled arrowheads indicate phosphorylated and dephosphorylated CCL, respectively. **e**, Experiment as in **d** using M/V-tagged CCL residues 104–616 or 104–606. Diaphanous (mDIA1) was used as a loading control. **f**, Experiment as in **d** using Myc/Cer-tagged CCL(104–616) with the indicated serine to alanine substitution. **g**, NF- κ B luciferase assay (mean and s.d. of triplicate experiments) of CARMA1-deficient Jurkat JPM50.6 cells reconstituted with either an empty vector (EV) or the indicated CARMA1 plasmid and stimulated with PMA and 1 μ g ml⁻¹ anti-CD28.

selectively lethal for ABC DLBCL cell lines (Fig. 4a). We cloned these CK1 α shRNA sequences into a GFP-expressing retroviral vector¹², and infected cell lines representing ABC DLBCL, GCB DLBCL and multiple myeloma. CK1 α shRNA expression decreased the fraction of GFP-positive, shRNA-expressing cells over time in all four ABC DLBCL cell lines but not in GCB DLBCL or multiple myeloma cell lines, confirming that CK1 α knockdown is specifically lethal to ABC DLBCL cells (Fig. 4b).

To evaluate CK1 α participation in the NF- κ B pathway in ABC DLBCL, the OCI-Ly3 cell line harbouring an IKK activity reporter consisting of an I κ B α -luciferase fusion protein was used¹². If IKK is inactivated, there is less phosphorylation and degradation of the I κ B α -luciferase fusion protein and luciferase activity rises. Induction of CK1 α shRNA expression increased luciferase activity, as did shRNAs targeting *IKK- β* (also called *IKKB*), *CARMA1*, *MALT1* and *BCL10*, whereas control shRNAs targeting the Spi-B transcription factor (*SPIB*) and *EGFP* had no effect (Fig. 4c). Consistently, CK1 α knockdown decreased NF- κ B in the nuclei of

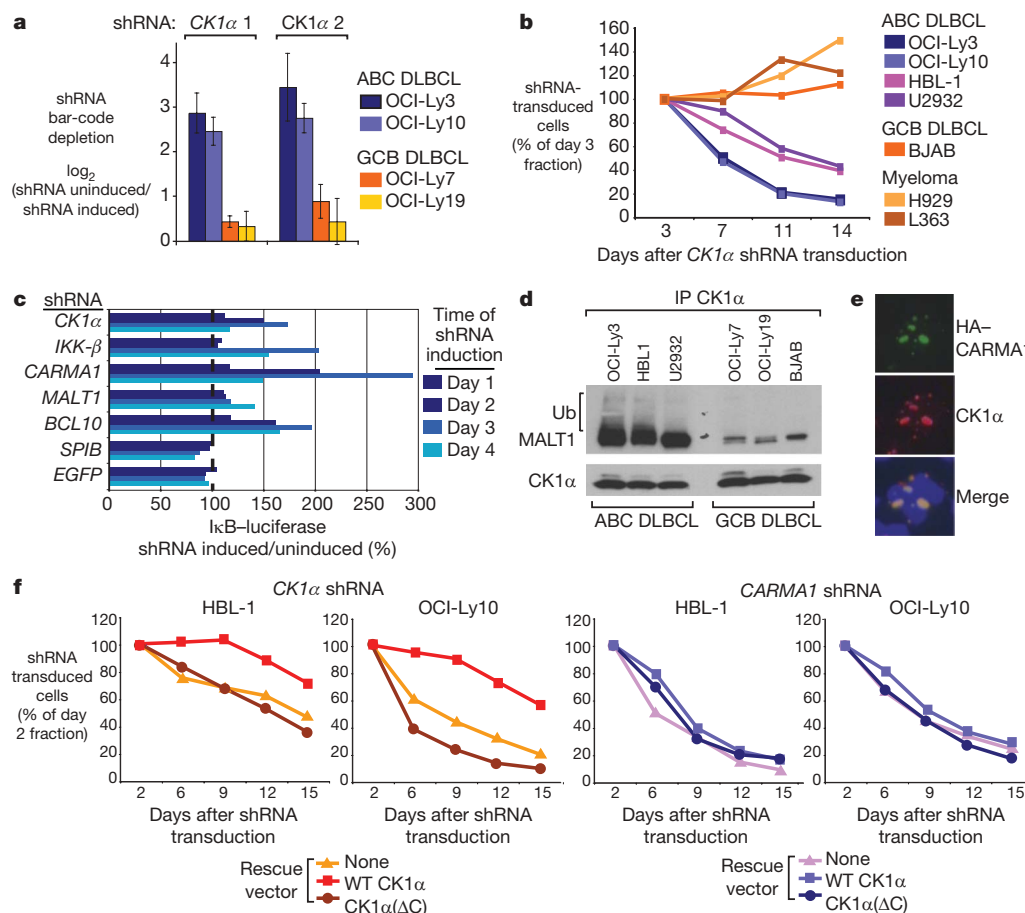


Figure 4 | Role of *CK1α* in ABC DLBCL survival and NF- κ B signalling. **a**, A genetic screen using 1,854 shRNA vectors targeting 683 genes identified two *CK1α* shRNAs that block the survival of ABC but not GCB DLBCL cell lines. Shown are the relative fluorescent signals from bar-code microarrays comparing shRNA-induced versus uninduced cells 21 days after shRNA induction. Data are mean \pm s.d. of four independent infections of the shRNA retroviral library. **b**, Survival analysis by flow cytometry of the indicated lymphoma and multiple myeloma cell lines retrovirally infected to express *CK1α* shRNA and GFP. **c**, An OCI-Ly3 cell line stably expressing an IkB α -luciferase reporter was retrovirally infected with the indicated

shRNAs. Shown is the percentage of luciferase activity in shRNA-induced cells compared to uninduced cells. **d**, Immunoprecipitation/immunoblot of cell lysates from the indicated cell lines. Ub, ubiquitin. **e**, Immunofluorescent staining for CARMA1 mutant 3²⁶ (HA epitope), and endogenous *CK1α* in OCI-Ly19 cells retrovirally transduced to express HA-tagged CARMA1 mutant 3. Shown are two adjacent cells with nuclei counterstained (blue). **f**, Indicated ABC DLBCL cells were transduced with wild-type *CK1α* or *CK1α*(ΔC) (Δ283–337), and subsequently with vectors co-expressing GFP and either *CK1α* shRNA or *CARMA1* shRNA. The GFP⁺ cell fraction was monitored as in **b**.

OCI-Ly3 cells and reduced IkB α phosphorylation in HBL1, U2932 and OCI-Ly3 cell lines (Supplementary Fig. 11). Thus, *CK1α* is required for the IKK–NF- κ B signalling pathway in ABC DLBCL cells. We also detected a strong binding of *CK1α* to MALT1 and ubiquitinated MALT1 in ABC DLBCL but not GCB DLBCL cell lines (Fig. 4d). Some ABC DLBCLs harbour mutant forms of CARMA1 that constitutively activate NF- κ B and generate cytoplasmic aggregates that co-localize with MALT1 and IKK²⁶. Such CARMA1 aggregates also contain *CK1α*, further implicating *CK1α* in CBM complex activity in ABC DLBCL (Fig. 4e). We next tested whether the lethality of an shRNA targeting the *CK1α* 3'-untranslated region could be prevented by wild-type *CK1α* or *CK1α*(ΔC), which does not bind CARMA1. Wild-type *CK1α*, but not *CK1α*(ΔC), rescued two ABC DLBCL cell lines from *CK1α* shRNA toxicity (Fig. 4f). In contrast, neither wild type nor *CK1α*(ΔC) rescued ABC DLBCL cells from *CARMA1* shRNA toxicity. Thus, direct interaction of *CK1α* with CARMA1 is apparently required for ABC DLBCL cell survival.

Our results have shown *CK1α* to be an important bifunctional modulator of lymphocyte adaptive immune responses. Whereas *CK1α* associates with CARMA1 and positively conveys TCR-induced NF- κ B, it also phosphorylates CARMA1, thereby dampening signalling. This provides a conceptual framework for *CK1α* as a signalling

gate, using both positive and negative influences to control the flow of information leading to gene induction. The phosphorylation and inactivation of CARMA1 by *CK1α* is reminiscent of the GSK3 β /*CK1α* cooperation to promote β -catenin destruction²⁷, and our preliminary data indicate that *CK1α* might contribute to CARMA1 degradation (Supplementary Fig. 10). We also provide genetic, biochemical and functional evidence that *CK1α* is an essential participant in the aberrant NF- κ B activity required for ABC DLBCL subtype survival. Similar to IKK- β ²², the positive function of *CK1α* supplants its negative role, probably because of the constitutive upstream activation signals. Of note, *CK1α* was neither mutated nor amplified in ABC DLBCL cell lines (data not shown), indicating that this *CK1α* dependency resembles the 'non-oncogene addiction' phenomenon in which the cancer cell phenotype depends on specific cellular genes^{28,29}. These 'conditionally essential malignancy' genes may or may not be oncogenes or the initiator genes for cancer, but they are essential for the propagation of a specific transformed phenotype and therefore attractive therapeutic targets^{28,29}. Notably, *CK1α* is required for the survival of ABC DLBCL cells with either mutant or wild-type CARMA1, revealing it to be a conditionally essential malignancy gene. However, *CK1α* is a complex target for chemotherapy given its contrasting roles in signalling.

METHODS SUMMARY

Cell culture and reagents. Jurkat E6.1, BJAB and HEK293T cells were purchased from ATCC. Peripheral blood T cells were isolated from normal healthy donors as previously described³⁰. CARMA1-deficient JPM50.6 Jurkat cells were provided by X. Lin¹¹. Lymphocytes were activated with anti-CD3 and anti-CD28 (BD Biosciences), or with PMA (Sigma) and ionomycin (Sigma), or TNF- α (R&D). siRNAs used (Invitrogen) were *BCL10*, 5'-GCCACGAACAACCUC-UCCAGAUCAA-3'; *CK1 α* , 5'-CCTAGCCTGGAAGACCTCTTCAATT-3'; *CK1 α* , 5'-GGCAAGGGCTAAAGGCTGCAACAAA-3'; *PKC θ* , 5'-AAUUGG-UGAUUUCACUUUCGGCCGG-3'; *p65*, 5'-GAGCACCAUCAACUAUGAUG-AGUUU-3'.

CARMA1-binding-partner screen by mass spectrometry. CARMA1 was immunoprecipitated from HEK293T cells overexpressing V5-tagged CARMA1. CARMA1-containing complexes were resolved on SDS-PAGE and stained with colloidal Coomassie blue (Invitrogen). Bands were excised, in-gel trypsin digested, and subjected to LC-MS/MS mass spectrometry analysis.

shRNA library screen. A retroviral shRNA library was constructed in the modified pRSMX plasmid containing a doxycycline-inducible H1 promoter for shRNA expression and a random 60-mer 'bar-code' sequence. The association of each bar-code with an shRNA sequence in each library plasmid was determined by sequencing. Screening used engineered cells that express the bacterial tetracycline repressor (TETR)¹². 500–1,000 individual shRNA plasmids were combined to generate retroviral pools, which were used to infect TETR-expressing lymphoma and multiple myeloma cell lines. Puromycin-selected, infected cells were induced with doxycycline for shRNA expression in half of the culture. Three weeks after shRNA induction, bar-code sequences were amplified from the genomic DNA of induced and uninduced cells, fluorescently labelled, and hybridized to bar-code microarrays to identify shRNA vectors that were relatively depleted from the induced population. The effective *CK1 α* shRNA sequences identified from the screen are: *CK1 α* 1, 5'-GACTCTGCATTAAGTCTATAA-3' and *CK1 α* 2, 5'-GAGCAAGCTCTATAAGATTCT-3'.

Full Methods and any associated references are available in the online version of the paper at www.nature.com/nature.

Received 28 July; accepted 5 November 2008.

Published online 31 December 2008.

- Hacker, H. & Karin, M. Regulation and function of IKK and IKK-related kinases. *Sci. STKE* **2006**, re13 (2006).
- Schulze-Luehrmann, J. & Ghosh, S. Antigen-receptor signaling to nuclear factor κ B. *Immunity* **25**, 701–715 (2006).
- Egawa, T. *et al.* Requirement for CARMA1 in antigen receptor-induced NF- κ B activation and lymphocyte proliferation. *Curr. Biol.* **13**, 1252–1258 (2003).
- Gaide, O. *et al.* CARMA1 is a critical lipid raft-associated regulator of TCR-induced NF- κ B activation. *Nature Immunol.* **3**, 836–843 (2002).
- Hara, H. *et al.* The MAGUK family protein CARD11 is essential for lymphocyte activation. *Immunity* **18**, 763–775 (2003).
- Jun, J. E. & Goodnow, C. C. Scaffolding of antigen receptors for immunogenic versus tolerogenic signaling. *Nature Immunol.* **4**, 1057–1064 (2003).
- Newton, K. & Dixit, V. M. Mice lacking the CARD of CARMA1 exhibit defective B lymphocyte development and impaired proliferation of their B and T lymphocytes. *Curr. Biol.* **13**, 1247–1251 (2003).
- Ruefli-Brasse, A. A., French, D. M. & Dixit, V. M. Regulation of NF- κ B-dependent lymphocyte activation and development by paracaspase. *Science* **302**, 1581–1584 (2003).
- Ruland, J. *et al.* Bcl10 is a positive regulator of antigen receptor-induced activation of NF- κ B and neural tube closure. *Cell* **104**, 33–42 (2001).
- Ruland, J., Duncan, G. S., Wakeham, A. & Mak, T. W. Differential requirement for Malt1 in T and B cell antigen receptor signaling. *Immunity* **19**, 749–758 (2003).

- Wang, D. *et al.* A requirement for CARMA1 in TCR-induced NF- κ B activation. *Nature Immunol.* **3**, 830–835 (2002).
- Ngo, V. N. *et al.* A loss-of-function RNA interference screen for molecular targets in cancer. *Nature* **441**, 106–110 (2006).
- Price, M. A. CKI, there's more than one: casein kinase I family members in Wnt and Hedgehog signaling. *Genes Dev.* **20**, 399–410 (2006).
- Oeckinghaus, A. *et al.* Malt1 ubiquitination triggers NF- κ B signaling upon T-cell activation. *EMBO J.* **26**, 4634–4645 (2007).
- Bidere, N., Snow, A. L., Sakai, K., Zheng, L. & Lenardo, M. J. Caspase-8 regulation by direct interaction with TRAF6 in T cell receptor-induced NF- κ B activation. *Curr. Biol.* **16**, 1666–1671 (2006).
- Matsumoto, R. *et al.* Phosphorylation of CARMA1 plays a critical role in T cell receptor-mediated NF- κ B activation. *Immunity* **23**, 575–585 (2005).
- Sommer, K. *et al.* Phosphorylation of the CARMA1 linker controls NF- κ B activation. *Immunity* **23**, 561–574 (2005).
- Shinohara, H. *et al.* PKC β regulates BCR-mediated IKK activation by facilitating the interaction between TAK1 and CARMA1. *J. Exp. Med.* **202**, 1423–1431 (2005).
- Shambharkar, P. B. *et al.* Phosphorylation and ubiquitination of the I κ B kinase complex by two distinct signaling pathways. *EMBO J.* **26**, 1794–1805 (2007).
- Davidson, G. *et al.* Casein kinase 1 γ couples Wnt receptor activation to cytoplasmic signal transduction. *Nature* **438**, 867–872 (2005).
- Peters, J. M., McKay, R. M., McKay, J. P. & Graff, J. M. Casein kinase I transduces Wnt signals. *Nature* **401**, 345–350 (1999).
- Wegener, E. *et al.* Essential role for I κ B kinase β in remodeling Carma1-Bcl10-Malt1 complexes upon T cell activation. *Mol. Cell* **23**, 13–23 (2006).
- Alizadeh, A. A. *et al.* Distinct types of diffuse large B-cell lymphoma identified by gene expression profiling. *Nature* **403**, 503–511 (2000).
- Rosenwald, A. *et al.* The use of molecular profiling to predict survival after chemotherapy for diffuse large-B-cell lymphoma. *N. Engl. J. Med.* **346**, 1937–1947 (2002).
- Davis, R. E., Brown, K. D., Siebenlist, U. & Staudt, L. M. Constitutive nuclear factor κ B activity is required for survival of activated B cell-like diffuse large B cell lymphoma cells. *J. Exp. Med.* **194**, 1861–1874 (2001).
- Lenz, G. *et al.* Oncogenic CARD11 mutations in human diffuse large B cell lymphoma. *Science* **319**, 1676–1679 (2008).
- Liu, C. *et al.* Control of β -catenin phosphorylation/degradation by a dual-kinase mechanism. *Cell* **108**, 837–847 (2002).
- Shaffer, A. L. *et al.* IRF4 addiction in multiple myeloma. *Nature* **454**, 226–231 (2008).
- Solimini, N. L., Luo, J. & Elledge, S. J. Non-oncogene addiction and the stress phenotype of cancer cells. *Cell* **130**, 986–988 (2007).
- Su, H. *et al.* Requirement for caspase-8 in NF- κ B activation by antigen receptor. *Science* **307**, 1465–1468 (2005).

Supplementary Information is linked to the online version of the paper at www.nature.com/nature.

Acknowledgements This work was supported by the Intramural Research Program of the NIH, NIAID, NCI, NIDDK and by the Agence Nationale de la Recherche (ANR). We thank M.-T. Auffredou for technical assistance; X. Lin and J. Gavard for reagents; R. Germain, R. Schwartz, U. Siebenlist, P. Schwartzberg, J. Bosco de Oliveira, L. Yu, D. Baltimore, P. Sharp, H. Varmus and A. Snow for discussions and comments; and S. Porcella and the DNA sequencing core facility of the Rocky Mountain Laboratories, NIAID.

Author Contributions N.B., V.N.N., J.L., C.C., L.Z., F.W., R.E.D., G.L., L.M.S. and M.J.L. carried out experimental design/discussion; N.B., V.N.N., J.L., C.C., L.Z., F.W., R.E.D., G.L., D.E.A., D.A., A.V., K.S., J.Z., Z.M. and T.D.V. carried out preparation and performance of experiments; N.B., V.N.N., L.M.S. and M.J.L. carried out manuscript preparation. All authors discussed the results and commented on the manuscript.

Author Information Reprints and permissions information is available at www.nature.com/reprints. Correspondence and requests for materials should be addressed to M.J.L. (lenardo@nih.gov) or L.M.S. (lstaedt@mail.nih.gov).

METHODS

Expression plasmids, transfections, antibodies and reagents. cDNAs from Open Biosystems and Origene were further cloned into HA-tagged-pCI-neo, pcDNA3.1D/V5-His-TOPO (Invitrogen), or pCEFL-Myc/Venus (M/V) expression vectors. CARMA1 mutant expression constructs, and human or mouse CK1 α kinase-dead constructs (K46R, D136N and D136A), were generated by site-directed mutagenesis, and were verified by sequencing (Rocky Mountain Laboratories; Genome express, Cogenics). The truncated CK1 α and CARMA1 constructs were made by polymerase chain reaction. HEK293T cells were transfected with Exgen (Fermentas). Primary blood T lymphocytes and Jurkat cells were transfected as previously described¹⁵. Antibodies to CK1 α , BCL10, MALT1, I κ B α , NF- κ B p65 and mDIA1 were from Santa Cruz. Antibodies to β -actin, to Flag and to HA (Sigma), to Myc, and to the phosphorylated forms of I κ B α , ERK and JNK (Cell Signaling Technologies), to PARP, IKK- β and to CD25 (BD Pharmingen), to GFP (Roche), to V5 and to phospho-serine (Invitrogen), to phospho-tyrosine (Millipore), and to CARMA1 (Alexis) were also used. HRP-conjugated secondary antibodies were from Southern Biotechnology. Amersham ECL or Pierce Supersignal West chemiluminescent substrates were used for immunoblot detection. The calcium-sensitive dye Fluo-3 was from Invitrogen, and CFSE was purchased from Sigma.

Cell lysates and immunoprecipitations. Stimuli were terminated by addition of ice-cold PBS, and cell pellets were lysed with TNT buffer (50 mM Tris pH 7.4, 150 mM NaCl, 1% Triton X-100, 1% NP-40, 2 mM EDTA) supplemented with complete proteases inhibitors (Roche) for 30 min. Samples were cleared by a centrifugation at 15,000g at 4 °C and pre-cleared with protein G-sepharose (Roche) for 1 h before immunoprecipitation with antibodies and additional protein G-sepharose at 4 °C. To evaluate CARMA1 phosphorylation, cells were lysed with TNT buffer containing 1 mM Na₃VO₄, 1 mM NaF, and complete proteases inhibitors (Roche). Precipitates were washed with TNT buffer without EDTA, and incubated for 30 min at 30 °C with λ -phosphatase (NEB) according to the manufacturer's instructions. Cytosolic and nuclear extracts were prepared as previously described³⁰. For immunodepletion experiments, cell lysates were first incubated with antibodies against CK1 α and protein G-sepharose. Supernatants were collected and underwent three sequential rounds of protein G-sepharose treatment previously and were then immunoprecipitated with BCL10 antibodies.

Immunofluorescence, ELISA and luciferase. For immunofluorescence studies, 5×10^5 Jurkat T cells were incubated on ice for 20 min with $10 \mu\text{g ml}^{-1}$ anti-CD3 (clone OKT3), washed twice with ice-cold PBS and CD3 receptors were cross-linked with $5 \mu\text{g ml}^{-1}$ donkey anti-mouse for 15 min on ice or at 37 °C. Samples were then processed as previously described^{15,30}. IL-2 production was determined 12 h after stimulation in the culture supernatants by an enzyme-linked immunosorbent assay (ELISA). Briefly, Immulon 4 plates coated with $2 \mu\text{g ml}^{-1}$

anti-human IL-2 capture antibody (R&D) were washed three times with 0.05% Tween-20 in PBS (PBS-T) and blocked with 0.5% BSA in PBS, for 2 h. The plates were then washed three times and incubated with triplicates of hIL-2 standards and the collected supernatants for 2 h. After three washes, plates were incubated for 2 h with biotin-anti human IL-2 antibody (R&D). The plates were washed three times and incubated with streptavidin-HRP (R&D) for 30 min. Wells were washed again and developed with TMB substrate (Sigma) for 30 min in the dark. Reactions were stopped by adding 2 N H₂SO₄ and the optical density at 450 nm was read through a BioRad plate reader. IL-2 concentrations were calculated from a regression formula derived from the standard curve. For luciferase reporter assays, firefly luciferase constructs driven by NF- κ B binding sequences and *Renilla* luciferase pRL-TK (Int⁻) plasmid were used (Promega). Lysates were analysed using the Dual-Luciferase Kit (Promega), with firefly fluorescence units normalized to *Renilla* luciferase fluorescence units.

Survival assay. A survival assay was done as previously described¹². Briefly, effective shRNAs identified from the library screen were re-cloned into a variant of pRSMX plasmid that expresses GFP. Cells were infected with retroviruses prepared from this plasmid and the fraction of GFP⁺ cells was measured over time by flow cytometry. At each time point, the observed GFP⁺ fractions in cultures transduced with an shRNA of interest were normalized to the GFP⁺ fractions in control cultures transduced with luciferase shRNA. The toxicity of an shRNA is indicated by the reduction over time in the GFP⁺ fraction compared with the GFP⁺ fraction at the earliest time point (day 3) after infection.

IKK reporter assay. IKK reporter cell lines (see ref. 12) were created by sequentially transducing TETR-expressing cells with I κ B α -Photinus and *Renilla* luciferase-expressing retroviruses. I κ B α -Photinus luciferase was a fusion protein used for measuring IKK activity, and *Renilla* luciferase was for normalizing viable cell number. IKK reporter cell lines were transduced with shRNA-expressing retroviruses and selected with puromycin. IKK reporter values were measured over time with a luminescence microplate reader in uninduced and doxycycline-induced cultures, using the Dual-Glo luciferase assay system (Promega).

Electrophoretic mobility shift assays. Nuclear protein extracts were obtained from the OCI-Ly3 cell line, and EMSAs were carried out with an EMSA kit (Promega) with modifications, as previously described³¹. I κ B double-stranded oligonucleotide probes (sense strand shown) used were: 5'-AGTTGAGGGG ACTTCCAGG-3'. 100-fold unlabelled immunoglobulin κ B (WT) was added for cold competition analyses. Samples were resolved on a 6% DNA retardation gel (Invitrogen) in 0.25 \times TBE buffer, and autoradiography was carried out on dried gels.

31. Wan, F. *et al.* Ribosomal protein S3: a KH domain subunit in NF- κ B complexes that mediates selective gene regulation. *Cell* **131**, 927–939 (2007).

Transcriptome sequencing to detect gene fusions in cancer

Christopher A. Maher^{1,3*}, Chandan Kumar-Sinha^{1,3*}, Xuhong Cao^{1,2}, Shanker Kalyana-Sundaram^{1,3}, Bo Han^{1,3}, Xiaojun Jing^{1,3}, Lee Sam^{1,3}, Terrence Barrette^{1,3}, Nallasivam Palanisamy^{1,3} & Arul M. Chinnaiyan^{1,2,3,4,5}

Recurrent gene fusions, typically associated with haematological malignancies and rare bone and soft-tissue tumours¹, have recently been described in common solid tumours^{2–9}. Here we use an integrative analysis of high-throughput long- and short-read transcriptome sequencing of cancer cells to discover novel gene fusions. As a proof of concept, we successfully used integrative transcriptome sequencing to 're-discover' the *BCR-ABL1* (ref. 10) gene fusion in a chronic myelogenous leukaemia cell line and the *TMPRSS2-ERG*^{2,3} gene fusion in a prostate cancer cell line and tissues. Additionally, we nominated, and experimentally validated, novel gene fusions resulting in chimaeric transcripts in cancer cell lines and tumours. Taken together, this study establishes a robust pipeline for the discovery of novel gene chimaeras using high-throughput sequencing, opening up an important class of cancer-related mutations for comprehensive characterization.

Characterization of specific genomic aberrations in cancers has led to the identification of several successful therapeutic targets, such as *BCR-ABL1*, *PDGFR*, *ERBB2* and *EGFR*^{11–14}. Therefore a major goal in cancer research is to identify causal genetic aberrations. Gene fusions resulting from chromosomal rearrangements in cancer are believed to define the most prevalent category of 'cancer genes'¹⁵. Typically, an aberrant juxtaposition of two genes may encode a fusion protein (for example, *BCR-ABL1*), or the regulatory elements of one gene may drive the aberrant expression of an oncogene (for example, *TMPRSS2-ERG*). Although gene fusions have been widely described in rare haematological malignancies and sarcomas¹, the recent discovery of recurrent gene fusions in prostate^{2,4} and lung cancers^{5–9} points to their role in common solid tumours as well. Considering their prevalence and common characteristics across cancer types, gene fusions may be regarded as a distinct class of 'mutations', with a causal role in carcinogenesis. In addition, being strictly confined to cancer cells, they represent ideal diagnostic markers and rational therapeutic targets.

As a proof of concept, we performed whole transcriptome sequencing of the chronic myelogenous leukaemia cell line K562, which harbours the classical gene fusion, *BCR-ABL1* (ref. 16). Using the Illumina Genome Analyser, we generated 66.9 million reads of 36 nucleotides in length and screened them for the presence of reads showing partial alignment to exon boundaries from two different genes. Although this approach was able to detect *BCR-ABL1*, it was one among a set of 111 other chimaeras (with at least two reads). Thus, in a *de novo* discovery mode, it would be difficult to pinpoint the *BCR-ABL1* fusion in the background of the other putative chimaeras. However, when we used the known fusion junction of *BCR-ABL1* (GenBank number M30829) as the reference sequence, we detected 19 chimaeric reads (Supplementary Fig. 1). Thus, we considered an

integrative approach for chimaera detection, using short-read sequencing technology for obtaining deep sequence data and long-read technology (Roche 454 sequencing platform) to provide reference sequences for mapping candidate fusion genes.

An important concern in transcriptome sequencing was whether we could detect chimaeric transcripts in the background of highly abundant housekeeping genes (that is, would complementary DNA (cDNA) normalization be required). To address this, we compared sequences from normalized and non-normalized cDNA libraries of the prostate cancer cell line VCaP, which harbours the gene fusion *TMPRSS2-ERG* (Supplementary Table 1). Overall, the normalized library showed an approximately 3.6-fold reduction in the total number of chimaeras nominated. Furthermore, although we expected the normalized library would enrich for the *TMPRSS2-ERG* gene fusion, it failed to reveal any *TMPRSS2-ERG* chimaeras, which suggested that we would not benefit from normalization in our analyses.

To assess the feasibility of using massively parallel transcriptome sequencing to identify novel gene fusions, we generated non-normalized cDNA libraries from the prostate cancer cell lines VCaP and LNCaP, and a benign immortalized prostate cell line RWPE. As a first step, using the Roche 454 platform, we generated 551,912 VCaP, 244,984 LNCaP and 826,624 RWPE transcriptome sequence reads, averaging 229.4 nucleotides. These were categorized as completely aligning, partly aligning or non-mapping to the human reference database (Fig. 1a). Sequence reads that showed partial alignments to two genes (Supplementary Methods) were nominated as first-pass candidate chimaeras. This yielded 428 VCaP, 247 LNCaP and 83 RWPE candidates. Admittedly, many of these chimaeric sequences could be a result of *trans*-splicing¹⁷ or co-transcription of adjacent genes coupled with inter-genic splicing¹⁸, or simply an artefact of the sequencing protocol. Surprisingly, among the 428 VCaP candidates, only one read spanned the *TMPRSS2-ERG* fusion junction using the long-read sequencing platform (Supplementary Table 2).

Next, using the Illumina Genome Analyser we obtained over 50 million short-transcriptome sequence reads from VCaP, LNCaP and RWPE cDNA libraries (Supplementary Table 3). Focusing initially on VCaP cells, we identified the *TMPRSS2-ERG* fusion as one among 57 candidates, many of them likely false positives. To overcome the problem of false positives, lack of depth in long reads, and difficulty in mapping partly aligning short reads, we considered integrating the long- and short-read sequence data. Following this strategy, we found the single long-read chimaeric sequence spanning *TMPRSS2-ERG* junction from VCaP transcriptome sequence, buttressed by 21 short reads (Fig. 1b), was one of only eight chimaeras nominated, overall. Thus, using the integrative approach, the total number of false candidates was reduced and the proportion of

¹Michigan Center for Translational Pathology, ²Howard Hughes Medical Institute, ³Department of Pathology, ⁴Department of Urology, ⁵Comprehensive Cancer Center, University of Michigan Medical School, Ann Arbor, Michigan 48109, USA.

*These authors contributed equally to this work.

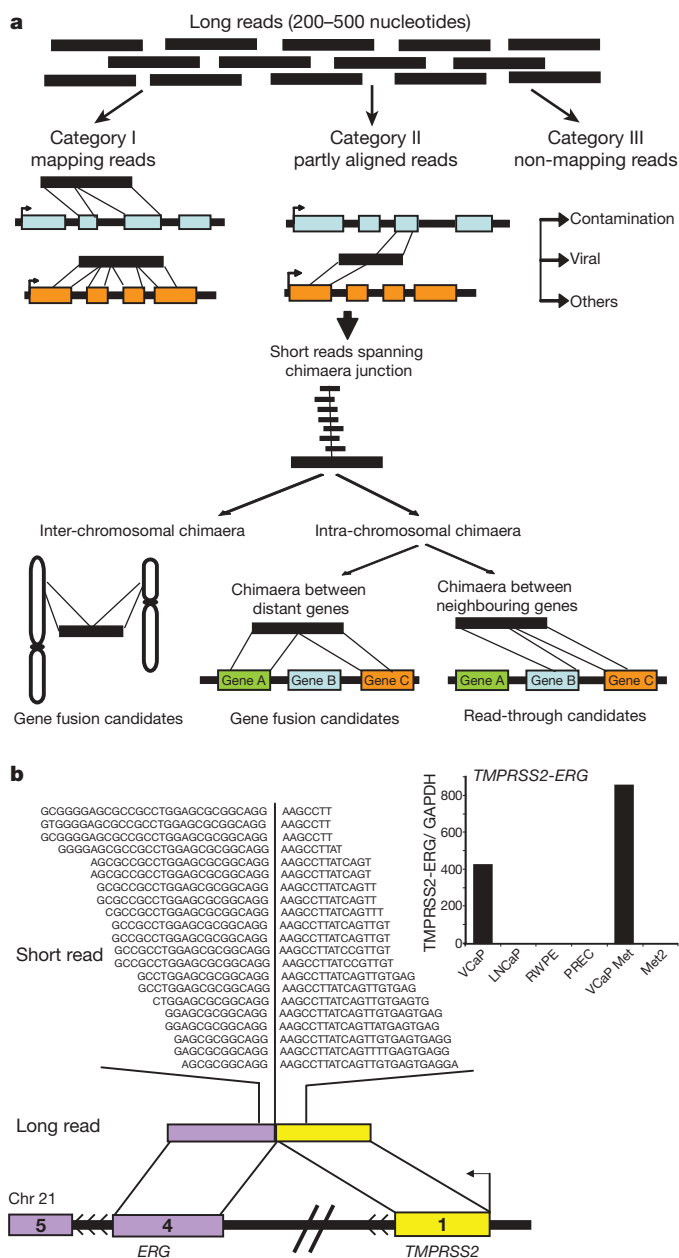


Figure 1 | Using massively parallel sequencing to discover chimaeric transcripts in cancer. **a**, Schema representing our use of transcriptome sequencing to identify chimaeric transcripts. ‘Long-read’ sequences compared with the reference database are classified as ‘mapping’, ‘partly aligned’ and ‘non-mapping’ reads. Partly aligning reads are considered putative chimaeras and are categorized as inter- or intra-chromosomal chimaeras. Integration with short-read sequence data are used for shortlisting candidate chimaeras and assessing the depth of coverage spanning the fusion junction. **b**, ‘Re-discovery’ of *TMPRSS2-ERG* fusion on chromosome (chr) 21. Short reads (Illumina) are overlaid on the corresponding long-read (454) represented by coloured bars. Sequences spanning the fusion junction are indicated by the partition in the short reads. Chromosomal context of the fusion genes is represented by coloured bars punctuated with black lines. Inset displays histogram of qRT-PCR validation of the *TMPRSS2-ERG* transcript.

experimentally validated candidates increased dramatically (Supplementary Fig. 2). Extending the integrative analysis to LNCaP and RWPE sequences provided a total of 15 chimaeric transcripts, of which ten could be experimentally confirmed (Supplementary Table 4). To ensure that the integration strategy filtered out only false positives and not valid chimaeras, we tested a panel of 16 long-read chimaera candidates that were eliminated upon integration and found that none of

them confirmed a fusion transcript by quantitative real-time PCR (qRT-PCR; Supplementary Fig. 3).

To leverage the collective coverage provided by the two sequencing platforms systematically, and to prioritize the candidates, we formulated a scoring function obtained by multiplying the number of chimaeric reads derived from either method (Supplementary Table 4). Further, we categorized these chimaeras as intra- or inter-chromosomal, based on their location on the same or different chromosomes, respectively. The latter represent bona fide gene fusions as do intra-chromosomal chimaeras aligning to non-adjacent transcripts; intra-chromosomal chimaeras between neighbouring genes are classified as read-throughs. Remarkably, *TMPRSS2-ERG* was our top ranking gene fusion sequence, second only to a read-through chimaera *ZNF577-ZNF649*.

In addition to *TMPRSS2-ERG*, we identified several new gene fusions in VCaP. One such fusion was between exon 1 of *USP10*, with exon 3 of *ZDHHC7*, both genes located on chromosome 16, approximately 200 kilobases (kb) apart, in opposite orientation (Fig. 2a and Supplementary Discussion). Furthermore, two separate fusions involving the gene *HJURP* on chromosome 2 were identified. A fusion between exon 2 of *EIF4E2* with exon 8 of *HJURP* generated the fusion transcript *EIF4E2-HJURP* and a fusion between exon 9 of *HJURP* with exon 25 of *INPP4A* yielded *HJURP-INPP4A* (Fig. 2b and Supplementary Fig. 4).

Interestingly, based on whole transcriptome sequencing, the highest-ranked LNCaP gene fusion was between exon 11 of *MIPOL1* on chromosome 14 with the last exon of *DGKB* on chromosome 7; this was confirmed by qRT-PCR and fluorescence *in situ* hybridization (FISH) (Fig. 3 and Supplementary Fig. 5). We recently demonstrated that overexpression of *ETV1*, a member of the oncogenic erythroblast transformation-specific (ETS) transcription factor family, has a role in tumour progression in LNCaP cells³. The mechanism of *ETV1* overexpression was attributed to a cryptic insertion of approximately 280 kb encompassing the *ETV1* gene into an intronic region of *MIPOL1*. Thus, although our previous study suggested that *ETV1* was rearranged without evidence of an *ETV1* fusion transcript, here we show the generation of a surrogate fusion of *MIPOL1* to *DGKB*, which appears to be indicative of an *ETV1* chromosomal aberration.

In addition to gene fusions, we also identified several transcript chimaeras between neighbouring genes, referred to as read-through events. Overall, the read-through events appear to be more broadly expressed across both malignant and benign samples whereas the gene fusions were cancer-cell specific (Supplementary Fig. 6 and Supplementary Discussion).

Next, we attempted to extend this methodology to tumour samples that represent the malignant cells often admixed with benign epithelia, stromal, lymphocytic and vascular cells. To accomplish this we conducted transcriptome sequencing of two *TMPRSS2-ERG* gene-fusion-positive metastatic prostate cancer tissues, VCaP-Met (from which the VCaP cell line is derived) and Met 3, and one *ERG*-negative metastatic prostate tissue, Met 4. Interestingly, in addition to the *TMPRSS2-ERG* fusion sequences detected in both VCaP-Met and Met 3 tissues, three novel gene fusions were identified (Supplementary Fig. 7a). One chimaeric transcript from Met 3 involves exon 9 of *STRN4* with exon 2 of *GPSN2* (Supplementary Fig. 7b). *GPSN2* belongs to the steroid 5- α -reductase family, the enzyme that converts testosterone to dihydrotestosterone, the key hormone that mediates androgen response in prostate tissues. Dihydrotestosterone is known to be highly expressed in prostate cancer, and is a therapeutic target¹⁹. Dihydrotestosterone, like its synthetic analogue R1881, has been shown to induce *TMPRSS2-ERG* expression as well as prostate-specific antigen (PSA)². Additionally, we found exon 10 of *RC3H2* fused to exon 20 of *RGS3* in the VCaP-Met (and VCaP cells) (Supplementary Fig. 7c). Another novel gene fusion was between exon 1 of *LMAN2* and exon 2 of *AP3S1* (Supplementary Fig. 7d).

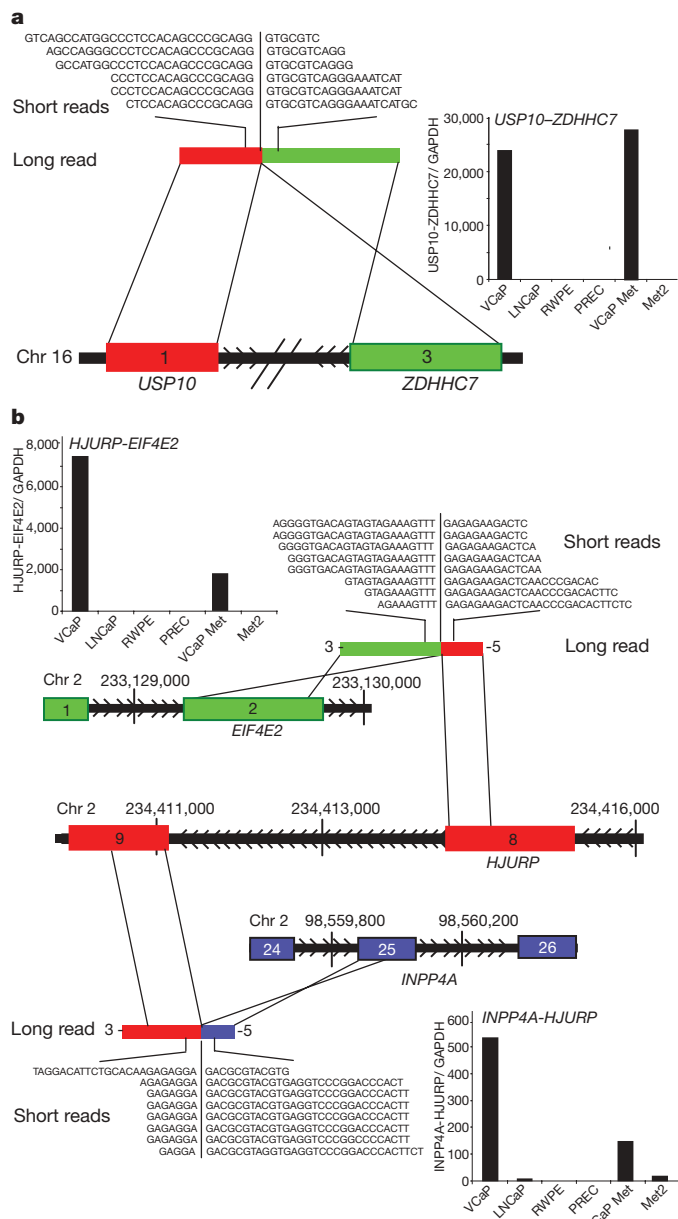


Figure 2 | Representative gene fusions characterized in the prostate cancer cell line VCaP. **a**, Schematic of *USP10-ZDHHC7* fusion on chromosome 16. Exon 1 of *USP10* (red) is fused with exon 3 of *ZDHHC7* (green), located on the same chromosome in opposite orientation. Inset displays histogram of qRT-PCR validation of *USP10-ZDHHC7* transcript. **b**, Schematic of a complex intra-chromosomal rearrangement leading to two gene fusions involving *HJURP* on chromosome 2. Exon 8 of *HJURP* (red) is fused with exon 2 of *EIF4E2* (green) to form *HJURP-EIF4E2*. Exon 25 of *INPP4A* (blue) is fused with exon 9 of *HJURP* (red) to form *INPP4A-HJURP*. Insets display histograms of qRT-PCR validation of *HJURP-EIF4E2* and *INPP4A-HJURP* transcripts.

Interestingly, one read-through chimera, *SLC45A3-ELK4*, between the fourth exon of *SLC45A3* with exon 2 of *ELK4*, a member of the ETS transcription factor family, was identified in metastatic prostate cancer, Met 4, and the LNCaP cell line, suggesting recurrence (Fig. 4a, upper panel). Taqman qRT-PCR assay for this fusion performed in a panel of cell lines revealed a high level of expression in LNCaP cells and much lower levels in other prostate cancer cell lines including 22Rv1, VCaP and MDA-PCA-2B. Benign prostate epithelial cells, PREC and RWPE, and non-prostate cell lines including breast, melanoma, lung, chronic myeloid leukaemia (CML) and pancreatic cancer cell lines were negative for this fusion (Fig. 4a, middle panel).

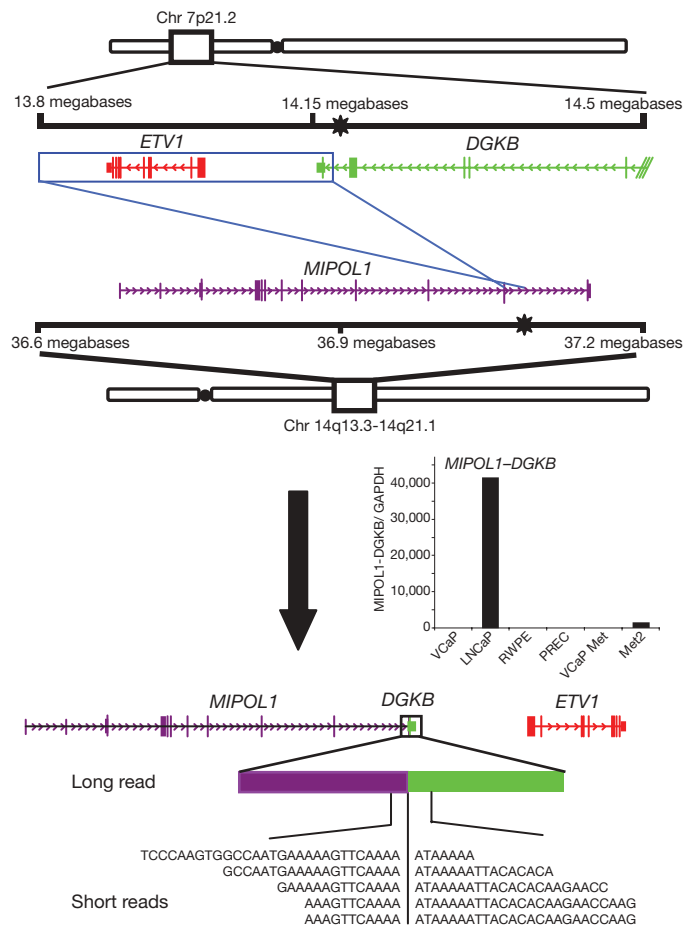
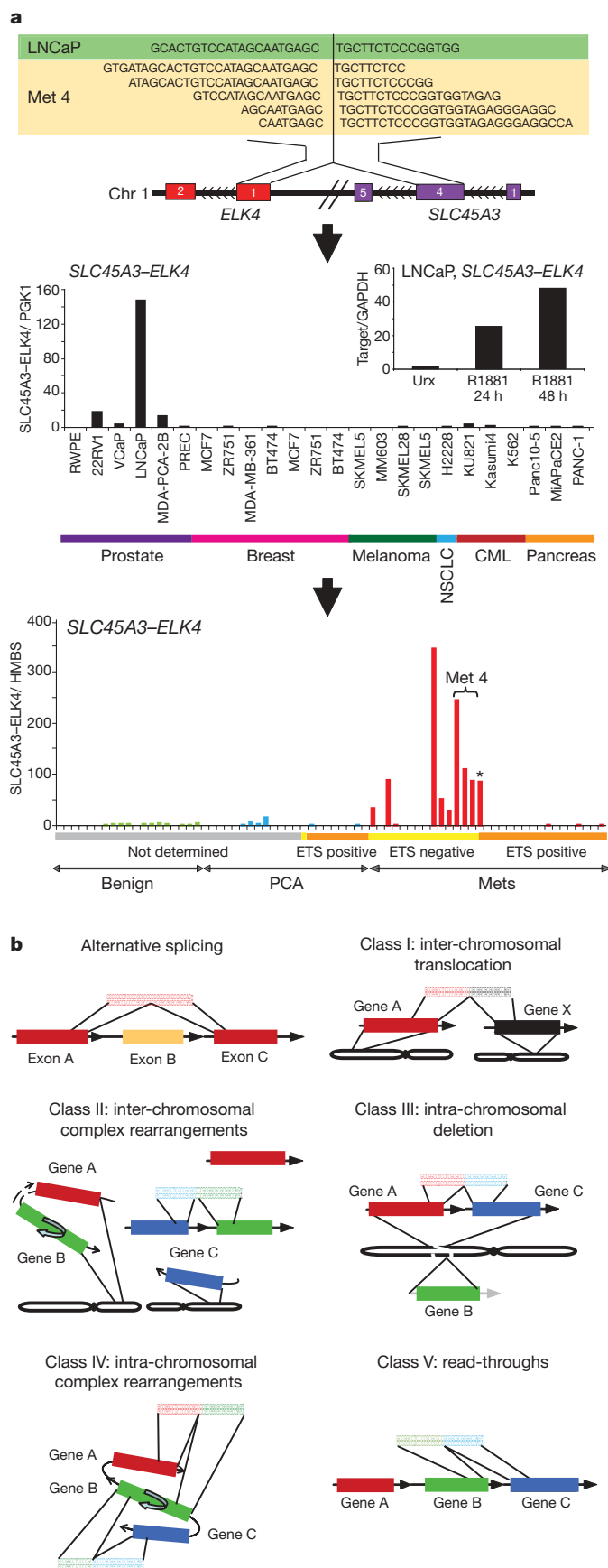


Figure 3 | Schematic of *MIPOL1-DGKB* gene fusion in the prostate cancer cell line LNCaP. *MIPOL1-DGKB* is an inter-chromosomal gene fusion accompanying the cryptic insertion of *ETV1* locus (red) on chromosome 7 into the *MIPOL1* (purple) intron on chromosome 14. Previously determined genomic breakpoints (black stars) are shown in *DGKB* and *MIPOL1*. An insertion event results in the inversion of the 3' end of *DGKB* and *ETV1* into the *MIPOL1* intron between exons 10 and 11. Inset displays histogram of qRT-PCR validation of the *MIPOL1-DGKB* transcript.

SLC45A3 has been reported to be fused to *ETV1* in a prostate cancer sample³; notably, it is a prostate-specific, androgen-responsive gene. Interestingly, the fusion transcript *SLC45A3-ELK4* was also found to be induced by the synthetic androgen R1881 (Fig. 4a, middle panel, inset). Further, we interrogated a panel of prostate tissues for this fusion, and found it expressed in seven out of 20 metastatic prostate cancer tissues examined (Fig. 4a, lower panel). Interestingly, six of those seven positive cases have been identified as negative for ETS genes *ERG*, *ETV1*, *ETV4* and *ETV5* in our previous work, based on a FISH screen²⁰. One *TMPRSS2-ETV1*-positive metastatic prostate cancer sample was also found to be positive for *SLC45A3-ELK4* (similar to LNCaP, which is also *ETV1* positive³). Unlike the previous ETS gene fusions identified, *SLC45A3-ELK4* is a read-through event between adjacent genes and does not harbour detectable alterations at the DNA level by FISH (Supplementary Fig. 8), array comparative genomic hybridization (aCGH) (data not shown) or high-density single nucleotide polymorphism (SNP) arrays (Supplementary Fig. 9). As LNCaP and Met 4 harbour genomic aberrations of *ETV1*, and express high levels of the *SLC45A3-ELK4* chimaeric transcript, this suggests that *ETV1* and *ELK4* may cooperate to drive prostate carcinogenesis in those tumours. To our knowledge, *SLC45A3-ELK4* may represent the first description of a recurrent RNA chimaeric transcript specific to cancer that does not have a detectable DNA aberration. Overall, *SLC45A3-ELK4* appears to be the only recurrent chimaeric transcript identified in our transcriptome sequencing



study, as other gene fusions tested in a panel of prostate cancer samples appeared to be restricted to the sample in which they were identified (at least in the limited number of samples we analysed) and thus may represent rare or private mutations (Supplementary Fig. 10).

Figure 4 | Discovery of the recurrent *SLC45A3-ELK4* chimaera in prostate cancer and a general classification system for chimaeric transcripts in cancer. **a**, Upper panel, schematic of the *SLC45A3-ELK4* chimaera located on chromosome 1. Middle panel, qRT-PCR validation of *SLC45A3-ELK4* transcript in a panel of cell lines. Inset, histogram of qRT-PCR assessment of the *SLC45A3-ELK4* transcript in LNCaP cells treated with R1881. Lower panel, histogram of qRT-PCR validation in a panel of prostate tissues: benign adjacent prostate, localized prostate cancer (PCA) and metastatic prostate cancer (Mets). ETS family gene rearrangement status (by FISH) indicated by horizontal coloured bars below graph. Grey, not determined; yellow, ETS negative; orange, ETS positive. Horizontal bracket indicates three different metastatic tissues from the same patient (Met 4). Asterisk denotes an ETV1-positive sample. **b**, Chimaera classification schema (described in the text).

Next, we tested if the novel gene fusions identified in this study represent acquired somatic mutations or simply germline variations. Based on qPCR (Supplementary Fig. 11) and FISH (Supplementary Figs 12 and 13) assessment of a representative set of fusion genes on patient-matched germline tissues, we found the chimaeras restricted to the cancer tissues. Further, we interrogated the 29 genes involved in our gene fusions in the Database of Genomic Variants (<http://projects.tcag.ca/variation/>) and found only eight of them with previously reported copy number variations (Supplementary Table 5). However, our matched aCGH data did not reveal any copy number variation in those genes (Supplementary Table 6), suggesting that our samples did not harbour copy number variations common to the human population.

Based on the gene fusions we have characterized (Supplementary Table 7), we propose a chimaera classification system (Fig. 4b). Inter-chromosomal translocation (Class I) involves fusion between two genes on different chromosomes (for example, *BCR-ABL1*). Inter-chromosomal complex rearrangements (Class II) occur when two genes from different chromosomes fuse together while a third gene follows along and becomes activated (*MIPOL1-DGKB*). Intra-chromosomal deletion (Class III) results when deletion of a genomic region fuses the flanking genes (*TPR22-ERG*). Intra-chromosomal complex rearrangements (Class IV) involve a breakpoint in one gene fusing with multiple regions (*HJURP-EIF4E2* and *INPP4-HJURP*). Read-through chimaeras (Class V) include chimaeric transcripts between neighbouring genes (*ZNF649-ZNF577*).

Overall, transcriptome sequencing was found to be a powerful tool for detecting gene fusions, exemplified by our ability to detect multiple gene fusions in cancer cell lines and tissues. One important limitation is in cases where the proximal partner contributes only the regulatory sequence to the fusion and no transcript sequence (for example IgH-Myc in Burkitt's lymphoma). Although it has been known that gene fusion events can play a causative role in cancer, the current study has demonstrated that a particular cancer cell line or tissue can harbour multiple gene fusions, many of which are likely not recurrent. Although it is unclear whether these private gene fusions play a role in malignant transformation, they could potentially cooperate with the driver mutation/gene fusions. Like the cataloguing of point mutations associated with cancer²¹⁻²⁷, it will be important to catalogue and investigate the function of the multiple gene fusions present in a single cancer. The discovery of the chimaeric transcript *SLC45A3-ELK4* underscores that a refinement of next-generation sequencing technologies and attendant analytical tools may well unravel the full scope of these 'dangerous liaisons' in carcinogenesis.

METHODS SUMMARY

Long-read sequencing was conducted using 454 FLX Sequencing, whereas short-read sequencing was performed on the Illumina Genome Analyzer. qPCR for fusion candidates was performed using indicated oligonucleotide primers (Supplementary Table 8). Interphase FISH was performed in cell lines and tissues using bacterial artificial chromosome probes (Supplementary Figs 4b-e, 5b, d, f, 8, 12, 13 and 14c, e). Oligonucleotide aCGH was performed using Agilent arrays, and copy number analysis was conducted in CGH Analytics. Affymetrix Genome-wide Human SNP Array 6.0 was processed using the Affymetrix

Genotyping Console. Prostate tissues were obtained from the radical prostatectomy series at the University of Michigan and from the Rapid Autopsy Program, University of Michigan Specialized Program of Research Excellence (SPORE) in prostate cancer.

Full Methods and any associated references are available in the online version of the paper at www.nature.com/nature.

Received 21 July; accepted 10 November 2008.

Published online 11 January 2009.

- Mitelman, F., Johansson, B. & Mertens, F. Fusion genes and rearranged genes as a linear function of chromosome aberrations in cancer. *Nature Genet.* **36**, 331–334 (2004).
- Tomlins, S. A. *et al.* Recurrent fusion of TMPRSS2 and ETS transcription factor genes in prostate cancer. *Science* **310**, 644–648 (2005).
- Tomlins, S. A. *et al.* Distinct classes of chromosomal rearrangements create oncogenic ETS gene fusions in prostate cancer. *Nature* **448**, 595–599 (2007).
- Kumar-Sinha, C., Tomlins, S. A. & Chinnaiyan, A. M. Recurrent gene fusions in prostate cancer. *Nature Rev. Cancer* **8**, 497–511 (2008).
- Choi, Y. L. *et al.* Identification of novel isoforms of the EML4-ALK transforming gene in non-small cell lung cancer. *Cancer Res.* **68**, 4971–4976 (2008).
- Koivunen, J. P. *et al.* EML4-ALK fusion gene and efficacy of an ALK kinase inhibitor in lung cancer. *Clin. Cancer Res.* **14**, 4275–4283 (2008).
- Perner, S. *et al.* EML4-ALK fusion lung cancer: a rare acquired event. *Neoplasia* **10**, 298–302 (2008).
- Rikova, K. *et al.* Global survey of phosphotyrosine signaling identifies oncogenic kinases in lung cancer. *Cell* **131**, 1190–1203 (2007).
- Soda, M. *et al.* Identification of the transforming EML4-ALK fusion gene in non-small-cell lung cancer. *Nature* **448**, 561–566 (2007).
- Rowley, J. D. Chromosome translocations: dangerous liaisons revisited. *Nature Rev. Cancer* **1**, 245–250 (2001).
- Lynch, T. J. *et al.* Activating mutations in the epidermal growth factor receptor underlying responsiveness of non-small-cell lung cancer to gefitinib. *N. Engl. J. Med.* **350**, 2129–239 (2004).
- Slamon, D. J. *et al.* Use of chemotherapy plus a monoclonal antibody against HER2 for metastatic breast cancer that overexpresses HER2. *N. Engl. J. Med.* **344**, 783–792 (2001).
- Demetri, G. D. *et al.* Efficacy and safety of imatinib mesylate in advanced gastrointestinal stromal tumors. *N. Engl. J. Med.* **347**, 472–480 (2002).
- Druker, B. J. *et al.* Five-year follow-up of patients receiving imatinib for chronic myeloid leukemia. *N. Engl. J. Med.* **355**, 2408–2417 (2006).
- Futreal, P. A. *et al.* A census of human cancer genes. *Nature Rev. Cancer* **4**, 177–183 (2004).
- Shtivelman, E., Lifshitz, B., Gale, R. P. & Canaani, E. Fused transcript of *abl* and *bcr* genes in chronic myelogenous leukaemia. *Nature* **315**, 550–554 (1985).
- Takahara, T., Tasic, B., Maniatis, T., Akanuma, H. & Yanagisawa, S. Delay in synthesis of the 3' splice site promotes trans-splicing of the preceding 5' splice site. *Mol. Cell* **18**, 245–251 (2005).
- Communi, D., Suarez-Huerta, N., Dussosoy, D., Savi, P. & Boeynaems, J. M. Cotranscription and intergenic splicing of human P2Y11 and SSF1 genes. *J. Biol. Chem.* **276**, 16561–16566 (2001).
- Gleave, M. *et al.* The effects of the dual 5 α -reductase inhibitor dutasteride on localized prostate cancer – results from a 4-month pre-radical prostatectomy study. *Prostate* **66**, 1674–1685 (2006).
- Han, B. *et al.* A fluorescence in situ hybridization screen for E26 transformation-specific aberrations: identification of DDX5-ETV4 fusion protein in prostate cancer. *Cancer Res.* **68**, 7629–7637 (2008).
- Barber, T. D., Vogelstein, B., Kinzler, K. W. & Velculescu, V. E. Somatic mutations of EGFR in colorectal cancers and glioblastomas. *N. Engl. J. Med.* **351**, 2883 (2004).
- Cheung, V. G. *et al.* Integration of cytogenetic landmarks into the draft sequence of the human genome. *Nature* **409**, 953–958 (2001).
- Greenman, C. *et al.* Patterns of somatic mutation in human cancer genomes. *Nature* **446**, 153–158 (2007).
- Stephens, P. *et al.* A screen of the complete protein kinase gene family identifies diverse patterns of somatic mutations in human breast cancer. *Nature Genet.* **37**, 590–592 (2005).
- Strausberg, R. L., Buetow, K. H., Emmert-Buck, M. R. & Klausner, R. D. The cancer genome anatomy project: building an annotated gene index. *Trends Genet.* **16**, 103–106 (2000).
- Weir, B. A. *et al.* Characterizing the cancer genome in lung adenocarcinoma. *Nature* **450**, 893–898 (2007).
- Wood, L. D. *et al.* The genomic landscapes of human breast and colorectal cancers. *Science* **318**, 1108–1113 (2007).

Supplementary Information is linked to the online version of the paper at www.nature.com/nature.

Acknowledgements We thank Illumina and 454 for technical support, R. Mehra and J. Siddiqui for providing tissue samples, Y. Gong, S. Shankar, X. Wang and A. Menon for technical assistance, J. Yu for help with the Illumina Genome Analyzer, and R. J. Lonigro for discussions. C.A.M. was supported by a National Institutes of Health Ruth L. Kirschstein post-doctoral training grant, and currently derives support from the American Association of Cancer Research Amgen Fellowship in Clinical/Translational Research, the Canary Foundation and American Cancer Society Early Detection Postdoctoral Fellowship. This work was supported in part by the National Institutes of Health (to A.M.C.), the Department of Defense (to A.M.C.), the Early Detection Research Network (to A.M.C.), and NCIBI (grant number U54 DA 021519).

Author Contributions C.A.M., C.K.-S. and A.M.C. wrote the manuscript. C.K.-S., X.C., X.J., B.H. and N.P. performed the sequencing and biochemical experiments. C.A.M., S.K.-S., L.S. and T.B. performed bioinformatics analysis.

Author Information Sequences of the gene fusion chimaeras are deposited in GenBank under accession numbers FJ423742–FJ423755. Reprints and permissions information is available at www.nature.com/reprints. Correspondence and requests for materials should be addressed to A.M.C. (arul@umich.edu).

METHODS

Samples and cell lines. The benign immortalized prostate cell line RWPE and the prostate cancer cell line LNCaP were obtained from the American Type Culture Collection. Primary benign prostatic epithelial cells (PrEC) were obtained from Cambrex Bio Science. The prostate cancer cell line MDA-PCa 2B was provided by E. Keller. The prostate cancer cell line 22-RV1 was provided by J. Macoska. VCaP was derived from a vertebral metastasis from a patient with hormone-refractory metastatic prostate cancer²⁸, and was provided by K. Pienta.

The androgen stimulation experiment was performed with LNCaP and VCaP cells grown in charcoal-stripped serum containing media for 24 h, before treatment with 1% ethanol or 1 nM of methyltrienolone (R1881, NEN Life Science Products) dissolved in ethanol, for 24 and 48 h. Total RNA was isolated with RNeasy mini kit (Qiagen) according to the manufacturer's instructions.

Prostate tissues were obtained from the radical prostatectomy series at the University of Michigan and from the Rapid Autopsy Program²⁹, University of Michigan Prostate Cancer Specialized Program of Research Excellence Tissue Core. All samples were collected with the informed consent of the patients and prior approval of the institutional review board.

454 FLX sequencing. PolyA⁺ RNA was purified from 50 µg total RNA using two rounds of selection on oligo-dT containing paramagnetic beads using Dynabeads mRNA Purification Kit (DynaL Biotech), according to the manufacturer's instructions. mRNA (200 ng) was fragmented at 82 °C in fragmentation buffer (40 mM Tris-acetate, 100 mM potassium acetate, 31.5 mM magnesium acetate, pH 8.1) for 2 min. First-strand cDNA library was prepared using Superscript II (Invitrogen) according to standard protocols, and directional adaptors were ligated to the cDNA ends for clonal amplification and sequencing on the Genome Sequencer FLX.

The adaptor ligation reaction was performed in Quick Ligase Buffer (New England Biolabs) containing 1.67 µM of the Adaptor A, 6.67 µM of the Adaptor B and 2,000 units of T4 DNA Ligase (New England Biolabs) at 37 °C for 2 h. Adapted library was recovered with 0.05% Sera-Mag30 streptavidin beads (Seradyn Inc.) according to the manufacturer's instructions. Finally, the single-stranded cDNA (ssDNA) library was purified twice with RNeasy (Qiagen) according to the manufacturer's directions, except that the amount of beads was reduced to 1.6× the volume of the sample. The purified ssDNA library was analysed on an RNA 6000 Pico chip on a 2100 Bioanalyser (Agilent Technologies) to confirm a size distribution between 450 and 750 nucleotides, and quantified with a Quant-iT Ribogreen RNA Assay Kit (Invitrogen Corporation) on a Synergy HT (Bio-Tek Instruments Inc.) instrument following the manufacturer's instructions. The library was PCR amplified with 2 µM each of Primer A (5'-GCC TCC CTC GCG CCA-3') and Primer B (5'-GCC TTG CCA GCC CGC-3'), 400 µM dNTPs, 1× Advantage 2 buffer and 1 µl of Advantage 2 polymerase mix (Clontech). The amplification reaction was performed at: 96 °C for 4 min; 94 °C for 30 s, 64 °C for 30 s, repeating steps 2 and 3 for a total of 20 cycles, followed by 68 °C for 3 min. The samples were purified using AMPure beads and diluted to a final working concentration of 200,000 molecules per microlitre. Emulsion beads for sequencing were generated using Sequencing emPCR Kit II and Kit III, and sequencing was performed using 600,000 beads.

Normalization by subtraction. mRNA from the prostate cancer cell line VCaP was hybridized with the subtractor cell line LNCaP first-strand cDNA immobilized on magnetic beads (Dynabeads, Invitrogen), according to the manufacturer's instructions. Transcripts common to both the cells were captured and removed by magnetic separation of bead-bound subtractor cDNA. The subtracted VCaP mRNA left in the supernatant was recovered by precipitation and used for generating the sequencing library as described. Efficiency of normalization was assessed by qRT-PCR assay of levels of select transcripts in the sample before and after the subtraction (data not shown).

Illumina Genome Analyzer sequencing. mRNA (200 ng) was fragmented at 70 °C for 5 min in a fragmentation buffer (Ambion), and converted to first-strand cDNA using Superscript III (Invitrogen), followed by second-strand cDNA synthesis using *Escherichia coli* DNA pol I (Invitrogen). The double-stranded cDNA library was further processed by Illumina Genomic DNA Sample Prep kit. It involved end repair using T4 DNA polymerase, Klenow DNA polymerase and T4 Polynucleotide kinase followed by a single <A> base addition using Klenow 3' to 5' exo⁻ polymerase, and was ligated with Illumina's adaptor oligo mix using T4 DNA ligase. Adaptor-ligated library was size selected by separating on a 4% agarose gel and cutting out the library smear at 200 base pairs (bp) (±25 bp). The library was PCR amplified by Phi polymerase (Stratagene), and purified by Qiaquick PCR Purification Kit (Qiagen). The library was quantified with Quant-iT Picogreen dsDNA Assay Kit (Invitrogen) on a Modulus Single Tube Luminometer (Turner Biosystems) following the manufacturer's instructions. Library (10 nM) was used to prepare flowcells with approximately 30,000 clusters per lane.

Sequence data sets. Human genome build 18 (hg18) was used as a reference genome. All University of California, Santa Cruz (UCSC) and Refseq transcripts were downloaded from the UCSC genome browser (<http://genome.ucsc.edu/>)³⁰. Sequences of previously identified *TMPRSS2-ERG* fusion transcript (GenBank accession number DQ204772) and *BCR-ABL1* fusion transcript (GenBank accession number M30829) were used for reference.

Short-read chimaera discovery. Short reads that do not completely align to the human genome, Refseq genes, mitochondrial, ribosomal or contaminant sequences are categorized as non-mapping. For many chimaeras we expect that there will be a larger portion mapping to a fusion partner (major alignment), and a smaller portion aligning to the second partner (minor alignment). Our approach is therefore divided into two phases in which we focus first on identifying the major alignment, and then performing a more exhaustive approach to identify the minor alignment. In the first phase, all non-mapping reads are aligned against all exons of Refseq genes using Vmatch, a pattern matching program³¹. Only reads that have an alignment of 12 or more nucleotides to an exon boundary are kept as potential chimaeras. In the second phase, the non-mapping portion of the remaining reads are then mapped to all possible exon boundaries using a Perl script that uses regular expressions to detect alignments of as few as six nucleotides. Only those short reads that show partial alignment to exon boundaries of two separate genes are categorized as chimaeras. It is possible to have a chimaera that has 28 nucleotides aligning to gene *x* and eight nucleotides that align to genes *y* and *z* because the eight-base polymer does not provide enough sequence resolution to distinguish between gene *y* and gene *z*. Therefore we would categorize this as two individual chimaeras. If a sequence forms more than five chimaeras it is discarded because it is ambiguous. To minimize false positives, we require that a predicted gene fusion event has at least two supporting chimaeras.

Long- and short-read integrated chimaera discovery. All 454 reads are aligned against the human Refseq collection using BLAT, a rapid mRNA/DNA alignment tool³². Using a Perl script, the BLAT output files were parsed to detect potential chimaeric reads. A read is categorized as completely aligning if it shows greater than 90% alignment to a known Refseq transcript. These are then discarded as they almost completely align and are therefore not characteristic of a chimaera. From the remaining reads, we want to query for reads having partial alignment, with minimal overlap, to two Refseq transcripts representing putative chimaeras. To accomplish this, we iterate the all the possible BLAT alignments for a putative chimaera, extracting only those partial alignments that have no more than a six-nucleotide, or two-codon, overlap. This step reduces false-positive chimaeras introduced by repetitive regions, large gene families and conserved domains. Additionally, although our approach tolerates overlap between the partial alignments, it filters those having more than ten or more nucleotides between the partial alignments.

The short reads (36 nucleotides) generated from the Illumina platform are parsed by aligning them against the Refseq database and the human genome using Eland, an alignment tool for short reads. Reads that align completely or fail quality control are removed, leaving only the 'non-mapping' reads; a rich source for chimaeras. These non-mapping short reads are subsequently aligned against all putative long-read chimaeras (obtained as described above) using Vmatch³¹, a pattern matching program. A Perl script is used to parse the Vmatch output to extract only those reads that span the fusion boundary by at least three nucleotides on each side. After this integration, the remaining putative chimaeras are categorized as inter- or intra-chromosomal chimaeras based on whether the partial alignments are located on different or the same chromosomes, respectively. Those intra-chromosomal chimaeras that have partial alignments to adjacent genes are believed to be the product of co-transcription of adjacent genes coupled with intergenic splicing (CoTIS)¹⁸, alternatively known as read-throughs. The remaining intra-chromosomal and all inter-chromosomal chimaeras are considered candidate gene fusions.

One additional source of false-positive chimaeras could be an unknown transcript that is not in Refseq. Owing to its absence in the Refseq database, the corresponding long read would not be able to show a complete alignment, but instead show partial hits. Subsequently, short reads spanning this transcript would naturally validate the artificially produced fusion boundary. Therefore, to remove these candidates, we aligned all of the chimaeras against the human genome using BLAT. If the long read has greater than 90% alignment to one genomic location, it is considered a novel transcript rather than a chimaeric read. The remaining chimaeras are given a score that is calculated by multiplying the long-read coverage spanning the fusion boundary against the short-read coverage spanning the fusion boundary.

Coverage analysis. Transcript coverage for every gene locus was calculated from the total number of passing filter reads that mapped, by ELAND, to exons. The total count of these reads was multiplied by the read length and divided by the longest transcript isoform of the gene as determined by the sum of all exon

lengths as defined in the UCSC knownGene table (March 2006 assembly). Nucleotide coverage was determined by enumerating the total reads, based on ELAND mappings, at every nucleotide position within a non-redundant set of exons from all possible UCSC transcript isoforms.

Array CGH analysis. Oligonucleotide comparative genomic hybridization is a high-resolution method for detecting unbalanced copy number changes at whole-genome level. Competitive hybridization of differentially labelled tumour and reference DNA to oligonucleotide printed in an array format (Agilent Technologies), and analysis of fluorescent intensity for each probe, will detect the copy number changes in the tumour sample relative to normal reference genome. We identified genomic breakpoints at regions with a change in copy-number level of at least one copy ($\log \text{ratio} \pm 0.5$), for gains and losses involving more than one probe representing each genomic interval, as detected by the aberration detection method (ADM) in the CGH analytics algorithm.

Real-time PCR validation. qPCR was performed using Power SYBR Green Mastermix (Applied Biosystems) on an Applied Biosystems Step One Plus Real Time PCR System as described³. All oligonucleotide primers were synthesized by Integrated DNA Technologies and are listed in Supplementary Table 8. *GAPDH*³³ primer was as described. All assays were performed in duplicate or triplicate, and results were plotted as average fold change relative to *GAPDH*.

qPCR for *SLC45A3-ELK4* was performed by the Taqman assay method using fusion-specific primers and Probe #7 of the Universal Probe Library (UPL) (Roche) as the internal oligonucleotide, according to the manufacturer's instructions. *PGK1* was used as the housekeeping control gene for the UPL-based Taqman assay (Roche), according to the manufacturer's instructions. HMBS (Applied Biosystems, Taqman assay Hs00609297_m1) was used as the housekeeping gene control for Taqman assays according to standard protocols (Applied Biosystems).

FISH. FISH hybridizations were performed on VCaP, LNCaP and FFPE tumour and normal tissues. Bacterial artificial chromosome clones were selected from

the UCSC genome browser. After colony purification, midi prep DNA was prepared using QiagenTips-100 (Qiagen). DNA was labelled by nick translation labelling with biotin-16-dUTP and digoxigenin-11-dUTP (Roche). Probe DNA was precipitated and dissolved in hybridization mixture containing 50% formamide, 2×SSC, 10% dextran sulphate and 1% Denhardt's solution. About 200 ng of labelled probes was hybridized to normal human chromosomes to confirm the map position of each bacterial artificial chromosome clone. FISH signals were obtained using anti digoxigenin-fluorescein and Alexa Fluor594 conjugate for green and red colours, respectively. Fluorescence images were captured using a high-resolution CCD (charge-coupled device) camera controlled by ISIS image processing software (Metasystems).

Affymetrix Genome-Wide Human SNP Array 6.0. One microgram each of genomic DNA samples was sent to Affymetrix service centres (Center for Molecular Medicine and Vanderbilt Affymetrix Genotyping Core) for genomic level analysis of 15 samples on the Genome-Wide Human SNP Array 6.0. Copy number analysis was conducted using the Affymetrix Genotyping Console software, and visualizations were generated by the Genotyping Console browser.

28. Korenchuk, S. *et al.* VCaP, a cell-based model system of human prostate cancer. *In Vivo* **15**, 163–168 (2001).
29. Rubin, M. A. *et al.* Rapid ('warm') autopsy study for procurement of metastatic prostate cancer. *Clin. Cancer Res.* **6**, 1038–1045 (2000).
30. Karolchik, D. *et al.* The UCSC Table Browser data retrieval tool. *Nucleic Acids Res.* **32** (Database issue), D493–D496 (2004).
31. Abouelhoda, M. I., Kurtz, S. & Ohlebusch, E. Replacing suffix trees with enhanced suffix arrays. *J. Discrete Algorithms* **2**, 53–86 (2004).
32. Kent, W. J. BLAT – the BLAST-like alignment tool. *Genome Res.* **12**, 656–664 (2002).
33. Vandesompele, J. *et al.* Accurate normalization of real-time quantitative RT-PCR data by geometric averaging of multiple internal control genes. *Genome Biol.* **3**, 34–50 (2002).

LETTERS

Protein structure determination in living cells by in-cell NMR spectroscopy

Daisuke Sakakibara^{1,2*}, Atsuko Sasaki^{1,2*}, Teppei Ikeya^{1,3*}, Junpei Hamatsu^{1,2}, Tomomi Hanashima¹, Masaki Mishima^{1,2}, Masatoshi Yoshimasu⁴, Nobuhiro Hayashi^{5†}, Tsutomu Mikawa⁶, Markus Wälcchli⁷, Brian O. Smith⁸, Masahiro Shirakawa^{2,9}, Peter Güntert^{1,3,10} & Yutaka Ito^{1,2,6}

Investigating proteins ‘at work’ in a living environment at atomic resolution is a major goal of molecular biology, which has not been achieved even though methods for the three-dimensional (3D) structure determination of purified proteins in single crystals or in solution are widely used. Recent developments in NMR hardware and methodology have enabled the measurement of high-resolution heteronuclear multi-dimensional NMR spectra of macromolecules in living cells (in-cell NMR)^{1–5}. Various intracellular events such as conformational changes, dynamics and binding events have been investigated by this method. However, the low sensitivity and the short lifetime of the samples have so far prevented the acquisition of sufficient structural information to determine protein structures by in-cell NMR. Here we show the first, to our knowledge, 3D protein structure calculated exclusively on the basis of information obtained in living cells. The structure of the putative heavy-metal binding protein TTHA1718 from *Thermus thermophilus* HB8 overexpressed in *Escherichia coli* cells was solved by in-cell NMR. Rapid measurement of the 3D NMR spectra by nonlinear sampling of the indirectly acquired dimensions was used to overcome problems caused by the instability and low sensitivity of living *E. coli* samples. Almost all of the expected backbone NMR resonances and most of the side-chain NMR resonances were observed and assigned, enabling high quality (0.96 Å backbone root mean squared deviation) structures to be calculated that are very similar to the *in vitro* structure of TTHA1718 determined independently. The in-cell NMR approach can thus provide accurate high-resolution structures of proteins in living environments.

In living cells, proteins function in an environment in which they interact specifically with other proteins, nucleic acids, co-factors and ligands, and are subject to extreme molecular crowding⁶ that makes the cellular environment difficult to replicate *in vitro*. Although *in vitro* methods of structure determination have made very valuable contributions to understanding the functions of many proteins, *in vivo* observations of 3D structures, structural changes, dynamics or interactions of proteins are required for the explicit understanding of the structural basis of their functions inside cells. Its non-invasive character and ability to provide data at atomic resolution make NMR spectroscopy ideally suited for the task. Indeed, recent advances in measurement sensitivity have permitted heteronuclear multi-dimensional NMR spectroscopy of proteins inside living cells by so-called in-cell NMR^{1–5}.

In-cell NMR has been used to detect protein–protein interactions inside *E. coli* cells⁷ as well as the behaviour of intrinsically disordered proteins^{8,9}. In eukaryotic cells, in-cell NMR studies have been performed by injecting proteins into *Xenopus laevis* oocytes or eggs^{10,11} and, more recently, cell-penetrating peptides have been used to deliver proteins that can be observed in living human cells¹².

Despite the interest in in-cell NMR, it has not yet been determined whether the established methods for the structure determination of purified proteins by NMR¹³ can be extended to proteins in living cells. To our knowledge, the only published 3D in-cell NMR experiments

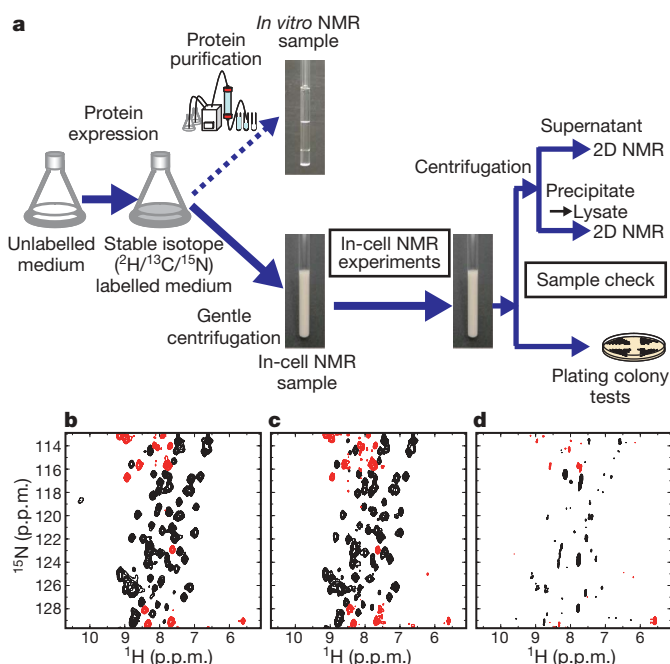


Figure 1 | Stability of *E. coli* cells expressing TTHA1718 under NMR measurement conditions. **a**, Scheme of the in-cell NMR experiments using *E. coli* cells. **b**, The ¹H–¹⁵N HSQC spectrum of a TTHA1718 in-cell NMR sample immediately after sample preparation. **c**, The ¹H–¹⁵N HSQC spectrum after 6 h in an NMR tube at 37 °C. **d**, The ¹H–¹⁵N HSQC spectrum of the supernatant of the in-cell sample used in **b** and **c**.

¹Department of Chemistry, Tokyo Metropolitan University, 1-1 Minami-Osawa, Hachioji, Tokyo 192-0397, Japan. ²CREST/Japan Science and Technology Agency (JST), 4-1-8 Honcho, Kawaguchi, Saitama 332-0012, Japan. ³Institute of Biophysical Chemistry and Center for Biomolecular Magnetic Resonance, J. W. Goethe-University Frankfurt, Max-von-Laue Straße 9, 60438 Frankfurt am Main, Germany. ⁴Cellular and Molecular Biology Laboratory, RIKEN, 2-1 Hirosawa, Wako-shi, Saitama 351-0198, Japan. ⁵Division of Biomedical Polymer Science, Institute for Comprehensive Medical Science, Fujita Health University, Toyoake-shi, Aichi 470-1192, Japan. ⁶Research Group for Bio-supramolecular Structure-Function, RIKEN, 1-7-29 Suehiro-cho, Tsurumi-ku, Yokohama 230-0045, Japan. ⁷Bruker BioSpin, 3-21-5 Ninomiya, Tsukuba-shi, Ibaraki 305-0051, Japan. ⁸Division of Molecular and Cellular Biology, Faculty of Biomedical and Life Sciences, University of Glasgow, Glasgow G12 8QQ, UK. ⁹Department of Molecular Engineering, Graduate School of Engineering, Kyoto University, Nishikyo-Ku, Kyoto 615-8510, Japan. ¹⁰Frankfurt Institute for Advanced Studies, Ruth-Moufang-Str. 1, 60438 Frankfurt am Main, Germany. [†]Present address: Department of Life Science, Graduate School of Bioscience and Biotechnology, Tokyo Institute of Technology, 4259 B-1, Nagatsuda-chou, Midori-ku, Yokohama, Kanagawa, 226-8501, Japan.

*These authors contributed equally to this work.

are projection reconstruction versions of triple-resonance experiments for backbone resonance assignment in *E. coli*¹⁴. *De novo* NMR protein structure determination in living cells requires methods for resonance assignment that do not rely on information obtained *in vitro*, as well as the efficient analysis of nuclear Overhauser effect (NOE)-derived information, in which broadened lines result in severely overlapped cross-peaks.

Here we have used the *T. thermophilus* HB8 TTHA1718 gene product—a putative heavy-metal binding protein consisting of 66 amino acids that was overexpressed in *E. coli* to a concentration of 3–4 mM—as a model system. First we examined the stability of the live *E. coli* samples under measurement conditions at 37 °C. The experimental scheme of our in-cell NMR experiments is presented in Fig. 1a. The virtual identity of ^1H – ^{15}N heteronuclear single quantum coherence (HSQC) spectra recorded immediately after sample preparation (Fig. 1b) and after 6 h in an NMR tube at 37 °C (Fig. 1c) show that TTHA1718 in-cell NMR samples are stable for at least 6 h. It is crucial for in-cell NMR to ensure that the proteins providing the NMR spectra are indeed inside the living cells, and that the contribution from extracellular proteins is negligible¹⁵. Most ^1H – ^{15}N HSQC cross-peaks disappeared after removal of the bacteria by gentle centrifugation after the measurement shown in Fig. 1c (Fig. 1d), whereas the lysate spectrum of the collected cells shows much sharper cross-peaks (Supplementary Fig. 1b). These results were corroborated by SDS–PAGE (Supplementary Fig. 1c), demonstrating that the contribution of extracellular protein to the observed signals is negligible. The viability of the bacteria in the in-cell samples after 6 h of NMR measurements was confirmed to be $85 \pm 11\%$ by plating colony tests. TTHA1718 was indicated to be in the cytoplasm by cell fractionation experiments (Supplementary Fig. 1d, e).

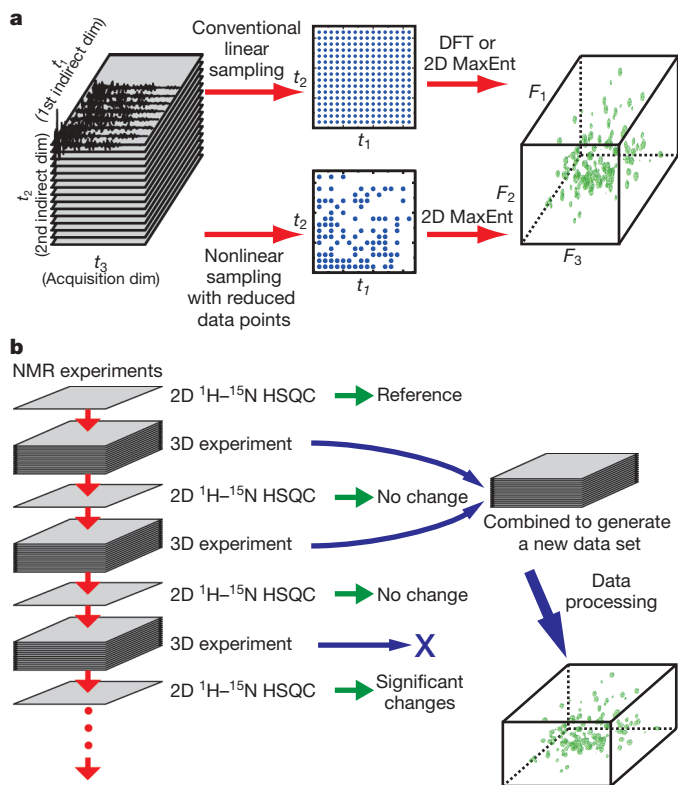


Figure 2 | Rapid acquisition of 3D NMR spectra of TTHA1718 in living *E. coli* cells. **a**, Rapid acquisition of 3D NMR spectra using a nonlinear sampling scheme. DFT, discrete Fourier transform; dim, dimension; MaxEnt, maximum-entropy processing. **b**, Repeated observation of 3D NMR spectra with intermittent monitoring of the sample condition by short $^2\text{D } ^1\text{H}$ – ^{15}N HSQC experiments.

Next we assigned backbone resonances of TTHA1718 in *E. coli* cells at 37 °C using six 3D triple-resonance NMR spectra. The short lifetimes of the in-cell NMR samples necessitated a large reduction in measurement times from the 1–2 days conventionally used for each 3D experiment. We therefore prepared a fresh sample for each experiment and applied a nonlinear sampling scheme for the indirectly acquired dimensions^{16–18}, which has been shown in combination with maximum-entropy processing to provide considerable time savings (Fig. 2a). With this technique the duration of each 3D experiment was reduced to 2–3 h. To ensure that only data of intact samples were acquired, each 3D experiment was repeated several times interleaved with monitoring of the sample condition by a short $^2\text{D } ^1\text{H}$ – ^{15}N HSQC experiment. These 3D data were combined to generate a new data set with improved signal-to-noise ratio until the 2D spectra showed marked changes (Fig. 2b). Typically, two 3D data sets were combined. All the expected backbone resonances were assigned except for Cys 11, Asn 12 and His 13 in the predicted metal-binding loop (Supplementary Fig. 2a, b). For comparison, the backbone resonances were also assigned for the purified TTHA1718 protein *in vitro*, in which Cys 11 was also assigned. A comparison of the chemical shifts under both conditions

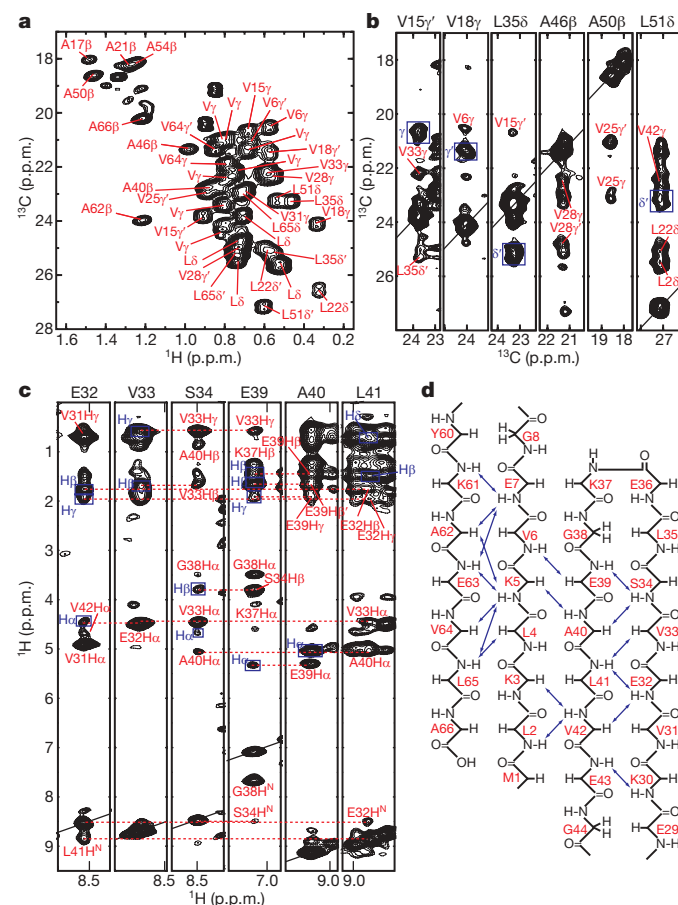


Figure 3 | Collection of NOE-derived distance restraints in TTHA1718 in living *E. coli* cells. **a**, Methyl region of the ^1H – ^{13}C heteronuclear multiple-quantum coherence (HMQC) spectrum of the selectively methyl-protonated sample. Assignments of the methyl groups of Ala, Leu and Val residues are indicated, if available. **b**, ^{13}C – ^{13}C cross-sections corresponding to the ^1H frequencies of representative methyl groups extracted from the $^3\text{D } ^{13}\text{C}/^{13}\text{C}$ -separated HMQC-NOE-HMQC spectrum. The cross-peaks due to interresidual NOEs are assigned in red. Intraresidual NOEs are indicated by blue boxes and annotated. **c**, ^1H – ^1H cross-sections corresponding to the ^{15}N frequencies of selected backbone amide groups extracted from the $^3\text{D } ^{15}\text{N}$ -separated NOESY-HSQC spectrum. The inter- and intraresidue NOEs are indicated as in **b**. **d**, Topology diagram of the β -sheet structure in TTHA1718. Interstrand backbone NOEs are depicted as double-headed arrows.

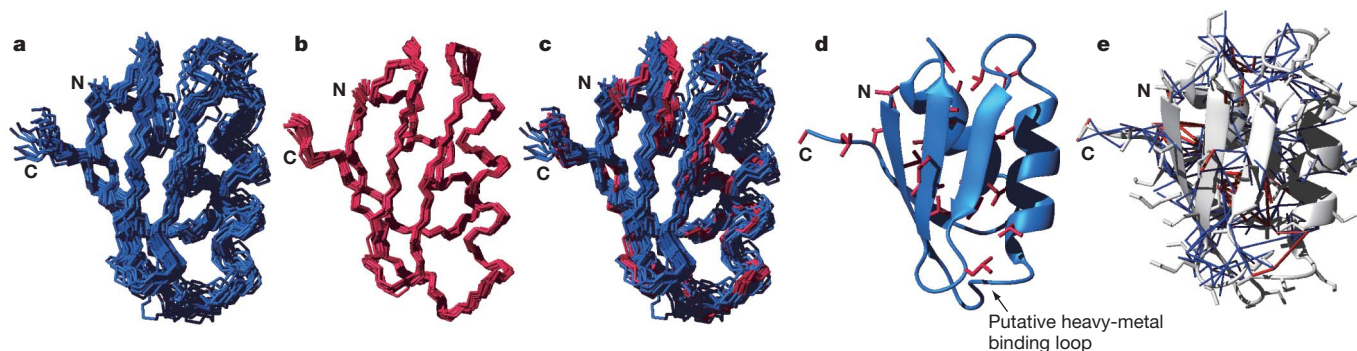


Figure 4 | NMR solution structure of TTHA1718 in living *E. coli* cells. **a**, A superposition of the 20 final structures of TTHA1718 in living *E. coli* cells, showing the backbone (N, C α , C') atoms. **b**, A superposition of the 20 final structures of purified TTHA1718 *in vitro*. **c**, A comparison of TTHA1718 structures in living *E. coli* cells and *in vitro*. The best fit superposition of backbone (N, C α , C') atoms of the two conformational ensembles are shown

with the same colour code in **a** and **b**. **d**, Secondary structure of TTHA1718 in living *E. coli* cells. The side chains of Ala, Leu and Val residues, the methyl groups of which were labelled with $^1\text{H}/^{13}\text{C}$, are shown in red. **e**, Distance restraints derived from methyl-group-correlated and other NOEs are represented in the ribbon model with red and blue lines, respectively.

shows the largest differences for residues adjacent to the region with missing ^1H – ^{15}N correlation peaks in the in-cell spectrum (Supplementary Fig. 2d). The chemical shifts of 86% of H α , 71% of H β , and 34% of the other aliphatic $^1\text{H}/^{13}\text{C}$ side-chain resonances of TTHA1718 in *E. coli* cells were also determined (Supplementary Fig. 2c).

Assignments to side-chain methyl groups have a large effect on the structure calculation¹⁹. Methyl protonation at methionine residues has previously been used as probes in in-cell NMR²⁰. We performed NMR measurements of TTHA1718 in *E. coli* cells selectively $^1\text{H}/^{13}\text{C}$ -labelled at methyl groups²¹ of Ala, Leu and Val (Supplementary Fig. 3), and assigned 31 out of 40 (78%) of their side-chain methyl ^1H and ^{13}C resonances (Fig. 3a). Overall, 148 NOEs involving methyl groups could be assigned (Fig. 3b) in the 3D nuclear Overhauser enhancement spectroscopy (NOESY) spectra and used in the structure calculation, including 69 out of all 89 long-range NOEs. Three-dimensional ^{15}N -separated and 3D ^{13}C -separated NOESY spectra measured on uniformly labelled *E. coli* samples yielded further NOE-derived distance restraints (Fig. 3c, d). In contrast to ^{15}N -labelling, uniform ^{13}C -labelling gave rise to a considerable number of 'background' cross-peaks (Supplementary Fig. 4)²⁰. NOE cross-peaks in the 3D ^{13}C -separated NOESY were therefore carefully analysed and only selected if they were highly likely to correlate TTHA1718 resonances.

The 3D structure of TTHA1718 in *E. coli* cells was calculated with the program CYANA²² on the basis of NOE distance restraints, backbone torsion angle restraints, and restraints for hydrogen bonds (Supplementary Table 1). The resulting structure is well-converged with a backbone root mean squared deviation (r.m.s.d.) of 0.96 Å to the mean coordinates (Fig. 4a), and is similar to the structure that was determined independently *in vitro* from a purified sample (Fig. 4b and Supplementary Table 1). The backbone r.m.s.d. between the in-cell and *in vitro* structures is 1.16 Å (Fig. 4c). Slight structural differences were found in the more dynamic loop regions, which may be due to the effects of viscosity and molecular crowding in the cytosol. In the putative heavy-metal binding loop, where the structural differences are corroborated by chemical shift differences, interactions with metal ions in the *E. coli* cytosol may affect the conformation of the region. Indeed, the C11S/C14S and C11A/C14A mutants, which lack metal-binding activity, showed almost identical ^1H – ^{15}N HSQC spectra in *E. coli* cells even when the cells were loaded with excess metal ions such that for the wild-type protein, the Thr 10, Cys 14 and Val 15 resonances disappear and Met 9 experiences further chemical shift changes (Supplementary Figs 5–7).

Our results demonstrate that high resolution 3D structures of proteins can be determined in the cytoplasm of bacterial cells. Rapid data collection using nonlinear sampling and selective protonation at methyl groups (Fig. 4d, e) to enable the identification of

unambiguous long-range NOE interactions was crucial for the success of this approach (Supplementary Fig. 8 and Supplementary Table 1).

The TTHA1718 protein was highly expressed in *E. coli* (3–4 mM in the NMR samples). Structural studies of less abundant proteins by in-cell NMR may however also be feasible, because 74% and 61% of the NOE cross-peaks used for the structure calculation could be still observed from in-cell NMR samples in which TTHA1718 expression level was controlled to approximately 1.2–1.5 and 0.6–0.8 mM ranges, respectively (Supplementary Fig. 9).

We have also tested the applicability of in-cell NMR to the structure determination of larger proteins by expressing rat calmodulin (17 kDa) in *E. coli* (concentration ~1.0–1.5 mM). Sequential backbone resonance connectivities and sequential H $^{\text{N}}$ –H $^{\text{N}}$ NOEs could be identified in the 3D spectra (Supplementary Fig. 10), suggesting that structural analysis of this size of protein in *E. coli* cells will be feasible. In-cell NMR structure determination in eukaryotic cells should also be possible, for example in *Xenopus laevis* oocytes, in which proteins can be introduced at up to ~0.7 mM intracellular concentration¹⁰, and here techniques developed for larger systems *in vitro*, for example, stereo-array isotope labelling²³ may be applied.

It has been proposed that the viscosity of the *E. coli* cytoplasm should be too high, and the tumbling of globular proteins therefore too slow to permit their NMR signals to be observed²⁴. Apparently, this is not the case for TTHA1718 and calmodulin (see Supplementary Fig. 11 and Supplementary Table 2 for ^{15}N relaxation parameters of TTHA1718). However, it is likely that for some proteins, their interactions with other cellular components will markedly affect their rotational correlation times to the point that they will be effectively invisible to solution state NMR techniques. In-cell structure determination applied to proteins that adopt more than one extensively populated conformation, for example due to binding to multiple ligands, will pose additional problems.

Our results open new avenues for the investigation of protein conformations at atomic resolution and how they change in response to biological events in living environments. In particular, this approach provides the tools that will permit the effects of molecular crowding in the cytosol, the conformations of proteins that are intrinsically disordered *in vitro*, and the 3D structures of proteins that are otherwise unstable and difficult to purify to be investigated in living cells.

METHODS SUMMARY

E. coli cells harbouring the plasmid encoding the *T. thermophilus* HB8 TTHA1718 gene were first grown in unlabelled LB medium. Protein production was induced after transfer of the bacteria into stable isotope-labelled medium (100 ml). The collected cells were placed as ~60% slurry into NMR tubes.

Sample stability was monitored repeatedly by 2D ^1H - ^{15}N HSQC spectra followed by plating colony tests. Samples for *in vitro* NMR experiments were purified by butyl-TOYOPEARL column chromatography. Sample preparation of TTHA1718 mutants and rat calmodulin was performed with essentially identical protocols. All NMR spectra were obtained at 37 °C using a Bruker Avance 600 spectrometer with Cryoprobe, processed using the AZARA 2.7 software (W. Boucher, www.bio.cam.ac.uk/azara), and analysed using the ANSIG 3.3 software²⁵. NMR resonances of TTHA1718 in *E. coli* cells were assigned by analysing nine 3D triple-resonance NMR spectra. Intraresidue and sequential NOEs involving methyl protons were also used. Four 3D NOESY spectra were analysed for the collection of NOE-derived distance restraints. For all 3D NMR experiments, a nonlinear sampling scheme^{16–18} was used for the indirectly observed dimensions to reduce experimental time. The 2D maximum-entropy method²⁶ was used for processing nonlinearly sampled dimensions. NMR analyses of purified TTHA1718 were performed using conventional approaches. TTHA1718 structures were calculated with the program CYANA using automated NOE assignment²⁷ and torsion angle dynamics²². Backbone torsion angle restraints from the program TALOS²⁸ were added to the input. Restraints were included for hydrogen bonds in regular secondary structure elements that were strongly supported by NOEs. The 20 final structures were embedded in a water shell and energy-minimised against the AMBER force field²⁹ with the program OPALp³⁰ in the presence of the experimental restraints.

Full Methods and any associated references are available in the online version of the paper at www.nature.com/nature.

Received 18 September 2008; accepted 22 January 2009.

- Serber, Z. *et al.* High-resolution macromolecular NMR spectroscopy inside living cells. *J. Am. Chem. Soc.* **123**, 2446–2447 (2001).
- Serber, Z., Corsini, L., Durst, F. & Dötsch, V. In-cell NMR spectroscopy. *Methods Enzymol.* **394**, 17–41 (2005).
- Serber, Z. *et al.* Investigating macromolecules inside cultured and injected cells by in-cell NMR spectroscopy. *Nature Protocols* **1**, 2701–2709 (2006).
- Reckel, S., Hänsel, R., Löhr, F. & Dötsch, V. In-cell NMR spectroscopy. *Prog. Nucl. Magn. Reson. Spectrosc.* **51**, 91–101 (2007).
- Selenko, P. & Wagner, G. Looking into live cells with in-cell NMR spectroscopy. *J. Struct. Biol.* **158**, 244–253 (2007).
- Ellis, R. J. Macromolecular crowding: obvious but underappreciated. *Trends Biochem. Sci.* **26**, 597–604 (2001).
- Burz, D. S., Dutta, K., Cowburn, D. & Shekhtman, A. Mapping structural interactions using in-cell NMR spectroscopy (STINT-NMR). *Nature Methods* **3**, 91–93 (2006).
- McNulty, B. C., Young, G. B. & Pielak, G. J. Macromolecular crowding in the *Escherichia coli* periplasm maintains α -synuclein disorder. *J. Mol. Biol.* **355**, 893–897 (2006).
- Dedmon, M. M., Patel, C. N., Young, G. B. & Pielak, G. J. FlgM gains structure in living cells. *Proc. Natl Acad. Sci. USA* **99**, 12681–12684 (2002).
- Selenko, P., Serber, Z., Gade, B., Ruderman, J. & Wagner, G. Quantitative NMR analysis of the protein G B1 domain in *Xenopus laevis* egg extracts and intact oocytes. *Proc. Natl Acad. Sci. USA* **103**, 11904–11909 (2006).
- Sakai, T. *et al.* In-cell NMR spectroscopy of proteins inside *Xenopus laevis* oocytes. *J. Biomol. NMR* **36**, 179–188 (2006).
- Inomata, K. *et al.* High-resolution multi-dimensional NMR spectroscopy of proteins in living human cells. *Nature* doi:10.1038/nature07839 (this issue).
- Wüthrich, K. *NMR of Proteins and Nucleic Acids* (Wiley, 1986).
- Reardon, P. N. & Spicer, L. D. Multidimensional NMR spectroscopy for protein characterization and assignment inside cells. *J. Am. Chem. Soc.* **127**, 10848–10849 (2005).
- Serber, Z., Ledwidge, R., Miller, S. M. & Dötsch, V. Evaluation of parameters critical to observing proteins inside living *Escherichia coli* by in-cell NMR spectroscopy. *J. Am. Chem. Soc.* **123**, 8895–8901 (2001).
- Barna, J. C. J., Laue, E. D., Mayger, M. R., Skilling, J. & Worrall, S. J. P. Exponential sampling, an alternative method for sampling in two-dimensional NMR experiments. *J. Magn. Reson.* **73**, 69–77 (1987).
- Schmieder, P., Stern, A. S., Wagner, G. & Hoch, J. C. Improved resolution in triple-resonance spectra by nonlinear sampling in the constant-time domain. *J. Biomol. NMR* **4**, 483–490 (1994).
- Rovnyak, D. *et al.* Accelerated acquisition of high resolution triple-resonance spectra using non-uniform sampling and maximum entropy reconstruction. *J. Magn. Reson.* **170**, 15–21 (2004).
- Mueller, G. A. *et al.* Global folds of proteins with low densities of NOEs using residual dipolar couplings: application to the 370-residue maltodextrin-binding protein. *J. Mol. Biol.* **300**, 197–212 (2000).
- Serber, Z. *et al.* Methyl groups as probes for proteins and complexes in in-cell NMR experiments. *J. Am. Chem. Soc.* **126**, 7119–7125 (2004).
- Rosen, M. K. *et al.* Selective methyl group protonation of perdeuterated proteins. *J. Mol. Biol.* **263**, 627–636 (1996).
- Güntert, P., Mumenthaler, C. & Wüthrich, K. Torsion angle dynamics for NMR structure calculation with the new program DYANA. *J. Mol. Biol.* **273**, 283–298 (1997).
- Kainosho, M. *et al.* Optimal isotope labelling for NMR protein structure determinations. *Nature* **440**, 52–57 (2006).
- Li, C. *et al.* Differential dynamical effects of macromolecular crowding on an intrinsically disordered protein and a globular protein: implications for in-cell NMR spectroscopy. *J. Am. Chem. Soc.* **130**, 6310–6311 (2008).
- Kraulis, P. J., Domaille, P. J., Campbell-Burk, S. L., Van Aken, T. & Laue, E. D. Solution structure and dynamics of Ras p21-GDP determined by heteronuclear three- and four-dimensional NMR spectroscopy. *Biochemistry* **33**, 3515–3531 (1994).
- Laue, E. D., Mayger, M. R., Skilling, J. & Staunton, J. Reconstruction of phase sensitive 2D NMR spectra by maximum entropy. *J. Magn. Reson.* **68**, 14–29 (1986).
- Herrmann, T., Güntert, P. & Wüthrich, K. Protein NMR structure determination with automated NOE assignment using the new software CANDID and the torsion angle dynamics algorithm DYANA. *J. Mol. Biol.* **319**, 209–227 (2002).
- Cornilescu, G., Delaglio, F. & Bax, A. Protein backbone angle restraints from searching a database for chemical shift and sequence homology. *J. Biomol. NMR* **13**, 289–302 (1999).
- Cornell, W. D. *et al.* A second generation force field for the simulation of proteins, nucleic acids, and organic molecules. *J. Am. Chem. Soc.* **117**, 5179–5197 (1995).
- Koradi, R., Billeter, M. & Güntert, P. Point-centered domain decomposition for parallel molecular dynamics simulation. *Comput. Phys. Commun.* **124**, 139–147 (2000).

Supplementary Information is linked to the online version of the paper at www.nature.com/nature.

Acknowledgements The authors thank S. Kuramitsu for providing the plasmid encoding TTHA1718, and D. Nietlispach for setting up 3D NMR experiments with nonlinear sampling schemes and ^{15}N relaxation experiments, T. Anzai for assistance with NMR measurements, and H. Koyama and A. Iwasaki for sample preparations. This work was supported in part by CREST, Japan Science and Technology Agency (JST), the Molecular Ensemble Program, RIKEN, Grants-in-Aid for Scientific Research of Priority Areas from the Japanese Ministry of Education, Sports, Culture, Science, and Technology on 'Molecular Soft Interactions Regulating Membrane Interface of Biological Systems' and 'Molecular Science for Supra Functional Systems – Development of Advanced Methods for Exploring Elementary Process', and by the Volkswagen Foundation.

Author Contributions B.O.S., M.S., P.G. and Y.I. designed the research and wrote the manuscript. D.S., A.S. and T.I. conducted the research including sample preparation, data acquisition, resonance assignment and structure calculation. M.M. and M.W. helped with NMR measurements. M.M. prepared TTHA1718 mutants. J.H. and T.H. measured NMR data on TTHA1718 mutants and ^{15}N -relaxation experiments. N.H. provided the expression vector for calmodulin. M.Y. measured NMR data on calmodulin in living *E. coli* cells. T.M. helped during the preparation and characterisation of TTHA1718.

Author Information Atomic coordinates of the structures of TTHA1718 in *E. coli* cells and *in vitro* have been deposited in the Protein Data Bank under accession codes 2ROG and 2ROE, respectively. Chemical shifts have been deposited in the BioMagResBank under accession numbers 11037 and 11035. Reprints and permissions information is available at www.nature.com/reprints. Correspondence and requests for materials should be addressed to Y.I. (ito-yutaka@tmu.ac.jp).

METHODS

Sample preparation. The expression plasmid encoding the *T. thermophilus* HB8 TTHA1718 gene was obtained from the 'Whole-Cell Project of a Model Organism, *T. thermophilus* HB8' (<http://www.thermus.org>). In-cell NMR samples were prepared as follows. JM109 (DE3) *E. coli* cells harbouring the TTHA1718 expression plasmid were first grown in unlabelled LB medium. The production of uniformly $^{13}\text{C}/^{15}\text{N}$ -labelled TTHA1718 was induced by the addition of isopropyl thio- β -D-thiogalactoside to a final concentration of 0.5 mM after transfer of the bacteria into M9 minimal medium (100 ml) containing 2 g l^{-1} [$\text{U-}^{13}\text{C}$]-glucose and 1 g l^{-1} $^{15}\text{NH}_4\text{Cl}$. For the production of TTHA1718 samples with selectively protonated side-chain methyl groups of Ala, Leu and Val residues in a uniform ^2H -background, protein expression was induced in 100% D_2O M9 medium containing 2 g l^{-1} unlabelled glucose, 1 g l^{-1} $^{15}\text{NH}_4\text{Cl}$, 100 mg l^{-1} [$3\text{-}^{13}\text{C}$]-alanine and 100 mg l^{-1} [$\text{U-}^{13}\text{C}$, $3\text{-}^2\text{H}$]- α -ketoisovalerate. For Val/Leu selective methyl protonation, [$3\text{-}^{13}\text{C}$]-alanine was excluded from the medium, whereas unlabelled leucine (100 mg l^{-1}) was added for Ala/Val selective protonation. The cells were collected by gentle centrifugation and placed as $\sim 60\%$ slurry with M9 medium containing 10% D_2O into NMR tubes. The concentration of TTHA1718 in *E. coli* samples was estimated by comparing the density of the Coomassie-stained bands in SDS-PAGE gels with those of proteins with similar molecular size and known concentration. The stability of TTHA1718 *E. coli* samples was monitored repeatedly by 2D ^1H - ^{15}N HSQC spectra followed by plating colony tests. The localization of TTHA1718 in *E. coli* cells was first predicted from its amino acid sequence by PSORTb v.2.0 (refs 31, 32) (<http://www.psorth.org/psorth/>) and SignalP 3.0 (refs 33, 34) (<http://www.cbs.dtu.dk/services/SignalP/>). The localization of overexpressed TTHA1718 was then analysed by measuring 2D ^1H - ^{15}N HSQC spectra of spheroplasts and periplasmic extract, which were fractionated from TTHA1718-expressing ^{15}N -labelled cells by lysozyme-EDTA treatment using the conditions described previously³⁵. Spheroplast formation was monitored by light microscopy.

TTHA1718 proteins for *in vitro* NMR experiment was purified by butyl-TOYOPEARL column chromatography after cell lysis, by sonication and high temperature (70°C) treatment for 10 min. The final TTHA1718 fractions were concentrated and dissolved in M9 medium containing 10% D_2O for NMR experiments.

Two cysteine residues (C11 and C14) were predicted to be responsible for metal binding activity on the basis of analysis of multiple sequence alignment with previously characterized homologous proteins. Two double mutations (C11S/C14S and C11A/C14A) were therefore introduced by site-directed mutagenesis to disrupt metal binding.

Rat calmodulin in-cell NMR samples were produced similarly from the expression plasmid³⁶.

NMR spectroscopy. NMR experiments were performed at 37°C probe temperature in a triple-resonance cryoprobe fitted with a z -axis pulsed field gradient coil, using a Bruker Avance 600 MHz spectrometer. NMR spectra were processed using the AZARA 2.7 software (W. Boucher, <http://www.bio.cam.ac.uk/azara/>), and analysed using an OpenGL version of the ANSIG 3.3 software^{25,37}.

Backbone $^1\text{H}^{\text{N}}$, ^{15}N , $^{13}\text{C}\alpha$, $^{13}\text{C}'$, and side-chain $^{13}\text{C}\beta$ resonance assignments of TTHA1718 in living *E. coli* cells were performed by analysing six 3D triple-resonance NMR spectra: HNCA, HN(CO)CA, CBCA(CO)NH, CBCANH, HNCO and HN(CA)CO. Three-dimensional HBHA(CBCACO)NH, H(CCCO)NH and (H)CC(CO)NH experiments were performed for side-chain ^1H and ^{13}C resonance assignments. Longitudinal (T_1) and transverse (T_2) ^{15}N relaxation parameters of TTHA1718 in living *E. coli* cells were obtained by

measuring 1D ^{15}N -edited ^{15}N T_1 or T_2 relaxation experiments on lysine-selectively ^{15}N -labelled samples. Intraresidue and sequential NOEs involving methyl protons were also used for the assignment of Ala/Leu/Val methyl groups. ^1H - ^{13}C HMQC spectra of in-cell NMR samples with three different methyl-selective labelling patterns, Ala/Val, Leu/Val, and Ala/Leu/Val, were used for amino acid classification of methyl ^1H - ^{13}C correlation cross-peaks. For the collection of NOE-derived distance restraints, 3D ^{15}N -separated and ^{13}C -separated NOESY-HSQC spectra were measured on uniformly labelled in-cell NMR samples. In addition, 3D ^{13}C -separated NOESY-HSQC and 3D $^{13}\text{C}/^{13}\text{C}$ -separated HMQC-NOESY-HMQC spectra were measured on Ala/Leu/Val-methyl-selectively protonated samples. For all 3D NMR experiments, a non-linear sampling scheme^{16–18} was used for the indirectly observed dimensions to reduce experimental time. In brief, approximately one-quarter of the points were selected in a pseudo-random fashion from the conventional regularly spaced grid of t_1 , t_2 points. The 2D maximum-entropy method²⁶ was used for processing nonlinearly sampled dimensions.

Backbone and side-chain resonances of purified TTHA1718 were assigned by analysis of seven 3D triple-resonance experiments: CBCA(CO)NH, CBCANH, HNCO, HN(CA)CO, H(CCCO)NH, (H)CC(CO)NH and HCCH-TOCSY, and almost completely assigned. NOE-derived distance restraints were obtained by analysing 3D ^{15}N -separated and ^{13}C -separated NOESY-HSQC spectra.

Structure calculation. TTHA1718 structures were calculated with the program CYANA³⁸ version 3.0 using automated NOE assignment²⁷ and torsion angle dynamics for the structure calculation²², which was started from 100 conformers with random torsion angle values. The standard CYANA simulated annealing schedule was applied with 10,000 torsion angle dynamics steps. Backbone torsion angle restraints obtained from chemical shifts with the program TALOS²⁸ were added to the input for CYANA. Distance restraints for hydrogen bonds were introduced for the particular positions in the β -sheet region where the existences of hydrogen bonds were strongly suggested by inter-strand NOEs. Some additional 'CYANA-estimated' hydrogen bond restraints were included during the calculation process. The 20 conformers with the lowest final CYANA target function values were embedded in a water shell of 8 Å thickness and energy-minimised against the AMBER force field²⁹ with the program OPALP³⁰ in the presence of the experimental restraints.

- Gardy, J. L. *et al.* PSORT-B: Improving protein subcellular localization prediction for gram-negative bacteria. *Nucleic Acids Res.* **31**, 3613–3617 (2003).
- Gardy, J. L. *et al.* PSORTb v.2.0: expanded prediction of bacterial protein subcellular localization and insights gained from comparative proteome analysis. *Bioinformatics* **21**, 617–623 (2005).
- Nielsen, H., Engelbrecht, J., Brunak, S. & von Heijne, G. Identification of prokaryotic and eukaryotic signal peptides and prediction of their cleavage sites. *Protein Eng.* **10**, 1–6 (1997).
- Bendtsen, J. D., Nielsen, H., von Heijne, G. & Brunak, S. Improved prediction of signal peptides: SignalP 3.0. *J. Mol. Biol.* **340**, 783–795 (2004).
- Thorntenson, Y. R., Zhang, Y., Olson, P. S. & Mascarenhas, D. Leaderless polypeptides efficiently extracted from whole cells by osmotic shock. *J. Bacteriol.* **179**, 5333–5339 (1997).
- Hayashi, N., Matsubara, M., Takasaki, A., Titani, K. & Taniguchi, H. An expression system of rat calmodulin using T7 phage promoter in *Escherichia coli*. *Protein Expr. Purif.* **12**, 25–28 (1998).
- Kraulis, P. J. ANSIG: a program for the assignment of protein ^1H 2D NMR spectra by interactive computer graphics. *J. Magn. Reson.* **84**, 627–633 (1989).
- Güntert, P. Automated NMR protein structure calculation. *Prog. Nucl. Magn. Reson. Spectrosc.* **43**, 105–125 (2003).

LETTERS

High-resolution multi-dimensional NMR spectroscopy of proteins in human cells

Kohsuke Inomata^{1,2}, Ayako Ohno¹, Hidehito Tochio^{1,2}, Shin Isogai¹, Takeshi Tenno^{2,4}, Ikuhiko Nakase⁵, Toshihide Takeuchi⁵, Shiroh Futaki^{3,5}, Yutaka Ito^{2,6}, Hidekazu Hiroaki^{2,4} & Masahiro Shirakawa^{1,2,7}

In-cell NMR is an isotope-aided multi-dimensional NMR technique that enables observations of conformations and functions of proteins in living cells at the atomic level¹. This method has been successfully applied to proteins overexpressed in bacteria, providing information on protein–ligand interactions² and conformations^{3,4}. However, the application of in-cell NMR to eukaryotic cells has been limited to *Xenopus laevis* oocytes^{5–7}. Wider application of the technique is hampered by inefficient delivery of isotope-labelled proteins into eukaryote somatic cells. Here we describe a method to obtain high-resolution two-dimensional (2D) heteronuclear NMR spectra of proteins inside living human cells. Proteins were delivered to the cytosol by the pyrenebutyrate-mediated action of cell-penetrating peptides⁸ linked covalently to the proteins. The proteins were subsequently released from cell-penetrating peptides by endogenous enzymatic activity or by autonomous reductive cleavage. The heteronuclear 2D spectra of three different proteins inside human cells demonstrate the broad application of this technique to studying interactions and protein processing. The in-cell NMR spectra of FKBP12 (also known as FKBP1A) show the formation of specific complexes between the protein and extracellularly administered immunosuppressants, demonstrating the utility of this technique in drug screening programs. Moreover, in-cell NMR spectroscopy demonstrates that ubiquitin has much higher hydrogen exchange rates in the intracellular environment, possibly due to multiple interactions with endogenous proteins.

We have established a method to observe in-cell NMR spectra of ¹⁵N-labelled proteins, which are delivered to cells by cell-penetrating peptides (CPPs)^{9–11}. First, the CPP sequence of Tat from HIV-1 (ref. 12) (CPP_{Tat}: 47-YGRKKRRQRRR-57) was fused to the carboxy terminus of a human ubiquitin derivative containing alanine substitutions at Leu 8, Ile 44 and Val 70 (designated Ub-3A). The fusion protein Ub-3A–CPP_{Tat} (Fig. 1a) was uniformly labelled with ¹⁵N, and then incubated with human HeLa cells in the presence of pyrenebutyrate (1-pyrenebutyric acid), which mediates the direct translocation of CPP-linked proteins into the cytosol⁸. The 2D ¹H–¹⁵N correlation spectrum of the cells gave well-resolved cross-peaks, showing a pattern typical of a stably folded and homogeneously dispersed protein (Fig. 1a). Comparison with the reference *in vitro* spectrum (Fig. 1b) showed that the positions of most cross-peaks were well preserved in the in-cell spectrum. However, an intense signal was observed at a position corresponding to the C-terminal Gly 76 of mature ubiquitin in the in-cell spectrum, but not in the *in vitro* spectrum. Conversely, the cross-peak of the C-terminal residue of CPP_{Tat} was missing in the in-cell spectrum. This observation suggested that the Ub-3A–CPP_{Tat} fusion protein was cleaved between Gly 76 and Asp 77—presumably by a group of endogenous ubiquitin-specific C-terminal proteases (DUBs)¹³—and that the clipped CPP peptide was not observed in the in-cell NMR spectrum (Fig. 1a and Supplementary Fig. 1). Cleavage of Ub-3A–CPP_{Tat} in the cells was further confirmed by electrophoretic analysis of transduced fluorescently labelled protein (Supplementary Fig. 1c). Because DUBs are localized in the cytosolic

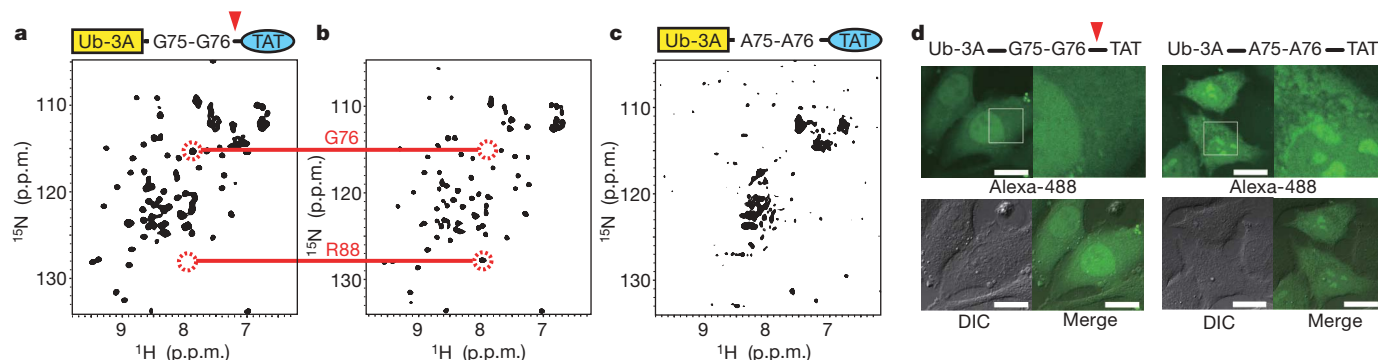


Figure 1 | In-cell NMR spectra and cellular distribution of transduced ubiquitin derivative. **a**, Spectrum of Ub-3A in HeLa cells. The cross-peak of the C-terminal Gly 76 is indicated. **b**, *In vitro* reference spectrum of the ¹⁵N Ub-3A–CPP_{Tat} fusion. The cross-peak of arginine at the C-terminal end of CPP_{Tat} (Arg 88) is indicated. **c**, Spectrum of HeLa cells treated with ¹⁵N Ub-3A–G75A/G76A–CPP_{Tat}. **d**, Distribution of transduced Alexa-488-labelled

Ub-3A–CPP_{Tat} and Ub-3A–G75A/G76A–CPP_{Tat} in HeLa cells observed by confocal laser-scanning microscopy. DIC, differential interference contrast. Scale bars, 20 μm. In **a** and **c**, the constructs used for intracellular transduction are schematically shown above the spectrum. The DUB cleavage site is indicated by a red triangle.

¹Department of Molecular Engineering, Graduate School of Engineering, Kyoto University, Nishikyo-Ku, Kyoto 615-8510, Japan. ²CREST, and ³SORST, JST, 4-1-8 Honcho, Kawaguchi, Saitama 332-0012, Japan. ⁴Division of Structural Biology, Graduate School of Medicine, Kobe University, 7-5-1, Kusunoki-cho Chuo-ku, Kobe, Hyogo 650-0017, Japan. ⁵Institute for Chemical Research, Kyoto University, Uji, Kyoto 611-0011, Japan. ⁶Department of Chemistry, Tokyo Metropolitan University, 1-1 Minami-Osawa, Hachioji, Tokyo 192-0397, Japan. ⁷RIKEN, Yokohama Institute, 1-7-22, Suehirocho, Tsurumi, Yokohama 230-0045, Japan.

space¹³, DUB-mediated cleavage suggested that pyrenebutyrate/CPP_{Tat}-treatment delivered Ub-3A into the cytosol.

The concentration of transduced ¹⁵N-labelled protein in the NMR sample was of the order of 20–30 μM, as estimated from the NMR signal intensities of the in-cell spectrum and the spectrum of Ub-3A recovered in the lysate (Supplementary Fig. 2b, c). The estimated concentration of endogenous ubiquitin is 13 μM, assuming that 1 × 10⁷ cells are contained in 200 μl of the NMR sample and that each cell contains 1.5 × 10⁸ ubiquitin molecules¹⁴. Leakage of ¹⁵N-labelled proteins from the cells during NMR measurement was negligible, as assessed by the 1D spectrum of extracellular fluid taken from the NMR sample (Supplementary Fig. 2a). Cell viability and the integrity of the plasma membranes were assessed by staining with 0.2% (w/v) trypan blue after the completion of each NMR experiment¹⁵. In each case of in-cell NMR experiments shown in this paper, we found that more than 90% of cells were resistant to trypan blue uptake. This high level of cell viability and membrane integrity is consistent with the reported low toxicity of pyrenebutyrate/CPP_{Tat} treatment⁸.

Having established that Ub-3A–CPP_{Tat} undergoes intracellular cleavage, we questioned whether detachment of Ub-3A from CPP_{Tat} is crucial for observing in-cell NMR spectra. We substituted the sequence G75–G76 of Ub-3A–CPP_{Tat} with two alanines to prevent intracellular cleavage by DUBs. Indeed, Ub-3A–G75A/G76A–CPP_{Tat} was resistant to cleavage in cells (Supplementary Fig. 1c). The ¹H–¹⁵N correlation spectrum of cells incubated with this uncleavable protein showed a pattern typical of an aggregated protein, with several overlapping signals (Fig. 1c), indicating that liberation of ubiquitin from CPP is essential for observing well-resolved in-cell NMR spectra.

CPPs are known to show binding to acidic membrane and cytosolic components¹¹. Thus, it seemed likely that the uncleaved Ub-3A–G75A/G76A–CPP_{Tat} aggregated with the inner plasma membrane or other intracellular components after delivery into the cytosol. To confirm this, we labelled the cleavable Ub-3A–CPP_{Tat} and uncleavable Ub-3A–G75A/G76A–CPP_{Tat} with the fluorescent probe Alexa-488, and observed their intracellular distribution by confocal laser-scanning microscopy. HeLa cells treated with Alexa-488-labelled Ub-3A–CPP_{Tat} showed a smooth and continuous distribution of the transduced protein throughout the cytosol and nucleus (Fig. 1d). This diffusion of internalized protein was observed in almost all cells. In contrast, treatment with the uncleavable Alexa-labelled Ub-3A–G75A/G76A–CPP_{Tat} resulted in an unsmooth and heterogeneous pattern of fluorescence in the cells, with intense staining of cytoplasmic components and nucleoli. Taken together, these results demonstrate that detachment from CPP seems to be required for both uniform distribution of the CPP-delivered proteins in the cytosol and the detection of high-resolution in-cell NMR spectra. Using

Ub-3A–CPP_{Tat}, we also obtained a spectrum of Ub-3A in monkey COS-7 cells, demonstrating the universality of this method (Supplementary Fig. 3).

To measure the in-cell NMR spectra of specific proteins, we used the method of linking CPPs to cargo proteins by means of disulphide bonds¹⁶. In the cytosol, CPP-conjugated proteins are subject to cleavage at disulphide bonds by autonomous reduction. The ¹H–¹⁵N correlation spectrum of HeLa cells treated with the B1 domain of streptococcal protein G (GB1) conjugated to CPP_{Tat} showed well-resolved signals, which could almost be superimposed on the corresponding signals in the reference *in vitro* spectrum (Fig. 2a, b). The same procedure also delivered Ub-3A into cells and gave a high-quality in-cell NMR spectrum (Fig. 2c). These results demonstrate that this method can be applied to various proteins.

The in-cell NMR experiments potentially provide a wealth of information on the conformation, dynamics and functions of proteins in the intracellular environment. The in-cell NMR spectrum of wild-type ubiquitin showed severe line-broadening effects: the intensities of most of the main-chain amide signals in the in-cell NMR spectrum (Supplementary Fig. 4) were markedly smaller than those in the spectrum of Ub-3A (Fig. 1a). In contrast, an intense signal was observed at a position corresponding to the C-terminal Gly 76 of mature ubiquitin in the in-cell spectrum of wild-type ubiquitin, as seen in Ub-3A, suggesting that the CPP was cleaved from Ub–CPP_{Tat} and that the transduced ubiquitin exists, at least partly, in a C-terminally unconjugated form in the cells. Because the mutation sites of Ub-3A (L8A, I44A and V70A) are located at the common binding interface of ubiquitin with ubiquitin-interacting proteins¹⁷, the observation that mutation leads to a large recovery of signal intensity suggests that the line broadening observed for wild-type ubiquitin is due to its interactions with endogenous proteins. The same effect of mutation on ubiquitin was previously observed in in-cell NMR experiments using *Xenopus* oocytes⁵.

In-cell NMR spectroscopy can also be applied to studying protein interactions with small compounds, such as screening drugs targeted to specific proteins. We measured the in-cell NMR spectrum of FKBP12, one of the targets of the immunosuppressants FK506 and rapamycin¹⁸ which are often used in organ transplantation. To introduce ¹⁵N-labelled FKBP12 into HeLa cells, we used another method¹³ to link the protein to a cleavable CPP, by constructing a CPP_{Tat}–Ub–FKBP12 fusion protein (Fig. 3a). The fusion protein was predicted to be cleaved at the C terminus of ubiquitin by endogenous DUBs¹³, thereby releasing FKBP12 into the cytosolic space. The ¹H–¹⁵N correlation experiment of HeLa cells treated with ¹⁵N-labelled CPP_{Tat}–Ub–FKBP12 provided an analysable high-resolution spectrum (Fig. 3a), which could be well superimposed on the reference *in vitro* spectrum (Fig. 3b), showing that the FKBP12 moiety of the fusion protein

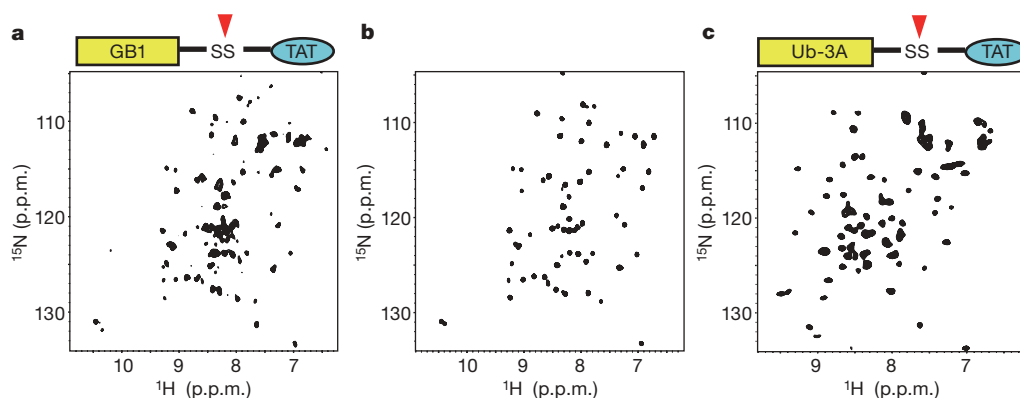


Figure 2 | In-cell spectra of proteins delivered by disulphide-linked CPP_{Tat}. **a**, In-cell ¹H–¹⁵N correlation spectrum of GB1. The construct used for intracellular transduction is schematically shown above the spectrum. CPP_{Tat} is conjugated at a cysteine introduced at the C-terminal end of GB1 via a disulphide bond. The red triangle indicates the reductive cleavage site.

b, *In vitro* reference spectrum of ¹⁵N-labelled GB1. **c**, In-cell spectrum of Ub-3A transduced with CPP_{Tat} linked through a disulphide bond. The construct used is schematically shown above the spectrum. CPP_{Tat} is conjugated at a cysteine mutated at the C-terminal Gly 76 residue of Ub-3A via a disulphide bond.

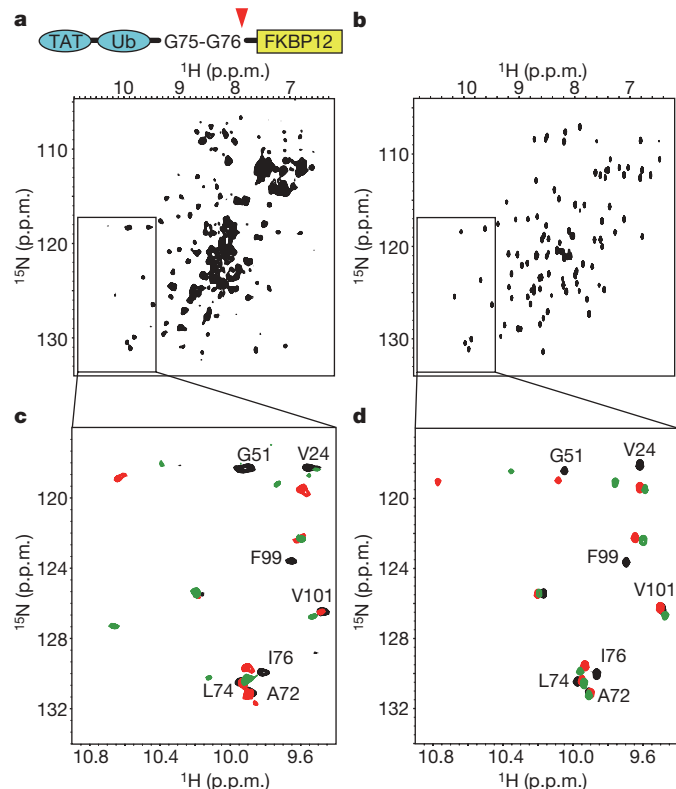


Figure 3 | In-cell NMR observation of specific complexes of FKBP12 with extracellularly administered immunosuppressants. **a, b,** Two-dimensional ^1H - ^{15}N correlation spectra of HeLa cells treated with ^{15}N -labelled $\text{CPP}_{\text{Tat}}\text{-Ub-FKBP12}$ (**a**) and FKBP12 *in vitro* (**b**). The construct used is schematically shown above the spectrum in **a**. The DUB cleavage site is indicated with a red triangle. **c,** Superposition of in-cell spectra of ^{15}N -labelled FKBP12 without (black) and with administration of either FK506 (red) or rapamycin (green). **d,** Superposition of *in vitro* spectra of ^{15}N -labelled FKBP12 in the absence (black) and presence of either FK506 (red) or rapamycin (green). To generate the in-cell NMR spectra shown in **a** and **c**, data from two (spectrum in **a** and spectrum shown in red in **c**) or three (spectrum shown in green in **c**) experiments, each with a measurement time of 3 h, were added and processed.

contributed to the well-resolved cross-peaks. In contrast, the contribution from the $\text{CPP}_{\text{Tat}}\text{-Ub}$ moiety seemed rather limited: a large proportion of strongly overlapping signals around the ^1H and ^{15}N chemical shifts of 7.8–8.5 and 119–125 p.p.m., respectively, were presumably attributable to the $\text{CPP}_{\text{Tat}}\text{-Ub}$ moiety (Fig. 3a), as similar overlapping signals were observed in the in-cell spectrum of the uncleavable $\text{Ub-3A-G75A/G76A-CPP}_{\text{Tat}}$ (Fig. 1c). From these observations, we concluded that FKBP12 was released from the $\text{CPP}_{\text{Tat}}\text{-Ub}$

moiety by DUB cleavage and gave analysable signals, whereas $\text{CPP}_{\text{Tat}}\text{-Ub}$ aggregated with cellular components through the CPP.

We then examined the effect of externally administered immunosuppressants on the in-cell NMR spectrum of FKBP12. When the cells were incubated with FK506 after the introduction of FKBP12, several cross-peaks in the in-cell spectrum of FKBP12 were markedly different from those observed in the absence of FK506 (Fig. 3c). The in-cell NMR spectrum of FK506-treated cells showed a similar pattern to the *in vitro* reference spectrum of FKBP12 complexed with FK506 (Fig. 3d). The administration of another immunosuppressant, rapamycin, to FKBP12-containing cells gave an in-cell NMR spectrum that was distinct from the in-cell spectrum after administration of FK506, but more similar to the *in vitro* spectrum of the FKBP12–rapamycin complex (Fig. 3c, d). These results indicated that exogenously applied FK506 and rapamycin autonomously entered the cells and formed specific complexes with FKBP12. This finding demonstrates that in-cell NMR spectroscopy can act as a powerful tool for screening drugs targeting specific intracellular proteins by, first, providing information about the efficiency of drug delivery to cells, and second, establishing whether the drug makes the same interactions with the target proteins, and exerts the same structural and functional effects, as identified from *in vitro* experiments.

Proteins in cells can have dynamic properties and folding stabilities that differ from those *in vitro*, due to both specific and nonspecific interactions with intracellular macromolecules and the cytoskeleton¹⁹. We analysed the folding stability of ubiquitin in the intracellular environment by performing a hydrogen exchange experiment coupled with in-cell NMR spectroscopy. Hydrogen exchange experiments can measure the equilibrium between folded and unfolded states of proteins, and thus reveal thermodynamic properties of proteins²⁰. We transduced $\text{Ub-CPP}_{\text{Tat}}$ in which the protected amide protons were replaced by deuterons, into HeLa cells and measured the ^1H - ^{15}N correlation spectrum of the cells to evaluate the hydrogen exchange of the main-chain amides of Val 5 and Leu 15, which are highly protected in the folded state and give well-isolated cross-peaks. We found that these amides were more highly exchanged to protons in the transduced protein than in the protein *in vitro* (Fig. 4a, b), raising the possibility that hydrogen exchange rates are increased in the intracellular environment.

To determine the exchange rates in the cells, we measured a series of spectra of ubiquitin recovered in lysates prepared by cell disruption at various times after protein transduction (Supplementary Fig. 5a). From the build-up curves of cross-peaks, the hydrogen exchange rates of all of the analysable protected amides, Val 5, Leu 15, Lys 27 and Ile 30, were approximately 15–22 times higher in cells than *in vitro* at pH 7.4 (Fig. 4c, d). Comparison of these higher exchange rates between wild-type ubiquitin and Ub-3A showed that mutation at the β -sheet surface caused a significant decrease in the amide hydrogen exchange rates (Fig. 4d and Supplementary Fig. 5b). Thus, the higher exchange rates in cells versus *in vitro* seem to be at least partly

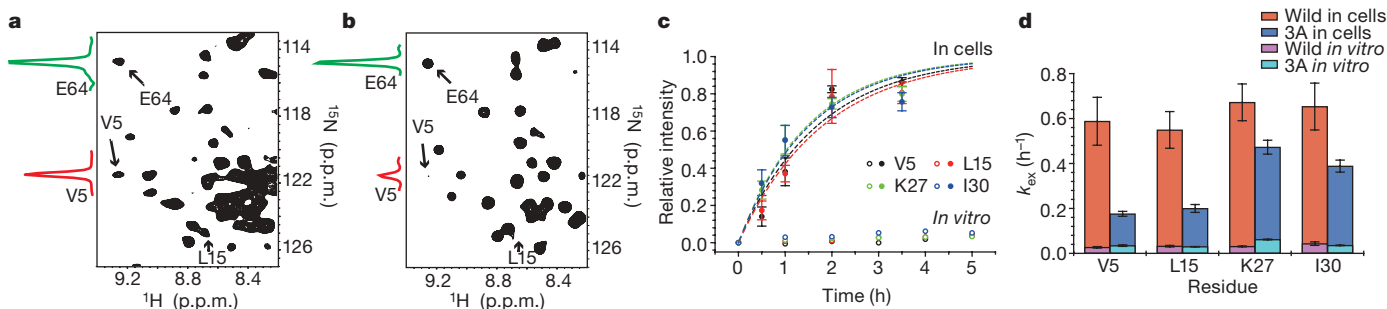


Figure 4 | Hydrogen exchange experiments. **a,** ^1H - ^{15}N correlation spectrum of HeLa cells treated with ^{15}N -labelled deuterated $\text{Ub-CPP}_{\text{Tat}}$. Data from two experiments, each with a measurement time of 3 h, were added. **b,** *In vitro* reference spectrum of ^{15}N -labelled deuterated $\text{Ub-CPP}_{\text{Tat}}$. Slices at ^1H frequencies of Val 5 (red) and Glu 64 (green) are also shown. The amide of Glu 64 is unprotected even in the folded state. **c,** Build-up of cross-

peaks of protected amides in the spectra of ubiquitin recovered in lysates collected at various times after protein transductions (filled symbols). Those *in vitro* at pH 7.4 are also shown (open symbols). For the lysates, averaged values over three independent trials are plotted with standard deviations. **d,** The hydrogen exchange rates (k_{ex}) in cells and *in vitro* at pH 7.4 of protected amides in ubiquitin and Ub-3A. Bars indicate standard errors.

due to interactions of ubiquitin with endogenous interacting proteins, as the mutation sites of Ub-3A are located at the common binding interface of ubiquitin with them¹⁷. Ubiquitin exhibits large structural heterogeneity both in itself and after binding to different partners²¹. Thus, binding to various proteins in cells might cause interconversion between different conformations of ubiquitin, which may destabilize folding and increase hydrogen exchange rates. Alternatively, some of these proteins may preferentially bind to less folded states of ubiquitin. The observation that Ub-3A still showed significantly higher exchange rates in cells than *in vitro* raises the possibility that nonspecific interactions with other macromolecules, the cytoskeleton and inner membranes may also decrease the folding stability of ubiquitin in cells (Fig. 4d). This result may challenge the general belief that the folding of proteins inside cells is stabilized through macromolecular crowding and macromolecular confinement effects¹⁹. A comprehensive analysis will be required to determine the mechanism and generality of the observed intracellular increase in hydrogen exchange rate by examining various proteins and cell types in the future.

In this report, we show that high-resolution in-cell NMR spectroscopy of proteins enables the investigation of the structures, functions and folding stabilities of specific proteins using human cells in an intracellular environment. Our results demonstrate that detachment of the proteins from CPPs yields a homogeneous dispersion of labelled proteins in the cytosol, which allows the proteins to form specific protein–protein and protein–drug complexes. Protein transduction by CPPs have been shown to be applicable to a variety of cells, including established cell strains, primary cultured cells and even cells of living animals^{10–12,22}. Thereby, the present in-cell NMR technique opens up a multitude of different applications, such as the study of protein dynamics, investigations of amyloid-forming or intrinsically unstructured proteins in neuronal cells, and molecular diagnostics by observing probe proteins in biopsy specimens.

METHODS SUMMARY

Protein transduction to HeLa cells for in-cell NMR spectroscopy. Protein transduction into HeLa cells was carried out as described previously⁸ with modifications. Approximately 2×10^6 cells were plated into two 90-mm Petri dishes and incubated in DMEM medium containing 10% FBS (Thermo Fisher Scientific), penicillin and streptomycin for 48 h under 5% CO₂ humidified atmosphere. After removing the medium, the cells were washed twice with PBS. The cells were incubated with 1-pyrenebutyric acid (Sigma-Aldrich) in PBS for 5 min at 37 °C, and then the CPP-linked protein dissolved in PBS was added. The final concentrations of both pyrenebutyrate and protein were 250 μM. After a 10-min incubation at 37 °C, the cells were washed five times with PBS. The pyrenebutyrate/CPP-treatment was repeated four times. After each of the four rounds of treatment, the cells were incubated for 40 min at 37 °C in medium. The cells were then detached from the dish by treatment with 0.01% (w/v) trypsin (5 ml per dish) for 10 min at 37 °C. The cells were then gently suspended in 20 ml of the medium containing 5 mM HEPES (pH 7.2) and 90 mM D-glucose. The resulting cell suspension (30 ml) was incubated for 30 min at 37 °C, and then centrifuged at 100g for 5 min at room temperature. Finally, the cell pellet was resuspended in DMEM containing 5 mM HEPES (pH 7.2), 90 mM D-glucose and 5% D₂O, yielding 200 μl of cell suspension, which was used for the NMR measurements.

NMR spectroscopy. In-cell and the reference 2D ¹H–¹⁵N correlation NMR spectra were obtained using the band-selective optimized flip-angle short transient (SOFAST)-heteronuclear multiple quantum coherence (HMQC) pulse sequence²³. The data for the indirectly acquired dimension (¹⁵N) were acquired by a nonlinear sampling scheme and processed by maximum-entropy reconstruction²⁴, except for those of cell lysates.

Full Methods and any associated references are available in the online version of the paper at www.nature.com/nature.

Received 16 October 2008; accepted 23 January 2009.

1. Serber, Z. & Dotsch, V. In-cell NMR spectroscopy. *Biochemistry* **40**, 14317–14323 (2001).

2. Burz, D. S., Dutta, K., Cowburn, D. & Shekhtman, A. Mapping structural interactions using in-cell NMR spectroscopy (STINT-NMR). *Nature Methods* **3**, 91–93 (2006).
3. Dedmon, M. M., Patel, C. N., Young, G. B. & Pielak, G. J. FlgM gains structure in living cells. *Proc. Natl Acad. Sci. USA* **99**, 12681–12684 (2002).
4. Sakakibara, D. *et al.* Protein structure determination in living cells by in-cell NMR spectroscopy. *Nature* doi:10.1038/nature07814 (this issue).
5. Sakai, T. *et al.* In-cell NMR spectroscopy of proteins inside *Xenopus laevis* oocytes. *J. Biomol. NMR* **36**, 179–188 (2006).
6. Selenko, P. *et al.* Quantitative NMR analysis of the protein G B1 domain in *Xenopus laevis* egg extracts and intact oocytes. *Proc. Natl Acad. Sci. USA* **103**, 11904–11909 (2006).
7. Selenko, P. *et al.* In situ observation of protein phosphorylation by high-resolution NMR spectroscopy. *Nature Struct. Mol. Biol.* **15**, 321–329 (2008).
8. Takeuchi, T. *et al.* Direct and rapid cytosolic delivery using cell-penetrating peptides mediated by pyrenebutyrate. *ACS Chem. Biol.* **1**, 299–303 (2006).
9. Futaki, S. Oligoarginine vectors for intracellular delivery: design and cellular-uptake mechanisms. *Biopolymers* **84**, 241–249 (2006).
10. Nakase, I., Takeuchi, T., Tanaka, G. & Futaki, S. Methodological and cellular aspects that govern the internalization mechanisms of arginine-rich cell-penetrating peptides. *Adv. Drug Deliv. Rev.* **60**, 598–607 (2008).
11. Wender, P. A. *et al.* The design of guanidinium-rich transporters and their internalization mechanisms. *Adv. Drug Deliv. Rev.* **60**, 452–472 (2008).
12. Schwarze, S. R., Ho, A., Vocero-Akbani, A. & Dowdy, S. F. *In vivo* protein transduction: delivery of a biologically active protein into the mouse. *Science* **285**, 1569–1572 (1999).
13. Loison, F. *et al.* A ubiquitin-based assay for the cytosolic uptake of protein transduction domains. *Mol. Ther.* **11**, 205–214 (2005).
14. Carlson, N. & Rechsteiner, M. Microinjection of ubiquitin - intracellular-distribution and metabolism in HeLa-cells maintained under normal physiological conditions. *J. Cell Biol.* **104**, 537–546 (1987).
15. O'Brien, R. & Gottlieb-Rosenkrantz, P. An automatic method for viability assay of cultured cells. *J. Histochem. Cytochem.* **18**, 581–589 (1970).
16. Gariat, I. & Muir, T. W. Protein semi-synthesis in living cells. *J. Am. Chem. Soc.* **125**, 7180–7181 (2003).
17. Hicke, L., Schubert, H. L. & Hill, C. P. Ubiquitin-binding domains. *Nature Rev. Mol. Cell Biol.* **6**, 610–621 (2005).
18. Itoh, S. & Navia, M. A. Structure comparison of native and mutant human recombinant FKBP12 complexes with the immunosuppressant drug FK506 (tacrolimus). *Protein Sci.* **4**, 2261–2268 (1995).
19. Ellis, R. J. Macromolecular crowding: obvious but underappreciated. *Trends Biochem. Sci.* **26**, 597–604 (2001).
20. Bai, Y. *et al.* Thermodynamic parameters from hydrogen exchange measurements. *Methods Enzymol.* **259**, 344–356 (1995).
21. Lange, O. F. *et al.* Recognition dynamics up to microseconds revealed from an RDC-derived ubiquitin ensemble in solution. *Science* **320**, 1471–1475 (2008).
22. Delom, F., Fessart, D., Caruso, M. E. & Chevet, E. Tat-mediated protein delivery in living *Caenorhabditis elegans*. *Biochem. Biophys. Res. Commun.* **352**, 587–591 (2007).
23. Schanda, P. & Brutscher, B. Very fast two-dimensional NMR spectroscopy for real-time investigation of dynamic events in proteins on the time scale of seconds. *J. Am. Chem. Soc.* **127**, 8014–8015 (2005).
24. Laue, E. D., Mayger, M. R., Skilling, J. & Staunton, J. Reconstruction of phase-sensitive two-dimensional NMR-spectra by maximum-entropy. *J. Magn. Reson.* **68**, 14–29 (1986).

Supplementary Information is linked to the online version of the paper at www.nature.com/nature.

Acknowledgements We thank M. Waelchli, A. Kidera and H. Akutsu for discussion, T. Kokubo for monkey COS-7 cells, H. Ohnishi for the plasmid for production of FKBP12 and M. Imanishi for taking gel fluorimaging. This work was supported by grants to M.S. from Japan Science and Technology Agency and the Ministry of Education, Culture, Sports, Science and Technology-Japan (MEXT), and also in part by the Global COE Program 'International Center for Integrated Research and Advanced Education in Materials Science' (No. B-09) of MEXT, administered by the Japan Society for the Promotion of Science. This work was partly supported by the Innovative Techno-Hub for Integrated Medical Bio-imaging Project of the Special Coordination Funds for Promoting Science and Technology, from MEXT to A.O. and M.S., and by grants from MEXT to S.F. and H.T.

Author Information Reprints and permissions information is available at www.nature.com/reprints. Correspondence and requests for materials should be addressed to M.S. (shirakawa@moleng.kyoto-u.ac.jp) or H.T. (tochio@moleng.kyoto-u.ac.jp).

METHODS

Protein preparation. All proteins used to obtain the in-cell and reference NMR spectra were expressed in *E. coli* BL21(DE3), grown in M9 minimal medium containing $^{15}\text{NH}_4\text{Cl}$ as the sole nitrogen source. Ub–CPP_{Tat} and its derivatives, which contain an extra aspartic acid at the amino terminus of CPP_{Tat}, were purified as described previously²⁵. A GB1 fusion protein that has a thrombin cleavable N-terminal 6-His-tag and a cysteine residue at its N and C terminuses, respectively, was purified using a similar procedure. After the His-tag was removed, GB1–SS–CPP_{Tat} was prepared using the GB1 derivative and Cys–(NPyS, 3-nitro-2-pyridinesulfonyl)–CPP_{Tat}²⁶ (TORAY RESEARCH CENTER Inc.) as described¹⁶. To generate Ub–3A–SS–CPP_{Tat} (Fig. 2c), Ub–3A with a cysteine substitution at Gly 76 was used. The GST–SUMO1–CPP_{Tat}–Ub–FKBP12 fusion protein, which has an additional DGA sequence between ubiquitin and FKBP12, was expressed, and was purified by glutathione (GSH) affinity chromatography. After cleavage by the catalytic domain of SENP2, the CPP_{Tat}–Ub–FKBP12 fusion protein was purified by chromatography.

Immunosuppressant administration. HeLa cells were treated with ^{15}N -labelled CPP_{Tat}–Ub–FKBP12 as described above, and were detached from the dishes, collected by gentle centrifugation and suspended in 20 ml of a medium/buffer cocktail containing 30 μM FK506 or rapamycin. The cell suspension was incubated for 1 h at 37 °C, and then centrifuged at 100g for 5 min. Finally, the cell pellet was resuspended in DMEM containing 5 mM HEPES (pH 7.2), 90 mM D-glucose, 5% D₂O, and 30 μM FK506 or rapamycin, yielding 200 μl of cell suspension, which was used for the NMR measurements. The resonance assignments of unliganded FKBP12 are on the basis of a previous report²⁷.

NMR experiments. All NMR experiments were performed at 37 °C on a Bruker Avance 700 spectrometer equipped with a cryogenic TCI probe head. The volume of each cell suspension used for NMR measurements was approximately 200 μl . NMR sample tubes with a diameter of 4 mm (Shigemi) were used for in-cell NMR measurements. All the 2D ^1H – ^{15}N correlation spectra were acquired using a SOFAST-HMQC pulse sequence²³. The spectral widths were 5597.015 Hz and 2128.792 Hz for ^1H and ^{15}N , respectively. Data in the indirectly acquired ^{15}N dimension were sampled non-uniformly and processed by the maximum-entropy procedure²⁴, unless mentioned otherwise. Thirty-two time-points were randomly selected from 64 conventional linear sampling points with a $t_{1\text{max}}$ of 7.52 ms. The final size of the matrix reconstructed was $512 (F_2) \times 256 (F_1)$ complex points. Measurement of each in-cell NMR sample took no longer than 3 h. Data were processed by NMRPipe²⁸ or AZARA 2.7 software (<http://www.bio.cam.ac.uk/azara/>), and analysed with Sparky²⁹.

Assessment of cell viability after in-cell NMR experiments. The viability of the cells after each in-cell NMR experiment was checked by trypan blue staining¹⁵. The cells recovered from the NMR tube were mixed with 0.2% (w/v) trypan blue, and the number of stained cells was counted under phase-contrast microscope.

Hydrogen exchange experiments. Replacement of the exchangeable protons of Ub–CPP_{Tat} with ^2H was achieved by unfolding the protein using 6 M guanidium hydrochloride in PBS (pH 7.3) containing D₂O. The protein was then refolded by repeated dialysis against PBS in D₂O. Finally, the sample was dialysed against PBS (pH 7.3) in H₂O. At this stage, only highly protected amides were deuterated. The deuterated protein was transduced into HeLa cells as described in the Methods Summary, except for the incubation temperature, which was room temperature. Data for the ^1H – ^{15}N -correlation spectrum of the cells were then collected at 37 °C for 3 h. For an *in vitro* reference, deuterated Ub–CPP_{Tat} was incubated in PBS (pH 7.3) at room temperature for 6 h and at 37 °C for 5 h, and then the spectrum was measured for 5 min. To measure hydrogen exchange rates

in cells, Ub–CPP_{Tat} and Ub–3A–CPP_{Tat}, in which the protected amides were deuterated, were transduced into HeLa cells as described above, except for times of pyrenebutyrate/CPP treatment, which were two. In addition, the treatments were done without an interval incubation. This procedure of pyrenebutyrate/CPP treatment took 30 min in total. The cells were then incubated at 37 °C until they were collected for disruption, except for the experiments for data collected at a time point of 30 min, in which the cells were collected for disruption immediately after the pyrenebutyrate/CPP treatment. At 30, 60, 120 and 210 min after the start of protein transduction, the cells were detached from the dishes, washed and disrupted in 100 mM ammonium acetate and 50 mM sodium chloride (pH 5) to obtain cell lysates. The lysates were concentrated approximately 1.5-fold by Microcon-YM3 (Millipore). ^1H – ^{15}N SOFAST-HMQC spectra of the lysates were acquired at 37 °C for 20 h by a linear sampling scheme and processed by Fourier transformation. Three independent experiments were performed for each time point. The signal intensities of the main-chain amides of Val 5, Leu 15, Lys 27 and Ile 30 were used for the analysis, because they were invariant for at least 20 h *in vitro* at pH 5. The cross-peak intensities were normalized by the averaged intensities of the main-chain amides of 14 residues, the hydrogens of which rapidly exchange with water even in the folded state.

To estimate the variance of the cross-peak intensities due to intracellular effects other than hydrogen exchange, we performed the same procedure using fully protonated proteins. The signal intensities were used to normalize the hydrogen exchange data. Furthermore, the protonation ratios of the samples used for the protein transductions were assessed by *in vitro* spectra, and were used to correct intensity data. The normalized intensities at time t after the start of protein transduction, $\text{Int}(t)$, were fitted to the equation $\text{Int}(t) = 1 - \exp(-k_{\text{ex}}t)$, in which k_{ex} is the hydrogen exchange rate. To obtain k_{ex} values for the *in vitro* condition, ^1H – ^{15}N SOFAST-HMQC spectra were acquired for ubiquitin every 24 h for 3 days in PBS (pH 7.4) at 37 °C, and for Ub–3A every 2 h for 12 h. One experiment was performed for each time point.

Confocal laser-scanning microscopy. To generate Alexa-labelled Ub–3A–CPP_{Tat} and Ub–3A–G75A/G76A–CPP_{Tat} proteins with a cysteine substitution of Gly 35 were treated with Alexa-Fluor-488 C5 maleimide (Invitrogen). Unliganded fluorescent reagent was removed using a PD-10 column (GE Healthcare). The ratios between the labelled and unlabelled proteins were approximately 0.1. Next, 2×10^5 HeLa cells were plated into 35-mm glass-bottomed dishes and cultured for 48 h. The cells were treated first with 50 μM pyrenebutyrate for 5 min, and then with 75 μM protein in the presence of 50 μM pyrenebutyrate for 10 min. Distribution of the Alexa-labelled proteins in HeLa cells was analysed without fixing using a confocal laser-scanning microscope (Olympus FV300) equipped with a $\times 60$ objective lens. The fluorescence signals were detected by excitation with the 488-nm Argon laser using an emission filter (510–530 nm).

25. Tenno, T. *et al.* Structural basis for distinct roles of Lys63- and Lys48-linked polyubiquitin chains. *Genes Cells* **9**, 865–875 (2004).
26. Mezo, G., Mihala, N., Andreu, D. & Hudecz, F. Conjugation of epitope peptides with SH group to branched chain polymeric polypeptides via Cys(Npys). *Bioconjug. Chem.* **11**, 484–491 (2000).
27. Rosen, M. K., Michnick, S. W., Karplus, M. & Schreiber, S. L. Proton and nitrogen sequential assignments and secondary structure determination of the human FK506 and rapamycin binding protein. *Biochemistry* **30**, 4774–4789 (1991).
28. Delaglio, F. *et al.* NMRPipe: a multidimensional spectral processing system based on UNIX pipes. *J. Biomol. NMR* **6**, 277–293 (1995).
29. Goddard, T. D. & Kneller, D. G. SPARKY 3 (University of California, 1999).

ADDENDUM

doi:10.1038/nature07825

Reconciling complexity with stability in naturally assembling food webs

Anje-Margriet Neutel, Johan A. P. Heesterbeek, Johan van de Koppel, Guido Hoenderboom, An Vos, Coen Kaldeway, Frank Berendse & Peter C. de Ruiter

Nature 449, 599–602 (2007)

In the Supplementary Information of this Letter, no biomass data were given for the two basal food-web compartments: roots and detritus. These were not measured in the soil samples (see also ref. 2). We used values for root biomass of $900 \text{ kg C ha}^{-1} \text{ cm depth}^{-1}$ in all webs with roots present. We used values for detritus biomass of 4, 25, 250 and $2,500 \text{ kg C ha}^{-1} \text{ cm depth}^{-1}$ for the successional stages 1 to 4, respectively, of both series (roughly corresponding to the increase in organic matter along the productivity gradients). Other than in the one replicate in stage 1 (Schiermonnikoog) where phytophagous nematodes were present (for which basal values of stage 2 were used), we assumed the same values for the replicates within each stage. The choice of these particular values does not affect our key findings. The data to do the stability analyses are provided in the Letter, its Supplementary Information or via refs 2 and 17. The estimated physiological parameter values, the matrix of feeding relations and prey preferences, formalization of detritus feedbacks and an example (Jacobian) community matrix are provided in the Supplementary Information to this Addendum.

Supplementary Information is linked to the online version of the paper at www.nature.com/nature.

naturejobs

**THE CAREERS
MAGAZINE FOR
SCIENTISTS**

The numbers have changed little in recent years. More white men work in the basic sciences than do either women or minorities, and they advance more quickly to higher positions. Several speakers sounded this refrain at the mid-February annual meeting of the American Association for the Advancement of Science in Chicago, Illinois. They noted that these trends continue to taint the international science community but also offered concrete suggestions for mitigating the disparity.

At a career workshop, Robert Fefferman, dean of physical sciences at the University of Chicago, said that both women and minorities must network more broadly. It's comforting and easier to stay within one's peer group, he noted, but doing so limits chances for visibility and advancement. "Overcome your shyness," he said. "Break through the temptation to stay with people who think like you."

At the same session, Catherine Cardelús, assistant professor of biology at Colgate University in Hamilton, New York, also encouraged participants to search for ways to get exposure and recognition. "You need to get your name out there," she said. "Walk up to people. Cold call. Do whatever it takes." Fefferman warned, however, that joining every possible committee or board isn't necessarily the best idea. "You'll make an impact," he said. "But they will expect you to do as good or better [in your work] as people who aren't on a committee."

Women, especially, must guard against the 'impostor syndrome', characterized by the inability to internalize one's accomplishments, instead attributing them to good luck or timing. Studies show more women than men do this, Cardelús said, adding that it helps to have female advisers and mentors who can empathize with such issues as the difficulty of long hours in the lab during pregnancy or the responsibilities of child care. These people can provide a shoulder to lean on and guide one down the thorny path of postdoc-dom and early career.

Still, little of this will make a difference if one's work is below par, speakers cautioned. "Your science," Cardelús said, "has to be excellent."

Karen Kaplan is assistant editor of *Naturejobs*.

CONTACTS

Editor: Gene Russo

Assistant editor: Karen Kaplan
e-mail: naturejobseditor@nature.com

European Head Office, London
The Macmillan Building,
4 Crinan Street, London N1 9XW, UK
Tel: +44 (0) 20 7843 4961
Fax: +44 (0) 20 7843 4996
e-mail: naturejobs@nature.com

European Sales Manager:
Dan Churchward (4966)
e-mail: d.churchward@nature.com
Assistant European Manager:
Nils Moeller (4953)

Natureevents:
Ghizlaine Ababou (+44 (0) 20 7014 4015)
e-mail: g.ababou@nature.com

Southwest UK/RoW:
Alexander Ranken (4944)

Northeast UK/Ireland:

Matthew Ward (+44 (0) 20 7014 4059)

France/Switzerland/Belgium:

Muriel Lestringuez (4994)

Scandinavia/Spain/Portugal/Italy:

Evelina Rubio-Hakansson (4973)

North Germany/The Netherlands/Eastern

Europe: Kerstin Vincze (4970)

South Germany/Austria:

Hildi Rowland (+44 (0) 20 7014 4084)

Advertising Production Manager:

Stephen Russell

To send materials use London address above.

Tel: +44 (0) 20 7843 4816

Fax: +44 (0) 20 7843 4996

e-mail: naturejobs@nature.com

Naturejobs web development: Tom Hancock

Naturejobs online production: Dennis Chu

US Head Office, New York

75 Varick Street, 9th Floor,
New York, NY 10013-1917

Tel: +1 800 989 7718

Fax: +1 800 989 7103

e-mail: naturejobs@nature.com

US Sales Manager: Ken Finnegan

India

Vikas Chawla (+91 1242881057)

e-mail: v.chawla@nature.com

Japan Head Office, Tokyo

Chiyoda Building, 2-37 Ichigayatamachi,
Shinjuku-ku, Tokyo 162-0843

Tel: +81 3 3267 8751

Fax: +81 3 3267 8746

Asia-Pacific Sales Manager:

Ayako Watanabe (+81 3 3267 8765)

e-mail: a.watanabe@natureasia.com

Business Development Manager, Greater

China/Singapore:

Gloria To (+852 2811 7191)

e-mail: g.to@natureasia.com

MOVERS

Mary Pearl, dean and administrative vice-president, Stony Brook University, Southampton, New York



1993–2009: President, executive director, Wildlife Trust, New York

1994–99: Associate director, Center for Environmental Research and Conservation, New York

1988–93: Assistant director, Wildlife Conservation International, New York

Conservation scientist Mary Pearl had no plans to leave her 15-year post as president and executive director of the Wildlife Trust. But when a headhunter told her about the position of dean and administrative vice-president at Stony Brook University's new Southampton campus, Pearl couldn't decline. The campus features an innovative curriculum centred on sustainability and the environment, and the post was an obvious match given Pearl's long-time devotion to education and environmental stewardship.

"She's driven by the desire to make a change in the world," says Peter Daszak, who succeeds Pearl as Wildlife Trust president. "She has such energy and passion. Every day she asks, 'What have I achieved for conservation today?'"

Initially interested in the evolution of social behaviour, Pearl realized while studying primates that she found sustainability and conservation more compelling. "I was doing my dissertation research in Pakistan at a time when dams were silting up because trees were being cut down for firewood," Pearl says. "I thought, 'I can study these monkeys, but the larger issue is, will they have a forest?'"

With a PhD in physical anthropology, Pearl began working at the World Wildlife Fund. "I had to talk my way into a job there, and the only job available was in corporate fundraising," Pearl remembers. "But it became a great lesson in bringing in different people to solve problems."

In her next position, at the Wildlife Conservation Society, Pearl developed an Asia-Pacific programme. Later, she became associate director of the Center for Environmental Research and Conservation, a consortium based at Columbia University, New York, that includes the Wildlife Trust. Pearl also co-founded the Consortium for Conservation Medicine, a collaboration of Wildlife Trust with other organizations and universities. Conservation medicine examines the links between wildlife, ecosystems and human health.

At Southampton, Pearl will bring her zeal to a new audience. She looks forward to overseeing a new curriculum centered around not departments but rather issues related to sustainability, public policy and natural resource management. "This is tremendously exciting, to create a new model of undergraduate education based on issues of sustainability," she says. "We will engage the bright and driven student who is interested in how our natural systems on this planet need to be managed. This is a serious enterprise, not some kooky experiment."

Karen Kaplan

BRICKS & MORTAR

Precourt takes up energy challenge

Stanford University's \$100-million new Precourt Institute for Energy, announced in January, has a bold mission: to tackle the spectrum of science and policy challenges needed to meet future energy demands.

It faces a complex mix of political, environmental and national security concerns. While developing renewable sources, the institute also plans long-term interdisciplinary research programmes aimed at making a new system sustainable. These will include social issues such as economics and behavioural aspects of energy use.

"By forging programmes across disciplinary boundaries, our efforts can become more than the sum of their parts," says director Lynn Orr.

The institute will start recruiting faculty soon, while using Stanford's existing talent: 137 specialists in sustainable energy, climate, energy efficiency and materials.

Materials science will be a key component. "You can argue that more than half the potential solutions to energy problems — particularly those involving energy harvesting, storage and transport — are related to materials," says Zhi-Xun Shen, director of Stanford's Geballe Laboratory for Advanced Materials. Shen says Precourt will allow the university to work on both immediate

improvements — such as developing nanostructured materials to improve solar conversion and manipulating electrochemistry to improve battery performance — and longer-term policy and infrastructure solutions.

With so many diverse researchers focused on the issue, Orr says, there will be training opportunities in almost every area. The first of 20 new graduate fellowships and five postdocs will be available through an internal competition among energy-related departments later this year.

Shen says it's becoming clear that energy decisions affect the economy as well as climate change and national security. The funders are a group of Stanford alumni (including Jay Precourt, who has given the new institute its name) with ties to the energy, oil and investment industries.

John Doerr, a partner at investment firm Kleiner Perkins Caufield and Byers, says that providing renewable-energy resources while protecting the planet presents an opportunity to remake the global economy. Orr says that the institute plans to attract those interested in both scientific innovation and economic feasibility. "We need to change an entire set of energy systems," he says. "To do that, we need as many players as we can get on the field."

Virginia Gewin

POSTDOC JOURNAL

Cyclical science

"I am sorry son, but I have just been laid off." Those were my father's words to me 16 years ago amid the recession of the early 1990s. It was a brutally hot summer's day in my hometown of Plano, Texas, when I received that worrisome news. I was 15 years old and he was a manager at Texas Instruments. Uncertainty about the future consumed my thoughts. Will we have to move? How will we be able to buy things such as food and clothes? Fortunately, my dad got a job a few months later.

Fast-forward 16 years. Another economic recession is leaving thousands of people jobless every week. As a postdoc, I am looking to establish a career soon. But I don't relish the possibility that one day I may have to tell my kids that their dad doesn't have a job. After all, I know how it feels.

With the current recession, questions race through my mind. How long will it last? Should I delay entering the job market and wait for the economy to get better? If I take a position too soon, will I be laid off shortly thereafter?

Nevertheless, at the end of the day I am an optimist. The US economy is usually cyclical, and so I am convinced that it will rebound. I don't know how bad the recession will become, but I know this too shall pass.

Bryan Venters is a postdoctoral fellow with the Center for Gene Regulation at the Pennsylvania State University.

A smooth hero

Dancing machine.

Julian Tang

"OK class, that's it for today," said Mr Phipps, wearily. "Read chapter five for tomorrow. James, can I see you for a minute?"

James looked up in surprise and saw Mr Phipps give him a wink. He liked science best and Mr Phipps knew it. He often stayed behind after class so that Mr Phipps could show him something new. Once everyone had gone, he approached the front desk, expectantly. Mr Phipps reached under his desk, producing a large cardboard box.

"Picked this up at a car-boot sale last weekend," he said. "From an old man who said he'd never used it. His son's some sort of inventor and gave it to him years ago. Must've had no idea what it could do. I'm still learning about it."

He lifted out a double-cassette/CD/radio ghetto-blaster, placing it carefully on the desk.

"OK, sooo ...?" James looked at him, questioningly.

"Have a closer look."

So, he did, and noticed that one side of the double-cassette player was actually a glass window with a funny-looking bulb behind it. The bulb's glass surface seemed to change colour and pattern as he moved his head around it, like a hologram. A rocker switch on the top panel was labelled 'Normal', 'Reality' and 'Reality Plus'.

"Hmm, OK it's strange, but what does it do?"

"You got a CD?"

James rummaged in his bag and handed him his Michael Jackson *Smooth Criminal* CD.

Just as Mr Phipps inserted it, loud gunshots sounded in the corridor, followed by children's screams. They looked at each other, wide-eyed.

Mr Phipps went quickly to the door, looked out, then hurried back. "Quick! Under the desk," he said.

They both crammed under the desk, an old-fashioned wooden thing that looked solid from the front and sides. It was a tight fit, but not a second too soon.

The door slammed open and heavy footsteps entered the room. After a short pause, a man's rather muffled voice shouted, "Clear here."

The footsteps receded quickly and the door slammed shut. They emerged cautiously. Mr Phipps grabbed the ghetto-blaster and beckoned for James to follow.

The science lab was on the first floor where there was a balcony overlooking the assembly hall. Hearing faint sounds of sobbing they carefully looked down into the hall below. His classmates and teachers were sitting on the floor, surrounded by at least six gunmen wearing black ski masks.

"We have to call the police!" whispered James urgently.

"You got a phone? Mine's in the staffroom downstairs," replied Mr Phipps in frustration. "The classrooms don't have any phones."

James was looking curiously at the ghetto-blaster. "Why did you bring that?"

Mr Phipps looked puzzled for a moment then his face lit up. "Ah, forgot about that! Come with me."

They stole back to the balcony door and pushed it open, quietly. Mr Phipps positioned the ghetto-blaster, facing the glass panel down into the main hall. He opened the back and unexpectedly produced a wireless games controller.

"What's this for?" asked James in surprise, fingering the controller, very similar to the one from his PlayStation.

"You like those kung-fu combat games?"

James nodded.

"OK, well then, get ready!" He pressed play.

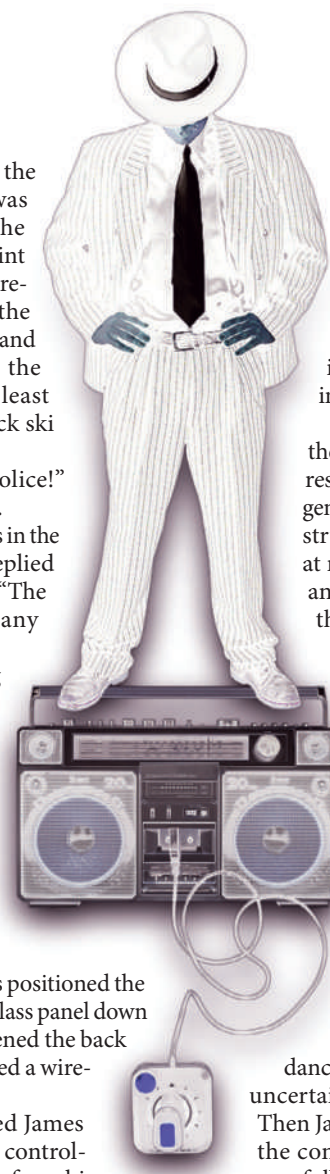
After a few seconds of silence, Michael's characteristic scream "Oww!" pierced the air of the hall, followed by the metallic beat of *Smooth Criminal*.

Startled, the gunmen looked around, frantically, for the origin of the music. Then after a few moments they started to move towards the stairs to the balcony.

James shook Mr Phipps's shoulder, desperately pointing at the men.

"Yes, I've seen them. Don't worry," said Mr Phipps. "Get ready with that controller." He pushed the rocker switch to 'Reality'.

Instantly, a dancing holographic image of Michael Jackson dressed in a white suit and hat appeared, suspended just above the heads of the sitting children. He looked



so solid and real! The gunmen fired, reflexively, but their bullets passed ineffectively through the image. Some of the children seemed to forget their fear, just staring in wonder at this dancing image above them.

Mr Phipps then flicked the switch to 'Reality Plus'. In response, MJ's image landed gently on the floor and started strutting around, seemingly at random, his gyrating feet and legs passing harmlessly through the children as he moved.

The gunmen fired again at his image, without effect. Then as MJ reached one of the gunmen, he performed his trademark high leg-kick that caught the gunman between his legs. His look of surprise turned to one of agony as he collapsed on the floor, howling.

The MJ image stayed, dancing at that spot, seemingly uncertain as to where to go next. Then James got the idea. He used the controller, moving MJ purposefully around the hall, disarming and disabling each gunman with well-aimed powerful dance moves.

Very soon, all the gunmen were down, either unconscious or writhing in pain. The teachers collected the guns. Luckily, no one had been hit by any stray bullets. Mobile phones were recovered and the police were called.

Mr Phipps clapped and hugged James. "Well done James!"

Leaving the ghetto-blaster where it was for the moment, they went downstairs, agreeing to feign ignorance. When the police arrived, nothing anyone said seemed to make any sense.

James and Mr Phipps nudged each other and just grinned.

Julian Tang is a clinical/academic virologist, who, among other things, enjoys reading science fiction, fantasy and horror. He has many story ideas, but needs time to commit them to paper. He lives and works in Singapore.

JACEY